Bridge Structural Health Monitoring Using a Cyber-Physical System Framework

by

Rui Hou

A dissertation submitted in partial fulfillment
of the requirements for the degree of
Doctor of Philosophy
(Civil Engineering)
in the University of Michigan
2020

Doctoral Committee:

Professor Jerome P. Lynch, Chair
Professor Kincho H. Law, Stanford University
Professor Victor C. Li
Associate Professor Gábor Orosz
Associate Professor Jeffrey T. Scruggs

Rui Hou
rayhou@umich.edu
ORCID iD: 0000-0001-5829-4628

DEDICATIONS

To my daughter Emma, my wife Cong, and my parents Xiangdong & Yufang.

To the memory of my grandfather, Yanxi.

ACKNOWLEDGMENTS

I would like to first express my great gratitude to my advisor Professor Jerome Lynch. I first met with Professor Lynch when I entered the University of Michigan as a master student taking his dynamics course. His passion and erudition in the class are still fresh in my mind, and largely triggered my interests in the domain of intelligent systems back then. After I joined his group, Professor Lynch offered me the best guidance and inspiration throughout my five-year Ph.D. education. I received insightful and patient guidance from him, motivating me to keep learning new knowledge, improving my research and achieving research goals. Besides academic guidance, Professor Lynch also taught me how to be dedicated, thoughtful and open-minded in my life, which is even more beneficial to me. I feel fortunate to have the mentorship and friendship with Professor Lynch.

I want to thank my dissertation committee members, Professor Kincho Law, Professor Victor Li, Professor Jeff Scruggs and Professor Gabor Orosz. Professor Kincho Law offered me professional guidance and supports in our collaborative research projects. Working with him had an enormous impact on forming the final framework of my dissertation on cyber-physical systems. He also provided me insightful advice regarding my career planning - being open-minded about all possibilities. From Professor Victor Li and Professor Jeff Scruggs, I gained deeper understandings on my research (especially on concrete and structural dynamics,respectively) from their courses as well as the discussions with them. I had the chance to participate into the connected vehicle project with Professor Gabor Orosz and learned many cutting-edge knowledge from him.

I am lucky to have outstanding colleagues throughout my Ph.D. life. Dr. Sean O'Connor, Dr. Yilan Zhang and Dr. Nephi Johnson were my mentors on wireless sensing and sensor instrumentation. The experience and skills that I learned from them are essential to the completion of my

doctoral research. I would also like to thank Dr. Seongwoon Jeong; we worked collaboratively on the cyber-physical system project and I learned quite a lot from him on cloud computing platforms and database management systems. I also worked with Dr. Wentao Wang, Dr. Peng Sun, Ms. Katherine Flanigan and Mr. Omid Bahrami on several different projects; these experiences are great fortunes for me to learn from them. I appreciated and enjoyed my time with Dr. Andy Burton, Mr. Mitsuhito Hirose, Mr. Hao Zhou and all other mates in the LIST lab at the University of Michigan.

My utmost appreciation goes to my family. I am especially grateful to my parents, who supported me emotionally and financially. It was their unconditional love that raised me up again when I got weary. I thank my beloved wife, Cong, for always standing behind me, adding joy to my life and being strong when I am not around. It is her love that keeps me moving forwarding without any hesitation. I also appreciate my little girl Emma for abiding my absence from home during my thesis writing. Words would never say how grateful I am to both of you.

The research work presented in this thesis was supported by a collaborative project funded by the US National Science Foundation (NSF) (Grant No. EECS-1446521 to the University of Michigan and Grant No. EECS-1446330 to Stanford University) and by a project funded by the National Institute of Standards and Technology (NIST) Technology Innovation Program (Cooperative Agreement 70NANB9H9008). Any opinions, findings, and conclusions or recommendations expressed in this thesis are those of the author and do not necessarily reflect the views of NIST and NSF. I would like to acknowledge the Michigan Department of Transportation (MDOT), especially Mr. Peter Jansson and Mr. Matt Niemi, for access to the I-275 northbound corridor including Telegraph Road Bridge and Newburg Road Bridge. I am grateful for their offering of support during on-site installation of the wireless monitoring systems utilized in this thesis. I would also like to thank the technicians in the Department of Civil Engineering, especially Mr. Bob Spence, Mr. Steve Dibajkowski and Mr. Ethan Kennedy for offering support on the design and manufacture of wireless sensing devices. This assistance is gratefully appreciated.

TABLE OF CONTENTS

LIST OF FIGURES

Figure

LIST OF TABLES

Table

ABSTRACT

Highway bridges are critical infrastructure elements supporting commercial and personal traffic. However, bridge deterioration coupled with insufficient funding for bridge maintenance remain a chronic problem faced by the United States. With the emergence of inexpensive sensors and wireless sensor networks (WSN), structural health monitoring (SHM) has gained increasing attention over the last decade as a viable means of assessing bridge structural conditions for asset management. Collected SHM data provides a quantitative basis for bridge performance assessment and to detect damages, thereby allowing informed maintenance decisions to be made. While intensive research has been conducted on bridge SHM, few studies have clearly demonstrated the value of SHM to bridge owners, especially using real-world implementation in operational bridges.

This thesis first aims to enhance existing bridge SHM implementations by developing a cyber-physical system (CPS) framework that integrates multiple long-term bridge SHM systems using the Internet with intelligent transportation systems including traffic cameras and weigh-in-motion (WIM) stations located along the same corridor. To demonstrate the efficacy of the proposed CPS, a 20-mile segment of the northbound I-275 highway between Newport and Romulus, Michigan is instrumented with four traffic cameras, two bridge SHM systems and a WIM station. Real-time truck detection algorithms are employed to intelligently trigger the bridge SHM systems for data collection during large truck events. Such a triggering approach is shown to be able to improve the efficiency of data acquisition by up to 70% (as compared to schedule-based data collection). Leveraging computer vision-based truck re-identification techniques applied to videos from the traffic cameras along the corridor, a two-stage data integration pipeline is proposed to fuse bridge input data (i.e. truck loads as measured by the WIM station) and output data (i.e. bridge responses to a

given truck load). From August 2017 to April 2019, over 20,000 truck events have been captured by the proposed CPS framework. To the author's best knowledge, the CPS implementation is the first of its kind in the nation and offers large volume of heterogeneous input-output data thereby opening new opportunities for novel data-driven bridge condition assessment methods.

Built upon the developed CPS framework, the second half of the thesis focuses on use of the data in real-world bridge asset management applications. Long-term bridge strain response data is used to investigate and model composite action behavior exhibited in slab-on-girder highway bridges. Partial composite action is observed and quantified over negative bending regions of the bridge through the monitoring of slip strain at the girder-deck interface. It is revealed that undesired composite action over negative bending regions might be a cause of deck deterioration. The analysis performed on modeling composite action is a first in studying composite behavior in operational bridges with in-situ SHM measurements. Second, a data-driven analytical method is proposed to derive site-specific parameters such as dynamic load allowance and unit influence lines for bridge load rating using the input-output data. The resulting rating factors more rationally account for the bridge's systematic behavior leading to more accurate rating of a bridge's load-carrying capacity. Third, the proposed CPS framework is shown capable of measuring highway traffic loads. A truck with a mobile WSN installed is used in the CPS framework to measure the truck dynamics when it crosses a bridge. The collected data enables a two-stage system identification approach to be developed for vehicle-bridge interaction modeling. The paired WIM and bridge response data can also be used for training a learning-based bridge WIM system where truck weight characteristics such as axle weights are derived directly using corresponding bridge response measurements. Such an approach is successfully utilized to extend the functionality of an existing bridge SHM system in the I-275 corridor for truck weighing purposes achieving precision requirements of a Type-II WIM station (e.g. vehicle gross weight error of less than 15%).

CHAPTER 1.

Introduction

1.1 Cyber-physical Systems in Civil Engineering

The concept of cyber-physical system (CPS) was first formalized by the National Science Foundation (NSF) during its first workshop on CPS in Austin, TX in 2006 and later recognized as a promising direction of the development of networking and information technologies by the President's Council of Advisors on Science and Technology (PCAST) in 2007 [1, 2, 3]. By definition, a CPS is an engineered system that integrates sensing, communication and computation technology into physical systems which can then be intelligently monitored, connected, coordinated and controlled [3, 4, 5]. It is typically composed of two critical component types: physical systems and cyber (or digital) systems. The architectural paradigm of a CPS can be illustrated as Figure 1-1. The physical system is the bases of a CPS and the target subject that the CPS is built to enhance. Depending on the domain of the CPS application, physical systems can range from manufacturing systems (e.g., welding machines, conveyors) [2] and transportation systems (e.g., aircraft, automobiles, traffic control systems) [6] all the way to medical devices (e.g., surgical robots) [7]. On the other hand, the cyber system is made up of a combination of cutting edge technologies, such as embedded systems, wireless sensing devices, communication infrastructures, and data management platforms. These cyber elements augment the function of the physical entities of a CPS to provide the capabilities of sensing, computing, communicating, and controlling [2]. Sensors and monitoring systems are the starting point of a CPS; they measure data and gather information from the physical system so that the physical system state is quantitatively identified for further analyses and control. The communication layer employs communication technologies (i.e. wired or wireless)

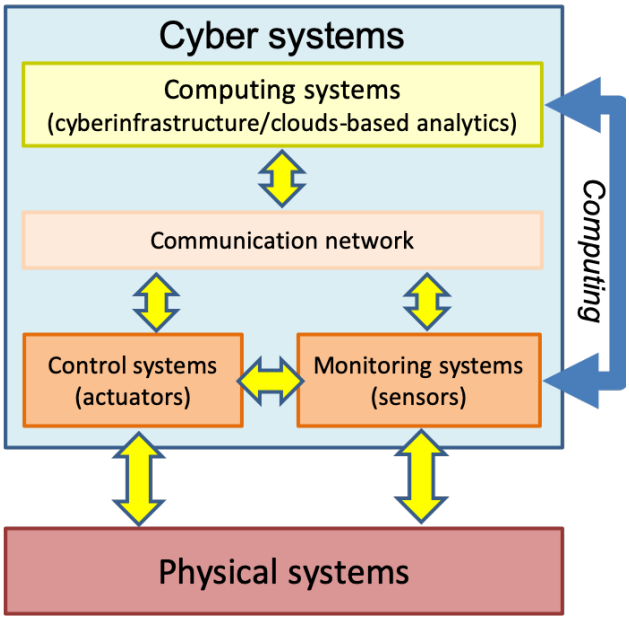

Figure 1-1: Schematic cyber-physical system paradigm.

to provide connectivity among different components within the cyber system. The communication network also facilitate interaction between different CPS that interact. In many respects, CPS is closely intertwined with the "Internet of Things (IoT)" especially from the aspect of state awareness and connectivity built by the cyber system components embedded with physical systems [8]. The computing systems integrated with CPS act as the brain of the CPS by automatically processing collected information and making decisions based on analysis outcomes. Depending on the design of the CPS, the computing system can be a centralized platform (e.g., cloud-based server), an edge-computing device (e.g., single board computer) directly tethered with sensors, or multiple edge-computing nodes cooperating in a distributed manner (e.g., in-network computing facilitated by local area network (LAN) connections) [9]. Finally, the control system achieves the objective of affecting the behavior and performance of the physical system by closing a feedback loop that allows data from the monitoring system to be used as an input to a control loop implemented in the computing system with outputs driving actuation of the physical system.

The rapid maturing of CPS as an established approach to enhancing the performance of physical systems is due to the emergence of new technologies in the computer and electronic fields. For example, embedded systems technologies including micro-controller, wireless transceivers and

miniaturized sensors has allowed low cost sensors to be quickly deployed in physical systems. Further, information technologies are offering increasing access to computational power including cloud-based computing and distributed database systems at a low cost. Various realms including manufacturing, health care, robotics and other industrial sectors have significantly profited from recent developments in CPS technologies over the last decade [3]. Similar to other domains, the adoption of CPS solutions has become one of the fastest-growing research topics in civil engineering [10, 11].

Transportation is one of the earliest areas in civil engineering that has embraced the benefits brought by CPS [12, 13, 14]. Intelligent transportation systems (ITS) utilize CPS architectures to equip conventional transportation systems (e.g., highway systems) with various types of high-tech devices such as sensors (e.g., radar detectors, cameras and inductive loops) [15] and actuators (e.g., smart traffic lights and dynamic traffic signs) [14]. These CPS elements allow traffic to be monitored and controlled with low latency. Aside from transportation infrastructures, a great amount of effort has also been made to build smarter vehicles that have perception and connectivity technology coupled with abundant computational capability that empower the vehicle to drive autonomously and to communicate with other vehicles and infrastructures for safer and faster travels. Such transformations are currently taking place all over the world covering almost every aspect of human mobility including driving, navigation, ride sharing and parking.

Another area now empowered by CPS is the smart city. Smart cities adopt CPS solutions to transform almost every aspect of urban life [16]. Energy transmission and consumption in cities is a domain where CPS plays an important role. For example, smart power grids are implemented to help better understand demand and supply relationships within the network and identify network issues (e.g., connection) at an early stage [17, 18]. Heat, air ventilation, and cooling (HAVC) systems in buildings can also be controlled by CPS in an intelligent and automatic way for better energy efficiency [19]. Instrumented with reliable sensors (e.g., flow meters) and smart actuators (e.g., automatic gate, valves), urban water networks can also be monitored and controlled in real-time for flood hazard management [20, 21]. Real-time measurements and reports of living

metrics, such as air quality, humidity and public safety, just to name a few, significantly facilitate the interaction that people have every day with their living environment [22]. The abundant data collected over time through CPS architectures embedded in the built environment offer a more resilient approach to offering infrastructure services to urban communities.

Structural health monitoring (SHM) and structural control is another field in civil engineering where the principles of the CPS framework are extensively leveraged [23, 24, 25, 26]. SHM requires sensor networks to be deployed on a structure, such as a building or a bridge, to collect data related to the structure's responses (e.g., vibration and deformation) and its relevant environmental and operational conditions (EOC) (e.g., temperature and external loads) [27]. The structural condition of the asset can then be quantitatively estimated through analyses based on the collected data. The assessed condition can then inform which actions (e.g., load posting and structural rehabilitation) can be taken to ensure safe use of the structure. When integrated with information systems, such as building information modeling (BIM) or bridge information modeling (BrIM), the measurements obtained from SHM can be better visualized and interpreted for asset management purposes [28]. Structural control on the other hand relies on the data collected to perform closed-loop control of the system to mitigate structural responses to extreme load events (e.g., earthquake) in order to prevent damage [29]. Driven by recent advances in CPS technology, this dissertation explores the creation of a CPS framework for bridge SHM. Specifically, the objective objective of the CPS will be to enhance existing practices of bridge condition monitoring and asset management.

1.2 Structural Health Monitoring and Asset Management for Bridges

According to the ASCE 2017 Infrastructure Report Card, the United States has witnessed a continuous improvement on the condition of national road bridges over the last decade. For example, the deficient bridge ratio dropped from 12.3% in 2007 to 9.1% in 2016 [30]. However, as of 2016, the situation is still not optimistic with 39% of the nation's 614,387 bridges being 50 years or older with 13.6% of them rated as functionally obsolete [30]. What makes it worse is that, on average,

there were 188 million trips across a structurally deficient bridge each day in 2016 [30] with user demands increasing every year (for instance, highway vehicle miles traveled increased 0.2% per year from 2004 to 2014) [31]. Considering most bridges were designed for an expected lifespan of 50 years, it was estimated that around $123 billion is needed to clear the backlog of bridge maintenance and rehabilitation in the limited states [30]. Consequently, aging and deteriorating bridges pose a potential risk to public safety making it an urgent issue for the country.

Routine visual inspection (VI) conducted by trained inspectors and engineers is the most common practice in the United States to assess bridges' conditions [32, 33]. It is recommended by the Federal Highway Administration (FHWA) that VI should be performed at least once every 24 months for a bridge [34, 35]. However, several limitations are associated with VI: 1) VI is a discrete monitoring process and the scheduled inspection frequency might result in ignorance of early-stage damage; 2) it might be difficult if not impossible to inspect some places of the structure due to limited accessibility or safety concerns; 3) inspection results are subject to inspectors' subjective judgement which introduce some challenges for objective interpretation; 4) VI is costly to perform in terms of labor, equipment and in some cases the downtime of the bridge to traffic [32, 33]. When it comes to material defects hidden from view (e.g., corrosion of reinforcement steel-bars, delamination of composite components), non-destructive testing (NDT) methods (e.g., electromagnetic testing and ultrasonic testing) can be adopted to exam the local condition of the structural element [36, 37]. While NDT provides a quantitative basis for condition evaluation, it too is costly due to the equipment needed and the trained personnel required to perform such methods. Also, these methods tend to be highly localized so prior knowledge of an issue is necessary.

With rapid growth of sensing technology, bridge structural health monitoring (SHM) has gained wide acceptance in both academia and industry in recent years [38, 27, 39]. A bridge SHM system usually consists of two parts: a sensor network and post-collection damage detection algorithms. The target bridge needs to be instrumented with sensors (e.g., accelerometers, strain gauges, thermistors) and a data acquisition system (e.g., wired or wireless sensor, signal communications, analog-to-digital conversion, data storage) to automatically collect data pertaining to bridge behav-

iors (e.g., vibration and deformation) and EOC (e.g., temperature and wind speed) continuously or at regular intervals. The observations are fed into an automated pipeline for data processing, feature extraction and performance assessment aiming to not only classify structural damage states but also identify damage (e.g. existence, location, severity). Existing damage detection algorithms mainly depend on two major sources of bridge responses: bridge vibration/accelerations and strain responses [38]. Vibration-based SHM frameworks seek to extract bridge dynamic characteristics (including natural frequencies, mode shapes, modal strain energy, and damping ratios) from vibration measurements and consider the changes of those characteristics over time as indicators of damage [40, 38, 41, 42]. While vibration-based methods are extensively explored, there is a growing interest in strain-based damage detection frameworks for bridge SHM [38]. Strain-based methods either directly observe discrepancies in terms of the amplitudes of strain time-histories [43] or derive unique metrics (e.g., neutral axis positions) for damage detection [44, 45, 46]. In contrast to manual inspection, the SHM approach offers quantitative measurements reflecting bridge structural conditions and thus avoids the issue of misinterpretation [47, 48]. Another benefit is that monitoring performed by SHM can be carried out more frequently (often continuously) than manual inspection, which allows condition assessment and decision-making to be based on a more rational condition-based framework [49, 32]. Although SHM provides a wealth of data, VI still represents the most comprehensive and proven approach to asset management. However, as SHM evolves it can grow to complement and potentially replace VI.

Since the emergence of bridge SHM, the technology has undergone constant refinement and improvements. The first trend has been the replacement of wired (tethered) sensor networks with wireless sensor networks (WSN) [50, 39, 51]. Numerous SHM systems deployed in operational bridges using WSNs have demonstrated the potential for WSNs for bridge SHM applications [39, 51]. The WSN is growing into a preferred approach for bridge SHM due to its low cost and less laborious installations. In addition, recent advances in edge computing and embedded systems are allowing SHM systems to be deployed in a distributed fashion using WSNs to further enhance its efficiency and computing capabilities.

Second, as SHM sensing technology (especially WSNs)have grown more mature, there has been a growth in long-term bridge SHM programs implemented in practice [47, 33, 52]. Temporary bridge SHM systems are usually deployed to: 1) address specific time-sensitive issues known to bridge owners, 2) act as quick testbeds for emerging techniques, or 3) to serve as data-collection platforms for bridge load rating [38]. In contrast, long-term programs mainly focus on the evolution of bridge condition over time and the effects of various EOCs on structural performance. Abundant bridge data can be collected using long-term SHM systems which accelerates the development of novel data-driven methods for bridge condition assessments. Some notable long-term bridge SHM programs include the Stork bridge (cable-stayed) in Switzerland monitored since 2006 [53], the Tamar bridge (suspension) in the United Kingdom monitored from 2006 to 2009 [54], the Jindo bridge (cable-stayed) in South Korea monitored from 2009 to 2012 [55], the Mjosund bridge (steel box-girder) in Norway monitored from 2000 to 2001 [56], the Cleddau bridge (steel box-girder) in the United Kingdom monitored from 2011 to 2013 [57], the New Carquinez bridge (suspension) in California monitored from 2011 to 2016 [58], Aizhai Bridge (suspension) in China monitored since 2013 [59], Tsing Ma Bridge (suspension) in Hongkong, China monitored since 1997 [60] and the Telegraph Road bridge in Michigan monitored since 2011 [61]. A thorough review and comparison of these long-term bridge monitoring programs can be found in [33].

Third, researchers have focused on developing SHM methodologies for local damage detection in recent years. Bridges are usually designed and constructed with systematic structural redundancy to enhance safety. Minor structural damage (e.g., concrete deck cracking, constrained bearings) commonly seen in bridges typically occur in local areas and may only lead to limited reductions in overall structural performance instead of a severe loss of functionality with a safety concern [49]. Such a fact makes it challenging for SHM algorithms, especially those based on global structural behaviors and frequency-domain signals (e.g., natural frequencies), to have sufficient sensitivity to identify local but small levels of damage [62, 49, 46]. To make things more challenging, it is known that dynamics characteristics like modal frequencies are sensitive to EOC parameters (e.g., ambient temperature), often more so than to damage, which renders many

theoretically-proven damage detection algorithms impractical for field use [63, 62, 64]. Robust SHM technology help address some of these challenges and limitations by facilitating denser sensor installations that offer spatially high-resolution bridge data that can lead to the development of novel damage detection algorithms. For example, local damage in bridges can be detected and localized with dense sensor networks (DSN) of strain gauges by constructing a mutual information matrix among different sensing channels within the network [65]. Sensor data reconstruction techniques allow anomalies to be identified at a specific sensing location by comparing measured time-history data with predicted ones. Such an approach can be realized using bidirectional recurrent neural networks (RNN) within a dense network of accelerometers, which is robust against environmental changes [66]. In another case, the auto-regressive with exogenous input (ARX) model and sensor clustering damage identification technique have been shown to detect artificial damage on a full-scale girder bridge using a dense network of inexpensive geophones [67]. In general, local damage detection algorithms offer more informative assessments of bridge conditions for decision making, and thus, more practical in real-world applications.

Despite recent advances in SHM, the SHM approach has not been widely accepted as an alternative to VI at this stage of development [49]. From a technical perspective, each bridge SHM system needs to be tailored for the specific target bridge considering its unique structural properties (e.g., geometry and materials) and potential damage patterns; this demands considerable efforts from engineers in the design of SHM systems. In terms of efficacy, few examples of SHM systems so far have managed to clearly demonstrate their value and effectiveness (when considering their costs) to the bridge owners, stakeholders and investors [33]. The necessity of customization, not-yet-validated commercial viability, and high long-term system maintenance cost make widespread adoption of SHM a slow process. An even more fundamental challenge for SHM is that most existing SHM methods have only been evaluated with simulation and laboratory experiments, which cannot represent the realistic and complex scenarios experienced by operational bridges in real-world environments. This is due to the fact that researchers lack access to operational bridges. More access to bridges, especially over long time periods, would allow researchers to explore

how to develop new approaches to bridge management that take full advantages of response data, especially as deterioration occurs. But today, only limited data sets of bridges being in both undamaged and damaged states are available making it difficult for methods proposed by researchers to be evaluated and compared [52]. Two notable benchmark SHM programs yielding data with damage states are: 1) the I-40 highway bridge in Albuquerque, New Mexico had its plate girders cut at different levels to simulate fatigue damages with vibration data before and after the damages were measured by 26 accelerometers [68]; and 2) the Z24 bridge, which was a pre-stressed concrete highway bridge in Switzerland that was monitored for one year and applied with a sequence of progressive damage states before its demolition [69]. Some other examples include creating artificial damages through steel girder flange cut [70] or installing sacrificial components [45] in real bridges for damage detection algorithm development. One area where there has been great effort to deploy SHM systems has been in long-span bridges [71, 72]. While long-span bridges are critical bridges to transportation networks and require more resources for maintenance, these SHM systems are often applied to newer bridges where deterioration is less prevalent. There is a more pressing need and opportunity for the SHM community to develop SHM systems for short-span bridges considering the fact that they make up a large fraction of the National Bridge Inventory (NBI) [27]. With the lack of binary state data (damage versus undamaged), many SHM algorithms have to be developed using methods that work on a statistically unsupervised manner. Clearly the gap in access to real bridges needs to be filled to transform in-lab experiments to real monitoring exercises that hold greater promise for advancing SHM [44]. In this dissertation, a series of novel applications of long-term SHM data collected from two SHM systems which are deployed in two short-span highway bridges in Michigan are presented to showcase the effectiveness and value of bridge SHM.

1.3 Cyber-physical System-enabled Bridge Structural Monitoring

Driven by recent advances in CPS technology, current research in SHM is now going beyond simply deploying sensors on civil infrastructure systems and collecting desired data to using more in-

novative techniques and tools such as data management platforms and data-driven analytics geared towards asset management [73, 74]. With the great amount of data generated from increasing deployments of long-term SHM systems, it has become a necessity for SHM engineers to develop scalable database management systems (DBMS) to ease the storage, management and access to enormous volumes of data [75]. Early-stage development of DBMS for SHM applications has mainly involved the use of relational database solutions such as MySQL for bridge data storage and retrieval [76, 77]. Hybrid solutions have also been explored. For example, SenStore was an implementation that takes advantages of non-relational database systems by building a hybrid DBMS based on Hierarchical Data Format (e.g. HDF5) and relational databases (e.g. PostgreSQL) [75]. The HDF5 portion of the system enables efficient storage of time history data while PostgreSQL offers efficient querying of monitoring system information. Recently, the benefits of NoSQL DBMS have been further explored to build cloud-based distributed peer-to-peer DBMS featuring high scalability and fault-tolerance [78, 79]. Following the success of Building Information Modeling (BIM) in the architecture, engineering and construction (AEC) industry, Bridge Information Modeling (BrIM) can be performed following the OpenBrIM standard. BrIM has been used in the design of MongoDB NoSQL DBMS for better atomicity and interpretability among different groups of users involved in SHM [80, 79]. Web-based and mobile-based applications have been written on top of the BrIM-based DBMS with a friendly graphical user interface (GUI) to enhance the visualization and access of heterogeneous SHM data stored in the DBMS [81].

Another difference that separates CPS-enabled SHM systems from conventional SHM systems is the integration of cross-domain and inter-network sensors to collect heterogeneous information for monitoring purposes [82]. Intensive studies have been conducted aiming at the integration of SHM systems and Intelligent Transportation Systems (ITS) to leverage data sources other than traditional bridge response data and environmental data [83]. CPS architecture can facilitate the integration of SHM and ITS systems. Traffic cameras commonly used in ITS provide image data regarding the passage of vehicular traffic over bridges, which can help identify realistic operational conditions and special events (e.g. overloaded trucks) experienced by the bridges [84]. Weigh-in-

motion (WIM) stations are another ITS innovation that offers direct quantitative measurements of vehicular loads (e.g., axle weight, axle spacing, gross vehicle weight, etc.), especially those from trucks. This data can be used to understand the truck loads experienced by the bridges. As a result, WIM data can provide input load data difficult to capture using sensors installed on bridges to enable structural analyses that can not be conducted with bridge outputs only [85]. For example, discrepancies between estimates of vehicle characteristics calculated by a calibrated bridge-WIM system and those directly measured by pavement-based WIM stations can be used as an indicator of bridge damages [86]. Apart from traffic cameras and WIM stations, other ITS sources include crowd-sourced smartphone vibration data [87] and vehicle-based mobile sensors [88] among others.

CPS can also integrate other data sources that can impact SHM. Integration among multiple bridge SHM systems possible by CPS has also been investigated. The correlation among strain responses of two adjacent bridges to the same group of vehicular loads measured by dense sensor networks can potentially reveal damage that has occurred to one or both of the bridges [65]. Two adjacent bridges instrumented with SHM systems can also work in a multi-agent manner with one SHM system activating the other when trucks are present [89].

Reviews of existing implementations of WSN-based bridge SHM systems reveal that power constraints is still a profound challenge associated with WSNs for SHM applications [39, 90]. Besides hardware solutions (e.g., low power-demand devices, energy harvesting [91]), the CPS approach can be used to mitigate this issue through distributed edge computing or intelligent control of SHM systems. Using distributed computing techniques, the extraction of desired information (e.g., model frequencies) or screening of data (e.g., selecting data corresponding to special loading events) can be completed within wireless sensors. As a result, to reduce power consumption, only information of interest, instead of the entire set of raw data, is transmitted [25, 74]. A SHM system can also be intelligently controlled such that the sensor network stay asleep until occurrences of certain structural events (e.g., structural damages or trucks with heavy loads). This can be realized using a separate sensor (e.g., an accelerator or an anemometer) as a trigger of the main network

constantly detecting events of interest beforehand [55].

In addition to the CPS innovations discussed, sensor anomaly detection (e.g., faulty sensor detection) [92] and the adoption of new communication middlewares (e.g., LTE, 5G) [93] are also exciting innovations that will accelerate CPS adoption for bridge SHM.

1.4 Data-driven Methods for Bridge Damage Detection and Performance Assessment

The emergence of reliable and inexpensive sensing technology has accelerated the deployment of long-term bridge SHM systems with dense sensor networks. These systems have the potential to produce massive amounts of SHM data. The acquired data especially its vast size has opened a new horizon for the development of data-driven methodologies for damage detection and performance assessment in bridge infrastructures. In general, the objective of data-driven methods is to find statistically significant patterns in data to identify the health conditions of the target structure [94]. Since data-driven methods don't rely on detailed physics-based models (e.g., finite element method models) which often involve approximations and assumptions, they can often be carried out with relatively low computational demand but also potentially higher accuracy in damage detection [65]. These methods follow a similar procedure consisting of two major phrases: baseline model training (or updating) based on available data and use of a trained model for monitoring (i.e., detection of damages and modifications) [52, 94, 95].

A prerequisite of baseline model training is to select features from data that are sensitive to changes in structural conditions, especially damage states of interest, but not sensitive to normal variation of EOCs such as seasonal temperature fluctuation [96]. With selected features, the essence of the baseline model training step is to find non-intersecting subspaces representing different states of structural health. Depending on the dimension of the features, the feature space can either be separated by a baseline threshold for a single value damage index or a set of planes (or hyper-planes) for multi-variable indicators [97].

One of the most direct ways of feature selection is to adopt features commonly used in mechanical model-based SHM methods and use them in a statistical manner. For example, load distribu-

tion factors of girders and neutral axis locations can all be used as indicators of bridge structural soundness [43]. A collection of modal frequency sets under different EOCs can also be extracted from long-term bridge vibration data using the stochastic subspace identification (SSI) technique [98, 99, 100]. Unlike mechanics-based methods, data-driven frameworks can use training data from when the structure is known to be in a healthy state to make future decisions through comparisons between newly extracted indicators and baseline (healthy) indicators without consulting theoretical parameters derived from mechanical analysis.

While mechanical parameters of bridge systems are usually preferred as health indicators for effective interpretation, features do not necessarily need to have physical significance. For example, the coefficients of trained auto-regressive (AR) models have been widely used as features [96, 101]. Moving principal component analysis (PCA) can be applied to time-history data over a long observation period to reduce the data dimensionality and extract major principle components as features [102, 103]. Damage detection can be conducted by observing the evolution of extracted principle components through robust regression analysis (RRA); changes in main eigenvectors may imply changes of structure performance at a location near corresponding sensors [102]. Recent research has also been performed in artificial symbolic metrics such as statistical manipulation of raw bridge response measurements. These methods have shown that raw data manifests sufficient sensitive information for condition assessment [104]. For example, peak (maximum) strain has been directly used in strain-based bridge SHM [43]. Different statistics such as root mean square (RMS), standard deviation and mean of the largest 10 measurements were successfully used as features for the health monitoring of the Sunrise movable bridge in Ft. Lauderdale, Florida based on four years of acceleration data [52]. Some other options of symbolic metrics include k-bin histograms and interquartile range (IQR) representing the statistical distribution of raw data [105, 104, 106]. Besides symbolic metrics of data in the time domain, those of processed frequency domain data (e.g., fast Fourier transform (FFT) of raw acceleration data) have also proven to be an effective addition to feature sets [106]. Signal processing techniques including the wavelet transform, Hilbert-Huang transform (HHT) and Teager-Huang transform (THT) have also been employed to convert raw data

into usable time-frequency domain features [107]. Spatial and temporal correlation hidden in data collected from sensors at multiple locations is another information source for structural condition representation. Correlation coefficients among different features from different sensors have been evaluated as powerful features for baseline learning through RRA [52].

After features are determined, they can be fed into machine learning models to recognize patterns regarding bridge structural conditions [94]. Common models include classification models (such as kernel-based support vector machine (SVM), Bayesian decision trees (BDT)) [105, 107], clustering models (such as k-means clustering) [106] and regression models (such as AR, Gaussian process regression (GPR), support vector regression (SVR)) [101, 61]. While classification and clustering models produce easily interpretable outputs (either a class label or a numerical distance from cluster centroids), statistical process control methods, such as mean and moving range (X-MR) control charts, are usually employed with regression models for damage detection [101, 61]. For example, prediction errors of trained GPR models can be used as samples for X-MR control charts [61].

EOC parameters (e.g., wind speed, temperature, vehicular loads) often have a strong influence on features, especially those with physical significance. EOC variability often prohibits direct use of the features for damage detection. For example, the correlation analysis between modal properties and ambient temperature reveals that uncertainties associated with modal properties due to effects of EOCs [95]. Such an issue makes it critical to perform necessary data normalization before feeding features into machine learning models for reliable detection results [108, 95]. The process of data normalization aims to eliminate undesired components in data that are induced by EOC influences. Regression models such as GPR, SVR and artificial neural networks are usually used to learn the mapping from EOCs to EOC-induced bridge responses (e.g., thermal response) [61, 95]. The trained regression models can predict EOC-induced responses allowing them to be removed from the measurement data. Signal processing in the frequency domain is also a means of data normalization. In the Tsing Ma Bridge SHM program, temperature- and traffic-induced strain components are separated from the measurement data through wavelet-based

multi-resolution analysis [109]. Many studies also attempt to derive features that are less dependent upon EOCs. Complex poles directly calculated by SSI, instead of real poles, are clustered using fuzzy c-means (FCM) clustering for the Z-24 bridge, which shows better sensitivity to damages than to EOCs [110]. EOCs can also be integrated as a feature into the baseline model training process. For example, the three dimensional relationship among local axial mechanical strain, global unrestrained displacement and uniform temperature variation has been established by clustering methods for the long-term health monitoring of a long-span tied-arch bridge in [111].

The latest research in the SHM field explores the effectiveness of deep learning methods for the monitoring of SHM systems and structure integrity [112]. Among all applications using deep learning, vision-based methods have received the most success in bridge SHM due to the easy application of such tools for binary data collection. Convolutions neural networks (CNN) trained with a large amount of labelled images are able to identify structural damage (e.g., deck cracks) outperforming human inspectors [113]. Raw SHM time-histories can also be converted into images and fed into a CNN to learn multi-category data anomaly classification [114].

1.5 Research Objectives and Dissertation Outline

Leveraging recent advances in CPS-related research, this doctoral dissertation focuses on the creation and application of a CPS framework tailored for civil infrastructure monitoring, especially in the SHM of highway bridges. Following the philosophy of CPS design, a connected corridor-based bridge SHM network is deployed along a section of the northbound I-275 freeway in southeast Michigan. The SHM network consists of two SHM systems installed on two short span highway bridges, a pavement-based two-lane WIM station and a series of traffic cameras along the 20-mile corridor. With the CPS installation initiated in 2011, a great amount of data from a heterogeneous set of data sources has been collected to date. To the best of the author's knowledge, this network is the first implementation of its kind with the value of the generated long-term data shown to be high.

This doctoral research program has three primary objectives surrounding the advancement of

CPS-enabled bridge SHM. First and foremost, this study aims to transform the concept of CPS-enabled bridge SHM to a real-world implementation such that the effectiveness and benefits of CPS can be tested under realistic field conditions. This goal is achieved by the installation of the aforementioned corridor-based bridge SHM network in Michigan. A considerable fraction of the research effort has been dedicated to the design and implementation of the CPS-based network. The network integrates several physical and cyber components, such as bridge SHM systems, cameras and cloud-based database platforms located on the Internet. Within each bridge SHM system, sensors and a dedicated base station at each bridge are connected wirelessly using ZigBee. Different subsystems at different locations are also linked to the Internet by cellular wireless communications. Many intelligent software modules, especially those utilizing real-time computer vision techniques, are deployed to facilitate the process of automatic system control, data transmission and data management. The efficacy of the network and many novel SHM applications driven by the data collected using the network are proven in this dissertation .

The second goal of this study is to demonstrate the value of long-term bridge SHM data in bridge performance assessment. While many long-term bridge SHM systems have been deployed, few studies clearly show the value of long-term measurement data. In this dissertation, the composite action behavior exhibited by one of the two bridges is investigated in detail using four years worth of bridge strain response and environmental data. Undesired partial composite action is observed over the negative bending region of a bridge span revealing the potential causes to rapid deterioration of bridge decks in negative bending region. A large amount of data also makes it possible to develop data-driven bridge condition evaluation methods. Fused with WIM data collected along the same corridor, long-term measurements of of bridge girder strain under traffic loads is used to extract site-specific load rating parameters which allows more realistic rating factors to be obtained. These applications show that long-term bridge SHM data provides an opportunity for better bridge asset management and design consideration.

The last objective of this study is to propose novel methodologies for bridge asset management that leverage the connectivity established by the CPS-enabled SHM system design. Apart

from data-driven load rating, the fusion of WIM data and bridge SHM data can also be used for data-driven bridge weigh-in-motion (BWIM), especially when the large volume of data is available. Recent years have witnessed the use of bridge sensors for weighing passing vehicles [115]. However, mechanics-based methods often suffer from the inaccuracy associated with the very nature of the inverse problem and uncertainties associated with bridge response measurements. This study shows that such issues can be resolved by leveraging the computational complexity of deep learning methods along with a large volume of load-response training data. The linkage between geometrically adjacent bridge SHM systems also allows bridge responses to same traffic loads to be paired. This type of previously unavailable data is utilized in this thesis for the exploration of a data-driven joint SHM strategy among multiple bridges. Herein, a learning-based model is trained to predict time-histories of one bridge response using the measured time-histories of another bridge to the same vehicular load. The discrepancy between the measured and predicted responses can be used as an indicator of bridge health. Such an approach further reduces the dependence of SHM frameworks on physics-based models and bridge-specific structural information.

The outline of the dissertation is illustrated in Figure 1-2. Chapter 2 first proposes the concept of the CPS-enabled bridge SHM system and then describes in detail the composition and operation of the CPS framework implemented along a 20-mile corridor of northbound I-275 between Newport and Romulus, Michigan. A two-stage data integration procedure is used to fuse a diverse set of data streams to match the response data of different bridges to the same truck load. The effectiveness of the SHM system and the data integration process are evaluated in terms of data collection efficiency and data quality. Chapter 3 focuses on the computer vision techniques that are employed in the CPS framework data integration process. Multiple object detection and re-identification algorithms are compared in terms of accuracy and inference time to evaluate which offer the best performance.

Chapter 4 and Chapter 5 showcase the value of long-term bridge data for bridge performance assessment. Chapter 4 uses long-term bridge monitoring data to quantitatively assess the composite action exhibited in slab-on-girder highway bridges and investigates the potential relationship

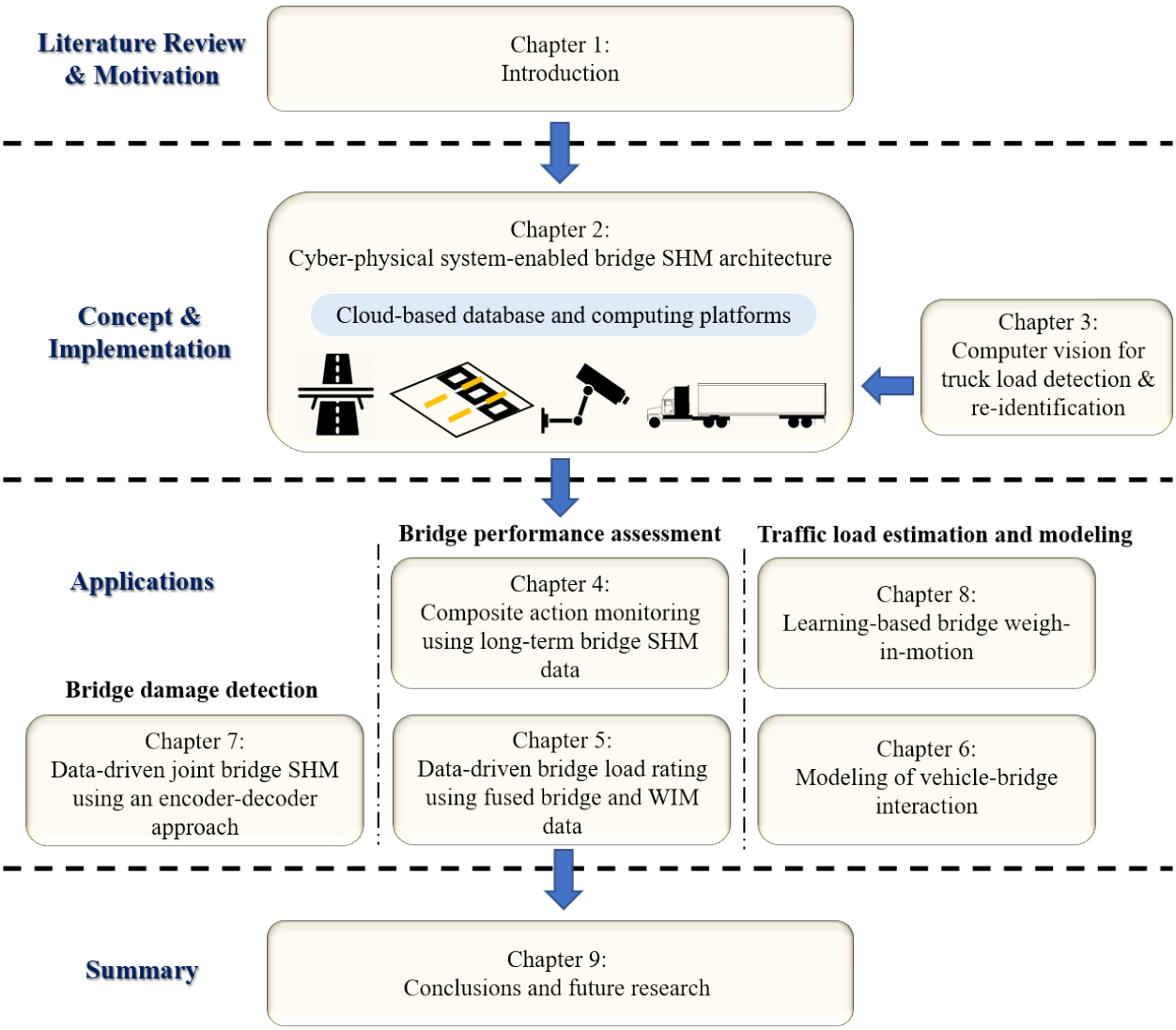

Figure 1-2: Chapter layout of the dissertation.

between composite action and deck deterioration over negative bending regions. The degree of composite action in composite and noncomposite sections of the bridge spans are quantitatively investigated using the position of neutral axis and the magnitude of slip strain as key response parameters correlated to composite action. It is shown that unintended nonlinear partial composite action exists in negative bending regions of the bridge. It is also concluded that the observed partial composite action results in higher tensile strains in the deck which is a likely culprit to accelerated deck deterioration. Chapter 5 utilizes the integrated bridge strain response and WIM data for extracting site-specific load rating parameters, especially dynamic load allowance and unit

influence lines. The two bridges within the CPS system are used as test beds for the proposed data-driven load rating methods. The resultant rating factors are compared with those obtained from conventional approximate and refined (finite element method) approaches.

Chapter 6 and Chapter 8 focus on the estimation and modeling of vehicular loads. Chapter 6 introduces a comprehensive wireless monitoring system that seamlessly integrates a mobile wireless sensor network installed in a tractor-trailer truck to measure dynamic truck behavior with a stationary wireless monitoring system installed in a bridge to measure vibrations and strains. Time-synchronized truck-bridge response data is used as the basis for modeling the interactions between the truck and the bridge. A two-stage subspace system identification modeling framework is proposed to create accurate input-output behaviors of the bridge response. Chapter 8 shows that paired bridge response and WIM data can be used as training data for a learning-based bridge WIM (BWIM) approach. The effectiveness of the method is first evaluated using simulation data and then tested using real data from the I-275 corridor.

Chapter 7 explores the feasibility of jointly monitoring structural health conditions of two adjacent bridges in a data-driven approach. An emerging encoder-decoder model is trained using bridge data with no damage present. Simulation data with artificial damage is used to evaluate the effectiveness of the trained model for bridge damage detection.

Chapter 9 concludes the dissertation by summarizing the research conducted in this thesis with key study findings and contributions identified. Future research directions are also presented in this chapter.

CHAPTER 2.

Structural Health Monitoring System Framework for Highway Bridges with Cyber-physical System Enabled

2.1 Introduction

An integral element of highway operations and management is the asset management of highway structural assets including bridges. For example, there are 616,096 bridges in the United States requiring significant investment to ensure they are safe for use and resilient to external loading [116]. As the national inventory of bridges ages, increasing levels of funding will be required to maintain bridge safety given existing asset management methods which rely on visual inspection methods. Given an $8 billion annual investment shortfall for maintaining our national bridge inventory, more cost efficient methods are needed for bridge asset management [117]. Recent advances in structural health monitoring (SHM) including the emergence of new sensors and scalable analytical frameworks have the potential to improve asset management decisions potentially leading to lower long-term management costs [118]. The adoption of SHM for bridges offer asset managers data-driven methods that can improve the quantification of structural conditions for asset risk assessment [38]. Current bridge SHM paradigms are based on systems designed to collect environmental and structural response data using sensors and a data acquisition system. Bridge response data can be used for damage detection [119], capacity estimation [120] and risk assessment [121]. While monitoring systems can reliably measure bridge behavior, such systems typically lack the capability to measure the vehicular loads inducing measured responses. As a result, bridge SHM frameworks often rely on output-only algorithms where the lack of a quantified input hinders accuracy, robustness, and generality. The challenges associated with output-only analyses are routinely

encountered in bridge modal analysis and time-series modeling where the absence of load measurements lead to simplifying assumptions such as the excitation source being a white noise process [122]. While this assumption may be reasonable in long-span bridges excited by a dense flow of traffic, it is often not suitable in short- and medium-span bridges where span lengths may only accommodate a small number of vehicles at a time. Furthermore, the ratio of vehicular live load to dead loads in short- and medium-span bridges is larger than in long-span bridges which places even greater importance on acquiring data related to vehicular loading [120]. Researchers have previously explored ways of acquiring data on vehicle loading of bridges. For example, controlled load testing using calibrated but unmonitored vehicles has been explored [123]. Another strategy is the use of instrumented trucks whose dynamics are recorded when driving over an instrumented bridge; combining time-synchronized data from the truck and bridge can offer input-output data sets for system identification and health assessment methods [124]. However, the cost and complexity of controlled truck loading prevents it from being applied to most bridges.

Advances in wireless communications and connected vehicles have opened opportunities for connectivity within highway systems including between vehicles and infrastructure. The SHM of bridges can benefit from connectivity by integrating bridge monitoring data with roadside traffic data sources including traffic cameras and weigh-in-motion (WIM) systems [83, 123]. For example, extensive research has explored the use of traffic cameras installed adjacent to bridges to capture images of vehicles loading the bridge. If roadside video and bridge monitoring data are synchronized, bridge responses can be visually linked to the vehicles inducing them [125, 84, 126, 127]. Others have explored the use of traffic video to extract traffic characteristics (e.g., speed, trajectory) using techniques from the field of computer vision. Gandhi et al. utilized an instrumented segment of a roadway to measure the road response to vehicles and to link vehicle loads to features extracted from roadside video using low-pass filtering, background subtraction with shadow suppression, and Kalman filtering methods [128]. Fraser et al. extended the work of Gandhi et al. by advancing similar computer vision methods to spatially map vehicle trajectories on a monitored bridge [129, 128]. Chen et al. adopted the use of a temporary camcorder to capture bridge

traffic so that vehicle type, speed and location were estimated for a spatial-temporal traffic model that maps traffic to bridge responses [130]. In a different approach, Zaurin and Catbas proposed the use of background subtraction methods using traffic cameras to identify vehicles crossing an instrumented small-scale bridge in the laboratory. Strain measurements synchronized with vehicle trajectories were then used to estimate unit influence lines (UILs) of the bridge [131] with UILs later used as damage-sensitive features for health assessments [132]. All of these approaches use cameras to acquire the state of traffic on a bridge but do not offer quantitative data specific to vehicular loading.

WIM stations are widely used in highway systems to acquire weight data on vehicles in a corridor including their gross weight, axle counts, axle spacing and axle weights. Traffic loads measured by WIM stations allow statistical models of vehicle live loads to be created for bridge load rating [133], fatigue analysis [134], and condition assessment [135, 136]. Researchers have begun to explore the fusion of cameras with WIM stations to assess bridge loads. For example, Han et al. adopted a traffic camera and a WIM station on a segment of the Xuanda Highway (China) to identify heavy trucks so that their temporal frequency and corresponding load profiles can be statistically modeled [133]. Chen et al. also explored the fusion of WIM stations and traffic cameras on the Hangzhou Bay Bridge to track truck bridge loads using background subtraction for truck identification and particle filters for trajectory estimation [130]. It also has been proposed recently to integrate WIM data into Bridge Information Modeling (BrIM) frameworks to improve the management of transportation infrastructure elements such as bridges [137]. While these studies have proven the utility of combing WIM stations with traffic cameras, they were also limited by the need to collocate the WIM station and camera at the asset of interest (i.e., bridge). With WIM stations costly to install, such stations also tend to be sparsely distributed in a network and are rarely collocated with bridges.

The goal of this study is to create a cyber-physical system (CPS) framework that integrates roadside traffic data collected using traffic cameras and WIM stations with response data collected using SHM systems on bridges. By using computer vision to spatially link measurements collected

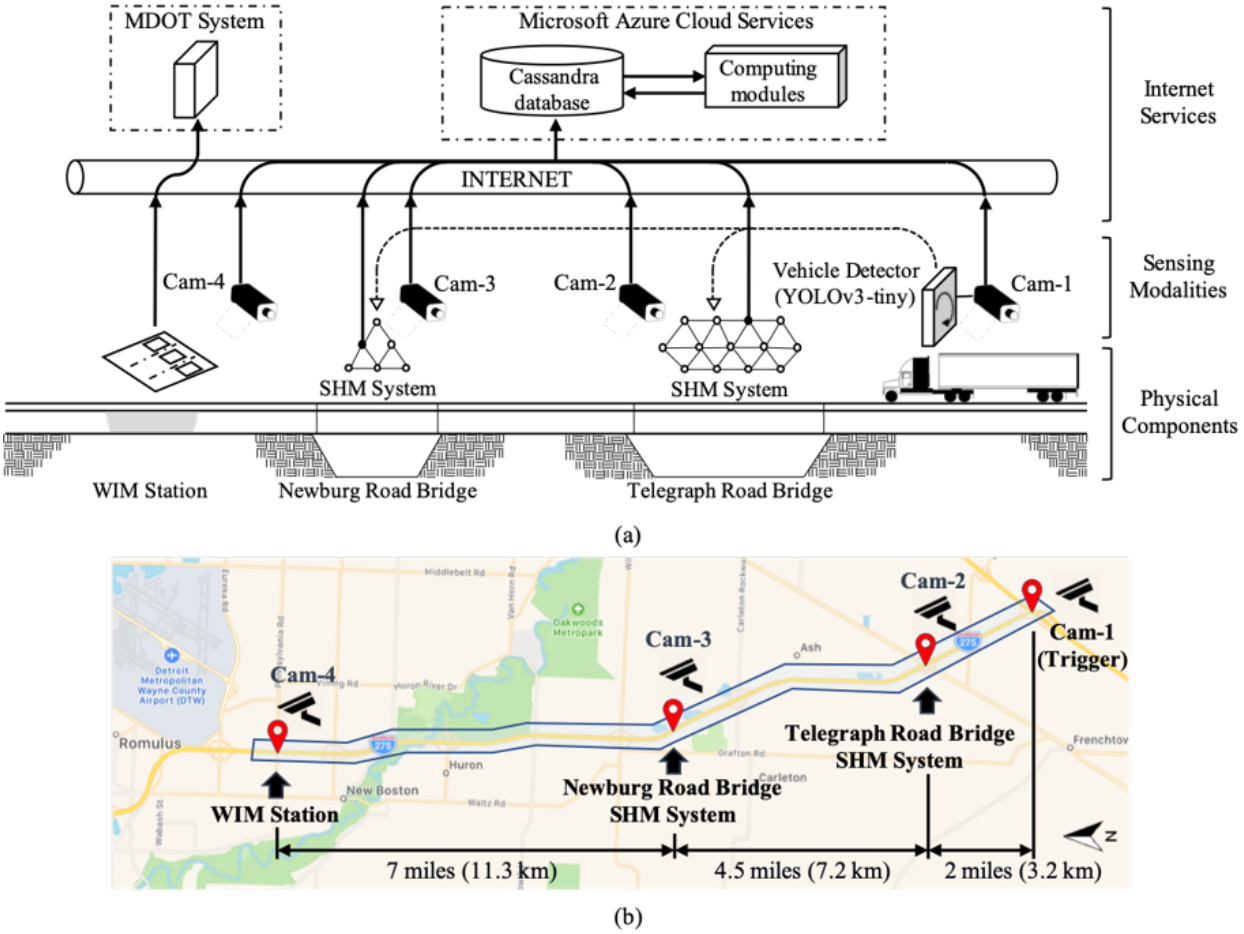

Figure 2-1: (a) Functional diagram of the CPS components and connectivity; (b) locations of the cyber-physical system (CPS) components for tracking truck loads in the I-275 highway corridor.

at different locations in the corridor, the proposed CPS framework does not require collocation of the WIM station with a bridge. The study adopts a 20-mile highway corridor along northbound I-275 between Newport and Romulus, Michigan for the design and deployment of the proposed CPS architecture. As illustrated in Figure 2-1(b), along this corridor are two instrumented highway bridges, one WIM station, and four traffic cameras, each connected to the Internet through cellular communications. To link bridge response data to the same vehicle, the CPS framework uses low-cost traffic cameras collocated with the bridge monitoring systems and WIM stations to capture images of the traffic associated with each measurement location. Computer vision methods based on convolutional neural networks (CNN) are adopted to automate the identification of heavy trucks at each measurement location and to link data associated with the same truck observed at the differ-

ent measurement locations. The CPS framework also leverages real-time truck identification using computer vision to trigger the bridge monitoring systems for more efficient data collection using a solar powered wireless SHM system. The proposed approach to linking response data collected at multiple locations in a corridor to the same truck event has many benefits including the ability to map truck weights to bridge responses and to correlate bridge responses to one another under the same load conditions. While the work is motivated by improving the asset management of highway structural assets, the proposed CPS system offers many other uses integral to operational management of highways including optimal routing of truck loads on bridges in a road network [117], quantitative tracking of truck loads in a network [138] and optimal infrastructure investment planning [139]. This chapter begins with a detailed description of the CPS architecture implemented in the I-275 corridor including a description of the triggering strategy adopted by the CPS to collect response data specific to truck load events. The chapter presents the CNN methods used to identify trucks at multiple locations based on camera images. Bridge response and WIM data corresponding to the same truck event are used to correlate bridge responses and truck weights, thereby offering a novel approach to baselining bridge behavior for SHM. The chapter concludes with a summary of findings and a description of future work.

2.2 Cyber-physical System Architecture

Cyber-physical systems (CPS) are systems in which sensors, actuators, and software components are linked and integrated to monitor, analyze, and control the physical system [5]. Unlike traditional monitoring and control systems, CPS utilize computing platforms made available through communication interfaces (wireless or wired) where data can be aggregated, curated and analyzed. With the scalable computing resources available via the Internet, CPS often expand the repertoire of computing methods from exclusively physics-based to also encompass data-driven methods such as machine learning techniques [140]. CPS architectures have been applied to a wide range of infrastructure applications including connected and autonomous vehicles [141], early earthquake warning systems [142], and smart grids [143], just to name a few. In this study, a CPS architecture

is proposed for highway corridors (i.e., the physical system) where heavy trucks load the corridor assets such as bridges. The role of the CPS is to improve the performance of SHM systems installed on bridges by quantitatively observing the truck loads. As shown in Figure 2-1(a), the CPS architecture contains three major types of components: namely, physical components, sensing modalities and Internet-based computing. The physical components of the system include highway bridges and passing vehicles. The sensing components of the CPS architecture include the bridge SHM systems that monitor bridge responses to traffic, WIM stations that measure the speed, gross weight and weight distributions of vehicles, and traffic cameras that capture optical data of the vehicles in the corridor. Notated as solid arrows in Figure 2-1(a), each of these sensing components are connected to the Internet via cellular communication where data can be communicated for storage in cloud-based database management systems and processed by deployed computing modules. The communication interfaces are also used by the CPS architecture to communicate commands to the sensing components where data collection processes can be actuated (i.e., triggered) as shown as dash arrows in Figure 2-1(a). The CPS architecture is designed to use the traffic camera images to identify trucks as they excite the monitored bridges and later cross over the WIM station. The CPS architecture is also designed to automate the identification of the same truck in the images so that truck weight parameters can be tied to bridge responses, thereby providing input-output data for bridge health assessments.

In this study, a 20-mile (32.2 km) segment of the northbound I-275 corridor between Newport and Romulus, Michigan is selected as a testbed to implement and demonstrate the CPS framework. The geographic locations of the CPS components along I-275 including two bridge SHM systems (i.e., Telegraph Road Bridge and Newburg Road Bridge), one WIM station and four traffic cameras are illustrated in Figure 2-1(b). One camera (labeled Cam-1) is installed at the southern end of the corridor to first identify vehicles entering the highway. The three remaining cameras (labeled Cam-2 through Cam 4) are installed at each bridge and the WIM station. From south to north, the travel distances between adjacent measurement locations are 2 miles (3.2 km), 4.5 miles (7.2 km), and 7 miles (11.3 km), respectively. It should be noted that exits are present along the 20-mile corridor

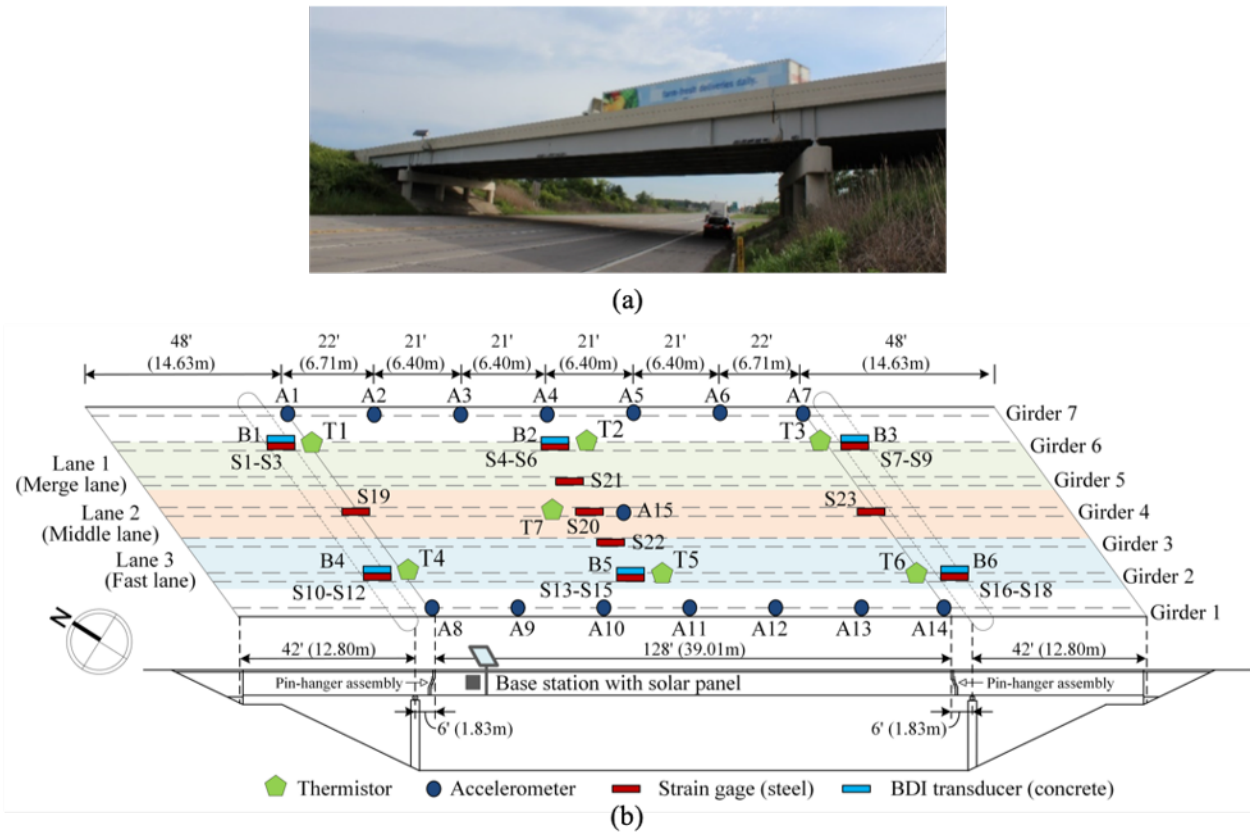

Figure 2-2: (a) Telegraph Road Bridge carrying I-275 northbound traffic over Telegraph Road; (b) overview of the wireless SHM system installed.

with one exit present between the Telegraph Road Bridge and Newburg Road Bridge and three between the Newburg Road Bridge and the WIM station; there are no exits between Cam-1 and the Telegraph Road Bridge. These exits allow trucks to enter and exit between the measurement locations, making truck re-identification a more challenging problem for the CPS architecture.

2.2.1 Highway Bridge SHM Systems

Along the selected I-275 northbound corridor, two highway bridges carrying I-275 traffic over local roads are monitored: Telegraph Road Bridge (TRB) and Newburg Road Bridge (NRB). Both bridges were built in 1973 and are owned by the Michigan Department of Transportation (MDOT). The TRB, shown in Figure 2-2, is a deck-on-steel girder bridge carrying three lanes of northbound I-275 on seven girder lines. One of the bridge lanes is the merge lane associated with the highway

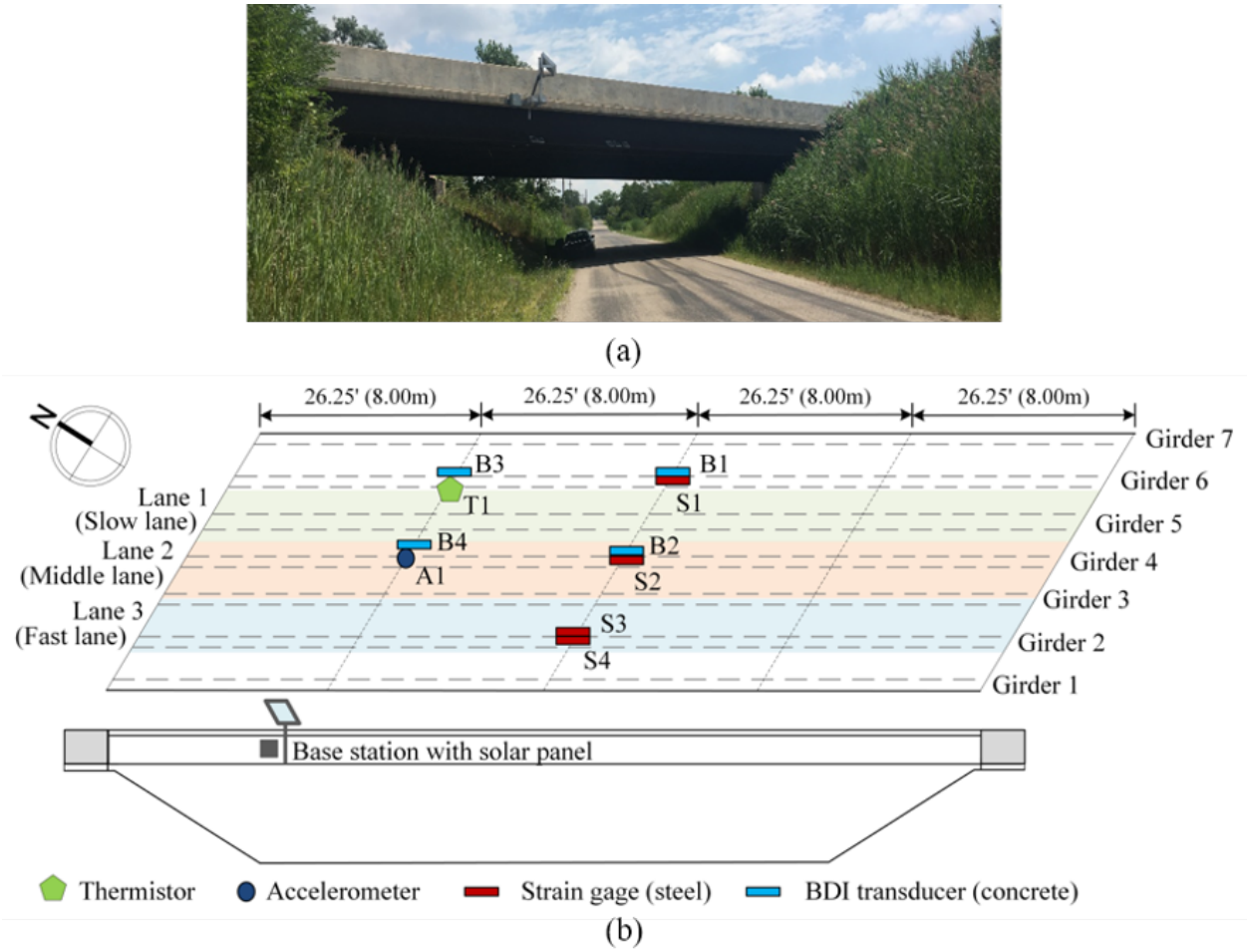

Figure 2-3: (a) Newburg Road Bridge carrying I-275 northbound traffic over Newburg Road; (b) overview of the wireless SHM system installed.

exit at the bridge location. The bridge spans a total of 224 feet (68.28 m) consisting of a main span of 128 feet (39.01 m) and two abutment spans of 48 feet (14.63 m) each. The reinforced concrete deck of bridge is 8 in. (20.3 cm) thick and is in composite action with the steel girders on the main span (but not in composite action on the abutment spans). The abutment spans are each supported on one end by the bridge abutments and a pier 6 feet (1.83 m) from the span end that is adjacent to the main span. The main span is connected to the cantilevered ends of the abutment spans through pin-and-hanger assemblies. Located 4.5 miles (7.2 km) north of the TRB, the NRB is a single span bridge with a total length of 105 feet (32.00 m) as shown in Figure 2-3. NRB carries three lanes of I-275 northbound traffic with seven steel plate girders and a 9 in (22.9 cm) reinforced concrete deck in composite action with the girders.

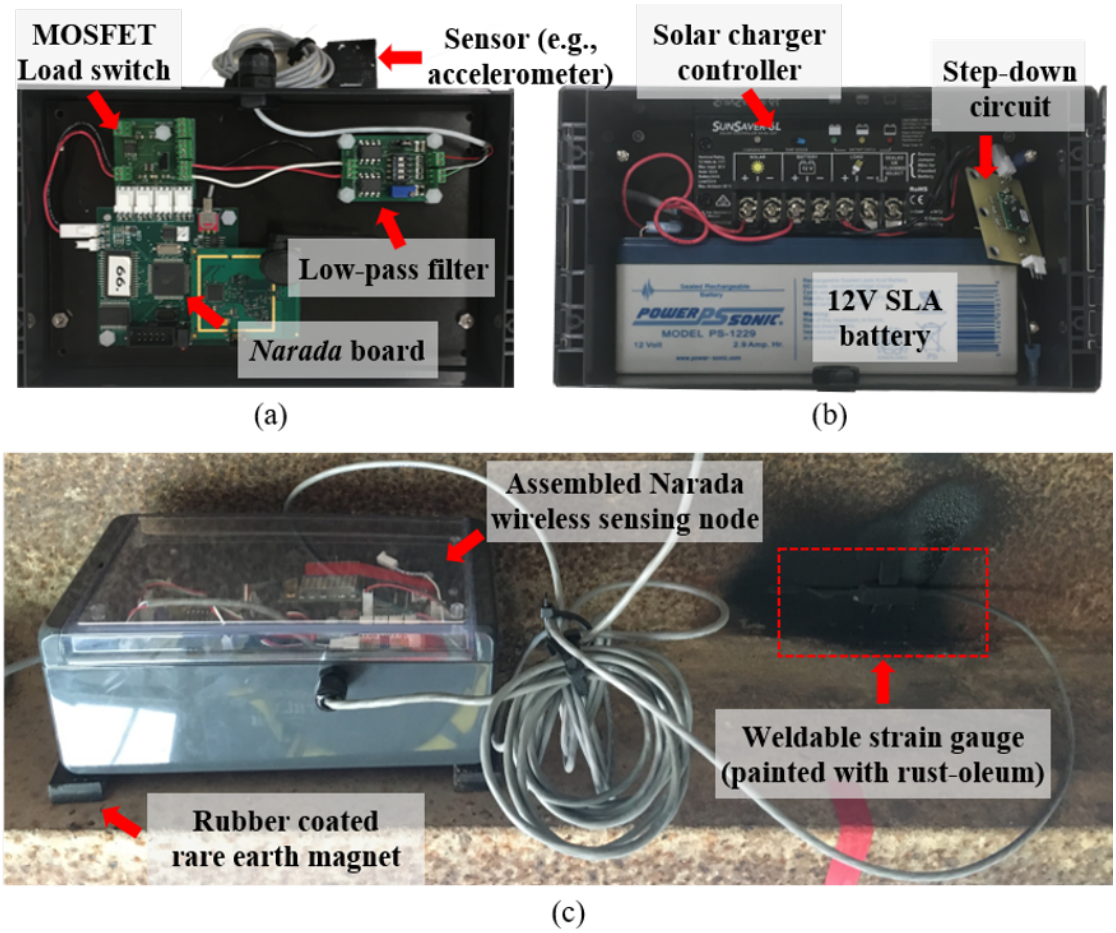

Figure 2-4: *Narada* wireless sensor nodes for field deployments in TRB and NRB: (a) *Narada* sensor with conditioning circuits and interfaced sensor (shown is an accelerometer); (b) power system of a *Narada* sensor node including rechargeable battery and solar charge controller; (c) weather-proof enclosure installed on a girder flange with strain gauge welded to the girder web.

The TRB and NRB had SHM systems installed in 2011 and 2016, respectively, using wireless sensors as the main data acquisition platform. Each wireless SHM system is composed of a wireless base station and a number of Narada wireless sensing nodes that have been developed at the University of Michigan [144]. Up to four sensors can be interfaced with one Narada node with an internal 16-bit analog-to-digital converter (ADC); sensors are attached to the ADC via a Metal Oxide Semiconductor Field Effect Transistor (MOSFET) switch (that allows sensors to be turned on and off by the node to save power) and signal conditioning circuits (e.g., low-pass filters) as shown in Figure 2-4(a) [145]. Internal to Narada is a 256 kB of SRAM that allows data to be stored locally before communication. The Narada nodes use power amplified IEEE802.15.4

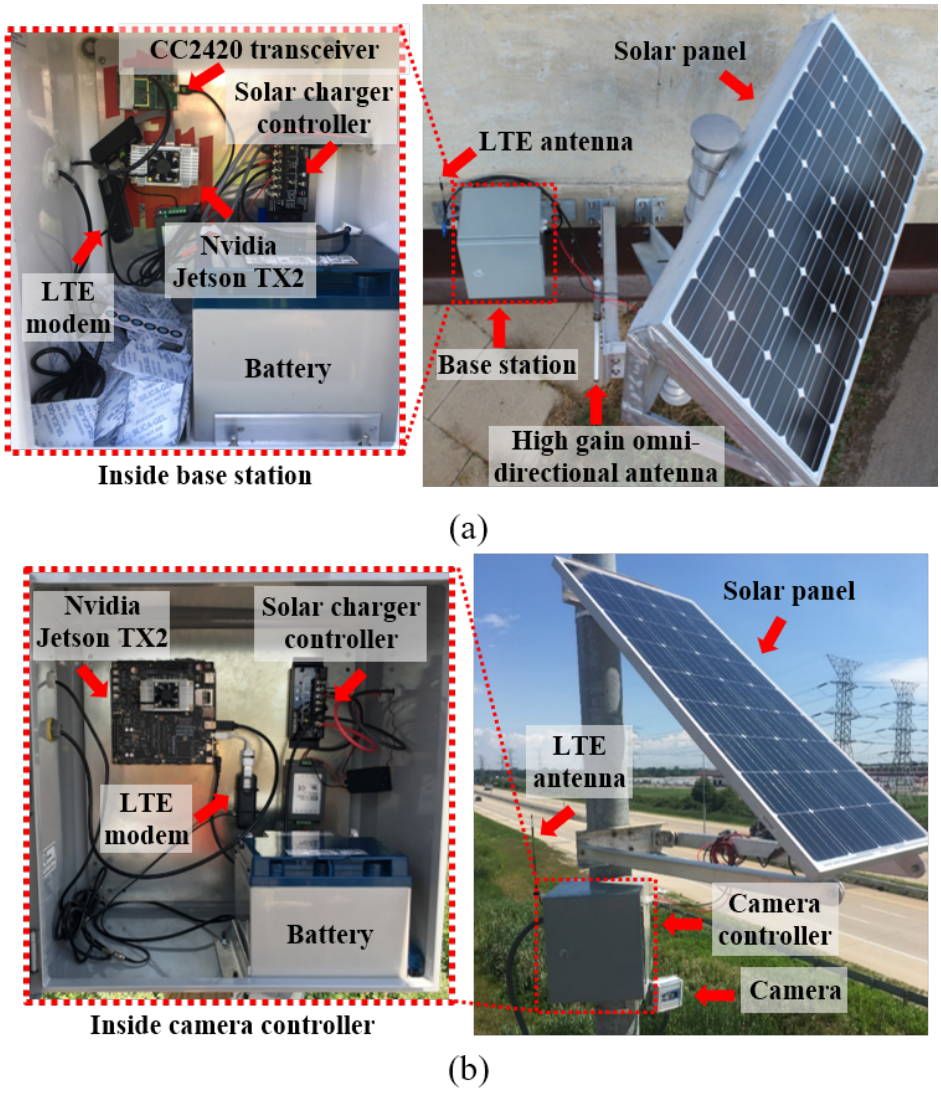

Figure 2-5: (a) Base station of the bridge SHM systems; (b) traffic camera installation along I-275.

transceivers (Texas Instruments CC2420) for wireless communication between nodes and the base station. Each Narada node is placed in a weather-proof plastic enclosure along with a 12V sealed lead acid (SLA) battery (PowerSonic PS-1229) with a 2.9A-hr capacity and a solar charge controller (Morningstar SunSaver SS-6L-12V) which controls the recharging of the battery using 10W solar panels (UL-Solar 10W 12V) installed along with the enclosure (Figure 2-4(b)). The enclosure has rubber coated rare earth magnets (Figure 2-4(c)) on its base allowing it to be magnetically mounted to the steel girders of the bridges. A more detailed description on the wireless sensing node can be found in O'Connor et al. [61].

Each base station (Figure 2-5(a)) is programmed to send operational commands to the Narada nodes (e.g., sleep, wake-up), trigger data collection, synchronize the nodes, collect sensor measurements and forward sensor data to a cloud database [146]. The primary component of the base station is an embedded Linux server implemented on a single board computer (Nvidia Jetson TX2). Attached to the Jetson TX2 are two radios: one is an IEE802.15.4 transceiver (Texas Instruments CC2420) that communicates with the Narada nodes on the bridges and the other is an LTE cellular modem (AT&T Velocity MF861) that communicates with a cellular network to access cloud services on the Internet. An external high-gain omni-directional antenna is attached to the CC2420 radio to improve the quality of communications between the base station and the Narada nodes. The base station is solar powered by a 110W solar panel (UL-Solar 110W 12V) that is used to recharge a 12V 40A-hr SLA battery (PowerSonic PS-12350NB) using a solar charge controller (Morningstar SunSaver SS-20L-12V) included in the base station enclosure.

This study applies Hitec HBWF-35-125-6-10GP-TR weldable strain gauges, BDI ST350 strain transducers, Silicon Design 2012-002 uniaxial accelerometers and Texas Instruments LM35DT thermistors for the measurements of steel girder strain responses, concrete slab strain responses, acceleration responses and the temperature of the bridge, respectively. The sensor layout of the TRB system is shown in Figure 2-2(b). A total of 14 accelerometers are distributed along Girder 1 and 7 at the main span in addition to an extra one (A15) located at the center of the bridge. The accelerometers are mounted to the bottom flange of girders using structural adhesive (i.e., epoxy) to measure vehicle-induced vibrations. Vibration data measured by the accelerometers are used to identify the modes and frequencies of the TRB for model updating (which is beyond the scope of this chapter). The TRB also features six locations where a BDI strain transducer is installed in the slab and three strain gauges are installed along the depth of the girder; these six locations are identified using BDI transducers B1 to B6 along Girder 2 and 6. At each of the six locations, the BDI strain transducer is bolted to the bottom surface of the bridge slab and the three strain gauges are installed on the web 3 in. (7.62 cm), 27 in. (68.58 cm) and 51 in. (129.54 cm) above the top surface of the girder bottom flange. Such an installation allows the profile of girder strain

responses to vehicular loads to be estimated for the assessment of composite behavior exhibited at the girder-deck interface [147]. Each location also has one thermistor to measure temperature. S19 and S23 are two strain gauges installed near the bottom pin hole on the two hanger plates of the middle girders. S20, S21 and S22 are three strain gauges welded to the web of the steel girders 3 in. (7.62 cm) above the bottom flange to measure the longitudinal bending strain at mid span of the corresponding girders caused by vehicular loads. Compared to the TRB, the NRB SHM system is a lighter weight configuration as shown in Figure 2-3(b). S1, S2 and S4 are three strain gauges welded to the girder web at mid span 3 in. (7.62 cm) above the bottom flange. S3 is installed 51 in. (129.54 cm)above the bottom flange at the same location as S4. B1 to B4 are four BDI transducers measuring bottom slab longitudinal strains especially local tensile strain peaks caused by direct wheel loads to identify the speed and the number of axles of a passing truck. A1 is used to identify the dominant frequencies of the NRB and T1 is to measure the bridge temperature. Calculated from measured acceleration data, the TRB and NRB exhibit a first modal frequency of 2.4 Hz and 4.2 Hz, respectively. Accordingly, sampling frequencies are set to be 100 Hz, 200 Hz and 1 Hz for strain gauges, accelerometers and thermistors, respectively. This study will mainly focus on girder longitudinal strain responses measured at mid span of each bridge to demonstrate the data collected by the CPS.

2.2.2 Weigh-in-motion (WIM) Station

The second data source on the I-275 corridor is a WIM station that records vehicle weight data. WIM stations are widely used by transportation officials to monitor highway freight movement and to track compliance to truck weight limits [148]. Compared to traditional weigh stations that require vehicles to exit the highway to measure their weight, WIM stations are built into the road pavement and take measurements without slowing traffic. Various WIM station types exist depending on the sensing transducer type used to make weight measurements (e.g., piezoelectric, bending plates, pressure cells). WIM stations often provide more than simply the gross vehicle weight but also the weight carried by each axle (or axle group), axle spacings, and vehicle speed.

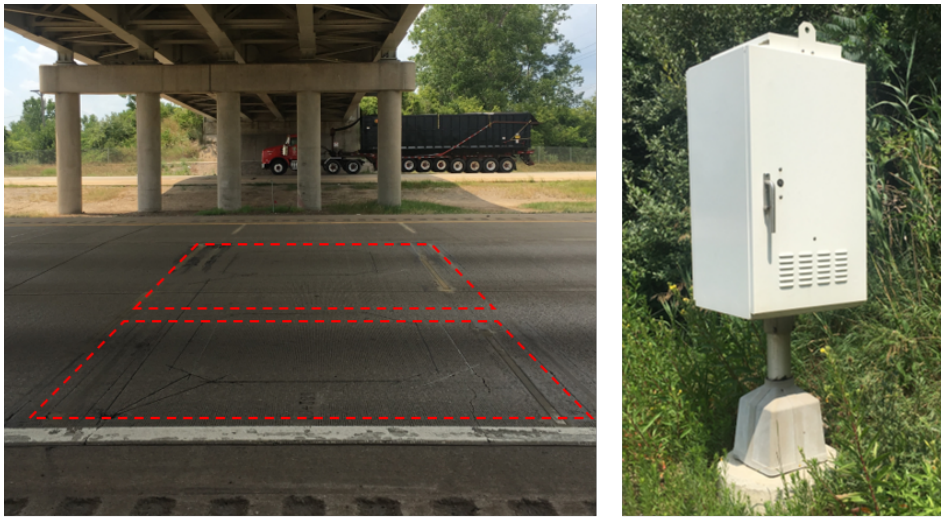

(a) (b)

Figure 2-6: Weigh-in-motion (WIM) station underneath the Pennsylvania Road Bridge: (a) sensors installed in the pavement of I-275 northbound; (b)data acquisition system on site to collect the WIM data.

Along the I-275 northbound corridor is one WIM station (Figure 2-6) located at Pennsylvania Road in Romulus, MI roughly 7 miles (11.3 km) north of the NRB. The WIM station is a two-lane Type II WIM station with quartz sensors installed under the pavement of each lane. For each lane, the WIM station records 9 vehicular load attributes: time, Federal Highway Administration (FHWA) vehicle class, vehicle speed, vehicle gross weight, number of axles, axle weights, axle spacing, direction and lane. The WIM station has a road-side data collection unit Figure 2-6(b)) that communicates measurements via a fiber optic network to a data server managed by the Michigan Department of Transportation (MDOT).

2.2.3 Traffic Camera Systems

As notated in Figure 2-1, four traffic cameras are installed by the authors along the I-275 roadside with a direct view of traffic: at the interchange of I-275 with I-75 (Cam-1), Telegraph Road Bridge (Cam-2), Newburg Road Bridge (Cam-3) and the WIM station beneath the Pennsylvania Road Bridge (Cam-4). Each camera station is responsible for collecting roadside images of traffic on northbound I-275, storing image data locally, and transmitting the images using a cellular modem.

Figure 2-7: Traffic image of the same truck captured by the four cameras along the I-275 NB corridor: (a) Cam-1; (b) Cam-2; (c) Cam-3; (d) Cam-4.

As shown in Figure 2-5(b), a Logitech C930e webcam camera is enclosed in a water-proof enclosure and mounted to a post on the highway roadside. The camera is controlled by a single board Linux server based on the Nvidia Jetson TX2 which internally contains a hex-core ARMv8 64-bit central processing unit (CPU) and an integrated 256-core Nvidia Pascal graphics processing unit (GPU). The inclusion of the GPU in the TX2 is beneficial for Cam-1 where images of trucks entering the corridor will be processed directly on the server to provide real-time triggering of the SHM systems within the CPS. The Nvidia Jetson TX2 is contained in a weather-proof enclosure and is set-up identically to the ones used on the TRB and NRB (i.e., same battery, charge controller, and solar panel). For communications, an LTE modem (AT&T MF861) is used for the roadside server to communicate data to and receive commands from the CPS architecture. The camera can capture images with a maximum resolution of 1920×1080 pixels but in this study, it is set to capture images at a frame rate of 10 frames per second (FPS) with a 1280x720 pixel resolution. Reducing the resolution helps reduce the time to transmit and process data. Each traffic image is labelled

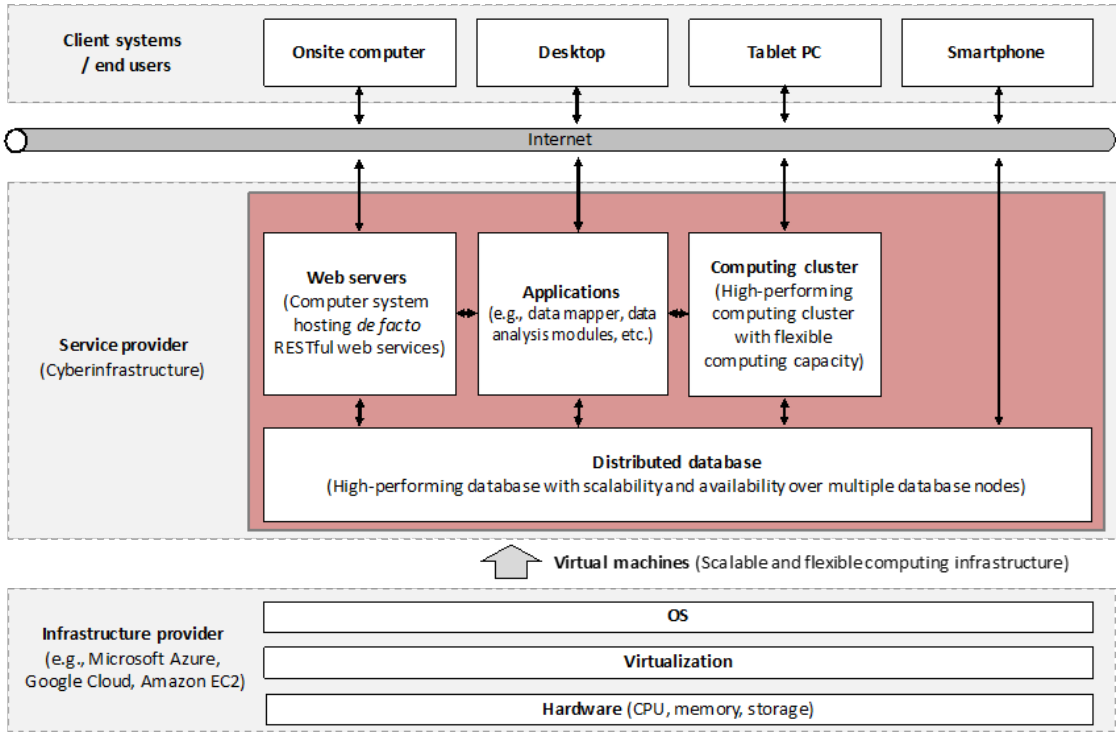

Figure 2-8: Computational framework of the cloud-based cyber-infrastructure database and computing platform.

with the time it is captured by the server. The server maintains clock synchronization based on the network time protocol (NTP) implemented via the cellular communication interface. Four sample images are presented in Figure 2-7 where the same truck is captured at Cam-1 through Cam-4.

2.2.4 Cloud-based Data Management and Computing Platform

A prerequisite to the implementation of a CPS architecture for observing and analyzing truck loads on the infrastructure assets of the I-275 corridor is the development of a scalable database system that can be used to store large sets of heterogeneous data (e.g., sensor data, camera feeds), expose data for analytics with low latency, and automate cyber-physical operations. For such a purpose, a NoSQL (Not Structured Query Language) database architecture based on Apache Cassandra (an open-source distributed NoSQL database management system) is implemented in a peer-to-peer distributed fashion for scalable and fault-tolerant data storage and management [146, 79]. The detailed architecture is shown in Figure 2-8 where the core database is built upon virtual machines

provided by commercial cloud computing platforms such as Microsoft Azure which is used in this study. The use of the cloud allows the CPS architecture to have maximum scalability as data sets and analytical needs grow. While the physical locations of the distributed database nodes are abstracted by the virtual machine framework within the cloud platform, virtual machines allow the CPS to scale the use of cloud computing resources up and down, as needed. Multiple peripherals such as RESTful web services (based on REpresentational State Transfer (REST) technology) and data processing applications are then designed on top of the database system which can be accessed from different end clients for data retrieval, visualization and interpretation purposes.

To support the integration and analysis of data collected from multiple sources, several automated data analytic modules are deployed on high-performance computing clusters which are also hosted on the cloud platform. These modules are developed to perform a variety of processing tasks associated with integrating data from multiple sources (e.g., vehicle detection and bridge response data filtering), characterizing bridge behavior (e.g., frequency identification and modal analysis) and long-term structural health monitoring (e.g., bridge response correlation) leveraging the computing available at the measurement locations (e.g., the CPU and GPU on the roadside servers) and cloud. This study will primarily focus on the analytical modules related to data integration (as will be later presented as grey blocks in Figure 2-11).

2.3 Computer Vision-based SHM System Triggering

Of primary interest in assessing the performance and condition of bridges is how they respond to vehicle live loads. For example, most existing bridge SHM frameworks utilize live load-induced bridge responses for damage detection and capacity evaluation [38]. While all vehicles induce a dynamic response in bridges, it is the large trucks that induce the greatest dynamic response offering high signal-to-noise ratio (SNR) measurements. Also, the load magnitude associated with trucks are a bigger contributor to long-term structural deterioration [149]. Solar-powered wireless SHM systems such as those used in this study are limited by their available power (especially during low-sunlight conditions during the winter months) and are therefore not operated continuously;

rather, they are designed to collect data regularly on a defined schedule. Due to collection of data being on a schedule, there is no guarantee that the data collected during each collection cycle will contain vehicles of primary interest such as heavy trucks. This limits the utility of the data set while consuming precious energy resources by the system. A much more effective approach to collecting data from bridge SHM systems is if the system could be triggered by the presence of heavy trucks which are the load of greatest interest. Triggering based on truck events can generate a rich set of bridge response data for SHM analyses while minimizing the consumption of limited SHM system battery power.

In this study, the CPS architecture is designed to apply computer vision methods on the camera images to identify trucks and to trigger the bridge SHM systems to collect data based on the identification of a truck. Architecturally, Cam-1 (Figure 2-1) at the southern end of the corridor is deployed to serve as the trigger camera. Cam-1 continuously records northbound traffic with an embedded truck detector implemented in the camera server. Once a truck entering I-275 is identified by Cam-1, the camera's server sends a trigger message to the TRB, NRB, Cam-2, Cam-3 and Cam-4 to begin data collection based on an estimated time of arrival of the truck at each downstream location. This triggering strategy ensures the same truck can be tracked at each location. While some trucks may exit the corridor, the framework would capture the trucks that remain on the corridor without exiting.

To intelligently detect passing vehicles, especially trucks, two object detection algorithms, YOLOv3-tiny and YOLOv3, are trained using a customized vehicle data set. After training, given an input image, the models are able to detect and localize three classes of vehicles (i.e., cars, pick-up trucks, trucks) in the image using a set of rectangular bounding boxes. The two algorithms are selected over other algorithms for their high accuracy and fast inference speed. While this chapter focuses on the architecture design and evaluation of the proposed CPS-enabled bridge SHM architecture, a detailed description and comparison of these object detection algorithms are provided in Chapter 3. When deployed upon the Nvidia Jetson TX2 which is the server hardware used at Cam-1, the YOLOv3-tiny model is capable of being executed in real time at an equivalent frame rate

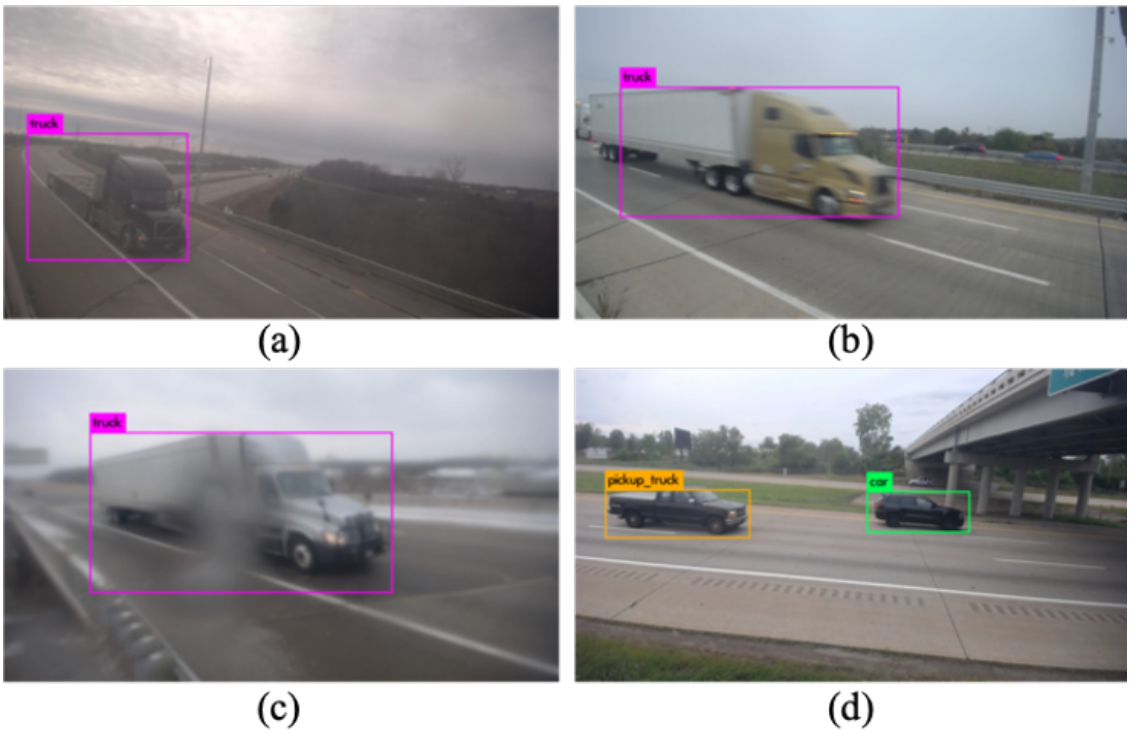

Figure 2-9: Truck detection results: (a) truck detected by the trigger using YOLOv3-tiny at Cam-1; (b) truck detected using YOLOv3 at the TRB; (c) truck detected using YOLOv3 during a rainy day at the NRB; (d) a pick-up truck and a car detected using YOLOv3 at the WIM station.

of 15 frames per second which satisfies real-time detection requirements of the CPS. In addition, the average precision of the YOLOv3-tiny in detecting trucks for an IOU threshold of 0.5 and 0.75 is 97.46% and 96.65%, respectively. The YOLOv3 model is used to perform vehicle detection on traffic images captured by the other cameras (namely, Cam-2 throughCam-4) using a server with a Nvidia Titan Xp GPU that is accessible to the CPS via the Internet. The time of execution for this more extensive CNN model on the Titan Xp is 19.7ms per image. The average precision for trucks is higher than that of YOLOv3-tiny with AP0.5 and AP0.75 at 98.91% for both IOU thresholds. Some visual results of vehicles detected by the two YOLO models are shown using images from the I-275 corridor under different field conditions in Figure 2-9.

With the aim of capturing the same truck traveling along the I-275 highway corridor, the first camera at the interchange of I-275 and I-75 (Cam-1) is used as the trigger for data collection in the CPS (Figure 2-10). The embedded YOLOv3-tiny model in the Cam-1 server is continuously

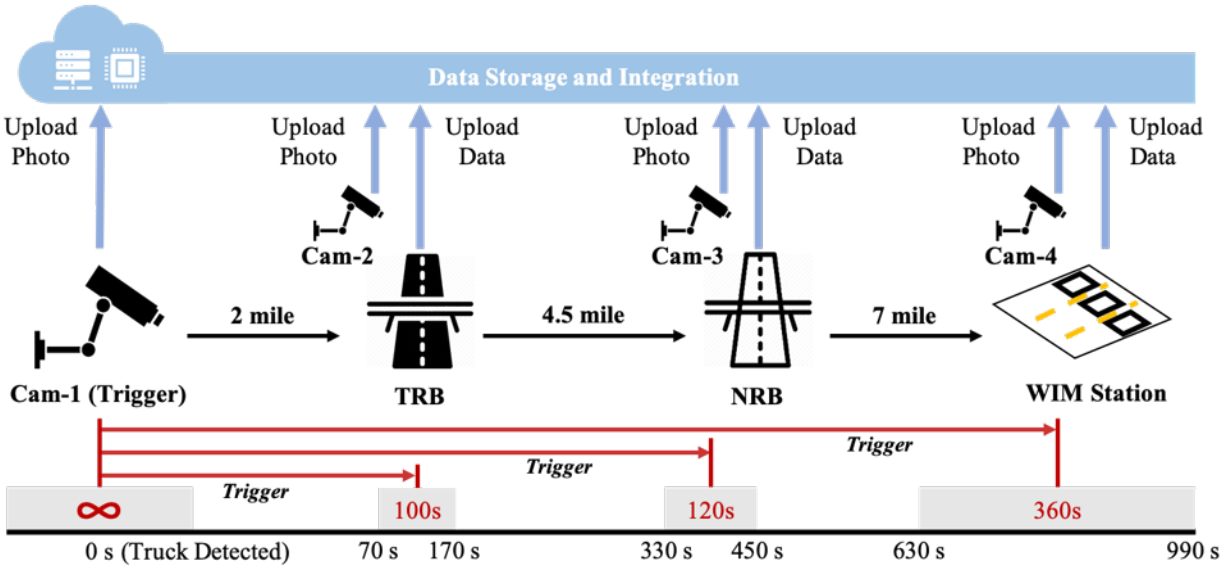

Figure 2-10: Trigger-based data acquisition strategy of the proposed CPS system.

executed in real-time to process camera images. Once a truck is detected by the detector, the Cam-1 server uploads the image of the detected truck into the Cassandra database hosted in the cloud and sends a wake-up message to the TRB SHM system server and the Cam-2 server using the low latency User Datagram Protocol (UDP). The wake-up message sent by the Cam-1 server contains the time to start data collection at the TRB bridge accounting for the distance between Cam-1 and the TRB and assuming a truck speed of 60 miles per hour (96.6 km per hour): this is estimated to be 120s. Due to this truck speed being conservative, the TRB data collection is commanded to occur 70s after the truck is detected (50s before the estimated time of arrival). After the TRB SHM system and Cam-2 receive their wake-up messages, both systems start their data collection at the time given by Cam-1 and collect data for 100s putting the mid-point in time for the data collection cycle at 120s after the truck is detected at Cam-1. After data is collected, the images and bridge response data are uploaded to the Cassandra database.

Following the same pattern, the SHM and camera systems at the NRB and WIM station are triggered in a similar fashion. Using the same conservative truck speed, the time the truck would take to travel between TRB and NRB is approximately 270s; hence Cam-1 commands the NRB

SHM system and camera system to collect data for 120s with the mid-point of that data collection cycle being 390s after the truck is detected at Cam-1 (i.e., 330s after trigger). Cam-4 at the WIM station is similarly triggered by Cam-1 to collect data for 360s with the mid-point of the data collection cycle being 810s after the truck is detected at Cam-1. All data collected in the same triggered cycle is stored and logged with timestamps in the cloud database for further data integration. It should be noted the increasing data collection window prescribed at TRB (100s), NRB (120s) and the WIM station (360s) is designed to account for uncertainties associated with the truck speed and to maximize the chance of capturing the same truck first detected at Cam-1 at each subsequent location.

When the TRB SHM system was first installed in 2011, a schedule-based data collection strategy was used to collect data with a support vector machine (SVM) classifier adopted to automate the identification of bridge response data containing large truck loads [61]. The schedule adopted for the TRB SHM system collected data for 100s every two hours. Since 2016, the CPS trigger strategy has been in use in lieu of the schedule-based strategy. To quantify the improvement of the trigger strategy compared to the schedule strategy in terms of data acquisition efficiency, two sets of data are collected at the TRB during July 2017. The first set records data at the TRB for 200 cycles (100s of bridge response data every half an hour) over daytime periods (i.e., 8 AM to 6 PM) onthe weekdays of two consecutive weeks. The second set is 200 data sets based on the trigger strategy over the same period during weekdays in the following two consecutive weeks. For the second set, it was controlled that Cam-1 sleeps for half an hour after each triggering event such that only one data collection cycle is activated every half an hour. The design of the schedule- and trigger-base data collection processes was to roughly ensure the statistical sampling of trucks were from similar distribution functions to make a fair comparison.

First, the number of truck events detected in each cycle were compared. The schedule-based strategy leads to 79.5% of the data cycles containing totally 456 truck events while the trigger strategy has 99% of its data cycles containing totally 775 truck events. To consider the dependence of the effectiveness of the trigger-based data collection on the data collection duration, another

experiment was performed with the TRB triggered by Cam-1 with varying data collection durations. With the data collection cycle set to be 100, 30, 25, 20, 15 and 10 s, the percentage of trucks captured at TRB is 99.1%, 95.5%, 95%, 94.5%, 90.5% and 74.5%, respectively. These results confirm the triggering strategy significantly outperforms the schedule-based SHM sensing strategy and is a powerful approach to maximizing the value of data collected by the solar-powered CPS data collection elements per unit of power consumed. They also suggest the time period of data collection at the TRB can be as short as 30s to preserve battery power at each wireless node.

2.4 Two-stage Data Integration by Truck Re-identification

To establish an input-output relationship between trucks and bridges, data corresponding to the same truck event collected at the TRB, NRB and WIM station must be matched with each other. This goal is achieved by two stages of data integration. The first stage is one of local integration where data collected by the bridge SHM system or WIM station must be synchronized with the camera data at the same location. The output of this stage of integration are segmented images of trucks detected and the corresponding bridge response data set or WIM record. The second stage is one of global integration where truck events captured at different locations are matched with one another through re-identification of the same truck in traffic images at the different data collection components in the CPS. Re-identification of the same truck at different camera locations will be done using a CNN-based embedding network with a nearest neighbor strategy applied to its output. At the end of the two-stage integration process, the final result will be TRB and NRB bridge response data and a WIM record linked to the same truck that is travelling northbound in the I-275 corridor.

The proposed data integration pipeline is organized within a microservices architecture which has gained popularity for building large-scale distributed web applications [150]. In a microservices architecture, a single application is developed as a suite of decoupled smaller services with each service running on its own independently but communicating with one another via lightweight communication mechanisms [150]. As depicted in Figure 2-11, the microservice architecture for

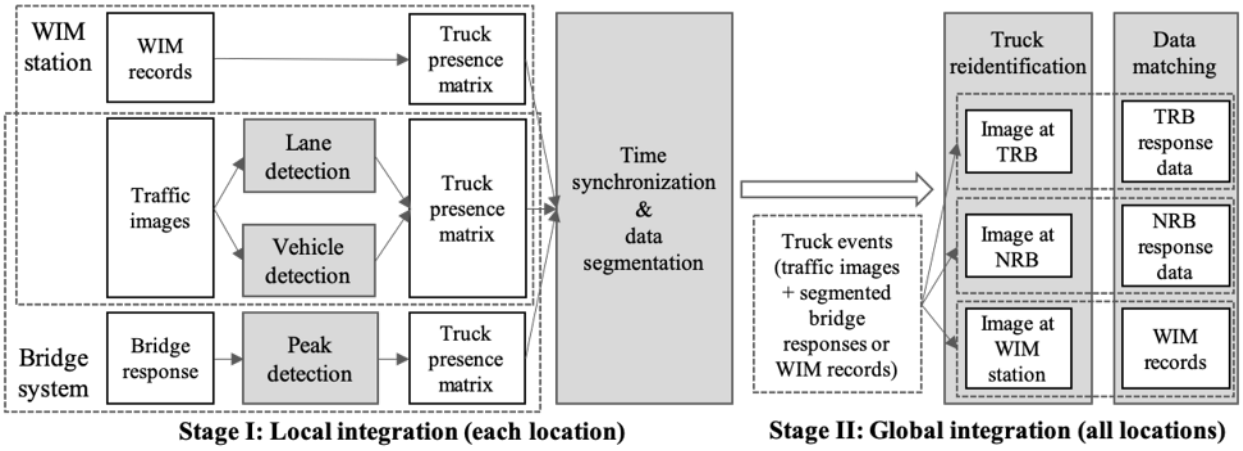

Figure 2-11: Data integration procedure following a microservices architecture: grey boxes correspond to computational modules and white boxes correspond to module input and outputs.

the integration of data across the CPS has computational modules (grey blocks) with defined functionality and a set of inputs or outputs (white blocks). A module output can be stored in the CPS database or as JavaScript Object Notation (JSON) file which can be further accessed by subsequent modules. This microservice architecture allows each module to be modified or upgraded without influencing the functionality of the entire application. In this study, the integration process is implemented in Python and performed autonomously in the CPS cloud computing platform (i.e., Azure).

2.4.1 Stage I: Local Integration

The local integration stage first extracts truck events separately from both traffic images and measured bridge responses collected at the same location during the same triggered data collection cycle. First, bridge strain response data and traffic images captured during the same cycle are retrieved from the database with their associated time stamps. Truck events at the bridge are detected from the strain response data measured by the three strain gauges installed on the bottom web at the midspan of girders 2, 4 and 6 in each bridge. As shown in Figure 2-2(b) and Figure 2-3(b), those sensors are denoted as S4, S20, S13 in the TRB, and S1, S2, S4 in the NRB. A script running a peak detection algorithm identifies the dominant strain peak (local maxima) greater than a defined response threshold (e.g., 12 $\mu\epsilon$) after the strain data has been filtered by a 2 Hz Butterworth low-

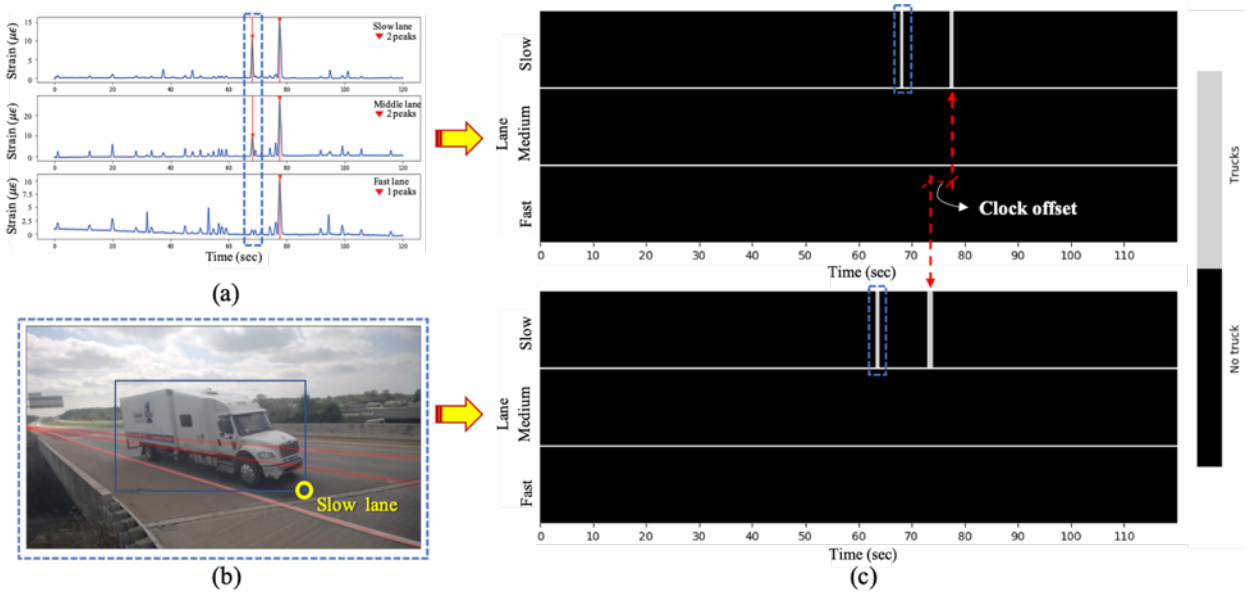

Figure 2-12: Time synchronization between bridge response data and traffic images by constructing two truck presence matrices at NRB with blue dash squares indicating information corresponding to the same truck in all three figure elements: (a) truck events identified from bridge strain data by detecting strain response peaks; (b) extracted truck event from Cam-2 images by detecting trucks using trained vehicle detector (blue bounding box) and identification of truck lane using box lower right corner (yellow circle) compared to lane boundaries (red lines); (c) truck presence matrices using extracted truck event information from strain data (top) and image data (bottom).

pass filter. These large strain peaks are assumed to be induced by heavy loads like trucks crossing the bridge. The left and right bounds of the peak defined at 0 $\mu\epsilon$ are taken as the start and end time of the corresponding truck event. By comparing the peak strain at each girder-line, the lane in which the truck is located can be identified with the peak value among the three gauges assigning the lane (due to each strain gauge being beneath a different lane).

Truck events are also identified from the traffic images with the detected vehicle class output from the trained YOLOv3 model executed in the cloud environment. Sequential camera images showing the same truck are assigned to the same truck event. Another analytical service is implemented to assign the detected truck to a lane on the bridge. This service first identifies the image pixels corresponding to the highway lane markings (e.g., white dash lines) using image processing techniques including Canny edge detection [151] and color thresholding on an image with no vehicles present in the camera field of view. The identified pixels of the lane markings are input into a

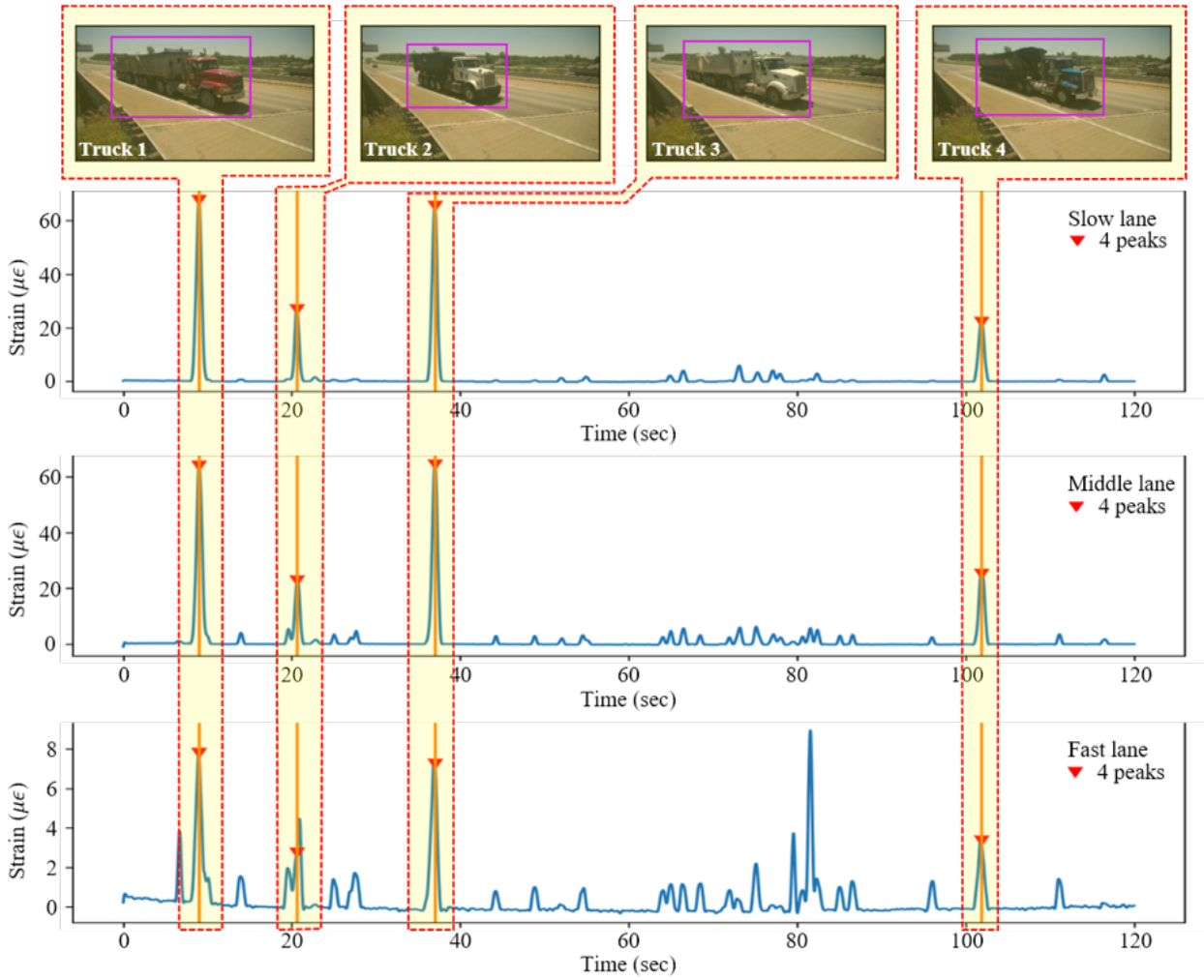

Figure 2-13: Result of time synchronization for integrating NRB strain response data with traffic images collected at Cam-3 (data collected August 2, 2017 at 6:34 pm).

polynomial fitting tool to calculate a continuous geometric boundary corresponding to edge of the lanes. This process is conducted daily due to slight movements of the installed traffic cameras over time due to vibration induced by traffic or weather conditions. The lane that a detected truck is in can be determined based on the relative position of the predicted bounding box (i.e., the position of the right bottom corner) with respect to the lane boundaries previously extracted from an image without a vehicle present as shown in Figure 2-12(b).

SHM data and traffic images are collected by different systems with their own clocks. While these clocks are synchronized over the cellular interface using the Network Time Protocol (NTP) regularly (i.e., every 20 min), they may not be perfectly aligned. Experience with the system de-

ployed on I-275 suggests the time offset is typically less than 1s but in extreme cases can be as large as 5 s, thereby inhibiting direct data integration using the local data timestamps. As a result, time synchronization between the SHM and camera datasets is necessary. Using truck event information extracted from the bridge and camera data, two sparse matrices are constructed to represent the truck presence from the traffic images and SHM data collected in the same data collection cycle. As visualized in Figure 2-12(c), this truck presence matrix has three rows representing the three lanes in which passing vehicles can travel; each column represents a discretized timestamp from the start of a data collection cycle. An entry is zero (black in Figure 2-12(c)) if no truck is present in that lane at that instant in time and one (white in Figure 2-12) if a truck is detected at that time. As the sampling rate of traffic images is 15 Hz, the truck presence information (i.e., a binary array) extracted from the camera is up-sampled using bilinear interpolation to have the same sampling rate (i.e., 100 Hz) as the bridge strain data. After the two truck presence matrices are obtained, cross-correlation is performed via fast Fourier transform (FFT) [152] to calculate the clock offset between the servers of the two data collection systems. As a result, truck event data collected in a single data collection cycle at the two systems can be synchronized in time; this allows a truck image to be linked to each strain peak identified in the strain data from each bridge. An example of four integrated truck events captured in the same data collection cycle at TRB are shown in Figure 2-13. By the same logic, traffic images and WIM records can be synchronized and linked.

2.4.2 Stage II: Global Integration

After the local integration stage, truck events captured in the same triggered data collection cycle are extracted at the two bridges and WIM station separately. The second stage aims to globally integrate these locally integrated data sets (i.e., truck image with a strain response or WIM station entity) for the same truck observed at the different locations. This global linking is done entirely by matching (or re-identifying) the same truck from images collected at the two bridges and WIM station. Among all traffic images assigned to a truck event at each measurement location, the one

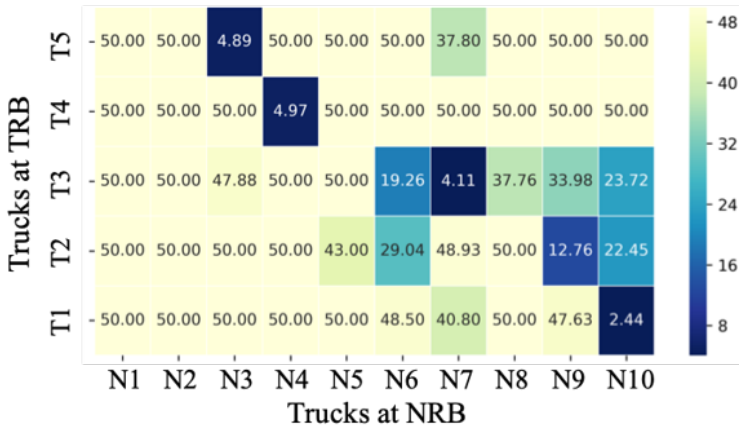

Figure 2-14: Heatmap of a correlation matrix for truck matching between two data sets collected at different bridge locations (NRB and TRB). Distance greater than 50 is clipped to 50 for better visualization.

that has the largest bounding box and includes the front part (e.g., tractor) of the truck is picked for vehicle re-identification. That image is cropped using the predicted bounding box to remove the redundant background. Such an image would contain the most information of the truck appearance and will therefore give better accuracy for re-identification.

Truck re-identification is conducted following a mutual nearest neighbor strategy. Multiple truck events can be captured at each measurement location during one data collection cycle. Furthermore, not all of the truck events captured at one location will be observed by the CPS architecture at subsequent locations because trucks may exit the corridor between two adjacent locations or not be within the assumed speed range that defines the time of data collection at each location relative to the trigger at Cam-1. To perform truck matching between two locations, every possible pair of truck images collected during the same data collection cycle at each location are compared through a similarity function which outputs a distance-based scalar metric (to be defined shortly). Consequently, a correlation matrix with m rows and n columns is used to store the similarity function output for the m truck events captured at the first location to the n truck events captured at the second location. A sample of a correlation matrix is shown in Figure 2-14 to show the re-identification between the TRB where 5 trucks were identified and NRB where 10 trucks were identified in the same collection cycle. In a mutual nearest neighbor strategy, two images with

index i and j are assumed to belong to the same truck if and only if the similarity metric at element (i, j) in the correlation matrix is below a pre-determined threshold and is the minimum of i-th row and j-th column simultaneously. Taking the matrix shown in Figure 2-14 as an example, four pairs of truck images are potential matches if the threshold is set to be 5: namely, T5 & N3, T4 & N4, T3 & N7 and T1 & N10.

To develop a robust similarity function, a CNN-based embedding network is used to convert each truck image into a vectorized feature representation with the Euclidean distance between the feature vectors used as a measure of the similarity between the two truck images. Similar to vehicle detection, details regarding the implementation and evaluation of the CNN-based embedding network will be described in Chapter 3 to avoid distraction. The trained embedding network obtains a precision of 100% on the test data, a recall of 95.00% and a F1-score of 0.97. Using this truck re-identification strategy, truck events captured at different locations but within the same collection cycle can be matched.

2.5 Results and Discussions

2.5.1 Integrated CPS Data

A complete data set containing response data from bridges, truck weight information measured by the WIM station and truck images taken at the bridges and the WIM station are obtained if the truck is re-identified at all three measurement locations; a sample is presented in Figure 2-15 to showcase such a data set. In some cases, the same truck might be observed at only two of the three locations; this data is also added to the database of integrated response data. This section presents some uses of the data collected related to SHM analyses. Specifically, the linked data between the bridges and WIM station for the same truck can serve as a powerful basis for correlating responses across the corridor and baselining performance using a consistent traffic load set. The results presented herein correspond to over one year of data collected by the CPS from August 2017 to April 2019.

Figure 2-15: An example of a complete data set collected by the CPS system containing response data from two bridges, WIM data and truck images captured at each location (data collected October 19, 2017 at 6:29 pm).

2.5.2 Truck Travel Time

The travel time of trucks between adjacent locations along the corridor can be calculated based on the timestamps of each truck passing all three data acquisition locations in the I-275 corridor. The three histograms plotted in Figure 2-16 show the distribution of travel time of trucks from the TRB to the NRB, from the NRB to the WIM station and from the TRB to the WIM station, respectively. These results confirm the time windows assigned to each location by the Cam-1 trigger are suitable for the majority of trucks observed in the corridor. It takes 248.48s and 392.30s on average for trucks to travel from the TRB to the NRB and from the NRB to the WIMS, respectively. Based on the distance between different locations along the corridor and the travel time extracted, trucks travel at a speed of approximately 64.5 mile per hour (103.8 km per hour) which agrees with the average speed observed at the WIM station. It can also be observed that longer travel distances introduce larger variations truck travel times because of the higher uncertainty associated with traffic conditions over a longer distance.

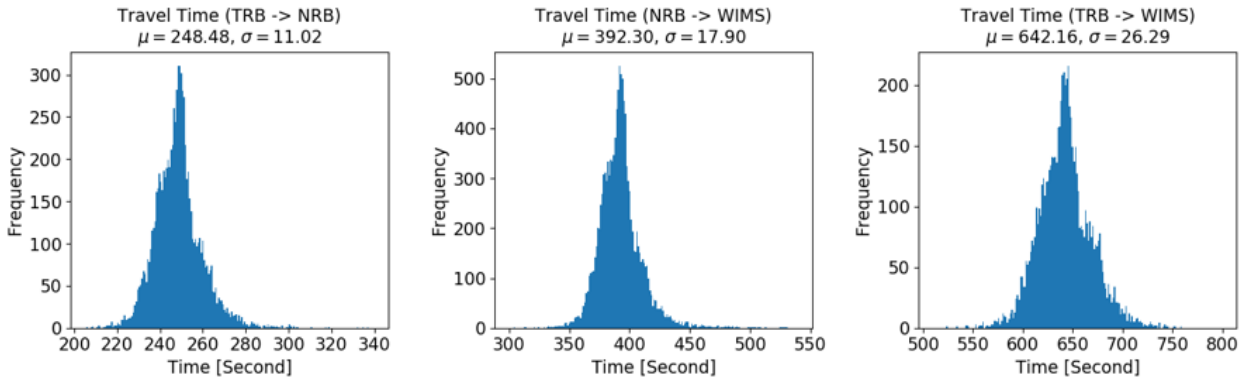

Figure 2-16: Histograms of truck travelling time between different segments along the corridor: (a) from the TRB to the NRB; (b) from the NRB to the WIM station; (c) from the TRB to the WIM station. Data corresponds to collection period from August 1, 2017 to April 30, 2019.

Bridge	# Truck events	Slow lane	Middle lane	Fast lane	Multiple trucks	Change lane
TRB	15,875	1,085	13,206	964	561	59
NRB	24,719	17,727	5,619	27	1,308	38

Table 2-1: Statistics of truck events matched from the Telegraph Road Bridge and the Newburg Road Bridge with the WIM station.

2.5.3 Truck Weight and Bridge Response Correlation

Given the bridge data that is linked to the WIM station data, correlations between the maximum truck-induced bridge strain response and the gross weight of the corresponding trucks can be investigated using the globally integrated data sets. This is very beneficial for load rating of bridges due to the integrated data offering in-situ bridge responses corresponding to a quantitative measure of the truck weight [153]. Depending on which lane of the bridge that a vehicle is in, three correlations can be created for the bridge response data measured by each sensor on each bridge. To do so, only the cases of a single truck crossing the bridge are selected with the cases of multiple trucks traversing the bridges simultaneously or in succession with a short headway are ruled out. In addition, data with trucks changing lanes while on the bridges are not considered. These more complicated scenarios are excluded not because they cannot be handled, but simply to establish a clearer linear correlation of bridge responses using the collected data as a way to demonstrate the effectiveness of the proposed CPS. The cases in which trucks and small vehicles (e.g., cars) are

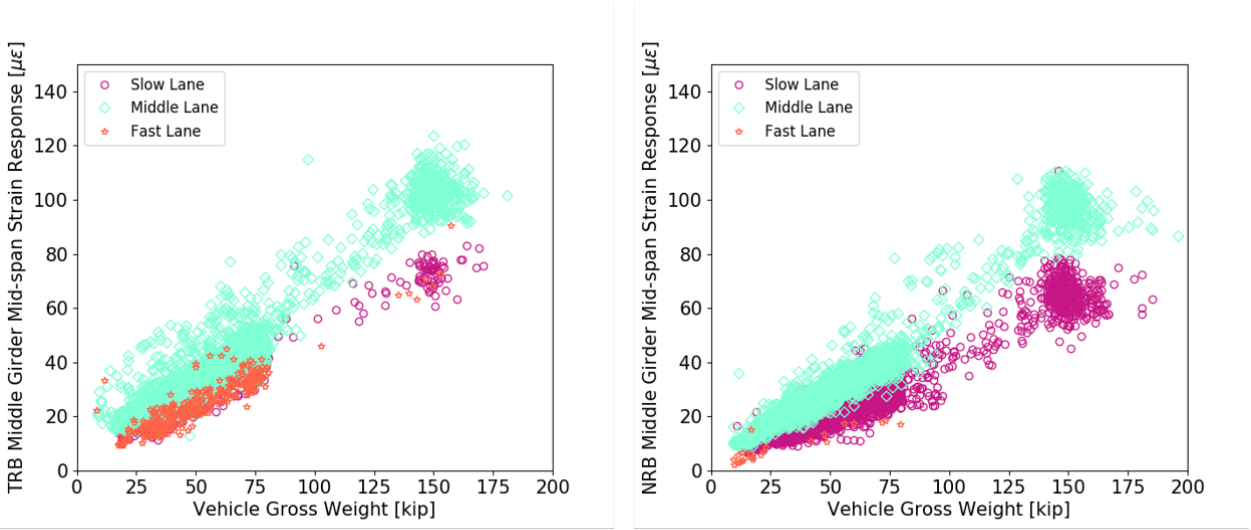

Figure 2-17: Correlation between bridge maximum strain responses and corresponding gross vehicle weight measured by the WIM station: (a) TRB strain measured at S20; (b) NRB strain measured at S2 (data collected from August 1, 2017 to April 30, 2019).

on the bridges at the same time are kept assuming the bridge response associated with the small vehicles are negligible compared to those of trucks. Figure 2-17(a) presents a scatter plot showing the correlation between the maximum strain response measured by gauge S20 on the TRB and the corresponding vehicle gross weights. Similarly, Figure 2-17(b) is a scatter plot of the maximum strain responses measured by gauge S2 on the NRB relative to the truck gross weights. Shown in both plots are three different scenarios, namely trucks on slow lane, middle lane and fast lane. Statistics of the truck events can be found in Table 2-1. As expected, there exists a strong positive linear correlation between the bridge strain response and the vehicle weight, as would be expected. The variations observed in the plots are mainly attributed to the various types of truck load configurations (including truck lengths and weight distributions), varying truck positions within an assigned lane and truck speeds. The variances observed in these relationships could possibly be reduced by distinguishing vehicles by their FHWA vehicle class or by removing cases where small vehicles are present.

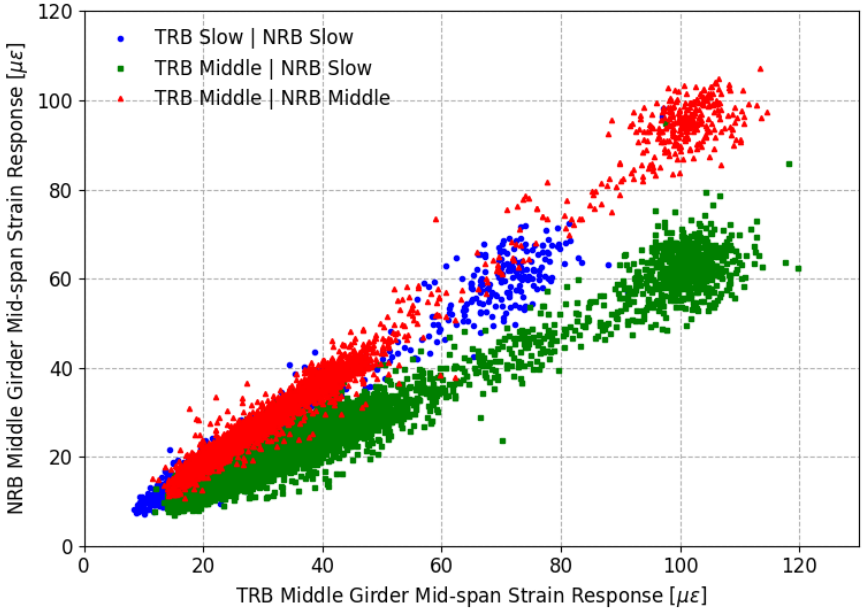

Figure 2-18: Correlation between TRB maximum strain responses (measured by S20) and NRB maximum strain responses (measured by S2) to the same truck loads (data collected from August 1, 2017 to April 30, 2019).

2.5.4 Bridge Response Correlation

Apart from mapping vehicle weights to bridge responses, the correlation between the responses of two bridges to the same vehicle load set can be also investigated and could naturally account for some of the variations associated with the previous cluster analyses. Maximum bridge strain responses measured by gauge S20 of the TRB and corresponding strain peaks measured by gauge S2 of the NRB are presented in Figure 2-18. Statistics of the truck events can be found in Table 2-2. Three major scenarios are presented depending on the lane that vehicles cross the bridges in: 1) on the slow lane of the TRB and the slow lane of the NRB, 2) on the middle lane of the TRB and the slow lane of the NRB, and 3) on the middle lane of the TRB and the middle lane of the NRB. An even stronger linear correlation between the two bridges' responses can be observed and the variation of the data around the linear regression would be much smaller when compared to the correlation between bridge responses and gross weights measured at WIM station.

	TRB-slow	TRB-middle	TRB-fast	Total
NRB-slow	1,227	12,851	737	14,815
NRB-middle	91	3,647	289	4,027
NRB-fast	0	6	10	16
Single truck		18,858		
Multiple trucks		2,282		
Change lane		203		
Total # truck events		21,343		

Table 2-2: Statistics of truck events matched between the Telegraph Road Bridge and the Newburg Road Bridge.

2.6 Summary and Conclusions

By leveraging computer vision techniques and cloud computing platforms, this study proposed a CPS framework to integrate vehicle-induced responses of two highway bridges measured by wireless SHM systems with corresponding vehicle weight information measured by a nearby WIM station located along the same highway corridor. In the framework, traffic images collected at each measurement location serves as the primary data source for integrating the data from the different locations along the same highway corridor to the same truck loads. The trained YOLOv3-tiny module with an average precision of 96.65% for truck detection is deployed in the first traffic camera to detect incoming trucks in real-time and to trigger data acquisition processes downstream in the highway corridor. The trigger-based data acquisition strategy proved to be at least 24.5% more efficient than previously used schedule-based data collection strategies leading to the collection of more bridge response data of greater value due to truck events present. Collected data was later automatically processed by a two-stage data fusion pipeline consisting of local truck detection and global re-identification so that data corresponding to the same truck events can be integrated for further analysis. The trained YOLOv3 model at the first stage had a truck detection average precision of 98.91% providing accurate detection results for further data analysis. The second stage employed a mutual nearest neighbor truck re-identification strategy by encoding truck images into feature vectors using a customized CNN embedding network trained by a triplet network

architecture, yielding a F1-score of 0.97. With the CPS framework implemented along the I-275 northbound highway corridor, around 20,000 data sets (including bridge response, load information and traffic images) of truck events have been collected since August 2017. Expected linear correlations are observed between peak bridge responses and corresponding truck gross weights, and between peak bridge responses of the two bridges to the same truck loads.

To the best of the authors' knowledge, this is the first CPS framework ever proposed to dramatically enhance the value of data collected for bridge SHM. The proposed system is highly scalable due to its proven abilities to automate the identification of trucks, mapping their travel history in corridors, and triggering SHM data collection in response. These leads to the quantitative mapping of vehicle loads to measured structural responses of multiple bridges. The impact of this innovation on the operational management of highways is enormous. For example, the CPS platform can serve as foundation for data-driven bridge damage detection methods, bridge load rating, and other health assessment approaches that are difficult to conduct without load information with bridge response data. By considering adjacent bridges located in close proximity experiencing similar environmental and operating conditions (EOC), the health of one bridge could be determined based on its response relates to the adjacent bridge. Such a framework may potentially derive innovative data-driven approaches for the diagnosis and prognosis of bridge structural health conditions. Specifically, the correlation between responses of different bridges to same load profile can be used to detect structural deterioration in the bridges through statistical process control methods. The CPS framework also offers a rich data set for supporting other decisions integral to highway operations including use of bridge responses to estimate the magnitude and spatial trajectories of truck loads in a highway network. The work lays a foundation for additional future research, part of which will be described in following chapters. In the presented study, only cases of a single truck were considered when performing the response correlation analyses. Introducing more complex loading scenarios in the correlation analysis including scenarios where multiple trucks are on a bridge could be investigated in future studies to allow a larger portion of the acquired data to be utilized. To do so, ways of combining the load effect of each truck weight based on their location

on the bridge to the net bridge response would be needed in order to perform a proper correlation analysis. One drawback of the current vision-based CPS is that it has been developed primarily for daytime use; future work is now focused on expanding the capabilities of the system to operate reliably during night or under extremely harsh weather (e.g., snowstorms). The CPS framework is also being extended to include other ways of identifying and tracking trucks based on wireless telemetry such as DSRC (Dedicated Short-Range Communications). DSRC could be a powerful approach to overcoming the challenges associated with computer vision methods applied to night and snow images.

CHAPTER 3.

Computer Vision for Truck Load Detection and Re-identification Within the Cyber-physical System Framework

3.1 Introduction

Tremendous progress has been made over the past decade in computer vision technology. Deep learning-based approaches to object detection, object tracking and semantic segmentation have shown remarkable performance in solving fundamental problems in many application areas including in intelligent transportation systems (ITS). Particularly, learning-based vehicle detection and re-identification methods have been previously proposed for large-scale urban surveillance [154], traffic flow analysis (e.g., vehicle speed estimation and accident detection) [155], and smart traffic signal control at road intersections [156]. Concurrent to the advancement of computer vision has been a growth in the capabilities of cost-efficient sensing technologies including low-cost sensors, wireless telemetry, and "smart" sensors capable of local data processing (i.e., edge computing) [157]. These advances have impacted the structural health monitoring (SHM) field as witnessed by the increasing number of monitoring systems that have been deployed in operational bridges [38]. While existing bridge SHM systems can accurately measure bridge responses (e.g., strain) and environmental conditions (e.g., temperature), most lack the capability of directly measuring traffic loads that induce bridge responses; this renders health assessment algorithms ill-posed and hinders their accuracy and generality [83, 64]. The possibility of vehicle detection by computer vision stands to dramatically enhance bridge monitoring by integrating vehicle load data with bridge response data for SHM analysis.

In the previous chapter, a truck re-identification framework is proposed to track truck loads in highway corridors with the aim of linking truck loads to bridge responses based upon the proposed CPS architecture. To recap, the framework utilizes traffic video feeds acquired at bridges and a WIM station along the same corridor as the basis for tracking trucks. First, the framework employs a convolutional neural network (CNN) detector to identify and segment vehicle events at each camera location (i.e., at each bridge or WIM station). Cameras are time synchronized with the bridge monitoring system and the WIM station to ensure trucks identified are linked to the bridge responses and vehicle weight measurements collected, respectively. Next, the trained vehicle detector is modified and fine-tuned within a triplet architecture to extract a vectorized feature representation of each truck image captured by the CNN detectors. Using a mutual nearest neighbor strategy, the Euclidean distance between the feature vectors of each captured truck is selected to serve as a scalar metric of truck similarity; high similarity implies the truck is successfully re-identified. Once a truck is detected at the bridge and later re-identified at the WIM station, measured bridge responses can be accurately associated with the weight parameters (i.e., gross vehicle weight, axle weight distributions, and axle spacings) of the truck as measured by the WIM station. Such a framework allows bridge responses to be precisely mapped to their corresponding vehicular loads using the CPS architecture described in Chapter 2. In this chapter, details of methodologies and corresponding comparison studies are described. Multiple CNN models are explored for vehicle detection at each measurement point in the CPS (namely at the bridges and WIM station). The various CNN models are compared using precision-recall curves to identify the most robust single-stage detector. In the next section, the implementation of the truck re-identification algorithm is presented. Finally, the chapter concludes with a summary of key findings and a description of future work.

3.2 Object Detection Algorithms

Object detection is a challenging computer vision problem that has been intensively researched over the past decade [158]. Object detection refers to automated methods that identify, locate, and

classify target objects within an image. Operation of transportation systems including managing vehicles on highways and users using public transit has emerged as one of the most active application domains for object tracking by computer vision methods [159]. Recent advances in deep learning have improved object detection techniques. This study leverages recent advances in deep learning-based object detection techniques, especially CNNs, for truck detection within the CPS architecture. Generally, there are two primary CNN architectures for object detection: two-stage and one-stage detectors. Two-stage detectors such as Regions with CNN features (R-CNN) [160], Fast R-CNN , Faster R-CNN [161] and their variants are designed with one stage used to propose candidate regions of interest in an image and the second stage used to perform object classification and detection for each region of interest generated by the first stage. In contrast, one-stage detectors such as You Look Only Once (YOLO) [158, 162, 163], Single Shot Detector (SSD) [164], RetinaNet [165, 166] and their variants, cast object detection into a single regression problem which predicts object classes, bounding boxes and confidence scores simultaneously within a single network inference. While two-stage detectors generally enjoy higher precision compared to one-stage detectors, their computational speeds are slower [166].

With real-time truck identification at Cam-1 requiring near real-time execution, this study adopts a one-stage detector framework for the identification of trucks. Four one-stage object detection paradigms proposed by other researchers are tested for truck identification: YOLOv3 [163], YOLOv3-tiny [163], RetinaNet [165] and SSD [164]. All four architectures utilize CNNs as the backbone for their feature extractions. Camera images of a pre-determined resolution and size are set as the CNN input while the CNN output is the location (i.e., bounding box) and detection confidence of the target object within the box. A brief description of the four architectures will be presented; interested readers are invited to read the implementation details of each method in the original papers. Based on evaluation results, the YOLOv3-tiny and YOLOv3 detectors are used within the CPS design in this study [163]. Recently, proposal-free and anchor-free object detection algorithms [167, 168] have emerged claiming to have a more straightforward design. Despite being innovative in their design, these algorithms cannot compete with YOLO in terms of inference

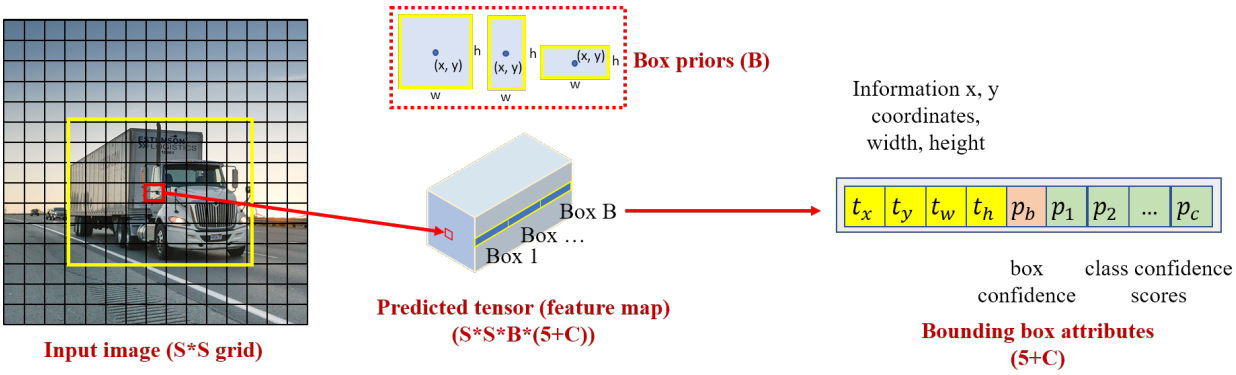

Figure 3-1: Framework design of YOLO for dense object detection.

speed due to their heavy backbone architectures and need for potential post-processing steps to recover bounding boxes.

3.2.1 You Only Look Once (YOLO)

YOLO is a single-stage CNN architecture for object identification where the input is the raw image. Its input-output design is illustrated in Figure 3-1. YOLO splits the image into an S-by-S grid with each grid cell responsible for predicting B candidate bounding boxes whose centroid fall inside that cell area and contains the object [158]. It should be noted the bounding box can be much larger than the cell itself and only the box centroid needs to be in the cell. The number of predicted candidate boxes B depends on the number of box priors selected for approximately representing the shape and dimension of the final bounding boxes [162]. Each bounding box is defined by a $(5 + C)$ element vector including information of its centroid x and y coordinates, box width, box height, a box confidence score representing the likelihood that the box contains an object, and the conditional probabilities corresponding to C target object classes given a detected object in the box. YOLO utilizes its underlying CNN network to encode an input image into a tensor with a shape of $S \times S \times (B \times (5 + C))$ containing the various bounding box predictions for the image [162]. For each predicted bounding box, its class confidence scores are equal to the product of the box confidence score and corresponding conditional class probabilities. Independent logistic classifiers are then used to determine the final class for each predicted bounding box; logistic

YOLOv3 Network						
Repeat	Layer	Type	# Output Channels	Size	Stride	Output Size
	1	Convolutional	32	3	1	256×256
	2	Convolutional	64	3	2	128×128
	3	Convolutional	32	3	1	
1	4	Convolutional	64	3	1	
		Residual				128×128
	5	Convolutional	128	3	2	64×64
	6,8	Convolutional	64	3	1	
2	7,9	Convolutional	128	3	1	
		Residual				64×64
	10	Convolutional	256	3	2	32×32
	11, 13, 15, 17, 19, 21, 23, 25	Convolutional	128	1	1	
8	12, 14, 16, 18, 20, 22, 24, 26	Convolutional	256	3	1	
		Residual				32×32
		Detection (1)	24	1	1	32×32
	27	Convolutional	512	3	2	16×16
	28, 30, 32, 34, 36, 38, 40, 42	Convolutional	256	3	1	
8	29, 31, 33, 35, 37, 39, 41, 43	Convolutional	512	1	1	
		Residual				16×16
		Detection (2)	24	1	1	8×8
	44	Convolutional	1024	3	2	
	45, 47, 49, 51	Convolutional	512	1	1	
4	46, 48, 50, 52	Convolutional	1024	3	1	
		Residual				8×8
		Detection (3)	24	1	1	8×8

Table 3-1: Layer types and primary parameters of the YOLOv3 model.

classifiers allow an object to be assigned to multiple classes which is beneficial when classes have overlap. Due to its model design, there might be multiple bounding boxes for the same object; non-maximal suppression (NMS) is then used by YOLO to remove bounding box duplications with lower scores. A global confidence threshold can also be set such that the model only outputs predictions with confidence scores higher than the defined threshold.

The third generation of the YOLO architecture, namely YOLOv3, features a deep 53-layer CNN architecture termed "Darknet-53" [163]. The overall backbone composition of Darknet-53 is shown in Table 3-1. Darknet-53 consists of 52 convolutional layers in total. In Darknet-53, each

convolutional layer is made of a set of convolutional filters generating feature maps given its inputs followed by a batch normalization (BN) operation [169] and a leaky ReLU activation [170]. For a single convolutional layer in YOLOv3, the properties of the convolutional filters are mainly defined by the number of output channels, the kernel size and the stride. The input of one convolutional layer is the output of the previous one and thus the total number of filters in one convolutional layer is the product of the number of input channels and the number of output channels. During forward inference, each filter kernel performs a convolutional operation on its corresponding input channel and all generated results (with the same size) are aggregated in a way that each output feature map channel is a combination of the processed information of all of the input channels. BN is a straightforward operation adjusting the output scale of the convolution filters to be in the range of 0 to 1. Such an operation makes it easier for the network parameters to converge to a local minimum and thus network learning is faster. Its operation is defined as:

$$\begin{aligned} \mu_B &= \frac{1}{m}\sum_{i=1}^{m} x_i \\ \sigma_B &= \frac{1}{m}\sum_{i=1}^{m}(x_i - \mu_B)^2 \\ \hat{x}_i &= \frac{x_i - \mu_B}{\sqrt{\sigma_B^2 + \epsilon}} \\ y_i &= \gamma\hat{x}_i + \beta \equiv BN_{\gamma,\beta}(X_i) \end{aligned} \tag{3.1}$$

where x_i is the output of convolutional filters in the same layer, m is the total number of output channels, and are two learnable parameters updated during training and y_i is the output of BN operation. Leaky ReLU is added to the architecture to introduce nonlinearity into each convolutional layer; the ReLU operation is defined as

$$y = \mathbb{1}(x < 0)(\alpha x) + \mathbb{1}(x \geq 0)(x) \tag{3.2}$$

where $\mathbb{1}$ is an indicator function having output of 1 when the condition inside the parentheses is

met and 0 otherwise. α is a small constant and represents the "leaky" aspect of the ReLU function. In YOLOv3, it is set to 0.1. The Darknet-53 backbone network also contains several residual (skip) connections [171] which directly add the activation outputs of a specific previous layer into those of the current layer. Skip connections were first proposed in the residual network (ResNet) to enable the convolutional layers to preserve an identity mapping of its input [171]. The sizes of the feature maps generated by primary convolutional layers are also shown in Table 3-1.

The YOLOv3 network also incorporates feature pyramid network (FPN) like up-sampling techniques [166] to improve its prediction performance (especially for detecting small objects). More specifically, it features three convolutional detection heads responsible for producing final dense predictions at different scales, which improves its performance on detecting objects of different sizes. As described previously, each detection head outputs a dense bounding box prediction by predicting a tensor of size $S \times S \times (B \times (5 + C))$ utilizing an additional convolutional layer. For example, in Table 3-1 the detection (1) layer before layer 27 outputs $32 \times 32 \times (3 \times (5 + 3))$ indicating the location and class information of the predicted bounding boxes, where 32×32 is the size of the feature map, 3 is the number of anchor boxes predefined for this scale, $(5+3)$ represents the bound box features which include four elements for bounding box location, one element for the bounding box confidence score and three elements for the class confidence score (i.e., truck, pick-up truck, and car classes). Unlike intermediate convolutional layers for feature extraction, this convolutional detection layer doesn't have a BN module and uses simple linear activation.

When a fast execution speed is an important requirement, a reduced-order version of YOLOv3 called YOLOv3-tiny can also be used. follows the same logical design as YOLOv3 but adopts a much more compact CNN backbone (i.e., 13 convolutional layers as opposed to 52) thereby reducing its computational cost and speeding its execution for real-time applications. The backbone of YOLOv3-tiny is shown in Table 3-4 [163]. YOLOv3 has three variants supporting image inputs of different sizes. This study selects the YOLO models that accept 416-by-416 pixel images as inputs for a balance of speed and accuracy [163]. The input image resolution is fixed by the CNN architecture; images from cameras of different resolutions must be modified to conform to the required

input image resolution.

3.2.2 RetinaNet

The RetinaNet CNN architecture consists of a backbone network and two task-specific sub-networks. The backbone network stacks an FPN on top of ResNet in order to extract several feature maps at different spatial scales from the input image [165, 166, 171]. The two sub-networks are responsible for object classification and convolutional bounding box regression based on the feature maps extracted by the backbone network [165]. In addition to its innovative unifying architecture, RetinaNet utilizes a novel loss function called focal loss. Focal loss was designed to resolve the challenging issue of class imbalance which is often encountered in one-stage detectors [165]. Towards this end, focal loss dynamically scales a cross entropy function during training to allow the training to focus more on those objects difficult to classify. The version which has the ResNet-50-FPN as its backbone is used in this study because it offers a good balance between speed and precision [165]. Input images of the RetinaNet model are resized such that the shorter side equals 600 pixels.

3.2.3 Single Shot Detector (SSD)

The SSD architectures select the VGG-16 [172] CNN architecture as the base network but discards the fully connected layers and adds auxiliary convolutional layers for extracting features at multiple scales [164]. The SSD divides each feature map into grid cells where each cell has a set of default boxes of different dimensions and aspect ratios associated [164]. For each default bounding box, the confidence for all object classes are predicted and the box location is adjusted to better match the object location through regression performed by the CNN. The SSD version which takes 300-by-300 pixels images as the network inputs is adopted in this study.

	Total Images	Online Images	I-275 Images	Total Vehicle Instances	Numbers of Trucks	Number of Pick-up Trucks	Number of Cars
Training Set	2600	1142	1458	4391	2947	344	1100
Test Set	900	0	900	1226	566	178	482
Total	3500	1142	2358	5617	3513	522	1582

Table 3-2: Statistics associated with customized vehicle data sets used for training and validation of CNN detectors.

Figure 3-2: Sample images in the customized vehicle detection data set: (top row) images from the Internet; (middle) images from the I-275 corridor; (bottom) images from the I-275 corridor under varying weather conditions.

3.3 Automatic Vehicle Detection

3.3.1 Customized Vehicle Dataset

The primary objective of this study is to detect three vehicle classes from camera images: large trucks, pick-up trucks and cars (e.g., sedans, SUV, vans). The four selected single-stage object detectors (YOLOv3, YOLOv3-tiny, RetinaNet, SSD) have their initial CNN architectures fixed with preliminary weights pre-trained on ImageNet [173] included. These four detectors are further fine-tuned and later tested using a diverse set of images manually prepared to improve the detectors for vehicle detection. The resultant data set is a combination of pictures of trucks crawled from the Internet and those manually selected from the traffic images captured by the four cameras installed

along the I-275 corridor. Ground truth bounding boxes are manually labelled in all figures by the authors using a customized annotation tool. The entire data set used to train the four detectors contains a total of 3,500 vehicle images. Approximately 70% of the pictures are used for CNN training with 30% held for testing. As listed in Table 3-2, the training set has 2,600 vehicle images that contain a total of 4,391 vehicle instances (2947 trucks, 344 pick-up trucks, and 1100 cars). In contrast, the test set is composed of 900 vehicle images with a total of 1,226 vehicle instances (566 trucks, 178 pick-up trucks, and 482 cars). One additional arrangement of the split is that all the vehicle pictures obtained online belong to the training data set. The reason for selecting online images for training is to generalize the detection capability of the CNN so that it can potentially detect vehicles that may not commonly appear in the videos captured on the I-275 highway corridor. To further generalize the detection capabilities of the four detectors, vehicle images from the Internet and the I-275 cameras are intentionally diversified to include a wide range of weather and illumination conditions (e.g., snow, rain or glare). This tactic ensures the final trained CNN architectures will offer robust detection performance even under harsh operational circumstances. Some sample images used to train the CNN architectures are shown in Figure 3-2.

3.3.2 Model Training

The four object detectors are based on open-source scripts published by the authors of the original work. More specifically, the implementation of YOLOv3 and YOLOv3-tiny is based on Darknet which is an open source neural network framework written in C and CUDA [174]. Similar to the original YOLOv3 model, the batch size is 64 and the initial learning rate is 0.001. The final model is trained for 23,000 iterations. RetinaNet is based on Detectron which is a software system developed by Facebook based on Python and the Caffe2 deep learning framework for novel object detection models [175]. The SSD implementation adopts the original open source code using the Caffe framework [164]. The model parameters of all four CNN architectures are initialized using the publicly available weights pre-trained based on the ImageNet dateset [173]. During further training using the data set of Table 3-2, back-propagation methods are used to update the CNN

Model	$mAP_{0.5}$	$mAP_{0.75}$	Speed	$AP_{0.5}^{truck}$	$AP_{0.5}^{pickup}$	$AP_{0.5}^{car}$	$AP_{0.75}^{truck}$	$AP_{0.75}^{pickup}$	$AP_{0.75}^{car}$
YOLOv3	93.64%	**92.56%**	19.7ms	**98.91%**	88.44%	93.58%	**98.91%**	85.73%	93.04%
YOLOv3-tiny	88.11%	86.20%	**3.2ms**	97.46%	82.13%	84.73%	96.65%	79.25%	82.71%
RetinaNet	**93.98%**	92.50%	77.3ms	97.67%	**90.02%**	**94.25%**	96.80%	**86.82%**	**93.89%**
SSD	90.68%	88.57%	48.2ms	98.03%	81.77%	92.26%	95.89%	78.58%	91.25%

Table 3-3: Test results of four selected single-stage vehicle detection models trained using the customized dataset.

weights to achieve a high level of detection accuracy and precision. Only minor changes (e.g., object classes, learning rate, batch size) are made to the original implementation to accommodate the customized training dataset and specific machine hardware used in this study so that convergence of loss is achieved during training. For example, the number of classes, the number of GPUs, the learning rate and the batch size are modified according to the hybrid (i.e., Internet and from I-275) training set. Both the training and testing processes are performed on an NVIDIA Titan Xp GPU.

3.3.3 Model Testing

After training, the four detectors are evaluated using the independent testing data set. The performance of each detection is based on average precision (AP) per class [176], mean AP (mAP) [176] and inference speed. By definition, precision is defined as the fraction of predictions that are correct (i.e., true positives dived by the number of true and false positives) and recall is defined as the fraction of ground truth events correctly predicted (i.e., true positives divided by the number of true positives and false negatives). Hence, average precision is an average of the maximum precision metrics at various recall rates. In the four object detectors, a global confidence threshold can be established to control the lower bound of the confidence score that a detector can have, and thus the number of prediction outputs. Consequently, a change of the global confidence threshold leads to a change of the precision and recall obtained on the test data. AP is calculated by averaging maximum precisions at different recall levels per class and mAP is the mean of AP of all detectable classes. AP is also associated with an intersection over union (IOU) threshold where IOU is the percentage of the detected object bounding box overlapping with the ground truth bounding box (i.e., a bounding box perfectly bounding the detected object). A higher IOU threshold means

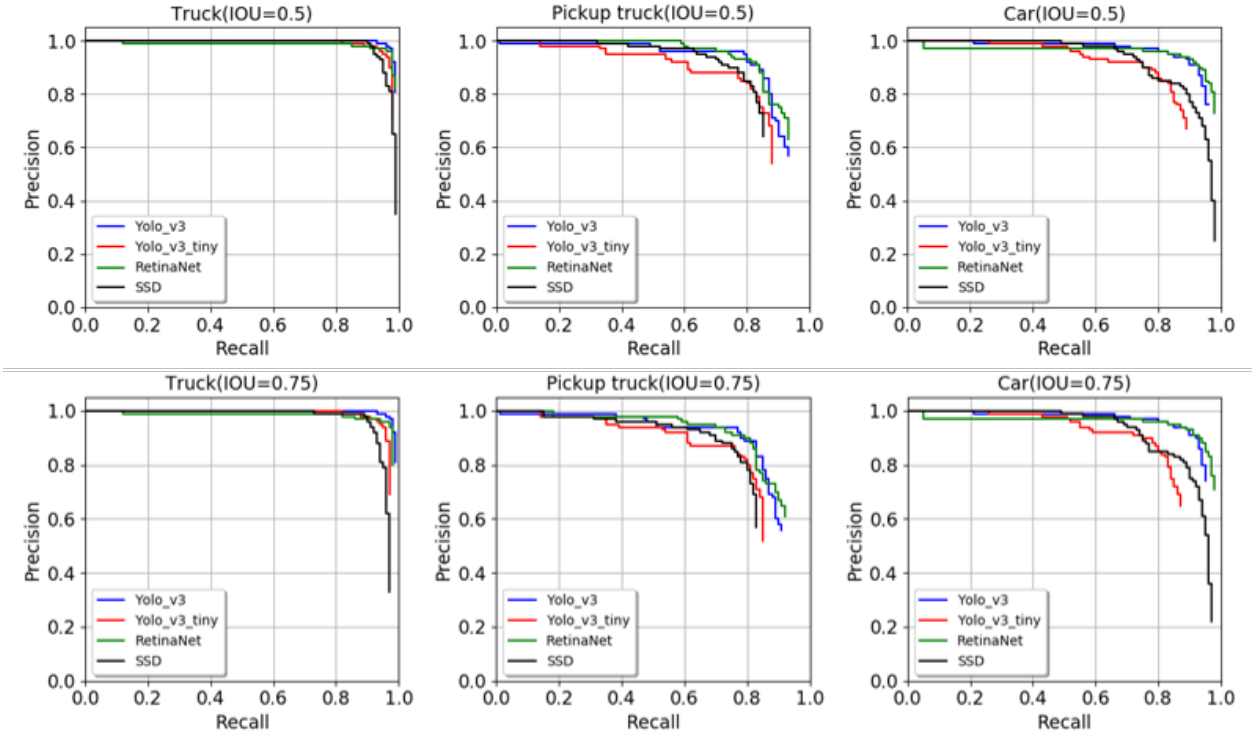

Figure 3-3: Comparison of precision-recall curves of the trained detection models per object category using different IOU thresholds.

the predicted bounding box of the detected object needs to have more overlap with the ground truth to be considered a correct detection. In this study, mAP and AP per class are both evaluated for two different intersection over union (IOU) thresholds: 0.5 and 0.75 which are denoted using subscripts (e.g., $AP_{0.5}$ and $AP_{0.75}$). Because predicted bounding boxes will also be used in other analyses such as detecting which lane the vehicle is in and for vehicle matching, a relatively high IOU threshold of 0.75 is investigated besides the most common 0.5 threshold used in computer vision studies. The detailed evaluation results (benchmarked using a Nvidia Titan Xp GPU) for the four detectors are shown quantitatively in Table 3-3 with the most competitive result bolded in each column. In addition, the precision-recall curves per vehicle class of the four detectors with two different IOU thresholds are presented in Figure 3-3 for comparison. The inference speed refers to the average time needed to perform vehicle detection on a single image, and it depends not only on the model complexity, but also on the computing hardware upon which the detector is implemented.

As shown in Figure 3-3, all four detectors achieve relatively high mAPs. This may be because vehicles have low variance on their appearance and the test images are limited to ones captured from the four identical cameras along the I-275 corridor. More specifically, YOLOv3 shows the highest accuracy for truck detection while RetinaNet slightly outperforms others in pickup and car detection due to the use of focal loss which addresses the class imbalance between large truck classes and small car classes. However, the lightweight YOLOv3-tiny model exhibits the fastest inference time while still achieving a sufficiently high level of accuracy, especially for truck detection - the average precision of the YOLOv3-tiny in detecting trucks for an IOU threshold of 0.5 and 0.75 is 97.46% and 96.65%, respectively.

Consequently, the YOLOv3-tiny model is deployed in the NVIDIA TX modules in the field for real-time truck detection at CAM-1 where latency is the most important performance metric. When deployed upon the Nvidia Jetson TX2 which is the server hardware used at Cam-1, the YOLOv3-tiny model is capable of being executed in realtime at an equivalent frame rate of 15 frames per second which satisfies real-time detection requirements of the CPS. YOLOv3 is selected as the primary detector used to detect trucks in the bridges and WIM station images (namely, Cam-2 through Cam-4) offline because real-time performance is not required - the time of execution for this more extensive CNN model on the Titan Xp is 19.7ms per image. The YOLOv3 model is used to perform vehicle detection on traffic images captured by the other cameras using a server with a Nvidia Titan Xp GPU that is accessible to the CPS via the Internet. Its average precision for trucks is higher than that of YOLOv3-tiny with AP0.5 and AP0.75 at 98.91% for both IOU thresholds. Besides, YOLOv3 is far superior when discriminating between the three different vehicle classes as is seen with notably higher AP scores for pickup-trucks and cars in Table 3-3. As a result, the higher precision and recall performance of YOLOv3 is desirable for confirmation of trucks crossing the bridges and WIM station. The YOLOv3 detection is an offline post-processing process performed on a server using an NVIDIA Titan Xp GPU after all data is uploaded into the cloud. Some qualitative detection results are shown in Figure 2-9 in Chapter 2. When using the models, the confidence threshold is set to 0.8 with the model only returning predictions with class

probabilities higher than this threshold. This high threshold minimizes false alarms in the real-time implementation of YOLOv3-tiny at Cam-1.

3.4 Truck Re-identification

The YOLOv3-tiny single-stage detector trained in the previous section and embedded in CAM-1 is used for real-time truck detection with the CPS architecture designed to autonomously trigger the bridge monitoring systems and subsequent cameras along the I-275 corridor. This triggering strategy is designed to capture bridge responses and truck weight measurements for the same truck as it may travel north on I-275. To confirm the same truck is evident at each section of the corridor, the YOLOv3 detector is implemented offline to extract truck events at each bridge and WIM station using videos from CAM-2, CAM-3 and CAM-4. Identified truck objects at each camera are collected during the data collection window triggered by CAM-1. This section describes the truck re-identification method used to match the same truck at different locations based on a mutual nearest neighbor strategy using extracted features from the truck objects identified. As multiple images (video frames) are associated with a single truck, the image that has the largest bounding box while shows the entire truck head is selected for the re-identification purpose. The image is cropped around the bounding box to remove redundant background information. Such an image is assumed to contain the most useful information of that truck's appearance and thus gives the best accuracy for re-identification.

Two approaches are explored to extract features from cropped truck images and to measure the similarity between a pair of images. One approach is to use traditional hand-crafted features and match detected key points between two candidate images with a stereo matching method. For example, the percentage of matched key points can be a direct measure of similarity between two trucks from two different images. The second approach is to extract a feature vector from each image using a learning-based CNN model and use the reciprocal of the Euclidean distance between the two feature vectors as a similarity metric.

3.4.1 Stereo Matching for Re-identification

In the first approach, the truck re-identification problem is posed as a wide baseline stereo matching problem. Stereo matching aims to estimate the fundamental matrix of a geometric transformation between images and to extract a common set of key points given two images with distinct views (e.g., views differing by rotation, translation or significant changes in illumination) of an identical object [177]. In a standard baseline matching problem, the first step is to detect key points and describe local features in two input images separately. The second step involves tentatively linking extracted key points of the two images followed by geometric verification using parameter estimation techniques such as RANSAC [178, 179]. In this study, two bounding box images of the same truck taken at different locations are treated like two images taken at the same location with distinct views. Thus, the ratio of the number of matched key points to the number of total extracted key points from the two input images can be used as a metric to describe the similarity between them. Due to large view transformations (e.g., tilt) and environment changes (e.g., illumination) associated with images taken at different locations in the I-275 corridor, commonly used short baseline stereo algorithms such as SIFT [180] and SURF [181] prove to be unsuccessful in robustly detecting key points; they are not considered further due to their lower than desired performance levels. As an alternative, the Affine-SIFT (ASIFT) algorithm which is designed for wide baseline stereo matching is explored [182]. ASIFT is fully affine invariant and has improved matching accuracy by synthesizing a series of views for both input images through image deformation (i.e., scale and tilt) before the feature detection step [182]. The approach entails n^2 independent matching problems derived from the original single matching problem where n is the number of synthesized (deformed) views per image. ASIFT also has a step of filtering out accumulated false matches that enhances its performance [182]. ASIFT is more robust than SIFT and SURF but its speed is not sufficiently fast in this application. In this study, the SIFT and SURF implementations in OpenCV and the ASIFT code published by the original author are evaluated.

The final approach explored is a wide baseline stereo matching algorithm called matching on demand with view synthesis (MODS) [179]. In addition to view synthesis introduced in ASIFT, the

Figure 3-4: Same truck with top matched feature points highlighted by the MODS algorithm: (left) TRB and (right) NRB.

most significant advantage of MODS is the employment of a combination of different detectors and descriptors. Following an iterative strategy, MODS adaptively attempts more powerful but slower detectors and descriptors until sufficient proof is found for a match [179]. In the meantime, MODS also synthesizes more views for each image, if necessary. Such an on-demand approach tackles the matching problem with a balance between matching robustness and computational speed. The implementation of MODS published in C++ by the original author is adopted in this study [179]. An example of matched pairs using the MODS algorithm is shown in Figure 3-4 with matched key points highlighted between the two views of the same truck at TRB and NRB. It is observed that the algorithm works well even in the case of harsh weather conditions (e.g., raining or snowing) or blurred images due to low light conditions and a slow shutter speed. As shown, MODS is able to match two truck images even when the views are transformed and with a partial occlusion of the complete truck. However, MODS performance is degraded with low contrast images such as those with glare or haze.

3.4.2 CNN-based Representation Learning for Re-identification

CNNs have been shown to be a powerful tool for the extraction of meaningful features (e.g., lines, shapes, colored patterns) from images; as a result, they can potentially be used for object re-identification. Within a CNN, each intermediate convolutional layer is responsible for extracting a feature map from previous network outputs. Some particular combination of those convolutional layers can be used to serve as a feature extractor to convert the characteristics of an image into a

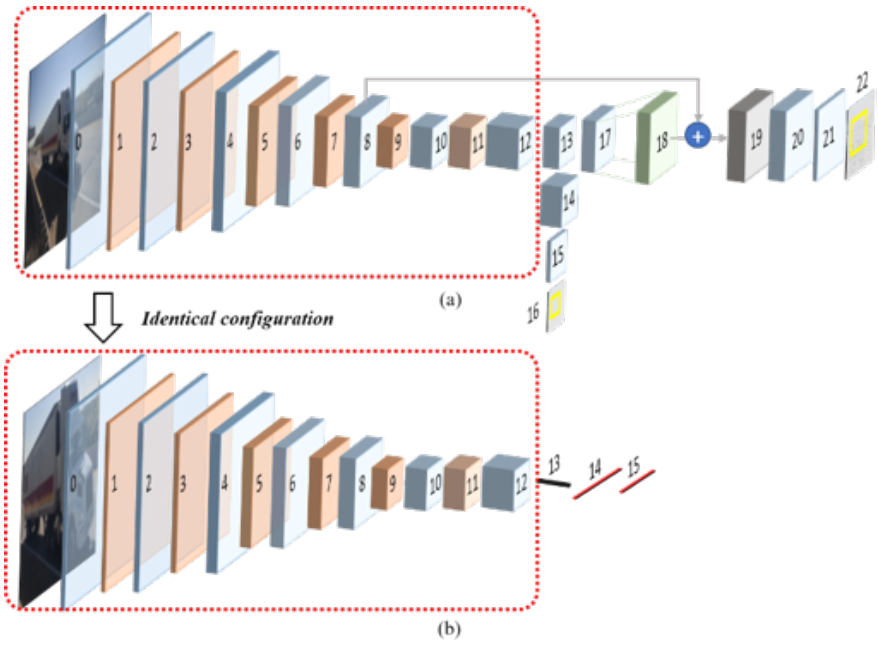

Figure 3-5: (a) The traditional YOLOv3-tiny CNN architecture; (b) modified YOLOv3-tiny CNN architecture for truck image matching.

feature vector [183]. In this study, a CNN-based approach to vehicle re-identification is considered; the approach leverages the previously trained YOLOv3-tiny model to extract features from traffic images for truck re-identification. The first 12 layers of the YOLOv3-tiny model are preserved and combined with: 1) a global average pooling (GAP) layer [184] (layer 13) and 2) two fully connected layers as a new embedding network (layers 14 and 15). The architectures of the two models are illustrated in Figure 3-5 and the layer types and primary parameters of the embedding network are listed in Table 3-4 [163]. The first 12 layers of the embedding network are identical to those of the YOLOv3-tiny network and thus each convolutional layer is followed by a batch normalization and then activated by a leaky rectified linear unit (ReLU) [163]. The total number of convolutional layers and fully connected layers in the CNN, seven and two, respectively, are determined by ablation experiments in order to extract the most profitable features for vehicle re-identification. The idea of adding the GAP layer is to enforce each feature map to represent meaningful characteristics of trucks and to reduce the dimensionality of the input fed into the subsequent fully connected layers to try to avoid overfitting. The proposed embedding network takes 416-by-416 pixels images as inputs, which is similar to the original YOLOv3-tiny model

	YOLOv3-tiny Network				Embedding Network			
Layer	Type	# Filter	Size	Stride	Type	# Filter	Size	Stride
0	Convolutional	16	3	1	Convolutional	16	3	1
1	Max pooling		2	2	Max pooling	2	2	
2	Convolutional	32	3	1	Convolutional	32	3	1
3	Max pooling		2	2	Max pooling	2	2	
4	Convolutional	64	3	1	Convolutional	64	3	1
5	Max pooling		2	2	Max pooling	2	2	
6	Convolutional	128	3	1	Convolutional	128	3	1
7	Max pooling		2	2	Max pooling	2	2	
8	Convolutional	256	3	1	Convolutional	256	3	1
9	Max pooling		2	2	Max pooling	2	2	
10	Convolutional	512	3	1	Convolutional	512	3	1
11	Max pooling		2	2	Max pooling	2	2	
12	Convolutional	1024	3	1	Convolutional	1024	3	1
13	Convolutional	256	1	1	GAP			13
14	Convolutional	512	3	1	Fully connected		1024	
15	Convolutional	24	1	1	Fully connected		512	
16	Detection							
17	Convolutional	128	1	1				
18	Up-sampling			2				
19	Concatenation							
20	Convolutional	256	3	1				
21	Convolutional	24	1	1				
22	Detection							

Table 3-4: Layer types and primary parameters of the YOLOv3-tiny model and the modified embedding network.

but is fed cropped truck images instead of the entire raw traffic images. The network output is a 512-entry feature vector for each truck image for matching.

Two general architectures, Siamese network [185] and triplet network [186], are used during training to learn similarity metrics between input images. The goal is to let the embedding network learn to extract vision features useful for truck re-identification. The primary differences between the two architectures are their input forms and the loss functions used. As shown in Figure 3-6(a), two identical CNNs, namely the prementioned embedding network, exist in a Siamese network with both CNNs sharing the same weights at all times [185]. During training, a pair of images either of the same truck or of different trucks is taken as an input to the Siamese network with each

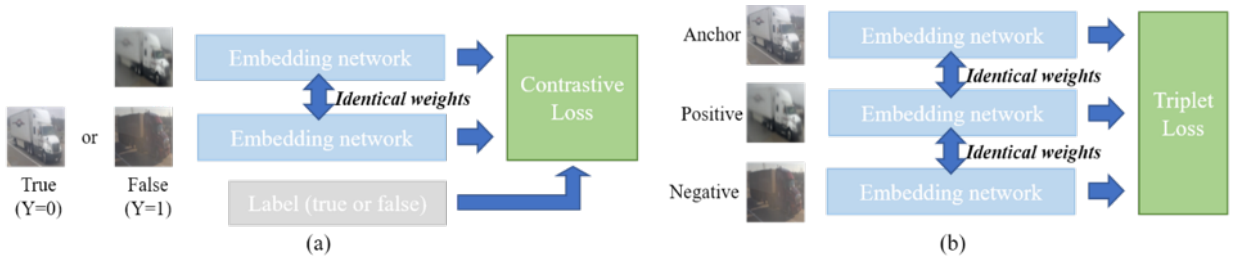

Figure 3-6: Coupled network architectures for the embedding network training: (a) Siamese network architecture; (b) triplet network architecture.

image fed to one of the two CNNs. The outputs of the two CNNs (i.e., two feature vectors) are then passed to a contrastive loss function [185]. The contrastive loss function, L, has the form:

$$L_{contrastive} = (1 - Y)\frac{1}{2}(D_w)^2 + (Y)\frac{1}{2}\{max(0, m - D_w)\}^2 \tag{3.3}$$

$$D_w = \|G_w(x_1) - G_w(x_2)\|_2 \tag{3.4}$$

where Y is the label of an image pair that is set to 0 if two input images belong to the same truck and 1 if the they are from different trucks, D_w the Euclidean distance between the outputs of the two branch networks which can be computed by Equation 3.4 where $G_w(x_1)$ and $G_w(x_2)$ are the vectorized outputs of the two CNNs, and m is a positive distance margin. The role of the contrastive loss function is to train the embedding networks to pull the feature vectors of two similar trucks together while separating those of dissimilar trucks. If the distance between two different trucks is larger than the specified margin, it then stops contributing to the loss.

$$L_{triplet} = \sum_{i=0}^{n} max(\|G_w(x_i^a) - G_w(x_i^p))\|_2^2 - \|G_w(x_i^a) - G_w(x_i^n))\|_2^2 + \alpha, 0) \tag{3.5}$$

A triplet network, shown in Figure 3-6(b), has three identical embedding networks. All three sub-networks have identical weights. During training, the network is fed with a triplet of truck images without any explicit labels attached. Among the three input images, one image is the anchor image, one is the positive image which shows the same truck as the anchor image and the last is the negative image of a truck that is different from the anchor image [186]. A triplet loss

Figure 3-7: Samples of manually prepared positive truck image pairs.

function (Equation 3.5) is employed to learn the parameters of the embedding network, in such a way that the feature vector of the positive truck image is trained to be closer to that of the anchor image than the negative sample by a margin α [186].

To train the embedding network, 1,300 truck image pairs are manually picked by the authors. Within each pair, the two images belong to the same truck but are captured at different locations in the I-275 corridor. Each traffic image is cropped and resized to 416-by-416 pixels to remove background objects; samples are shown in Figure 3-7. To prevent overfitting of the embedding network during training, the datasets are also augmented by flipping the images both vertically and horizontally, which results in a total of 3,900 image pairs for training. During the training of the Siamese network, negative pairs are randomly generated in each iteration by combining a truck image from one pair to a different truck image that has been processed identically (i.e., flipping vertically, flipping horizontally or unchanged). The total number of negative pairs is set to be equal to that of positive pairs in each iteration. The negative samples in each data set for the triplet network are generated following the same logic. Following this approach, the Siamese and triplet networks see an abundance of different negative samples than positive samples throughout the entire training process. The CNN of the embedding network is initialized using the corresponding weights of the trained YOLOv3-tiny model. The weight of this part is frozen for the first 5 epochs and then fine-tuned in the training process along with the fully connected layers which are randomly initialized using an Xavier uniform distribution [187]. A dropout rate of 0.5 is also added before the first fully connected layer to overcome overfitting. The two embedding networks are trained using an Adam optimizer [188] with a base learning rate of 5×10^{-4} and a batch size of

Method		Precision	Recall	F1-score	Speed per comparison (sec)	Device
CNN-based	triplet	**100%**	**95.00%**	**0.9743**	**0.0035**	GPU
	Siamese	**100%**	93.57%	0.9668	**0.0032**	GPU
Wide Stereo Baseline	MODS	98.49%	93.57%	0.9597	1.73	CPU
	ASIFT	99.22%	91.43%	0.9517	20.52	CPU
Short Stereo Baseline	SIFT	93.68%	63.57%	0.7574	0.06	CPU
	SURF	90.13%	52.14%	0.6606	0.08	CPU

Table 3-5: Evaluation results of truck re-identification using MODS, embedding network trained from Siamese and triplet network

32. The margin is set to be $\alpha = 5$ due to this margin offering the best performance as observed using the data from I-275. The entire process is implemented using the PyTorch framework [189] and is executed on an NVIDIA Titan Xp GPU. After the training of the embedding network, the reciprocal of the Euclidean distance (i.e., L2 distance) between the two truck images' embedding vectors is selected to be the proxy for their similarity.

3.4.3 Evaluation

To evaluate the performance of the two approaches (i.e., hand-crafted stereo matching features and CNN-based embedding network) for truck re-identification, 150 truck image pairs that are not included in the training set of the CNN-based embedding networks are selected to serve as a testing data set. The 150 images are split into 15 sets of 10 trucks to mimic the real application in this study, which leads to 1500 (15*10*10) similarity metric calculations. The performance of the models is evaluated in terms of precision, recall, F1 score [190] and inference speed. The F1 score is the harmonic mean of precision and recall which can calculated as

$$F1score = \frac{2 \times recall \times precision}{recall + precision} \tag{3.6}$$

The results are compared in Table 3-5. Since the CNN embedding networks trained from the Siamese and the triplet network follow the same procedure during testing, they have inference speeds close to one another. In addition, cumulative match characteristic (CMC) curves averaged

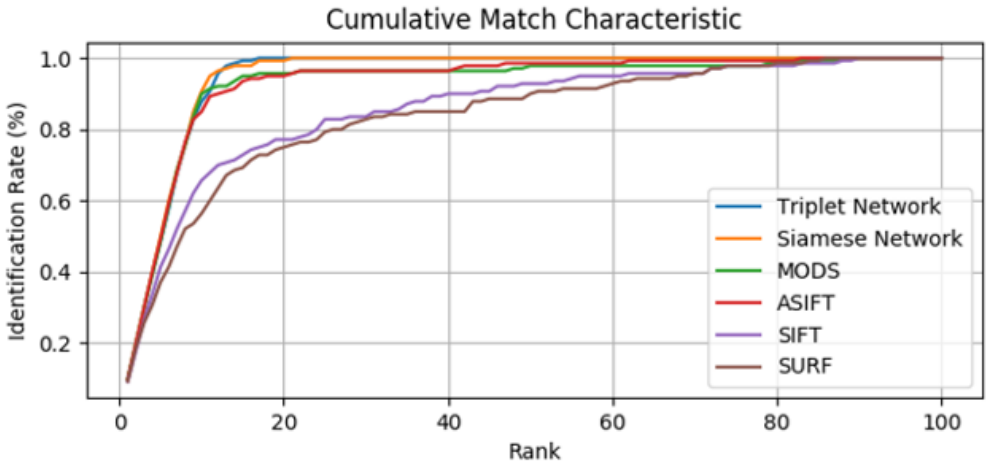

Figure 3-8: Cumulative match characteristic curves for truck matching using SURF, SIFT, ASIFT, MODS, and CNN-based embedding networks (Siamese and triplet networks).

from all 15 test sets are plotted in Figure 3-8. According to the evaluation results, the embedding network trained from the triplet architecture gains the highest F1 score as well as the fastest speed; it is thus employed for the truck re-identification in the production version of the system. Nevertheless, all methods fail to distinguish some extremely similar truck pairs. Some false positives are shown in Figure 3-9. For examples, some trucks seen at different locations along the corridor may come from the same freight transportation company or they are of the same truck type with the same color. Besides, a truck image in one set might be matched with a distinct but similar truck in another set if the same truck is not captured in the second set. The performance also downgrades in the case of harsh weather (e.g., raining or snowing), blurring (dark light and low shutter speed) or low contrast images (e.g., glare or haze). Those false positives might be ruled out by checking if the corresponding travel time is feasible or the input-output mapping of the two bridge systems are reasonable, which will be discussed in the next section.

3.5 Summary and Conclusions

In this chapter, a computer vision-based truck re-identification framework is proposed to automatically link truck-induced bridge response data measured by bridge SHM systems to truck load data measured by a nearby WIM station following the framework proposed in Chapter 2. The first

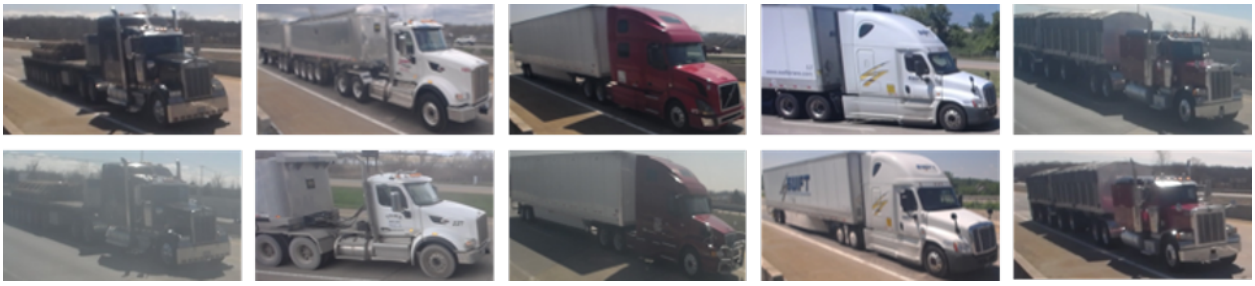

Figure 3-9: Examples of false positives of matched truck during the truck re-identification phase: top row are images at the Telegraph Road Bridge and the bottom row are images at the Newburg Road Bridge with manual checking revealing these are not the same truck.

stage of the truck re-identification involves training CNN models for vehicle detection. Trained using a customized data set, four advanced CNN architectures are evaluated in this study in terms of average precision and inference speed. Being the fastest detector, YOLOv3-tiny is selected for real-time detection of incoming trucks to trigger the subsequent systems so that all systems can track the same trucks along the corridor. YOLOv3 is used to identify truck events captured by the cameras at the bridge SHM systems and the WIM station offline due to its high precision and fast execution speed. At the second stage, features are extracted from identified truck images to match identical trucks captured at different locations following a mutual nearest neighbor fashion. Multiple hand-crafted feature extraction algorithms and customized CNN-based feature extraction models are compared for truck re-identification purpose. It is shown that the CNN-based embedding network trained using a triplet architecture outperforms its hand-crafted counterparts. Linked by the matched truck images, the corresponding data collected by different systems (i.e., bridge SHM systems and WIM station) can be fused. Future work will be focused on adopting a deeper CNN architecture to extract features from truck images and visualizing extracted features for a better interpretation of the model working mechanism.

CHAPTER 4.

Partial Composite Action and Durability Assessment of Slab-on-girder Highway Bridge Decks in Negative Bending Using Long-term Structural Monitoring Data

4.1 Introduction

Stringer/multibeam bridges are a common highway bridge type in the United States accounting for over 40% of the National Bridge Inventory (NBI) [191]. This type of bridge consists of a concrete deck on top of parallel steel girders with the deck often designed to be in composite action with the girders [192]. The purpose of composite action is to let components with different materials act cooperatively against external loads. A composite slab-on-girder bridge under positive bending moment has the concrete deck mainly in compression and steel girders mainly in tension, resulting in both high load-carrying capacity of the span and reduced tensile load on the slab. This is achieved by installing connectors at the girder–deck interface, such as steel studs welded to the top flange surface of the steel girders [193, 194]. Multispan slab-on-girder bridges that have internal supports experience negative bending moments over the supports. The flexural capacity gained by composite action is unnecessary over the internal support and can lead to higher tensile strain in the top surface of the bridge deck. Hence, older slab-on-girder bridges were designed without composite action in the negative moment sections of their spans. Current design methods supported by AASHTO specifications encourage composite action over the full span although composite action over the internal support will induce high tensile strain in the concrete deck over the support [192]. To control cracks, AASHTO prescribes additional steel reinforcement in negative bending regions by establishing a minimum area of steel in the deck section.

According to the 2017 ASCE Infrastructure Report Card, the condition of US bridges has improved with structurally deficient bridges in the national inventory dropping from 12.3% in 2007 to 9.1% in 2016 [30]. While the percentage of structurally deficient bridges may have gone down, the national bridge inventory is rapidly aging with 39% of the 614,387 highway bridges in the US now 50 years or older [30]. This growing inventory of aging bridges will necessitate increasing attention to ensure bridges remain safe and cost efficient for further operation. Based on the NBI, 54% of bridges rated as structurally deficient are steel stringer/multibeam bridges although they account for only 40% of the national inventory [191]. This suggests that stringer/multibeam bridges require more attention than other bridge types in the NBI. A significant concern associated with slab-on-girder bridges is long-term deck deterioration including concrete cracking and spalling. In Michigan, where stringer/multibeam bridges make up 43% of the Michigan Department of Transportation (MDOT) inventory, poor deck condition is listed as the most significant highway bridge issue in the state's long-range transportation plan [195, 191]. Deck deterioration can result from a number of factors such as concrete shrinkage and the corrosion of steel reinforcement, but it is often accelerated in multispan bridges above internal supports, in which decks are subject to higher tensile strains due to negative bending moment [196, 197]. This is especially true for older bridges designed without shear connectors (or explicit composite action) in their negative moment sections. In Michigan, there are 979 steel multistringer bridges in the MDOT inventory without full composite action (compared with 2,576 with composite action). When shear connectors are not used, it is assumed by the designer that the section has zero composite action, which implies complete freedom for the deck lower surface to displace relative to the top surface of the girder flange. However, the assumption made during the design of negative moment sections does not reflect the true in-service behavior of these sections. Specifically, partial composite action will be observed in sections without shear connectors owing to surface friction and chemical bonding between the concrete and steel [196]. While not fully composite nor noncomposite, these sections can be characterized by a measure of the degree of composite action (DCA). Partial composite action (as defined by DCA) is important to consider because it controls the ultimate limit states

and serviceability of the bridge deck making it an important management issue in bridge engineering [198]. More specifically, compared with noncomposite design, unintended partial composite action will lead to an increase in tensile strain in the top layer of concrete decks over negative bending regions.

Partial composite action was first systematically studied by Newmark et al. who carried out numerous experimental studies of slabs bonded to steel surfaces in a lab setting [199]. Since that seminal study, different analytical models have been proposed to model the nonlinear and time-dependent behavior of composite structural components [200, 198, 201, 202]. More recently, a generalized analytical model has been proposed for composite beams with no restrictive assumptions on the connection and interaction between the components [203, 204]. Finite-element modeling has also been intensively used to model partial composite interaction in composite beams [205, 206]. From previous studies, DCA has been found to strongly affect the flexural stiffness and strain distribution of composite beam sections [207, 208]. In particular, partial composite action over negative bending regions is a major research topic in the bridge engineering community [196]. In sections designed to not have composite action in negative bending, partial composite action can elevate deck strains, resulting in durability issues over the service life of the deck. Even in negative bending sections designed with shear connectors, cracks in these decks near the connectors reduce the connector stiffness, thereby limiting their effectiveness; this in turn results in a reduction of composite action [208] and changes the moment distribution in the span [209].

Currently, visual inspection is the primary method of observing bridge conditions and deciding upkeep and retrofit strategies. Structural monitoring can also be used to augment visual inspections to overcome the limitations of visual methods (e.g., interpretability and accessibility) [32]. Monitoring data can be a valuable resource that helps engineers understand bridge behavior, validate design assumptions, and detect anomalous bridge behavior including damage [210, 211, 99]. Most prior research on composite action has been carried out by means of theoretical analysis, experimental study in the laboratory, or by finite-element analysis. Comparatively, few studies have explored DCA in operational bridges over long observation periods. One of the few examples

of in-service assessment was done by Cardini and DeWolf who installed a dense group of strain gauges on a multispan composite highway bridge to assess the location of the section neutral axis to identify deck cracking [43]. The same technique was later applied using Fiber Bragg grating strain sensors for damage detection [211]. A relative displacement sensor has also been developed to directly measure the relative slip between the concrete deck and steel girder in composite bridges [212].

The primary goal of this chapter is to use long-term structural monitoring of operational multi-span slab-on-girder bridges to study the DCA in positive and negative bending sections of bridges under vehicular loads. An emphasis is placed on modeling partial composite action in negative moment sections, in which shear connectors are not used and the designer has assumed no composite action is present. A highway bridge, Telegraph Road Bridge, located in Monroe, Michigan, has been monitored with a wireless structural monitoring system continuously since 2011. The bridge is a three-span slab-on-girder bridge consisting of two tail spans cantilevering past internal piers to support the bridge center span via pin and hanger assemblies. The monitoring system measures flexural strain in the steel girder–concrete deck section at numerous locations along the bridge span, thereby providing an extensive data set from which DCA can be studied. The study uses a data-driven approach to measure slippage at the deck–girder interface as a function of live load magnitude to quantify and model DCA in span sections with and without shear connectors (i.e., positive and negative bending, respectively). Regression modeling of measured slip strain and bottom-girder strain is used to extract a parametric model that describes the behavior of composite action in each steel girder–concrete deck section. This parametric model serves as the basis of analyses of strain in the bridge deck to understand how composite action affects long-term deck durability. Analytical and numerical modeling reveals that partial composite action in sections of negative bending results in significantly higher top surface strains of the deck not accounted for in design when no composite action is assumed; this reduces the long-term durability of the deck. The chapter concludes with a summary of key findings and a description of future work that can be performed to refine the DCA models developed.

(a)

(b)

(c)

(d)

Figure 4-1: Telegraph Road Bridge (Monroe, Michigan): (a) perspective view of bridge; (b) view of bridge from bottom; (c) severe deck deterioration of northern tail span (October 2010); (d) spalled concrete at steel girder interface on tail span (June 2012).

4.2 Telegraph Road Bridge Monitoring Program

The Telegraph Road Bridge (Figure 4-1) is a three-span slab-on-girder highway bridge located in Monroe, Michigan, and carries three lanes of northbound Interstate 275 over Telegraph Road. The slab-on-girder cross section is shown in Figure 4-2. The bridge was constructed in 1973 and is owned by MDOT. The bridge carries truck loads with approximately 6,000 trucks crossing daily, as measured from the weigh-in-motion station at Pennsylvania Road (which is 12 miles north of Telegraph Road) [213]. As shown in Figure 4-3, the bridge spans 224 ft. (68.28 m) and has a 33-degree skew. The center span of the bridge is 128 ft (39.01 m) and is supported at its two ends by pin-and-hanger connections. Load from the main span is transferred by the pin-and-hanger connections to tail spans located on both sides (i.e., north and south). Each tail span is 48 ft (14.63 m) long and supported by an abutment on one end and a concrete pier located 6 ft (1.83 m) from the pin-and-hanger assemblies at the other. The piers induce negative moments in the tail spans

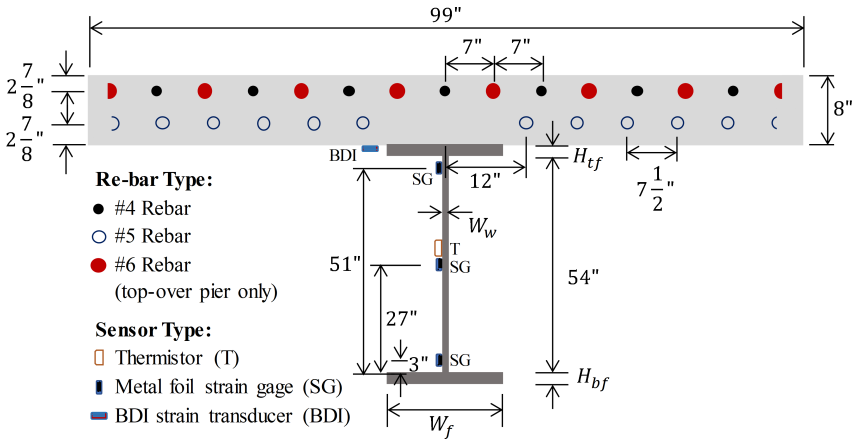

	Wing span	Main span
W_f	12"	19"
H_{bf}	$\frac{5}{8}$"	$1\frac{7}{8}$"
H_{tf}	$\frac{1}{2}$"	1"
W_w	$\frac{1}{2}$"	$\frac{9}{16}$"
Shear Studs	No	Yes

Figure 4-2: Interior cross section of Telegraph Road Bridge with key structural dimensions documented for the tail (wing) and main spans.

when vertical load is applied to the main span.

Each span contains an 8-in. (20.32 cm) thick concrete slab placed upon seven 54-in. (136.16 cm) deep steel-plate girders. Steel shear studs are welded to the steel girders of the main span spaced at 18 in. (45.72 cm) to provide full composite action in the section. However, studs are not installed in the tail spans and it was assumed during design that composite action does not develop in the section [192]. Figure 4-2 shows a typical girder-deck T-beam cross section of the Telegraph Road Bridge with the dimensions of the girders shown for both the tail and main spans. The web and flange thicknesses of the main span girders are larger owing to higher flexural stress demand. Two layers of steel reinforcement are included in the concrete slab with #4 and #5 reinforcement bars placed on the top and bottom layers, respectively. An additional set of #6 reinforcement bars are added to the top layer over the piers in regions of negative moment to support higher tensile strain demand. The effective width of the T-beam section in Figure 4-2 is 99 in. (2.51 m) which is the distance between the centerlines of two adjacent girders [192, 214].

4.2.1 Bridge Condition

The Telegraph Road Bridge has been repaired multiple times over its 45 years of service. The latest rehabilitation was a resurfacing of the bridge deck in 2011 due to deteriorating deck conditions. Table 4-1 is a summary of the condition ratings assigned to the deck during biennial bridge

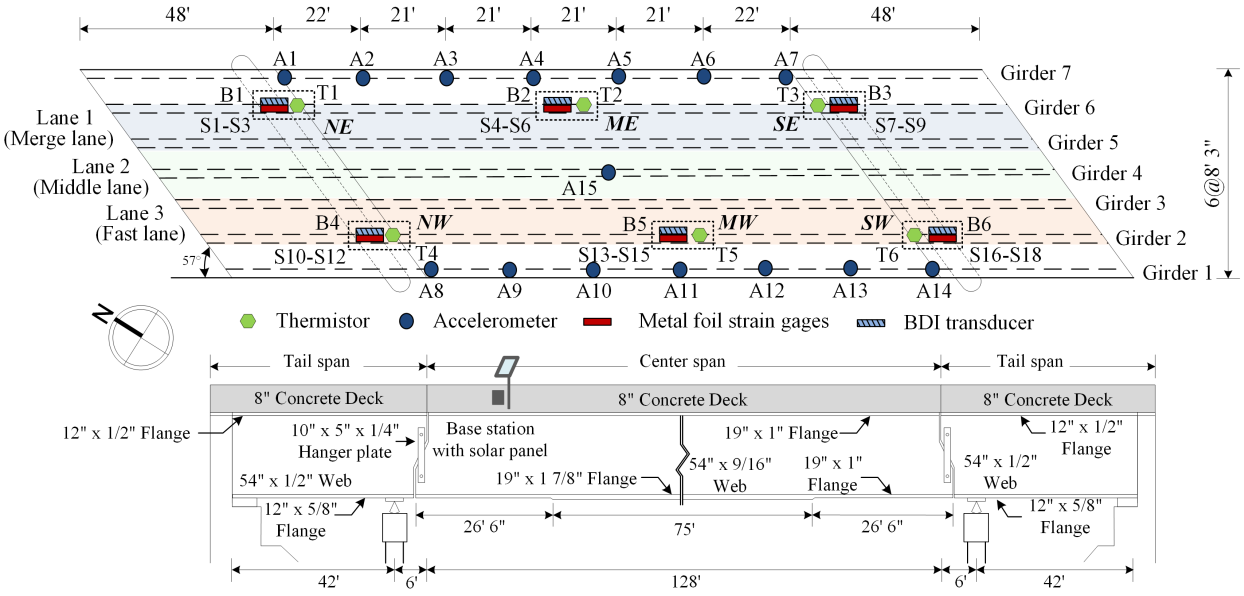

Figure 4-3: Sensor layout of the wireless sensing network drawn on the schematic diagram of the Telegraph Road Bridge with sensor types and location convention defined.

safety inspections from 2001 to 2015. From 2001 to early 2011, the deck condition score dropped from 5 (fair) to 4 (poor) as increasingly more concrete cracks and spalls were observed. On-site observation of the top deck in 2010 [Figure 4-1(c)] demonstrated severe deck deterioration in the tail spans with large areas of the top deck spalled. Additional evidence of tail span deck distress were areas of shallow spalling at the top flange–haunch interface [Figure 4-1(d)]. During the 2011 deck repair, hydro-demolition was performed to remove the upper half of the original concrete slab followed by a new silica fume–modified concrete overlay placed upon the remaining slab. The original concrete deck had a nominal compressive strength of 3,000 psi (20.7 MPa) but the new overlay was specified with a 7,000 psi (48.3 MPa) compressive strength; cylinder tests during the 2011 resurfacing resulted in compressive strengths between 6,400 psi (44.1 MPa) and 7,400 psi (51.0 MPa). After resurfacing, the decks obtained a condition rating of 7 representing a good condition for the deck. The 2013 and 2015 inspections rated the deck as 6 (fair) owing to the development of traverse cracks appearing in the top deck surface.

Deck deterioration on the Telegraph Road Bridge is a persistent issue that requires continuous attention to ensure decks offer a safe road condition to traffic. While deck deterioration is com-

Year	Score	Southern tail span	Main span	Northern tail span
2001	5 (Fair)	Few open spalls; transverse cracks throughout	Few open spalls; transverse cracks throughout	Few open spalls; transverse cracks throughout
2003	5 (Fair)	Few open spalls; transverse cracks throughout	Few open spalls; transverse cracks throughout	Few open spalls; transverse cracks throughout
2005	4 (Poor)	1.77 m^2 (19 SFT) of bit patched areas, 2.51 m^2 (27 SFT) of concrete patched areas, and no open spalls	0.19 m^2 (2 SFT) of bit patched areas, 7.62 m^2 (82 SFT) of concrete patched areas, and 0.93 m^2 (10 SFT) of open spalls	3.44 m^2 (37 SFT) of bit patched areas, 8.45 m^2 (91 SFT) of concrete patched areas, and 1.39 m^2 (15 SFT) of open spalls
2006	4 (Poor)	1.77 m^2 (19 SFT) of bit patched areas, 2.51 m^2 (27 SFT) of concrete patched areas, and 0.19 m^2 (2 SFT) of open spalls	0.19 m^2 (2 SFT) of bit patched areas, 7.62 m^2 (82 SFT) of concrete patched areas, and 0.46 m^2 (5 SFT) of open spalls	3.44 m^2 (37 SFT) of bit patched areas, 8.45 m^2 (91 SFT) of concrete patched areas, and 1.39 m^2 (15 SFT) of open spalls
2008	4 (Poor)	2.32 m^2 (25 SFT) of bit patched areas, 2.51 m^2 (27 SFT) of concrete patched areas, and 1.39 m^2 (15 SFT) of open spalls	0.56 m^2 (6 SFT) of bit patched areas, 7.62 m^2 (82 SFT) of concrete patched areas, and 0.56 m^2 (6 SFT) of open spalls	2.60 m^2 (28 SFT) of bit patched areas, 8.45 m^2 (91 SFT) of concrete patched areas, and 1.39 m^2 (15 SFT) of open spalls
2010	4 (Poor)	3.72 m^2 (40 SFT) of bit patched areas, 2.51 m^2 (27 SFT) of concrete patched areas, and 1.11 m^2 (12 SFT) of open spalls	2.32 m^2 (25 SFT) of bit patched areas, 8.36 m^2 (90 SFT) of concrete patched areas, and 1.39 m^2 (15 SFT) of open spalls	4.65 m^2 (50 SFT) of bit patched areas, 8.45 m^2 (91 SFT) of concrete patched areas, and 2.32 m^2 (25 SFT) of open spalls
2011	7 (Good)	New concrete overlay	New concrete overlay	New concrete overlay
2013	6 (Fair)	Several transverse cracks along center line and reference lines	Several transverse cracks along center line and reference lines	Several transverse cracks along center line and reference lines
2015	6 (Fair)	Several transverse cracks along center line and reference lines	Several transverse cracks along center line and reference lines	Several transverse cracks along center line and reference lines

Table 4-1: Deck surface condition of the Telegraph Road Bridge from 2001 to 2015.

mon to many slab-on-girder bridges in northern climates, the Telegraph Road Bridge exhibits some unique damage patterns. First, in 2009 the two tail spans had much more severe deck deterioration than the main span (as supported by bridge safety inspection reports from 2001 to 2010, as reported in Table 4-1). An intuitive explanation to these observations is that the midspan experiences positive bending moments during vertical loading with the section composite action ensuring the deck is in compression. In addition, diurnal and seasonal thermal variations will introduce tensile expansion in the deck. In contrast, the tail spans have large areas of the span in negative bending due to the pier support on the interior of the spans. Although the two tail spans are designed to be non-composite, there is likely some degree of composite action occurring at the girder–slab interface

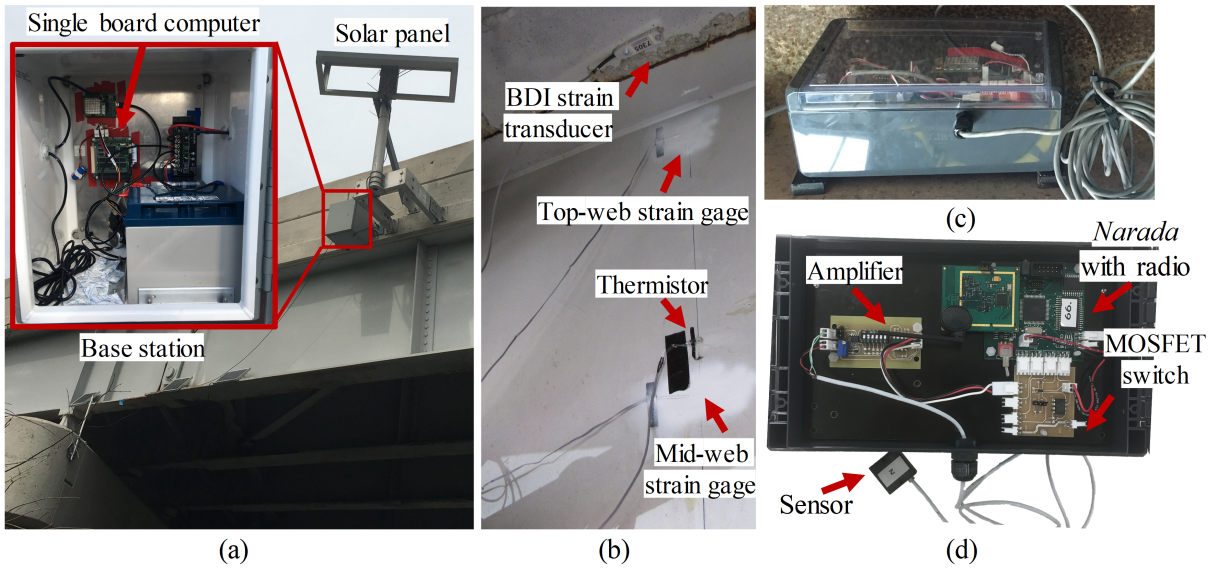

Figure 4-4: Highlights of Telegraph Road Bridge instrumentation: (a) base station with solar panel used for power; (b) installation of strain sensors (BDI strain transducer on slab and metal foil gauges on girders); (c) wireless sensor enclosure for strain gauge data collection magnetically mounted to steel girder flange; (d) internal components of wireless sensor node.

owing to adhesion, chemical bonding, and mechanical friction [196]. As a result, it is hypothesized that the deck in the negative bending region of the tail spans experience much greater tensile strains than considered during design. Hence, the existing steel reinforcement is likely insufficient for the higher tensile strain demand leading to larger cracks and a more rapid deterioration of the decks owing to surface water and chlorides penetrating into the deck.

4.2.2 Structural Health Monitoring System Configuration

To investigate the potential causes of the observed deterioration in the deck and also to better understand the composite behavior manifested in the bridge, a long-term structural health monitoring (SHM) system was installed on the Telegraph Road Bridge in September 2011 shortly after the new concrete overlay was installed. O'Connor et al. provide a detailed review of the SHM system and its design; only a brief review of the SHM system pertinent to the assessment of the deck behavior will be offered herein [61]. The SHM system is comprised of a base station and a Narada wireless sensor network (WSN) (University of Michigan, Ann Arbor, Michigan), as shown

in Figure 4-3. The base station, shown in Figure 4-4(a), contains a single board computer (Nvidia TX2) that wirelessly sends operational commands to the WSN including time synchronization, the start of data collection (with a specified sample rate), and request to receive data. The base station also aggregates data from the WSN during each data collection cycle before transmitting data to a cloud-based database system via a cellular modem (AT&T Velocity MF861) [146]. The base station is powered by a 12V rechargeable battery (PS-12350NB, PowerSonic, Reno, Nevada) that is charged using a solar charge controller (Sun Saver 10L, Morningstar, Newtown, Pennsylvania) and a solar panel (110W 12V, UL-Solar, Brea, California). The single board computer, battery, cellular modem, and charge controller are contained within a water-tight metal enclosure bolted to the bridge concrete barrier.

Narada wireless sensing nodes [144] are responsible for collecting measurements from a variety of physical sensors interfaced (e.g., accelerometers, strain gauges, thermistors). Narada [Figure 4-4(d)] has a 16-bit analog to digital converter that can sample data from four channels with a maximum sample rate of 100 kHz. The node uses a power amplified IEEE802.15.4 transceiver (Texas Instruments CC2420) for wireless communications. The nodes deployed are contained within small water-tight enclosures [Figure 4-4(c)] along with conditioning circuitry, solar charge controllers (Morningstar SunSaver SS-6L-12V), and 12V rechargeable batteries (PowerSonic PS-1229). A small solar panel (UL-Solar 10W 12V) is attached to each node to recharge the node battery.

The WSN consists of nodes measuring three response parameters: acceleration, strain, and surface temperature. The system has six locations with a local array of strain measurements that is identical at each location. On Girder Line 2 (and identically on Girder Line 6) arrays are installed above the north pier denoted as NE and NW, south pier denoted as SE and SW, and on the centerline of the main span denoted as ME and MW (Figure 4-3). At each of these six locations, four strain sensors and one thermistor are installed. As shown in the section schematic of Figure 4-2, at each location three Tokkyo Sokki FLA-6-11-3LT 6 mm 120 Ω metal foil strain gauges are installed on the girder web 3 in. (7.62 cm), 27 in. (68.58 cm), and 51 in. (129.54 cm) from the

top surface of the bottom flange to measure girder strain responses. One additional Bridge Diagnostics, Inc. (BDI) ST350 strain transducer is bolted to the bottom surface of the concrete deck using bolt fasteners to measure strain. The four strain gauges combined can provide strain measurements at different positions along the height of the slab–girder cross section which serve as the basis for estimating the strain profile of the cross section subject to vehicular loads. One thermistor (USP13187, US Sensor, Orange, California) is mounted to the girder using thermal epoxy to measure structural temperature which will be used to eliminate temperature-induced sensor error as well as for correlating bridge behavior with temperature. The strain gauges, BDI sensor, and thermistor are shown in Figure 4-4(b). The strain sensors (metal foil) and thermistors are interfaced to each Narada node using a Wheatstone bridge and instrumentation amplifier (amplified by 1,000x and 1x, respectively) with a MOSFET switch included to allow the nodes to turn power on and off to the sensors. The BDI sensors which have a full bridge embedded in them are interfaced using an instrumentation amplifier (amplifying by 500x) with a MOSFET switch. There is also a small array of vertically oriented uniaxial accelerometers (Silicon Design 2012-002) installed along Girder Lines 1 and 7 to measure vibrations from which natural frequencies of the bridge can be identified and used for model updating.

4.2.3 Data Management and Processing

The Telegraph Road Bridge monitoring system has been operated on a scheduled basis since it was deployed in 2011. The system is turned on every 2 h to collect data for 1 min with strain, acceleration, and temperature sampled at 100, 200, and 1 Hz, respectively. The first modal frequency of the bridge is estimated to be around 2.5 Hz from collected acceleration data [61]. A typical response is shown in Figure 4-5 showing time synchronized data from the strain gauges on the bottom of the girder web (S1 at NE, S4 at ME, and S7 at SE on Girder Line 6; S10 at NW, S13 at MW, and S16 at SW on Girder Line 2) along with two accelerometers installed along the centerline of the main span (A4 and A11). During this 60-s segment of data, two trucks are captured and classified on the basis of the strain magnitude: a large truck at around 8 s and a smaller truck at 47 s. Negative

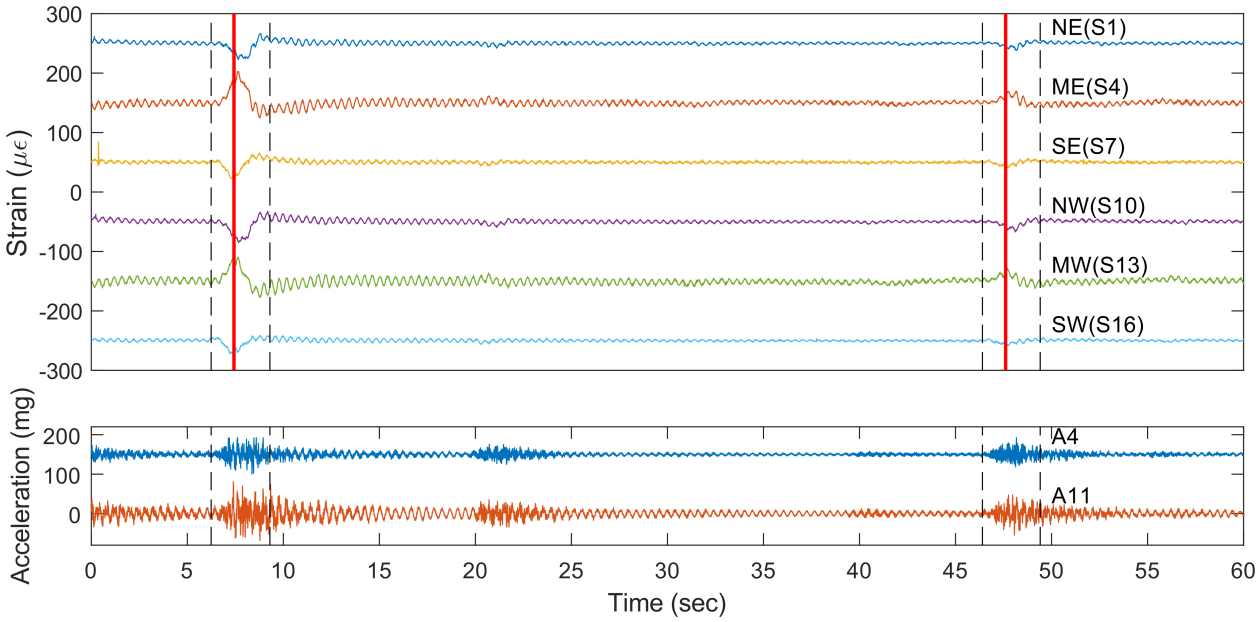

Figure 4-5: Typical strain responses and acceleration responses measured by the structural health monitoring system with truck events identified and baseline shifted for each sensor for better visualization.

bending is evident on the two tail spans, as seen by the negative strain measurement at S1, S7, S10, and S16.

The data analysis performed in this chapter is primarily focused on the bridge dynamic response to truck loads to investigate the correlation between the flexural behavior of each section and load magnitude. In addition, the static bottom-deck strain response without the presence of vehicular loads will be used to investigate the thermal expansion of the bridge deck. Data is collected on the basis of the established schedule over 3.5 years of observation (October 1, 2013–April 30, 2016). An automated algorithm is used to process all of the measurement data to identify truck events (thereby eliminating data associated with no vehicles and cars). To distinguish bridge responses associated from trucks, a threshold based peak-picking algorithm is applied to the strain measured at the bottom of the girder webs (such as those shown in Figure 4-5). The approach begins with first passing the strain data through a low-pass filter (with a cut-off frequency of 2 Hz) to eliminate high-frequency signal noise. Then, the maximum measured strain from across all six lower web strain gauges is identified; those with maximum strains above a defined threshold (e.g., 5 $\mu\epsilon$) are

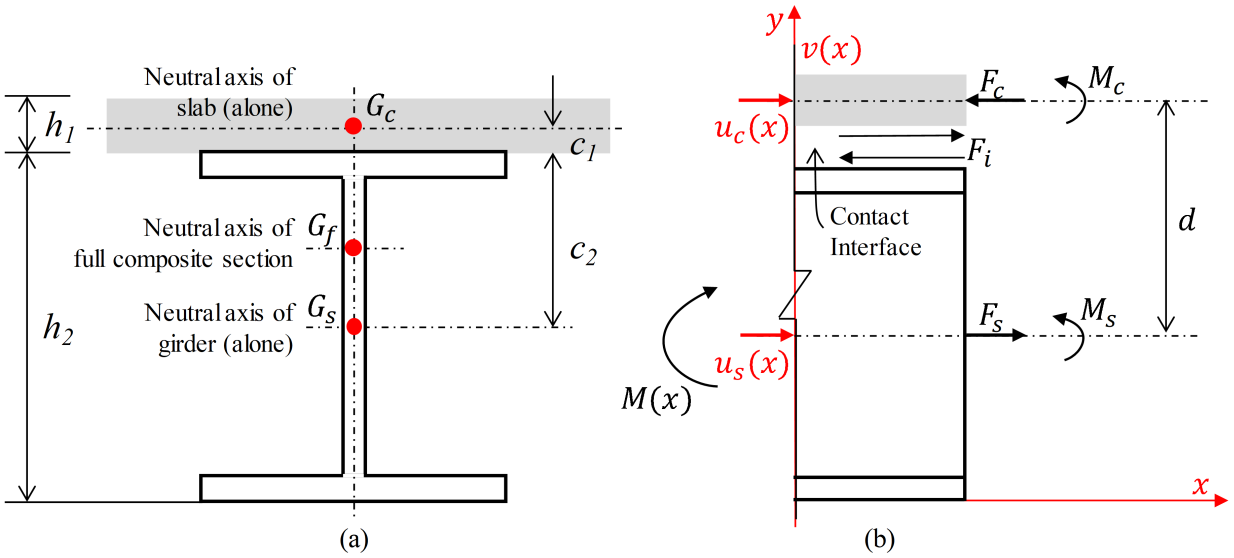

Figure 4-6: Analytical model of the concrete slab and steel girder composite section: (a) cross section with key dimensions; (b) side profile with force and moments defined under flexural moment.

identified as truck-induced responses. The time history before and after the maximum strain is searched to find when the response is oscillating around the 0 $\mu\epsilon$ baseline at all of the lower web strain gauges to isolate the truck event in the time history data. In Figure 4-5, the dotted vertical lines correspond to the truck start and end time of the isolated truck event while the solid vertical line correspond to the time of maximum strain.

4.3 Model of Slab-Girder Flexural Behavior

A model is required to help analyze the measured bridge strain response and to describe the behavior of the bridge under loading. This study adopts a model based on the Newmark model for the theoretical analysis of the slab-on-girder span behavior [199, 207]. The model consists of two Euler–Bernoulli beams (namely the steel girder and the overlying reinforced concrete slab) coupled by means of deformable shear connectors, friction, and chemical bonding. Several assumptions are made to simplify the analysis. First, it is assumed that plane sections remain plane and perpendicular to the longitudinal axis which ensures a linear strain profile through the two beam sections. Second, it is assumed that the reinforcement bars are bonded perfectly to the surrounding concrete

so slip between the steel bars and concrete slab can be neglected [196]. Third, it is assumed that the concrete slab and the steel girders are vertically compatible (i.e., they do not separate) and share the same vertical displacement under external load. Fourth, flexural and axial stresses are assumed to dominate while shear and torsion stresses are neglected in the Euler–Bernoulli beam model [198]; this is owing to shear deformation being very small when elements are in bending [202]. Finally, the Young's modulus of the concrete is assumed to be identical in tension and compression in the linear region. The Newmark model is sufficiently descriptive and allows the measured strain response of monitored bridge beam sections to be interpreted on the basis of simple beam mechanics. While more advanced analytical models exist, such as the generalized model proposed by Focacci et al. [203], the simpler model used herein is a reasonable model choice. A typical T-beam section (Figure 4-2) under a positive bending moment M is shown in Figure 4-6. Three equilibrium conditions must be established in the section: moment equilibrium in the total section, lateral force equilibrium of the concrete section, and lateral force equilibrium of the steel section, as established in Eqs. 4.1, 4.2, and 4.3, respectively

$$M = M_s + M_c + F_i d \tag{4.1}$$

$$F_c = F_i \tag{4.2}$$

$$F_s = F_i \tag{4.3}$$

where d = distance between the equivalent geometry centroids of the reinforced slab and the girder; F_c = internal resultant force acting on the slab; F_s = internal resultant force acting on the steel girder; and F_i = interaction force at the concrete–steel interface. The relative slip at the concrete–steel interface, ξ, is defined as the relative longitudinal deformation between the concrete slab and the steel girder, which can be calculated as [193]

$$\xi(x) = u_c(x) - u_s(x) + \frac{\partial v(x)}{\partial x} d \tag{4.4}$$

where $u_c(x)$ and $u_s(x)$ are the lateral displacements of the slab and girder at their centroids, and $v(x)$ is the vertical displacement of the section. Assuming small rotations, the first derivative of vertical displacement relative to longitudinal length is the rotation of the section plane.

The section behaves differently for three cases: noncomposite action, full composite action, and partial composite action. The full composite action case is obtained from the infinite stiffness of the shear connectors ensuring no slip at the contact interface ($\xi = 0$). In this case, the concrete slab can be replaced with an equivalent steel slab based on the modulus ratio $\alpha = E_s/E_c$, where E_s and E_c are the Young's modulus of the steel and concrete, respectively [193]. The slab and girder then act together to resist the external moment, M. In the case of noncomposite action, free sliding is allowed between the slab and girder owing to $F_i = 0$. The concrete slab and steel girder act against the net section moment separately with the moment partitioned into two portions of the section (Ms and Mc) on the basis of the ratios of flexural rigidity

$$M_s = \frac{E_s I_s}{E_s I_s + E_c I_c} M \text{ and } M_c = \frac{E_c I_c}{E_s I_s + E_c I_c} M \tag{4.5}$$

where I_s and I_c = area moment of inertia of the slab and girder, respectively. The cases of full composite action and noncomposite action represent the upper and the lower bounds for the behavior at the slab–girder interface. Partial composite action has some slip at the slab–beam interface with an interface force, F_i, present on the contact surface. The slip is smaller than that associated with the noncomposite case. Response parameters, r_{pc}, of the partial composite beam can therefore be represented as a weighted mean of the two limit cases of the full, r_{fc}, and noncomposite, r_{nc}, beam responses [193]

$$r_{pc} = \eta r_{fc} + (1 - \eta) r_{nc} \tag{4.6}$$

where η is a nondimensional control parameter ranging from zero to one to adjust the DCA. The neutral axis of a beam is defined as the axis in which longitudinal strain/stress in the section is zero under external loads (e.g., moment and normal force). The neutral axis subject to the moment

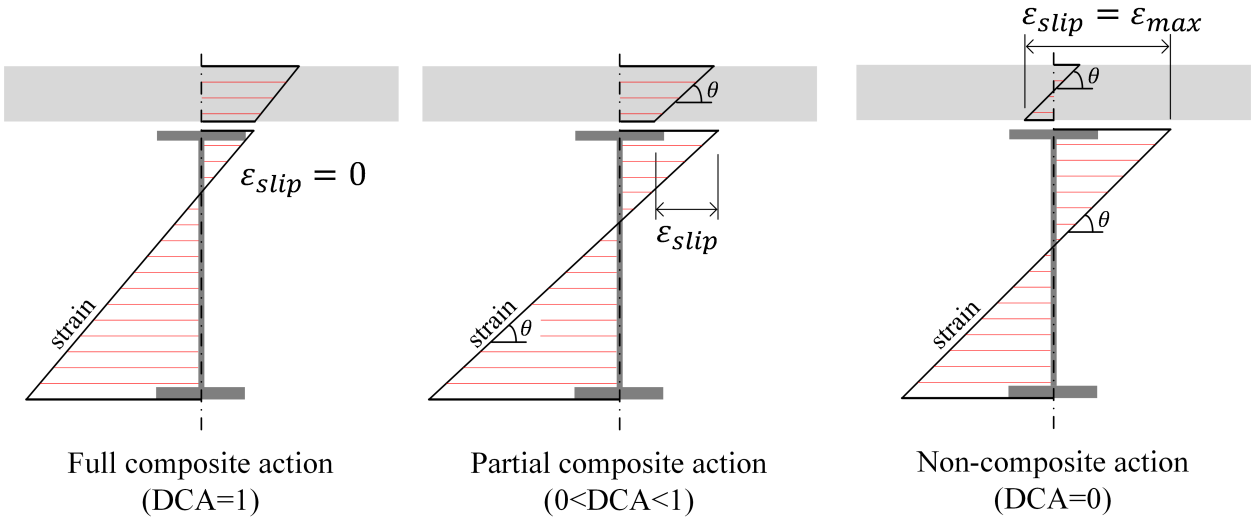

Figure 4-7: Three cases of slip strain depending on the degree of composite action shown within the strain profile of the composite section: (a) full composite action ($DCA = 1$); (b) partial composite action ($0 < DCA < 1$); (c) noncomposite action ($DCA = 0$).

load induced by vehicular loads is selected in this study, serving as an important parameter for describing the partial composite action case. In the case of noncomposite action, the steel girder and the concrete slab act separately under moment; the steel and concrete sections have their own neutral axes at their geometric centroids, G_s and G_c, respectively. When full composite action is exhibited, the entire cross section acts together with a single neutral axis located at G_f which falls between G_s and G_c, as shown in Figure 4-6. As slip begins to develop at the concrete deck–steel girder interface owing to the emergence of partial composite action, the neutral axis in the girder moves downward from G_f to some location between G_s and G_f. The dropping of the neutral axis from G_f can also be an indication of deck cracking and a weakening of the interface between the shear stud and the surrounding deck for the full composite case. As a result, the neutral axis position has been proposed as a damage-sensitive feature to assess the condition of bridge decks in many studies [43, 215, 209, 211]. In this study, the neutral axis position is estimated from the strain measurements taken in each section of the Telegraph Road Bridge and is used as an indicator of the DCA maintained at the girder–deck interface.

The relationship between slip in the steel–concrete interface and moment is an important property related to the shear stiffness at the interface. In a laboratory setting, the shear stiffness at an

interface with shear studs can be extracted from push-out tests for individual shear connectors in which the beam is gradually loaded with increasing axial loads [216, 199]. However, such tests are not feasible in an operational bridge. Instead of using slip, this study adopts slip strain, ϵ_{slip}, which is defined as interface slip per unit longitudinal (i.e., x-axis in Figure 4-6) length of the beam. More specifically, the slip strain is equal to the difference between the strain of the bottom fiber of the deck and the strain of the top fiber of the girder [207, 203, 199]. Slip strain, ϵ_{slip}, is used to quantify the DCA where [207, 217]

$$DCA = 1 - \frac{\epsilon_{slip|pc}}{\epsilon_{slip|nc}} \tag{4.7}$$

In doing so, DCA is essentially equal to η of Eq. 4.6 where

$$\epsilon_{slip|pc} = (1 - \eta)\epsilon_{slip|nc} \tag{4.8}$$

with $\epsilon_{slip|pc}$ essentially equal to zero owing to full composite action. As shown in Figure 4-7, the slip strain is zero in the case of full composite action and reaches to its maximum value in the case of noncomposite action. The partial composite action case has a slip strain, $\epsilon_{slip|pc}$, at an intermediate value between zero and $\epsilon_{slip|nc}$. Traffic load and resulting bending moment in the instrumented cross section cannot be directly measured. As a result, the strain response measured by the bottom-web gauges will be used as a proxy for the moment magnitude in the section. The relationship between the slip strain, ϵ_{slip}, and strain on the bottom of the steel girder, ϵ_{bw}, will be used to map the shear stiffness of the interface between the deck and the girder.

4.4 Observed Behavior of Slab-Girder Sections

4.4.1 Processing of Girder and Deck Strain Measurements

The strain data collected in the six sections (NE, ME, SE, NW, MW, and SW) on the Telegraph Road Bridge is processed to observe the flexural behavior of the slab–girder sections. A typical strain response in the NE section due to a truck load is shown in Figure 4-8(a). A high DCA is

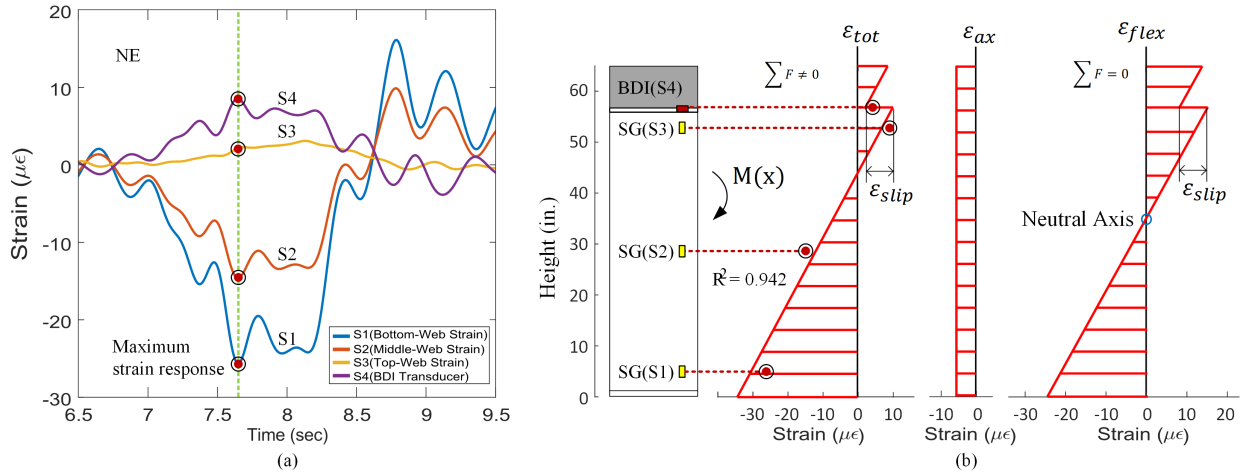

Figure 4-8: Process of neutral axis position estimation: (a) typical strain time history to truck loading at NE; (b) best fit linear strain profile with axial force (and corresponding strain) eliminated to impose equilibrium on the section.

evident at the section with maximum negative (compressive) strain at the bottom web strain gauge (S1) and the maximum positive (tensile) strain at the deck bottom surface, as measured by the BDI transducer (S4). In processing the strain data, it will again be assumed that plane sections remain plane and the deck is compatible with the steel girder. A linear strain profile is fit to the three strain measurements in the girder (i.e., top web, middle web, and bottom web) using the least square method, as shown in Figure 4-8(b). The linear strain profile fit to the measurements can be sensitive to a number of factors with signal-to-noise ratio (SNR) as the most important factor [211]. To ensure a high SNR, only heavy truck load events are considered, which ensure a high amplitude strain response in the section; furthermore, the estimation of neutral axis and slip strain, ϵ_{slip}, is performed using the maximum strain response for each truck event captured in the data [as shown in Figure 4-8(a)].

The strain profile, ϵ_{tot}, estimated in the section using the measurements, is shown in Figure 4-8(b). Based on the assumptions, the slope of the linear profile of strain in the girder is assumed to also occur in the deck. The strain profile is converted to a stress distribution. To do so, the steel girder is assumed to be in its linear response with axial stress, σ, linearly proportional to axial strain, ϵ, through the material modulus, E, with Poisson's ratio considered. The tensile strength of

the concrete is considered during calculation. Concentrated axial forces, F, in each layer of steel reinforcement is estimated on the basis of the strain at the height of the steel reinforcement and the area, A, of the steel ($F = AE\epsilon$). Under pure bending, $M(x)$, the sum of forces in the section must be zero. Using the stress profile in the steel girder and the concentrated forces in the steel reinforcement, the sum of force in the section is calculated. The sum of forces is typically small but not zero in the six sections of the Telegraph Road Bridge. This can be due to a number of factors such as measurement noise, response parameters not explicitly accounted for in the simpler model (e.g., longitudinal shear in the skewed deck), or potentially some mild restrictions in the beam supports. To focus on the flexural response of the beam sections and to establish equilibrium in the section, the uncertainties are treated as an equivalent axial force in the section inducing axial strain (ϵ_{ax}), as shown in Figure 4-8(b). This axial strain, ϵ_{ax}, is subtracted from the strain profile, ϵ_{tot}, to isolate the flexural strain profile, ϵ_{flex}. It is the flexural strain profile, ϵ_{flex}, that is used to estimate the neutral axis of the section. Slip strain, ϵ_{slip}, is calculated on the basis of the difference in the top girder strain extrapolated from the fitted linear strain profile, ϵ_{tot}, and the strain measured by the BDI transducer at the bottom deck surface.

4.4.2 Neutral Axis Behavior

During the observation period (October 1, 2013–April 30, 2016), over 2,000 truck events were observed. Histograms of the estimated neutral axis at the six instrumented sections are plotted in Figure 4-9. It should be noted that each histogram has a different number of observed events, N, based on the quality of the linear fit of strain through the height of the steel section. The coefficient of determination, R^2, is used to assess the linear regression with $R^2 > 0.75$ used as the acceptance criteria. Besides, data samples with strain measurement at the bottom of the steel girder less than 5 $\mu\epsilon$ are not considered for estimating neutral axis locations owing to their low SNRs. Also plotted in Figure 4-9 are the theoretical neutral axis locations for sections in full (FC) and noncomposite (NC) action as indicated by dashed lines. Using the geometries of Figure 4-2, the neutral axis when the spans are in full composite action are $G_f = 51.84$ in. (131.68 cm) and 45.02 in. (114.35 cm)

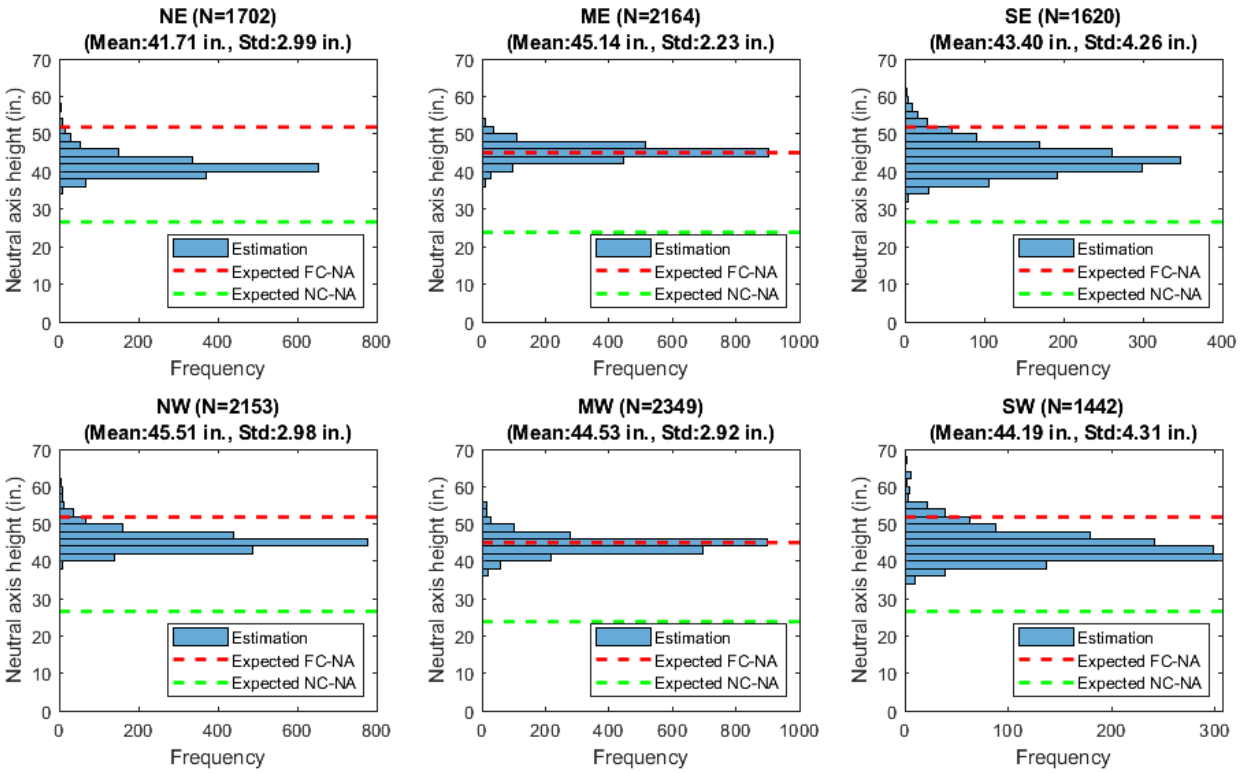

Figure 4-9: Histograms of estimated position of neutral axis at the six measurement locations. The as-designed neutral axis under assumption of full and no composite action is also shown for the as-designed sections.

from the bottom of the girder for the tail and main spans, respectively. Using the elastic modular ratio of the steel to the concrete, the neutral axis position is calculated by transforming the area of the concrete slab section into an equivalent steel section taken into account the area of steel reinforcement bars and different concrete materials [218]. In the case of noncomposite action, the neutral axis sits at the centroid of the steel girder section which is $G_s = 26.61$ in: (67.59 cm) and 23.83 in. (60.53 cm) for the tail and main spans, respectively.

As expected, the neutral axis at the main span sections (ME and MW) have an average neutral axis within 1 in. (2.54 cm) to the theoretical full composite action neutral axis. This indicates that the shear studs and concrete deck are in excellent condition. The average neutral axis at ME is higher [45.14 in. (114.66 cm)] than that at MW [44.97 in. (113.11 cm)] implying a stronger coupling between the girder and the deck at this location. At locations NE, NW, SE, and SW, the neutral axes lie between the two limit positions, G_s and G_f, revealing partial composite action.

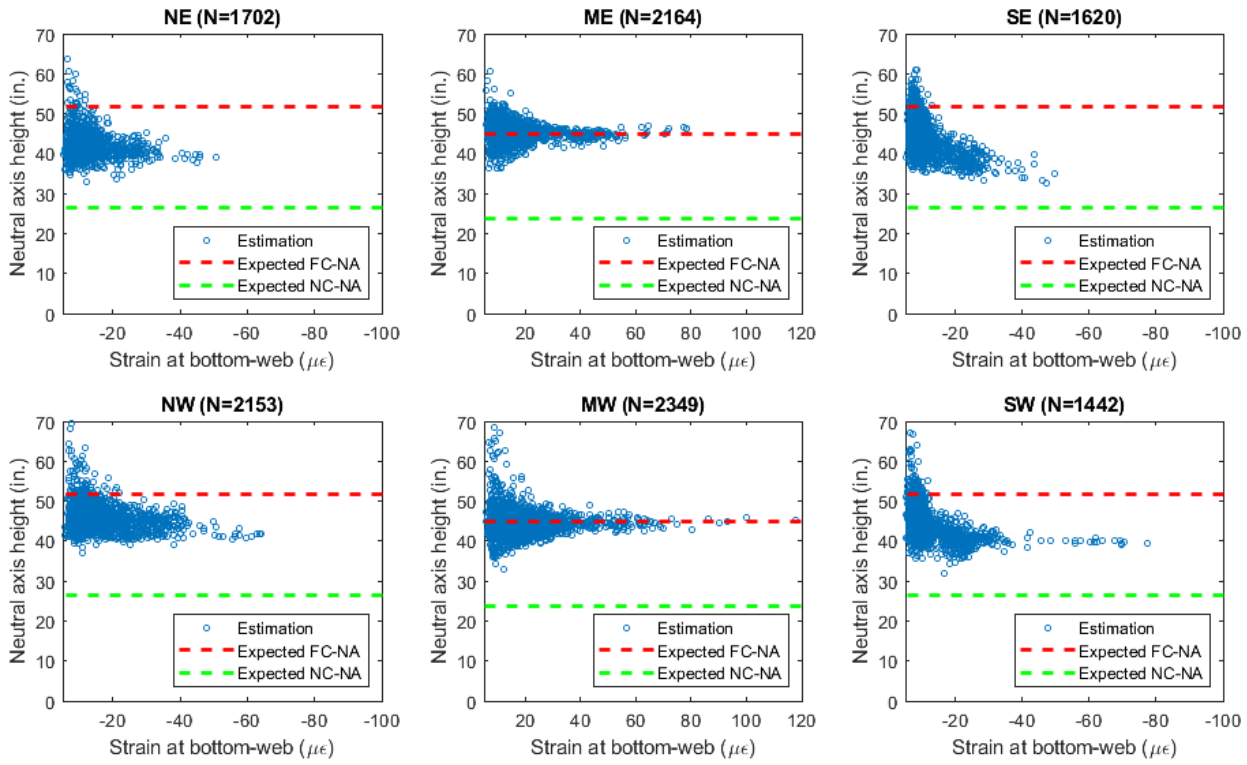

Figure 4-10: Scatter plots of the relationship between strain at the bottom of the steel girder and the estimated neutral axis positions.

While the neutral axis position estimated at SE and SW have larger standard deviations [4.26 in. (10.82 cm) and 4.31 in. (10.95 cm), respectively] than those at NE and NW [2.99 in. (7.59 cm) and 2.98 in. (7.57 cm), respectively], the neutral axis at NW is higher than those at the other three locations [45.51 in. (115.60 cm)].

The high degree of variation in the average neutral axis at the four tail span sections is attributed to variations in friction and chemical bonding on the steel–concrete interface. This would suggest sensitivity of the neutral axis on load (i.e., larger loads will more easily overcome the friction and chemical bonding) and environment (i.e., temperature). To illustrate the potential correlation between the neutral axis position and the load, the estimated neutral axis and bottom-web strain measurement (which is used to indicate the magnitude of section moment) are plotted in Figure 4-10. When the bottom-web strain is small (i.e., small traffic load), the estimated neutral axis exhibits a larger variation owing to the lower SNR associated with the strain measurements. As the load increases, the SNR rises and the uncertainty in the estimated neutral axis reduces. The

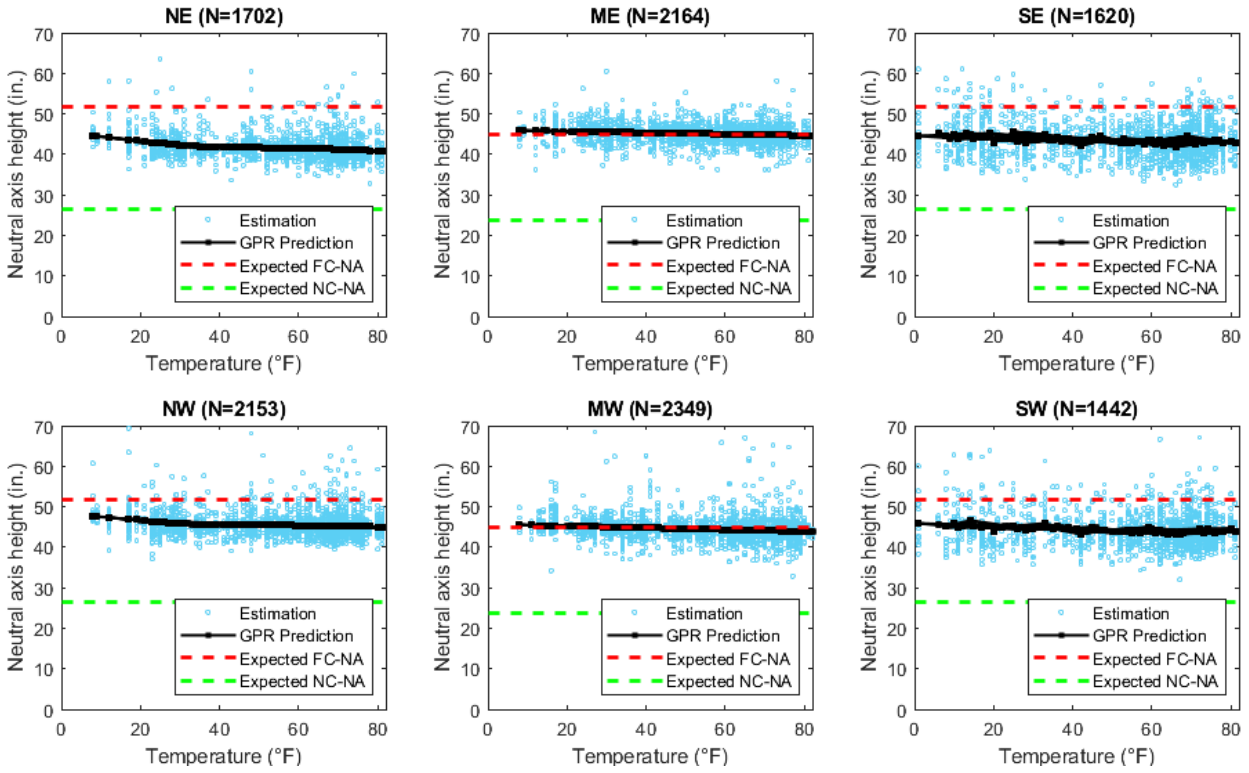

Figure 4-11: Correlation between estimated neutral axis position and ambient temperature with Gaussian process regression prediction.

neutral axis mean does not vary for the full composite sections (ME and MW) but exhibits dependence on load for the tail span sections confirming that larger loads are overcoming the friction and chemical bonding at the steel–concrete interface resulting in the neutral axis trending toward the noncomposite neutral axis. Figure 4-11 presents the correlation between neutral axis and temperature. The results of a Gaussian process regression (GPR) [219] are overlaid to model neutral axis dependency on temperature. It can be observed that the average neutral axis goes down slightly with the elevation of temperature. It is also observed that neutral axis temperature dependency is most pronounced in the four partial composite sections (as opposed to the full composite sections).

4.4.3 Slip Strain Curves

Slip strain, ϵ_{slip}, is plotted as a function of the maximum strain at the bottom web, ϵ_{bot}, for each truck event, as shown in Figure 4-12. Contrary to the extraction of neutral axis position, data samples with strain measurement at the bottom of the steel girder less than 5 $\mu\epsilon$ are considered to

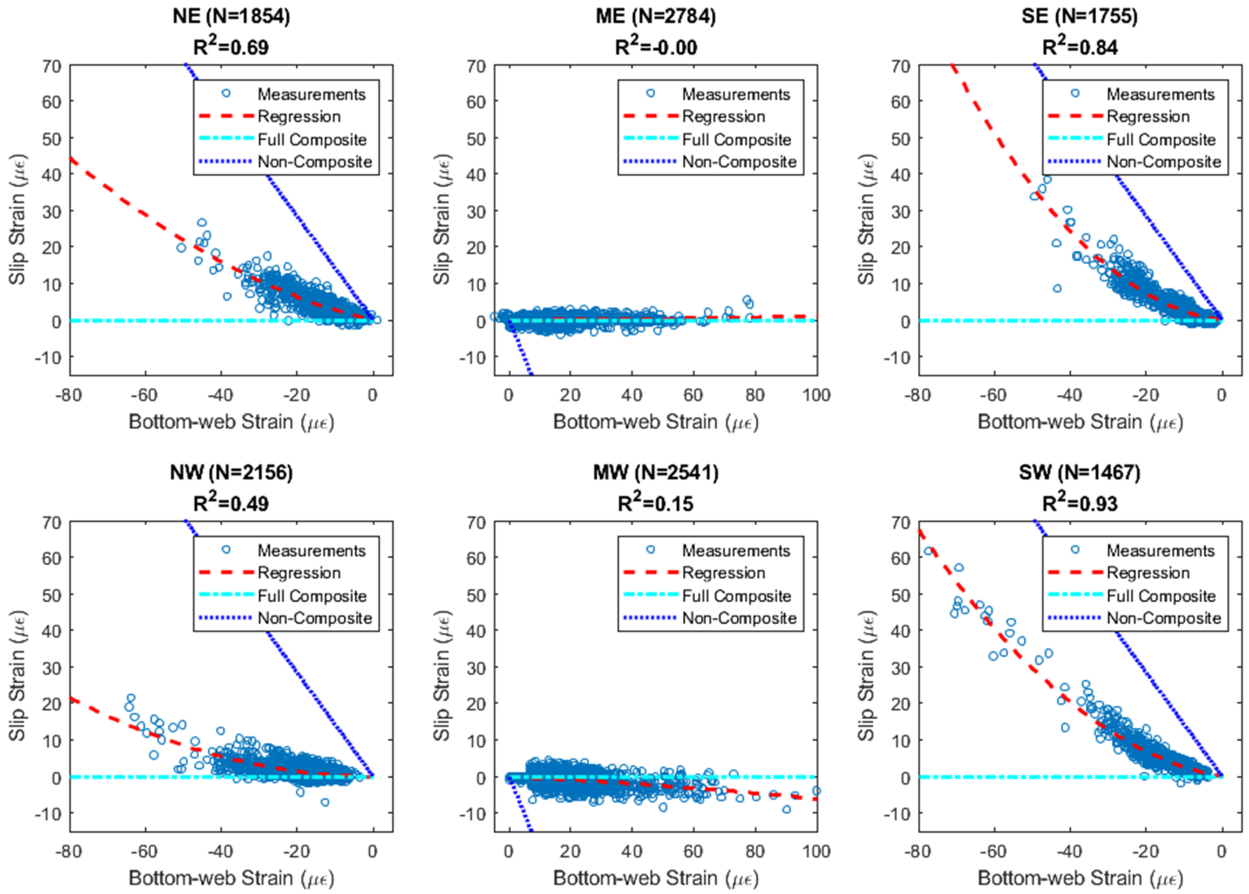

Figure 4-12: Bottom-web strain and slip strain relationships at the six measurements locations.

provide samples near the origin despite their low SNRs. Based on the scatter plots of Figure 4-12, load–slip curves are obtained by a linear regression analysis using a quadratic functional form

$$\epsilon_{slip} = a\epsilon_{bot}^2 + b\epsilon_{bot} \tag{4.9}$$

The function is forced to intercept the origin assuming slip only occurs with the presence of external load. The estimated parameters of Equations 4.9 are presented in Table 4-2. Other functional forms were attempted but the quadratic function offered the greatest fit with respect to the coefficient of determination. Also plotted on Figure 4-12 are the theoretical curves of slip strain as a function of bottom-web strain for full- and noncomposite action for each section. The slip strain curves at ME and MW are close to the theoretical full composite action case, as is expected. It is interesting to note that the studs at MW appear to be weaker than at ME with some

modest loss of composite action occurring under load conditions; this might suggest the start of local cracking in the deck near the studs. The slip–strain curves at the negative moment sections NE, NW, SE, and SW again show partial composite action that is quadratic in nature. Among the four negative moment sections, NW shows the highest degree of coupling associated with partial composite action. After the NW section, the NE section exhibits a little more composite action than the SE and SW sections. Evidence for this are the second-order coefficients at NE and NW being less than those at SE and SW (Table 4-2). Based on Figure 4-12, it is clear that the northern tail span is experiencing more friction and bonding on the steel–girder interface resulting in a higher DCA. This will induce greater tensile stress in the top of the deck slab which could accelerate deterioration. This observation confirms the inspection findings in the biannual bridge inspection presented in Table 4-1. The area of patched spalling on the top deck is always greater in the northern span compared with the southern tail span.

4.4.4 Deck Expansion

The deck behavior under thermal load is also considered over the same observation period. Figure 4-13 plots the static responses (without the presence of vehicles on the bridge) measured by the six BDI strain transducers as a function of ambient temperature. The manufacturer of the transducer (Bridge Diagnostics, Inc.) provides a calibration that minimizes temperature-induced error of the transducers so that the actual thermal strain in the deck can be estimated. As expected, the thermal strain is linearly proportional to the ambient temperature showing no indication of undesired constrained expansion. The coefficient of thermal expansion, α_T, ranges from 4.4 to 8.1 $\mu\epsilon/^\circ F$ which is reasonable given the fact that the coefficient of thermal expansion for concrete is between 3 and 8 $\mu\epsilon/^\circ F$ while that of steel is around 6.7 $\mu\epsilon/^\circ F$ [192]. It is concluded that the decks are free to expand and no restraint is imposed that would limit thermal expansion.

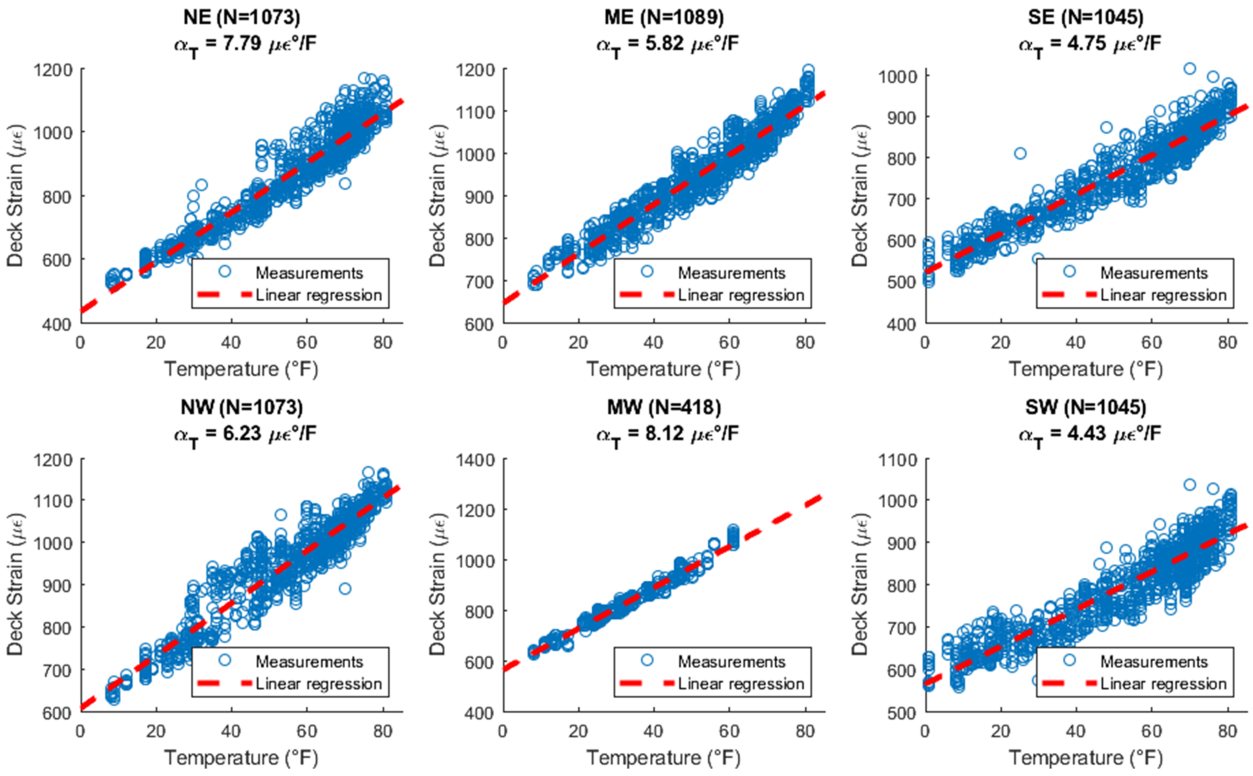

Figure 4-13: Correlation between static deck strain and ambient temperature with estimated concrete coefficient of thermal expansion.

4.5 Modeling of Deck Strain under Partial Composite Action

As previously described, the tail spans of the Telegraph Road Bridge have a history of accelerated deterioration with cracking and spalling present in the top deck surface, especially in the negative moment sections of these spans. This suggests greater strain in the top surface of the deck leading to long-term durability issues associated with water penetrating the section and corroding the steel reinforcement. The thermal expansion of the tail spans is confirmed to not be impeded; this suggests that the culprit is associated with the flexural response behavior of the tail spans in their negative bending regions. The quadratic model of Eq. 4.9 between slip strain, ϵ_{slip}, and bottom-web strain, ϵ_{bot}, in the negative bending regions of the tail span can be used to assess the strain in the concrete deck. The current strain profile can be compared with that assumed by the designer when designing the negative moment span as a no-composite action. This will serve as the basis for assessing the deck for long-term durability issues.

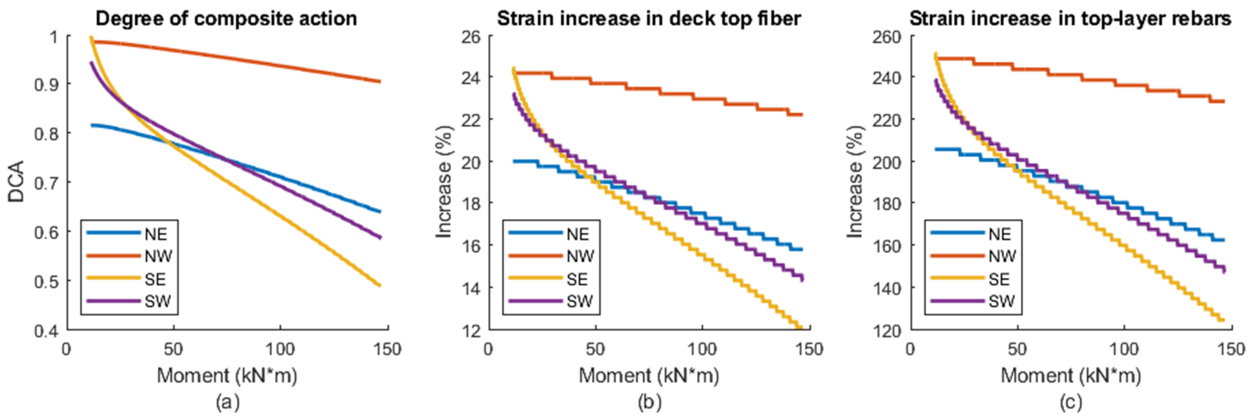

Figure 4-14: Relationship between the magnitude of negative bending moment imposed: (a) degree of composite action; (b) strain increase at the top surface of the deck (compared with no composite action); (c) strain increase in the top-layer rebars (compared with no composite action).

4.5.1 Analytical Model Calibration

Given the regressed quadratic relationship between slip strain, $\epsilon_{slip|pc}$, and bottom-web strain, $\epsilon_{bot|pc}$, described in Eq. 4.9, the analytical model discussed in section "Model of Slab-Girder Flexural Behavior" can be calibrated to reflect the actual composite behavior exhibited at the specific measurement location. The calibrated analytical model can then be used to estimate the strain profile in the negative bending sections of the tail spans. This would permit the DCA [Eq. 4.7], strain in the top surface of the deck, and strain in the top-layer deck steel reinforcement to be calculated analytically as a function of net flexural moment, M. Eq. 4.6 can used to find the parameter $\eta \in (0, 1)$ that describes the partial composite section strain as compared to the case of no composite action. Given η, the strain profile in the partial composite action section can be calculated for each applied moment, M, from which slip strain and bottom girder strain is extracted. A range of moments is applied in this analysis to yield a slip strain versus bottom girder strain curve. Then, a line search strategy is used to find the optimal control parameter, $\eta \in (0, 1)$, for each moment for which there is minimal error between the observed (Figure 4-12) and the analytical slip strain–bottom girder strain curve.

Given this calibrated model, Figure 4-14 is the model estimation of DCA, top deck strain and top steel reinforcement strain as a function of net section moment for the NE, NW, SE, and

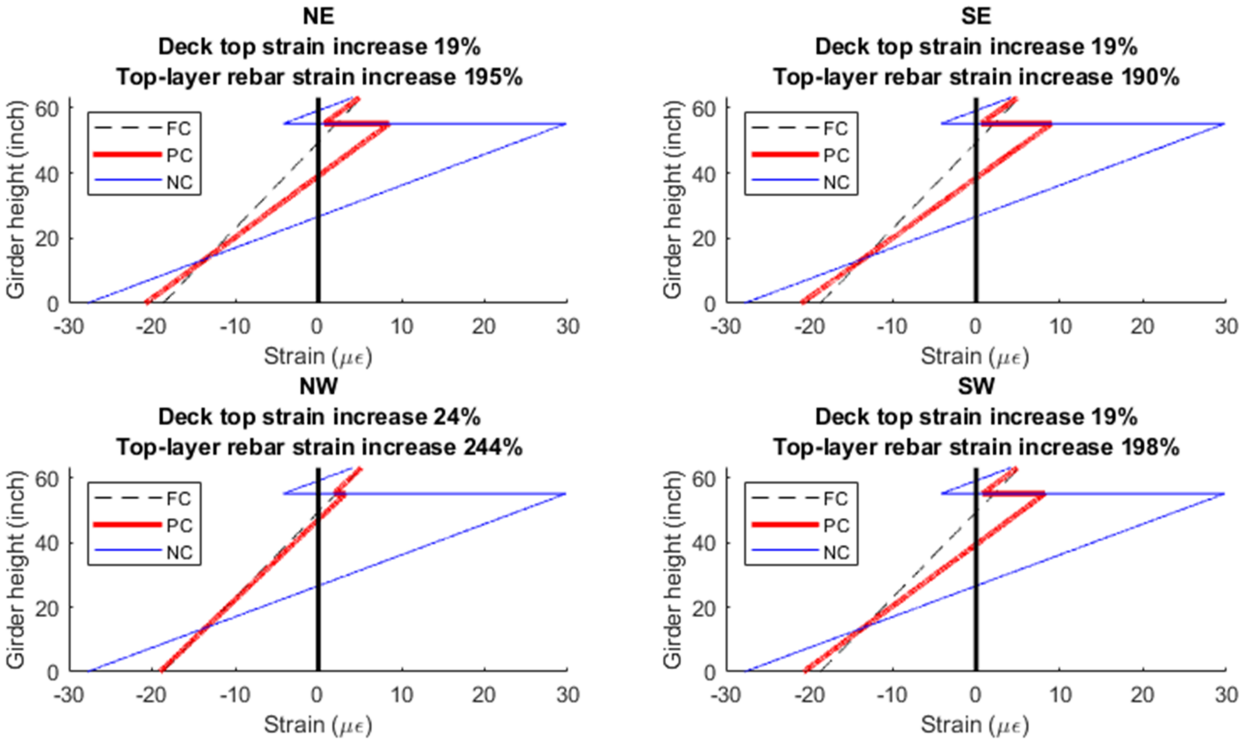

Figure 4-15: Strain profiles of the section in different cases of composite action under a 58 kN · m moment.

SW negative moment sections. For the top deck strain [Figure 4-14(b)] and the top-layer steel reinforcement strain [Figure 4-14(c)], the partial composite action section is compared with the no-composite action section to determine the strain increases. As expected, DCA degrades with an increase in the applied load [Figure 4-14(a)]. As a result, the strain increases in the top fiber of the concrete deck and in the top layer of the steel reinforcement because estimates by the model of the instrumented section are lower than the as-designed no-composite section. Depending on the moment magnitude and the DCA, the increase of the tensile strain in the deck top fiber and in top reinforcement bars range from 12% to 24% and from 120% to 250%, respectively. Such an increase will inevitably result in the concrete slab experiencing more serious cracking [220]. Figure 4-15 is an example of the strain profiles in the four negative moment sections (NE, NW, SE, and SW) for no (NC), partial (PC), and full (FC) composite action under a moment of 42,779 lbf · ft (58 kN · m) which results when a 62,500-lb (28.3 t) truck is on the bridge in the middle lane (Figure 4-2) at midspan.

Parameter	NE	NW	ME	MW	SE	SW
Coefficients of Eq. 4.9						
a	0.0039	0.0033	0	-0.0002	0.0121	0.0830
b	-0.2424	-0.0029	0.0023	-0.0417	-0.1267	-0.1775
Coefficients of Eq. 4.10						
F_{max}	40,000	40,000	-	-	80,000	80,00
α	-36.98	-19.97	-	-	-583.57	-534.46
β	1.12	1.87	-	-	1.90	1.90

Table 4-2: Estimated coefficients for Equations 4.9 and 4.10 for each measurement location considered.

4.5.2 Finite Element Modeling

The analytical modeling is based on an isolated two-dimensional deck–girder cross section which cannot represent the complexity of the actual bridge. To simulate a more realistic scenario of the observed partial composite behavior, a finite element method (FEM) model [Figure 4-16(a)] is built in CSiBridge, which is a commercial structural analysis software for bridge design and modeling [221].

The geometry and material properties of the structural components (e.g., concrete deck, steel girders, hanger plates) used in the model are based on the bridge drawings and construction records before the deck overlay. More specifically, the minimum yield stress strength of steel as $F_y = 50$ Ksi (344 MPa); the 28-day compressive cylinder strength of the concrete as $f_c^{'} = 3$ Ksi (20.7 MPa); concrete elastic modulus as $E_c = 1820\sqrt{f_c^{'}}$ =3,152 Ksi (21,732 MPa) [192]; and, concrete tensile strength as $f_t = 0.23\sqrt{f_c^{'}}$ =398 psi (2.74 MPa) [192]. The concrete starts to lose tensile strength when tensile stress exceeds f_t. The beneficial effect of tension stiffening between the cracked concrete sections is not modeled in this study. The deck is modeled using shell elements. The top flange, web, and bottom flange of each steel girder is modeled separately using connected shell elements. The hanger plates, cross-bracings, and stiffeners are all modeled using frame elements. Abutments and piers are modeled as pinned supports and rollers, respectively, with additional transitional and rotational springs deployed in the unconstrained degrees of freedom for extra stiffness. To investigate the strain increase in the deck and reinforcement bars caused by the partial compos-

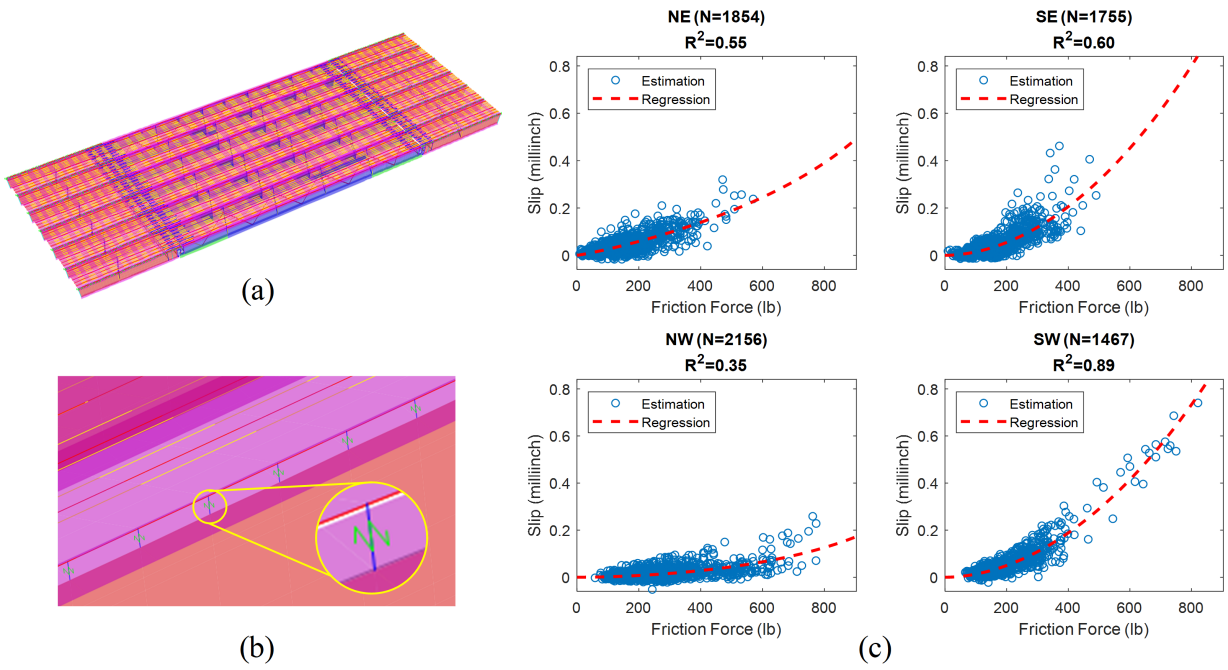

Figure 4-16: (a) Finite-element model for the Telegraph Road Bridge in CSiBridge; (b) link elements deployed along the deck–girder interface for modeling the partial composite action; (c) estimated load–slip curves obtained from collected strain responses.

ite action compared with the noncomposite action, the concrete deck is manually meshed into 19,464 refined elements with longitudinal reinforcement bars explicitly modeled and embedded in the deck using frame elements. The total model contains 26,660 shell elements and 5,486 frame elements.

The full composite action over the main span is modeled using body constraints to restrain the relative displacement between the deck and underlying girders. Nodes on the girder top flanges are connected to the corresponding nodes associated with the deck every 30.48 cm (12-in.) to be consistent with rest of chapter citation of dimensions along the longitudinal direction of the bridge. For the tail spans in which there is partial composite action, two approaches could be used to model the interaction: one is deploying distributed springs with longitudinal stiffness between the deck and the girder [198] and the other is to generate smeared interaction forces (e.g., friction) along the steel–concrete interface [193]. This study adopted distributed springs which is common to implement in finite-element analyses. In CSiBridge, as shown in Figure 4-14(b), the spring is

achieved by link elements connected to two joints (one on the deck and the other on the girder) and provides stiffness to relative displacement in the specified degree of freedom which, in this case, is along the longitudinal length of the girder. In the bridge model, the vertical stiffness of the link is set to be infinite to ensure that the slab and girder remain in contact at all times.

The longitudinal stiffness of the link is set based on nonlinear load–slip curves extracted from the measurement data. Using the measured section strain in the negative bending sections, the vertical distribution of strain is estimated, as illustrated in Figure 4-8. The friction force is then extracted from an equilibrium analysis of the girder [Eq. 4.3] while slip strain is obtained directly from the measurements. The slip at the contact interface is the product of the measured slip strain and the spring spacing in the model which is set to be 12 in. (30.48 cm) for the two tail spans. Figure 4-14(c) plots the calculated slip versus friction force for the four negative moment sections.

Many analytical models have been introduced to describe load–slip curves for individual shear connectors. This study applies the constitutive relationship proposed in [222] and extended in [223]. The relationship between friction force F attributed to a single shear connector and the corresponding slip s is modeled using the following exponential-like formula:

$$F(s) = F_{max}(1 - e^{-\beta s})^{\alpha} \tag{4.10}$$

where F_{max} is the ultimate connector strength and α and β are two constant parameters controlling the shape and initial slope of the curve, respectively. Although the formula is proposed for shear connectors, it still provides a good fit for the estimated frictional force and the relative slip to model the partial composite action without shear connectors, as shown in Figure 4-14(c). A grid search along with nested least-squares–based regression is performed to optimize the three functional parameters (F_{max} , α, and β) to achieve the best fit. The estimated parameters are listed in Table 4-2. In the model, the DCA for the tail span girders is assumed constant along each girder. To model the girder lines which are not monitored, a statistical model is assumed for the parameters of Eq. 4.10. Probability distributions of F_{max} , α, and β are estimated using a maximum likelihood estimation with a Rayleigh distribution using the parameters from the four sections monitored. The Rayleigh

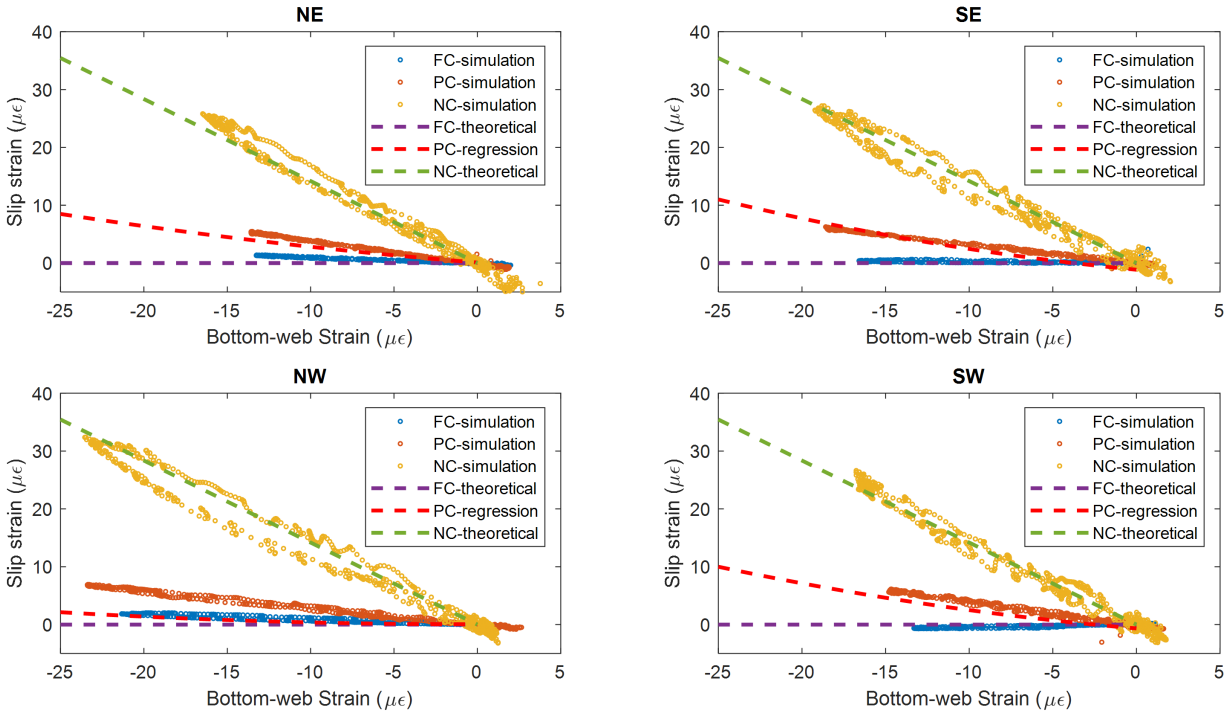

Figure 4-17: Simulation results of bottom-web strain versus slip strain curves at the four measurement locations on the tail spans: (a) NE; (b) SE; (c) NW; (d) SW.

distribution is selected because it is a continuous probability distribution for positive random variables (e.g., spring coefficients). The spring properties on the girder lines without monitoring data are then randomly sampled using the distributions of F_{max} , α, and β. In CSiBridge, the continuous nonlinear curves of slip versus friction force are discretized as piecewise linear functions.

The fully constructed CSiBridge model is validated in the time and frequency domains using previously collected truck test data [145] and extracted modal properties [224], respectively. Two comparative models are also built in CSiBridge with the tail spans modeled with no and full composite action. The full composite action model uses rigid body constraints at the deck–girder interface while the no-composite action model uses link elements at the deck–girder interface with zero stiffness along the longitudinal direction (and infinite stiffness vertically). To verify the effectiveness of the choices made in modeling the deck–girder interface, the bottom-web strain versus slip strain curves at the NE, NW, SE, and SW are plotted from the simulation results (of a single truck driving over the bridge) and compared with the regressed curves from Figure 4-12. As shown

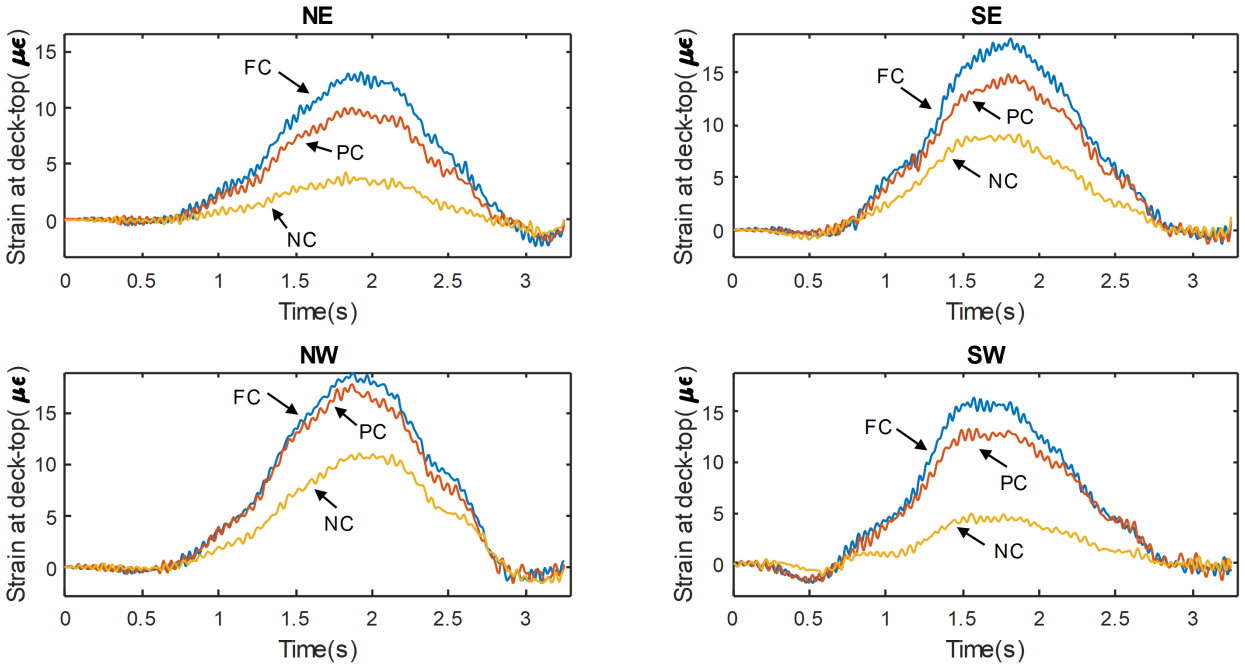

Figure 4-18: Simulation results of tensile strain experienced on the deck top surface at the four tail span measurement locations for an unsprung four-axle 28.3-t (62,500 lb) truck driving at 88.5 km/h (55 mi/h): (a) NE; (b) SE; (c) NW; (d) SW.

in Figure 4-17, despite the presence of slight discrepancies, the simulation results are close to the analytical curves. Some discrepancies may result from both the skewness of the bridge as well as from the fact that the girder lines are coupled through the deck (which contrasts with isolating the girder lines, as was done in Figure 4-12).

With the tail span slab durability of primary interest, the strain of the deck top surface at the four monitored negative moment locations are plotted in Figure 4-18 for the no (NC), partial (PC), and full composite (FC) action models under an unsprung 62,500-lb (28,349 kg) truck driving at 55 mi/h (88.5 km/h) in the center lane. Compared with the noncomposite action case for which the bridge is designed, a significant increase of the tensile strain is experienced by the top fiber of the concrete deck in the partial composite action. Comparing the partial composite action and the noncomposite action, the spatial distribution of the longitudinal tensile strain increases of the deck top surface is presented as a percent increase in Figure 4-19. In order for a clearer visualization, percentages that are greater than 100% are clipped to be 100%. As expected, the increase in tensile

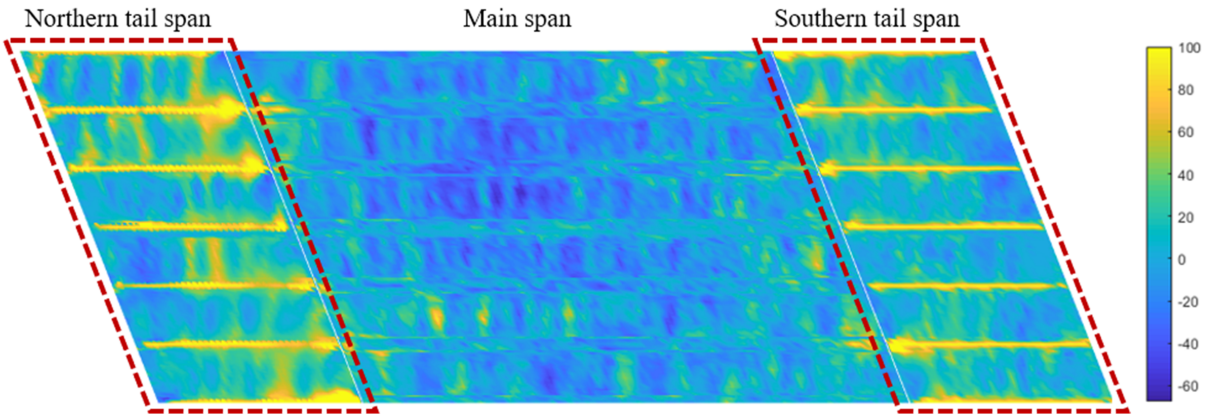

Figure 4-19: Simulation results of spatial distribution of longitudinal tensile strain increase (in percentage) in the deck top surface for the partial composite action case compared with the no composite action case.

strain in the deck mainly concentrates in the negative bending regions, especially above the girders; this is consistent with the observation of deck cracks often occurring over girder lines in real bridges [225]. More specifically, the northern tail span experiences higher tensile strain increases than the southern tail span. Considering the midspan, it undergoes a modest decrease in the top surface tensile strain because of moment redistribution associated with the change in flexural rigidity of the tail spans. While the percent increase in tensile strain is informative, if the tensile strain is small, even a large percent increase can be insignificant. As an alternative, Figures. 4-20(a and b) plot two histograms of the maximum longitudinal tensile stress in the top-layer reinforcement bars and in the deck over the pier caps, respectively, between the no and partial composite action cases. The reinforcement bars and the deck in the partial composite action take considerably higher tensile stresses then those in the noncomposite action under vehicle loads. Partial composite action not only introduces higher tensile stresses in the concrete deck compared to the no composite action case, but it also redistributes larger moment loads to the negative bending regions due to the larger flexural rigidity the partial composite action section offers. Consequently, the tensile strain increase at the deck top surface obtained from FEM simulation is much larger than that calculated from the analytical model of section “Analytical Model Calibration.”

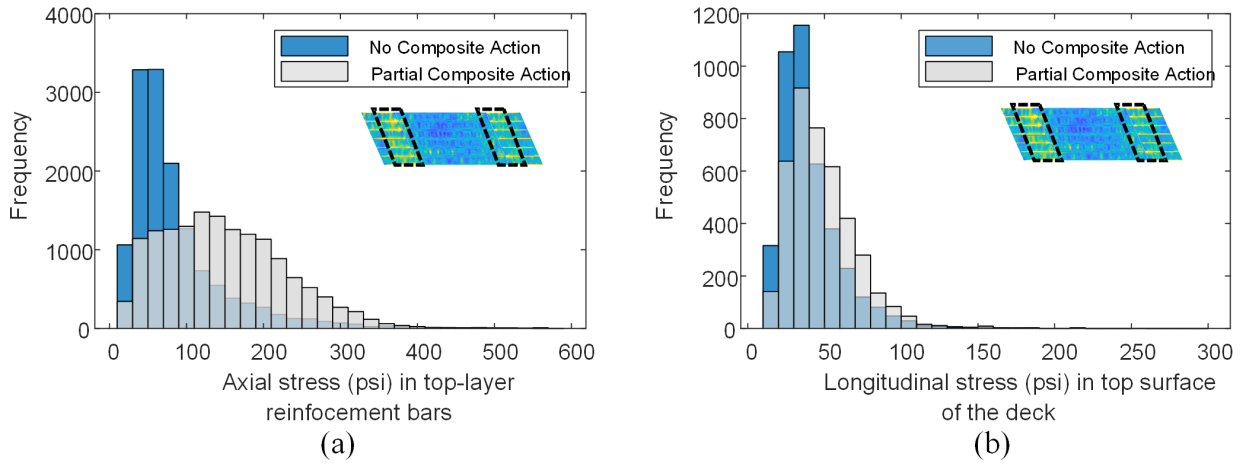

Figure 4-20: Simulation results of histograms of maximum tensile stress over the interior pier supports (negative bending region) experienced by: (a) top-layer rebars; and (b) deck top surface.

4.6 Extensions to Deck Durability

It has been seen that the observed partial composite action can lead to significant increases of stress and strain in the concrete deck over the negative bending regions. While the primary contribution of this chapter is the monitoring and modeling of the composite action behaviors exhibited in the bridge, this section explores the potential relationship between the observations and analysis outcomes made previously to the deck durability issues reported prior to the deck overlay repair in 2011.

Concrete cracking and spalling are two major forms of deck deterioration that influence the serviceability of a bridge and pose a potential danger to vehicles [225, 226]. Cracking and spalling have occurred on the Telegraph Road Bridge tail spans over its lifespan with the spatial distribution of deterioration consistent with the strain results of section “Modeling of Deck Strain under Partial Composite Action.” However, besides vehicular live loads, cracks in bridge decks can be induced by several other factors including shrinkage, creep, and temperature variation [220]. The shrinkage and creep effect of the concrete, especially drying and thermal shrinkage, can lead to restrained deformation of the concrete deck and therefore induce tensile stresses and cause early cracks [225, 227]. Temperature differences occur right after concrete casting owing to the heat generated by the

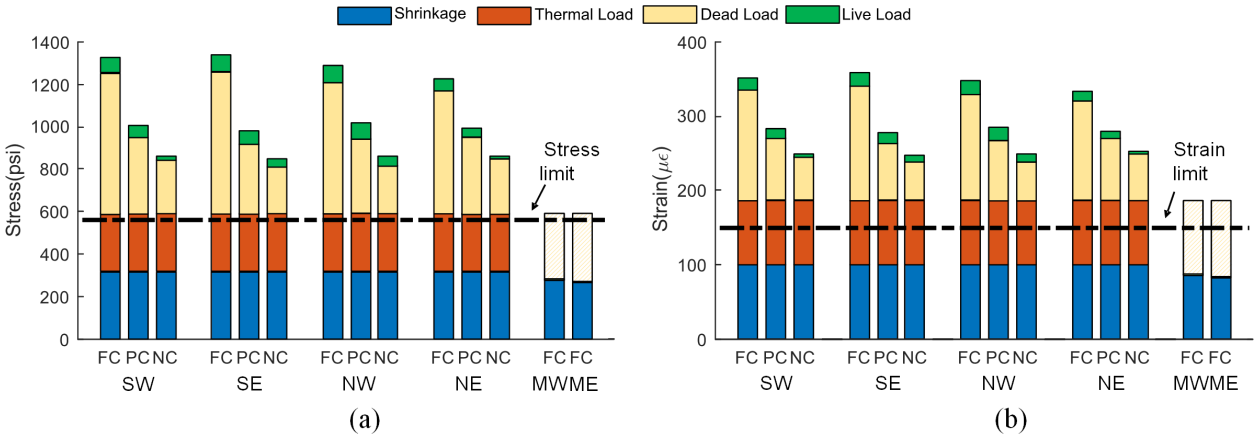

Figure 4-21: Estimated bridge responses to live load, dead load, temperature variation, and shrinkage with black dashed lines indicate the limit state of cracking: (a) stress responses; (b) strain responses. (Note: negative responses due to dead load over the main span are represented by hatching patterns in the same color.)

cement hydration process during curing. The early cracks that result effectively reduce the tensile strength of the hardened concrete. Later, environmental temperature changes can produce large tensile strains in the concrete deck. Environmental temperature changes are typically nonlinear across the cross section of the superstructure often leading to restrained deformation in the concrete deck [228]. Strain associated with temperature, shrinkage, and creep of the deck is impossible to measure in the field for existing bridges and can only be estimated. The dead (self-weight) and vehicular live load strain can be evaluated with greater accuracy to assess the durability of the bridge deck. The simulation of the bridge in CSiBridge has demonstrated that partial composite action not accounted for in the bridge design introduces higher tensile strains in the top of the bridge deck over the negative bending regions under vehicular loading.

To assess the durability of the Telegraph Road Bridge, the tensile limit of the concrete must be estimated. Concrete will crack when its tensile stress exceeds its tensile strength or when the tensile strain exceeds between 100 and 120 $\mu\epsilon$ [220]. The 95th percentile of the tensile strength, f'_{t95}, can be taken as the tensile strength of the concrete for the determination of crack formation, which can be calculated as $f'_{t95} = 2.7(f'_c)^{2/3}$ [220]. Using this relationship, the concrete tensile strength in the Telegraph Road Bridge before deck resurfacing is 562 psi (3.87 MPa). The depth

of cracking can be calculated by considering the maximum concrete tensile strain of 150 $\mu\epsilon$ [black dash line in Figure 4-21(b)] [220].

To begin to quantify the impact of DCA on deck crack development, the values of the stresses and strains experienced by the deck top surface owing to various causes (shrinkage/creep, thermal load, dead load, and live load) at the measurement locations over the negative bending regions are estimated for three different DCA scenarios (no, partial, and full composite action) based on intact concrete. For comparison, the same stress and strains are estimated for the locations over the main span in which full composite action exists in positive moment. In this chapter, the tensile stresses due to the live and dead load of the deck top surface are derived from the CSiBridge simulations. The restrained tensile stresses due to temperature variation at the deck top surface are calculated using the recommended temperature gradient for Michigan based on the AASHOTO design specification [192, 229]. The negative temperature variation across the bridge superstructure section can introduce a tensile stress of 272 psi (1.88 MPa) to the extreme tensile fiber of the deck which results in a tensile strain of 86 $\mu\epsilon$. The detailed calculation for these stresses is beyond the chapter scope and therefore not shown. In this study, the restrained stress due to shrinkage takes the restrained stresses corresponding to a 100 $\mu\epsilon$ uniform shrinkage in the deck of a typical continuous-span bridge with steel girders as a reasonable approximation [228]. The resulting stress can be as large as 315 psi (2.17 MPa). Additional shrinkage stresses may develop over the interior supports of continuous-span bridges but are neglected here. Besides, the higher DCA between the deck and the girders is supposed to bring larger restrained stresses to the bridge superstructure. However, the bridge responses to shrinkage, creep effect, and temperature variation are assumed to be identical for all cases to simplify the analysis.

Figure 4-21 plots the estimated shrinkage/creep, thermal load, dead load, and live load stress and strains at the top of the deck at the six monitored sections. While these stresses and strains are estimates, the plot gives a sense of the elevation in stress and strain in the top deck due to partial composite action. From the standpoint of the stress, we can see from Figure 4-21(a) that partial composite action contributes an addition 0.34–0.69 MPa (50–100 psi) of tensile stress in

the deck. Similarly, from Figure 4-21(b), the additional tensile strain ranges from 25 to 75 $\mu\epsilon$. If the deck exceeds its strain limit for cracking, then the higher tensile strain also opens those cracks wider. It has been shown that the width of flexural concrete cracks is positively proportional to the strain within reinforcing steels [230]. As a result, the tensile strain increase in the reinforcing steels caused by the partial composite action enlarges the width of the cracks and the depth, which in turn allows greater ingress of the chlorides and expedites the corrosion of the reinforcing steels. This will lead to durability issues due to concrete spalling stemming from the corrosion of reinforcement bars that are exposed to chloride contamination [231, 232]. Deck cracks accelerate the movement of moisture, oxygen, carbon dioxide, and chlorides through the concrete cover to the reinforcement bars. In snowy regions such as Michigan, chloride-based deicing salts are applied during winter to keep bridge surfaces in a safe condition, which leads to an aggravating corrosion of the reinforcement bars.

4.7 Summary and Conclusions

Deck deterioration has been recognized as one of the most severe issues undermining the serviceability of slab-on-girder bridges in northern climates. The Telegraph Road Bridge studied in this chapter is more than 40 years old and has been reported to have consistent deck cracking and spalling issues in regions of negative bending over interior piers. To study this issue, a long-term bridge structural health monitoring system was installed in the bridge to measure the composite action behavior of the bridge at six different locations over a 3.5-year period. Two innovative features including neutral axis position and slip strain were considered as response features from which the degree of composite action could be assessed. Partial composite action was characterized for the negative bending regions of the bridge by assessing the location of the neutral axis in the steel girder; neutral axes were approximately between the full and no composite action cases. In the main span where full composite action was designed, the neutral axis was nearly identical with its theoretical location. The neutral axis estimation proved to be stable when large vehicular loads were applied to the bridge span owing to a high SNR associated with the data. The partial

composite action observed in the bridge tail spans was also observed to have a modest dependency on temperature whereas the full composite sections were less affected by temperature. To model the behavior of composite action in each of the instrumented sections, slip strain was modeled as a quadratic function of the bottom-web strain which is correlated to the moment in the section. The quadratic functions fit to the monitoring data later served as the basis of assessing the impact partial composite action has for the long-term durability of the bridge tail span decks. The northern tail span, compared with the southern tail span, had the greatest degree of partial composite action evident in the models derived. This correlates to past deck inspections that report the northern tail span having disproportionately greater deck cracking and spalling compared with its southern counterpart. The study highlighted how the model for slip strain can be used to model the deck durability using both analytical and numerical models. Using these models, it is demonstrated that the as-built tail spans have much higher tensile strains and stresses in both the concrete deck and internal reinforcement bars owing to the partial composite action that develops on the deck–girder interface compared with the case of assuming no composite action. Higher than anticipated tensile strain in the deck top surface and in the top-layer reinforcement will inevitably accelerate the development and propagation of concrete cracking and spalling over the tail span decks, especially in a northern climate area like Michigan where deicing salts are used in the winter.

There are three major contributions associated with this study. First, it highlights the power of intentionally designing the monitoring system instrumentation to monitor specific behaviors in bridges; in this study, the strain sensors are installed to monitor DCA in slab-on-girder bridges. Second, this study represents one of the very few studies of partial composite action in an operational bridge using long-term monitoring data. Neutral axis and slip strain are offered as response parameters extractable from long-term monitoring data from which partial composite action can be tracked and the deck health assessed based on changes in DCA. Partial composite action was quantitatively confirmed in the bridge tail spans over their negative moment region although they are designed to have no composite action. Finally, the study discovers that the developed partial composite action introduces increased tensile strain in the deck and thus affects its durability. Very

few structural health monitoring studies consider the implication of damage sensitive features on the prognosis of the structure; in this study, the DCA is linked to deck durability offering bridge owners a more rational basis for making decisions on the retrofit of their bridge decks.

Future work will be focused on deploying more sensors in the slab–girder cross section to obtain more information describing the structural behavior of the cross section, and thus allowing one of the more advanced analytical model previously discussed to be adopted for partial composite action modeling. Besides, the evolution of the composite behavior and the deck condition in the Telegraph Road Bridge will also be investigated for a longer period of observation so that changes in DCA parameters such as neutral axis and slip strain can be correlated to deterioration observed by biannual bridge inspections. In addition, future efforts will explore instrumentation of additional negative moment sections to study the statistical distribution of DCA model parameters.

CHAPTER 5.

Fusion of Weigh-in-motion System and Bridge Monitoring Data for Bridge Load Rating

5.1 Introduction

Bridges represent critical transportation structures that are designed to safely carry traffic loads over topographic features such as bodies of water, valleys, and other roads. Their designs ensure safe operations even when exposed to a wide range of gravity and lateral loads. Traffic loads are one of the largest live loads bridges that bridges will be exposed to over their life spans, especially in medium and small span bridges [120]. Given their importance, bridges are regularly inspected to assess the structural condition of their components. Bridges are also regularly evaluated to ensure their reserve structural capacity is sufficient to accommodate future live load demands encountered with some safety margin. If the reserve structural capacity is not sufficient to carry future live load demands, then bridge rehabilitation, load posting, or closure must be considered to ensure public safety. Hence, load rating is an essential asset management tool used by bridge owners to assess the margin between the reserve structural capacity of the bridge and future live load demand. Current load rating practice for highway bridges in the United States is established by the Manual for Bridge Evaluation (MBE) published by the American Association of State Highway and Transportation Officials (AASHTO) [35, 233]. As specified in the MBE, bridge load rating considers the structural design, current structural conditions, material properties and anticipated future loading of the bridge to assess the margin between reserve structural capacity and traffic live load demand [35]. Two general load rating approaches are specified by the MBE: approximate and refined analytical methods. The approximate method uses simplified mechanical models of the

bridge (e.g., line girder) and empirical parameters (e.g., distribution factors) to analyze the ratio between reserve structural capacity and live load demand associated with current and future traffic loads [234, 235]. While analytically easy to execute, such a simplified approach neglects the true, systematic behavior of the bridge resulting in conservative rating factors [236, 237]. If cost and time allow, the MBE permits refined load rating analyses that rely on the use of more sophisticated structural models that better reflect the behavior of the bridge system (e.g., finite element (FE) analysis). Refined analyses can also include on-site load testing where bridge responses to controlled loads are measured by data acquisition systems installed in the bridge [35, 236]. However, the costs associated with load testing of operational bridges can be prohibitive for many bridges thereby resulting in load ratings done exclusively by analytical means [238].

To improve bridge rating accuracy, measurement data can be introduced to lower uncertainties with analytical methods. For example, material testing can reduce uncertainties associated with the estimation of material properties when estimating structural capacities [238, 239, 240, 241, 242, 243]. When using refined analytical load rating methods such as those based on three-dimensional FE models, model validation is essential to ensure the model represents the true bridge behavior [239, 234]. Such models are best calibrated through vibration testing (e.g., modal parameters) [244, 245, 246]. As previously mentioned, static load testing can offer insight to the true behavior of the bridge including the composite action between structural elements (e.g., deck and girders) and boundary conditions (e.g., behavior of supports) allowing FE models to be refined [234, 239, 246, 247, 248, 249]. While short-term instrumentation can provide modal parameters for model updating or used to measure responses during load testing, there are opportunities for permanent monitoring system to provide even greater insight into bridge behaviors under varying operational environments. For example, long-term monitoring allows for probabilistic models of traffic live load effects to be created through direct or extreme value analyses [250, 251, 252, 253]. While probabilistic live load effect models could improve the accuracy of load rating methods, the traffic load themselves are not directly measured making ratings based on live load effects difficult to compare to those based on standardized truck loads associated with MBE-based analytical

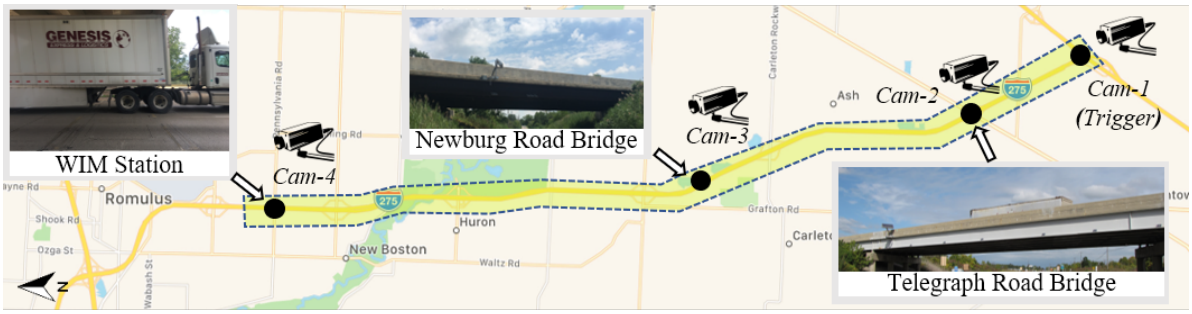

Figure 5-1: Locations of the subsystems of the cyber-physical system along the selected I-275 northbound corridor.

methods. Long-term monitoring has also been explored to quantify live load distribution factors that represent realistic distributions of the truck loads to bridge girder line. Live load distribution factors based on measurement reduce the conservative nature of the load distribution factors widely used in the MBE approximate methods (e.g., 54% of a standard truck load carried by each external girder line and 63% by each interior girder line) [242, 234]. Monitoring of bridge responses synchronously with camera images of trucks crossing the bridge can be used to estimate a unit influence line (UIL) that can be used to predict design load effects [120]. However, UIL estimated from the response data have uncertainty due to the absence of the distribution of truck loads across multiple axles. This uncertainty could be reduced if weigh-in-motion data is then used to measure the axle spacing and the distribution of vehicle gross weight over the different axles [153].

The goal of this study is to improve the accuracy of analytical load rating methods using long-term monitoring data collected from a cyber-physical system (CPS) implemented along a highway corridor that comprehensively integrates bridge response monitoring, truck tracking using traffic cameras, and measurement of truck loads using weigh-in-motion stations [254]. The study specifically focuses on statistical modeling of live load parameters to improve the realism of approximate load rating methods. Using long-term bridge response data, the dynamic load allowance (DLA) and UIL are extracted from a large database of bridge response-truck weight measurements collected by the CPS. The DLA and UIL extracted from the data represent the true behavior of a bridge leading to a much more accurate load rating. The benefit of the proposed approach is that it is non-invasive (e.g., does not require closure of the bridge like in static load testing) and provides

a powerful statistical basis to aggregating long-term observation of bridge behavior. The study utilizes a CPS architecture installed along a 20-mile I-275 highway corridor between Newport and Romulus, Michigan which includes two highway bridges instrumented with long-term wireless structural health monitoring (SHM) systems, four traffic cameras along the corridor, and a WIM station for measuring truck gross weight, axle spacing, and axle weights, which is also described in Chapter 2 and 3 in details. For each of the two highway bridges along the I-275 corridor, three interior girders are rated following the Load and Resistance Factor Rating (LRFR) criteria for design load rating [35]. The proposed data-driven load rating method using long-term monitoring data is evaluated by comparing it to rating factors obtained by conventional approximate and refined, FE-based methods.

5.2 Bridge Systems and Measured Data

The details regarding the implemented cyber-physical-system enabled bridge SHM network (Figure 5-1) has been described in Section 2.2. Herein, the description will not be repeated, and the focus will be on the instrumentation of strain gauges which measure girder strain responses in the six target interior bridge girders to be rated to traffic loads. Of primary interest in this study is the flexural response of the bridges. Hence, the strain gauges installed near the lower flanges of the girders are the sensors of primary interest. Three gauges are installed on girder lines 2, 4 and 6 on both TRB and NRB. These girder lines are immediately below the three primary lanes of traffic. The sensors consist of weldable strain gauges (Hitec HBWF-35-125-6-10GP-TR) welded 3 inches (7.62 cm) above the bottom flange of the I-section web (Figure 5-3) at the midspan of the bridges where the largest bending moment is anticipated when the bridges are vertically loaded by trucks. The strain gauges on girder line 2, 4 and 6 on the TRB (NRB) are denoted as TS1 (NS1), TS2 (NS2) and TS3 (NS3), as shown in Figure 5-2. Each strain gauge is interfaced to a *Narada* wireless sensor node that collects data at 100 Hz for 100 and 120 seconds at TRB and NRB, respectively, once triggered by the CPS architecture. After data collection, data is communicated by each *Narada* node using the IEEE802.15.4 communication protocol to a local base station which

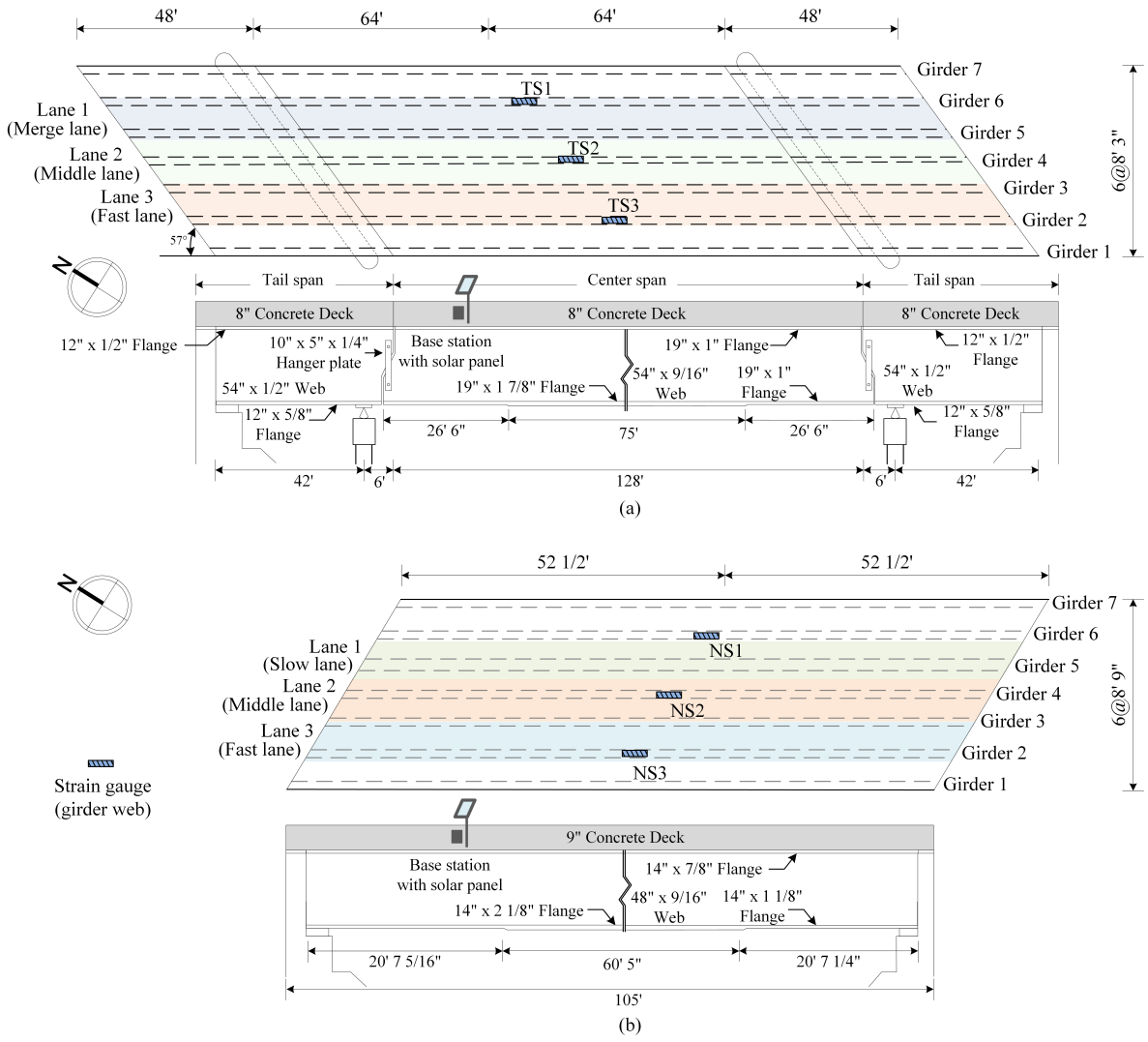

Figure 5-2: Sensor layout of the strain gauges used in this chapter: (a) Telegraph Road Bridge and (b) Newburg Road Bridge.

then communicates the strain response via a cellular model to the CPS database server.

Two FE models (shown in Figure 5-4) have also been created in CSiBridge [221] based on the engineering drawings of each bridge and calibrated using measured response data to known truck loads. Additional details on the modelling of the two bridges can be found in other papers by the authors [153, 61, 147]. The CSiBridge models are used to extract dead load effects to be used in load ratings performed for each bridge.

Also involved is the WIM station along the same I-275 northbound highway corridor, which provides measurements of truck loads passing the two bridges. The WIM station (Figure 5-1) is

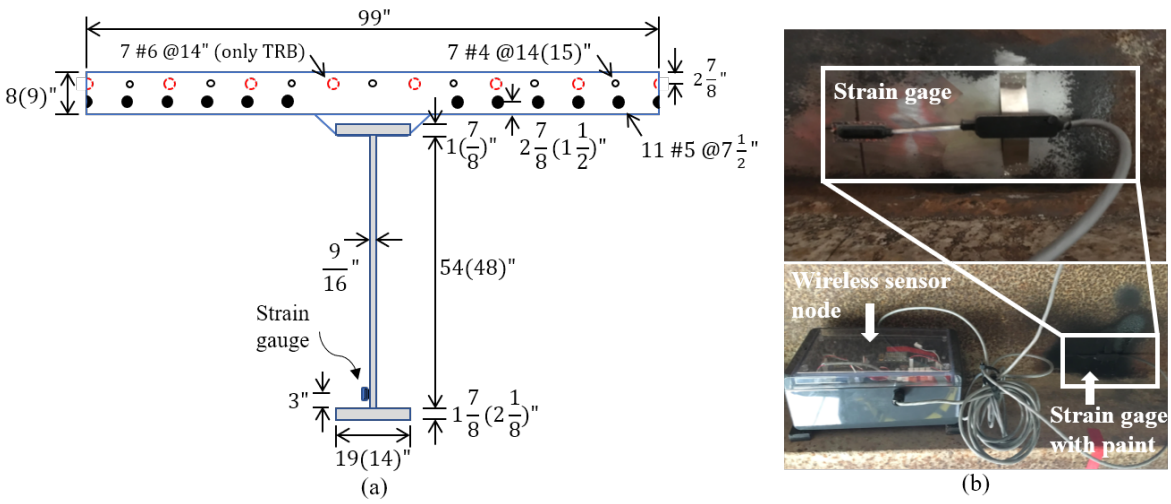

Figure 5-3: (a) Location of the strain gauge on the rated girder cross section with key dimensions notated for the Telegraph Road Bridge and the Newburg Road Bridge (dimensions for the Newburg Road Bridge are shown in parentheses if not identical with the Telegraph Road Bridge dimensions); (b) a typical strain gauge and *Narada* wireless sensor installed on a steel girder web.

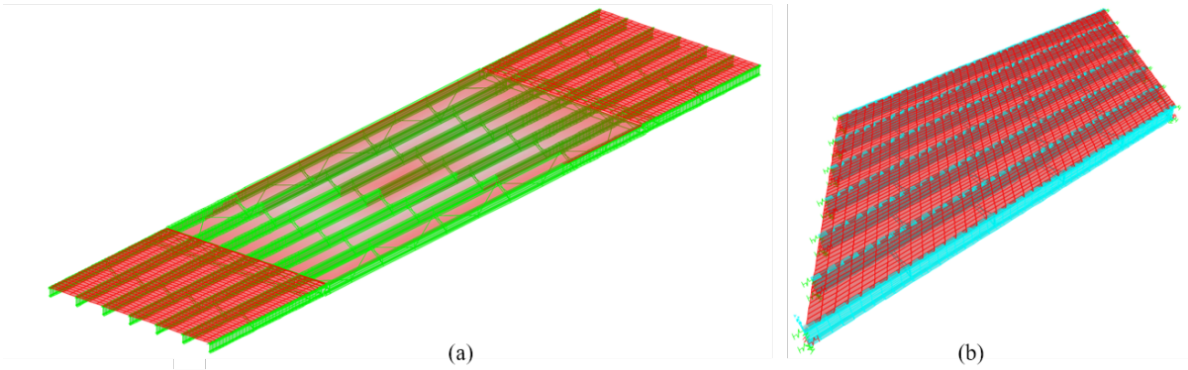

Figure 5-4: Finite element models of the (a) Telegraph Road Bridge and (b) Newburg Road Bridge.

installed 7 miles (11.27 km) north of the NRB near Romulus, Michigan. It is a type II quartz station that constantly measures vehicle gross weight, speed, number of axles, axle spacing, axle weight and vehicle class. According to the standard specification for highway WIM systems, the type II station has ±30%, ±20%, ±15%, ±1 mph (2km/h), ±0.5 ft (0.15m) tolerance within a 95% confidence on axle load, axle group load, gross vehicle weight, speed and axle spacing, respectively [255]. The station along I-275 is installed within two of the three lanes (i.e., slow and middle lanes).

The installation of the CPS architecture along I-275 (including the SHM systems on TRB and

Figure 5-5: Examples of truck events that are removed from the original integrated dataset: (a) truck events that contain multiple trucks on the bridges at the same time; (b) truck events where trucks change lanes on the bridge.

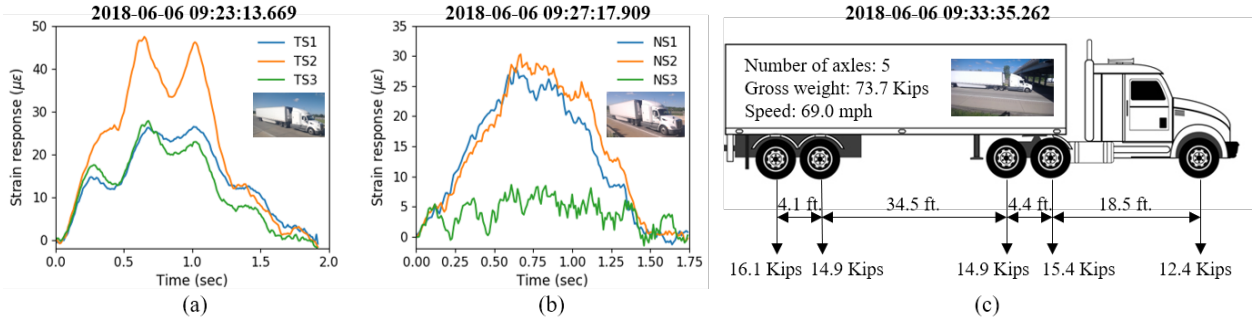

Figure 5-6: A sample of integrated data set including bridge response data, truck images and weigh-in-motion data collected by the corridor-based cyber-physical system at (a) Telegraph Road Bridge, (b) Newburg Road Bridge and (c) weigh-in-motion station.

NRB, four traffic cameras, WIM station and cloud-based database system) was completed in July 2017. Since that time, a large database of corridor data has been collected for each truck event that triggered the CPS data collection. The database consists of measured strain responses of the TRB and NRB bridges, weight data from the WIM station, and an image of the confirmed re-identifies truck at Cam-1 through Cam-4. In this study, the data collected by the CPS from July 2017 to April 2019 is utilized to demonstrate the proposed data-driven load rating approach. For the purpose of load rating, only the data corresponding to events where a single truck travels on each bridge are considered in the analysis. In other words, cases where multiple trucks travelling in parallel or in series on the bridge (as shown in Figure 5-5(a)) are removed from consideration because they introduce high levels of uncertainty (e.g., it is difficult to estimate distances between trucks) and unnecessary complicate the estimation of load rating parameters (e.g., unit influence

Telegraph Road Bridge			
Slow Lane	Middle Lane	Fast Lane	Total
1,085	13,206	964	15,255
Newburg Road Bridge			
Slow Lane	Middle Lane	Fast Lane	Total
17,727	5,619	27	23,373

Table 5-1: Distribution of integrated data for the Telegraph Road Bridge & Newburg Road Bridge.

lines). Furthermore, cases where trucks are actively changing lanes (as shown in Figure 5-5(b)) are also excluded. During some of the truck events, there are small vehicles (e.g., cars) present on the bridges but because their weights are comparatively very small, these cases are not pruned from the data set used in this load ratings.

Over the 22 months the CPS architecture has been in use along I-275, a total of 15,283 and 23,421 truck events have been observed on the TRB and NRB, respectively, each matched with a WIM station measurement of the truck gross weight, axle counts, axle distances, and axle weights. An example of an instance of the integrated data set from June 6, 2018 is shown in Figure 5-6 including mid-span flexural strain at the lower web of each girder on TRB (denoted as TS1, TS2, TS3) and NRB (denoted as NS1, NS2, and NS3), WIMS station measurement (Figure 5-6(c)), and pictures of the truck at each location. It should be noted that the number of trucks observed for each bridge are not expected to be identical due to the presence of a highway exit between the TRB and NRB where trucks exit and enter northbound I-275. Furthermore, the distribution of the lanes used by trucks crossing the bridges are summarized in Table 5-1. Trucks tend to take the slow highway lane as much as possible; in the case of TRB, the "slow" lane is a merge lane making the middle lane the one commonly taken by trucks already on the corridor. The integrated dataset of bridge response data and WIMS data will be employed to rate the instrumented girders on both bridges.

5.3 Methodology: Data-driven Load Rating Framework

5.3.1 Load and Resistance Factor Rating

Three different analytical methods are presented in the MBE: Load and Resistance Factor Rating (LRFR), Allowable Stress Rating (ASR) and Load Factor Rating (LFR) methods [35]. ASR method evaluates the rating factor using allowable stress as the rated member capacity and unfactored (actual) loads. The LFR method uses the strength of rated components for their capacity and applies factors on dead and live loads established over time by engineering judgement. Finally, LRFR is a broader rating method offering a range of limit states (i.e., strength, service, fatigue) to evaluate and explicitly considers bridge deterioration and usage; importantly, it also adopts load and resistance factors consistent with the reliability index, β, of components established in Load and Resistance Factor Design (LRFD). A recent study indicates that the LRFR method is becoming the most popular bridge load rating method in the United States [233]. As a result, it will be used herein as the baseline analytical method to which the proposed data-driven load rating approach will be compared. The LRFR method specifies three levels of evaluation (i.e., design, legal and permit load ratings) with the difference between them primarily in the type of live load scenarios applied. Design load ratings (where the HL-93 notional vehicle load is used) are performed for all bridges with the rating factor reported to the National Bridge Inventory (NBI) while legal load ratings are performed for bridges (where local legal-weight trucks are used) when the design load rating factor is less than 1. The permit load rating is performed to assess the safety of the bridge for over-weight trucks may cross a bridge. This paper only showcases the proposed method by performing a design load rating for the two bridges (TRB and NRB) but the other two rating levels (legal and permit) can be easily performed following the same framework as that proposed for design load rating.

In the LRFR method, the general load rating formula at the component level under a single force effect (i.e., flexure) can be expressed as follows [35]:

$$RF = \frac{C - (\gamma_{DC})(DC) - (\gamma_{DW})(DW) \pm (\gamma_P)(P)}{(\gamma_{LL})(LL + IM)} \tag{5.1}$$

where RF is the rating factor of a structural component (with $RF > 1$ indicating a bridge with a safe margin between capacity and demand), C is its capacity given the member's current structural condition, DC is the dead load effect due to structural components and attachments, DW is the dead load effects due to wearing surface and utilities, P is the permanent load effects other than those from the dead loads, LL is the live load effects, and IM accounts for the additional live load effect based on the dynamic response of the bridge due to vehicle-bridges interaction (and thus associated with DLA). All of the γ-values are Load and Resistance Factor Design (LRFD) load factors for scaling the corresponding load effects [192]. In this study, all capacity and load effects are presented with respect to strain responses presented in microstrain (i.e., $\mu\epsilon$).

The capacity of the component can be calculated as follows [35]:

$$C = \phi_c \phi_s \phi R_n \tag{5.2}$$

where R_n is the nominal member resistance with ϕ_c, ϕ_s and ϕ representing the condition, system and resistance factors, respectively. The condition factor allows the capacity to reflect the reduction in the nominal resistance due to structural deterioration and the system factor considers if a bridge is redundant or non-redundant; both are optional. In this study, the nominal resistance, R_n, of the girders is calculated based on yield strain at the sensing location in the girder cross section Figure 5-3 under flexural behavior. The values of DC, DW and P are determined as per the bridge design drawings and the calibrated finite element models discussed in Section 5.2. Both inventory- and operating-level ratings under the Strength I limit state (basic load combination relating to the normal vehicular use of the bridge without wind effects) are investigated for the target components to represent the upper (β=3.5) and lower (β=2.5) bounds of safe load capacity, respectively [35, 192, 256]. The values of all γ or ϕ factors that are adopted according to the MBE are listed in Table 5-2 along with their considerations.

γ_{DC}	γ_{DW}	γ_P	γ_{LL} (operating)
1.25	1.50	1.00	1.35
γ_{LL} (inventory)	ϕ_s	ϕ_c	ϕ
1.75	1.00	0.95 (fair condition)	1.00 (for flexure, interior girder)

Table 5-2: Values of selected $\gamma-$ or $\phi-$ factors for load rating.

The load rating methods prescribed by the MBE apply notional vehicle loads on bridges with the live load effects approximately estimated using girder line analyses. These live load effect estimates are not reflective of the true behavior of the bridge and therefore lead to conservative load ratings. Long-term monitoring data that capture the behavior of the bridge system can provide more realistic estimates of the live load effect variables in the denominator of the load rating formula (Equation 5.1). One strategy could be to select maximum live load effect as measured over a long period of observation to estimate the $LL + IM$ parameter of the load rating formula. However, this approach would lose consistency with the reliability-based rating framework prescribed by the LRFR methodology. The approach would also be vulnerable to not observing some of the more extreme load cases during the period of data collect. Hence, a more rational approach is necessary to ensure live load effect parameters extracted from long-term bridge monitoring data remain consistent with the reliability basis of the LRFR framework. This study proposes such a framework for converting bridge response data from trucks of known axle configurations and weights (as measured by the WIM station) to estimate live load effect parameters reflective of the true, systematic behavior of bridges leading to more accurate and less conservative load ratings.

5.3.2 Data-driven Load Rating Method

The main contribution of the proposed data-driven load rating method is in how it efficiently calculates realistic live load effects corresponding to standard truck loads while explicitly capturing systematic bridge behavior and the actual condition of bridge components. As opposed to using the measured live load effect directly as an input for the load rating formula, the methodology utilizes measured live load effect to extract UILs and DLA which correspond to the calculation of *LL* and

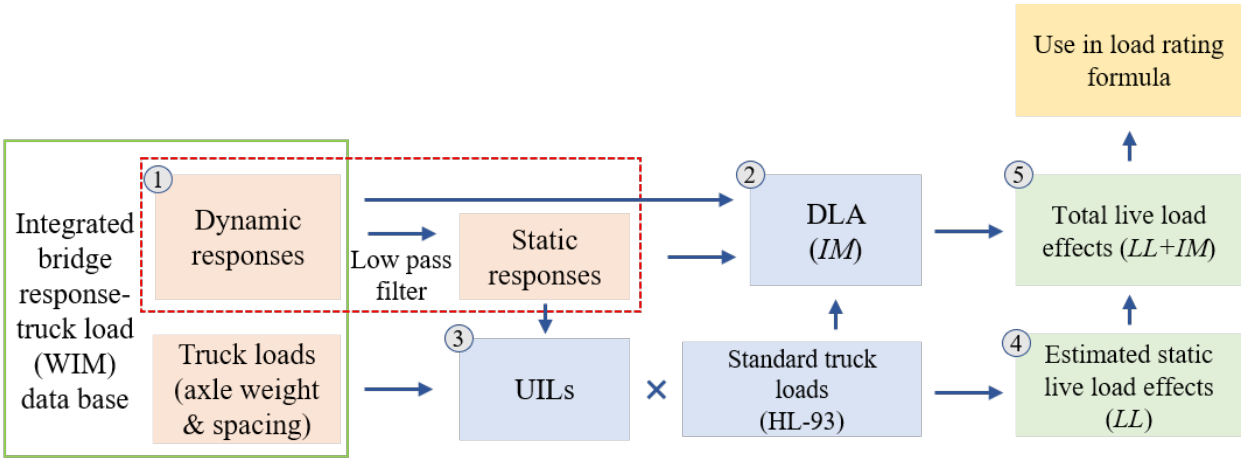

Figure 5-7: Workflow of the proposed data-driven load rating method for estimating realistic live load effects for a bridge component subject to standard truck loads.

IM in Equation 5.1, respectively.

The proposed data-driven load rating framework is presented in Figure 5-7. The basis of the proposed methodology is the availability of truck weight data as measured by a WIM station linked by the CPS architecture to the bridge responses measured by the bridge SHM systems (Figure 5-6). Given this integrated database of bridge response-truck weigh data, the first step is to process the dynamic (raw) bridge responses using a low-pass filter to obtain the static bridge response to the truck load. Subtracting the static response from the raw response, the peak absolute difference is used in the second step to estimate the DLA (which is the peak absolute difference divided by the peak absolute static response). Grouping the low-pass filtered bridge responses (i.e., static bridge responses) with corresponding truck load data (i.e., truck axle spacing and weights) measured by the WIM station, the third step extracts realistic UILs from the response measurements. In the fourth step, each UIL vector extracted from the response data is then used to estimate the static live load effects at a certain sensor location of the bridge to a given truck load model (e.g., HL-93 for design load rating or local legal-weight loads for legal load rating) by multiplying the UIL vector with the load model axle weight and superimposing them on the bridge span to yield the static live load effect, *LL*, in Equation 5.1. As the fifth and final step, the total load effect is calculated as:

$$LL + IM = LL * (1 + DLA) \tag{5.3}$$

which is ultimately used for computing a rating factor following Equation 5.1 [35].

The HL-93 design load is used with the extracted UIL to perform design load ratings consistent with LRFR. All combinations of different load scenarios (e.g., single-lane and multiple-lane loads) are explicitly considered to generate the maximum live load effect [192]. To perform legal and posted load ratings, vehicle load models associated with these ratings types can be used in the same manner as that shown for the design rating HL-93 load. The detailed processes for DLA and UIL extraction along with the extraction of these parameters for the TRB and NRB will be presented in section 5.4 and 5.5, respectively.

5.4 Dynamic Load Allowance

5.4.1 Dynamic Load Allowance Extraction

DLA reflects the response amplification of the bridge live load effect due to vehicle-bridge interactions as compared to statically applied truck loads. The additional dynamic effect may come from two sources: 1) wheel hammering loads induced by poorly maintained bridge deck joints or major surface imperfections (e.g., potholes); 2) the dynamic interactions associated with the behavior of a sprung mass vehicle coupling with bridge dynamics [192]. The DLA recommended in the LRFD design code for girders is 0.33 under the Strength I limit state [192]. The value is empirically determined based on field tests, which represents an upper bound of the ratio of the dynamic component to the static response to vehicular loads for most highway bridges [192]. The DLA of a bridge component is strongly influenced by two categories of factors: one are the bridge properties (e.g., bridge type, geometry, fundamental frequencies, road roughness) and the other are the vehicle load characteristics (e.g., vehicle speed, weight and suspension system) [257, 258, 259, 260]. Due to these factors controlled the DLA, a bridge will experience variation in its DLA [261].

In this study, a DLA value is extracted for each captured truck event based on the use of low-pass filtering of the measured bridge strain data [258, 262]. The final DLA value selected for the load rating purpose is determined according to the vehicle gross weight of the specific design truck load. The low-pass filter is required to have a cut-off frequency lower than the bridge's first natural

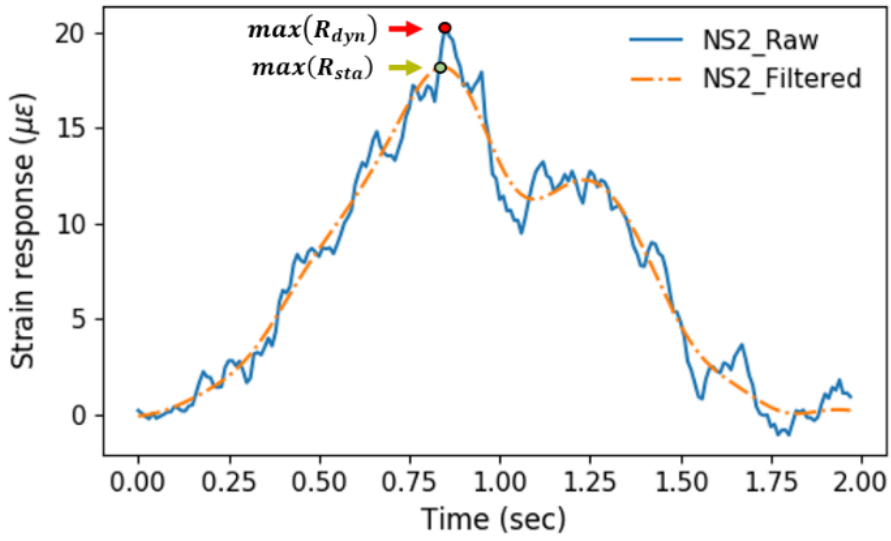

Figure 5-8: Illustration of dynamic load allowance (DLA) extraction from measured strain responses.

frequency and a passband of v/L Hz, where v is the speed of passing vehicles and L is the bridge span length [258, 262]. The TRB and NRB exhibit their natural frequencies of first mode at 2.5 Hz and 4.5 Hz, respectively, according to modal analysis performed using acceleration responses in previous studies [224, 213]. Assuming a normal vehicle speed ranging from 55 mph to 80 mph, the vehicle passing frequency can range from 0.36 Hz to 0.52 Hz for the TRB and from 0.77 Hz to 1.12 Hz for the NRB. It is also recommended that the cutoff frequency of the filter should be out of the range between 2 Hz and 5 Hz so that the vehicle body bounce effect is avoided [262]. Consequently, a 10^{th} order Butterworth low-pass filter with a cut-off frequency of 2 Hz is used to filter out high-frequency dynamic components from measured strain responses to derive the static bridge responses [262]. Figure 5-8 highlights the process using measured raw strain data from the NRB (sensor NS2) with the low-pass (static) and raw measure strain response shown. The DLA is then calculated for a given truck event as follows [257, 258]:

$$DLA = \frac{max(R_{dyn}) - max(R_{sta})}{max(R_{sta})} \tag{5.4}$$

where R_{dyn} is the dynamic response and R_{sta} is the static response (i.e., low-pass filtered response).

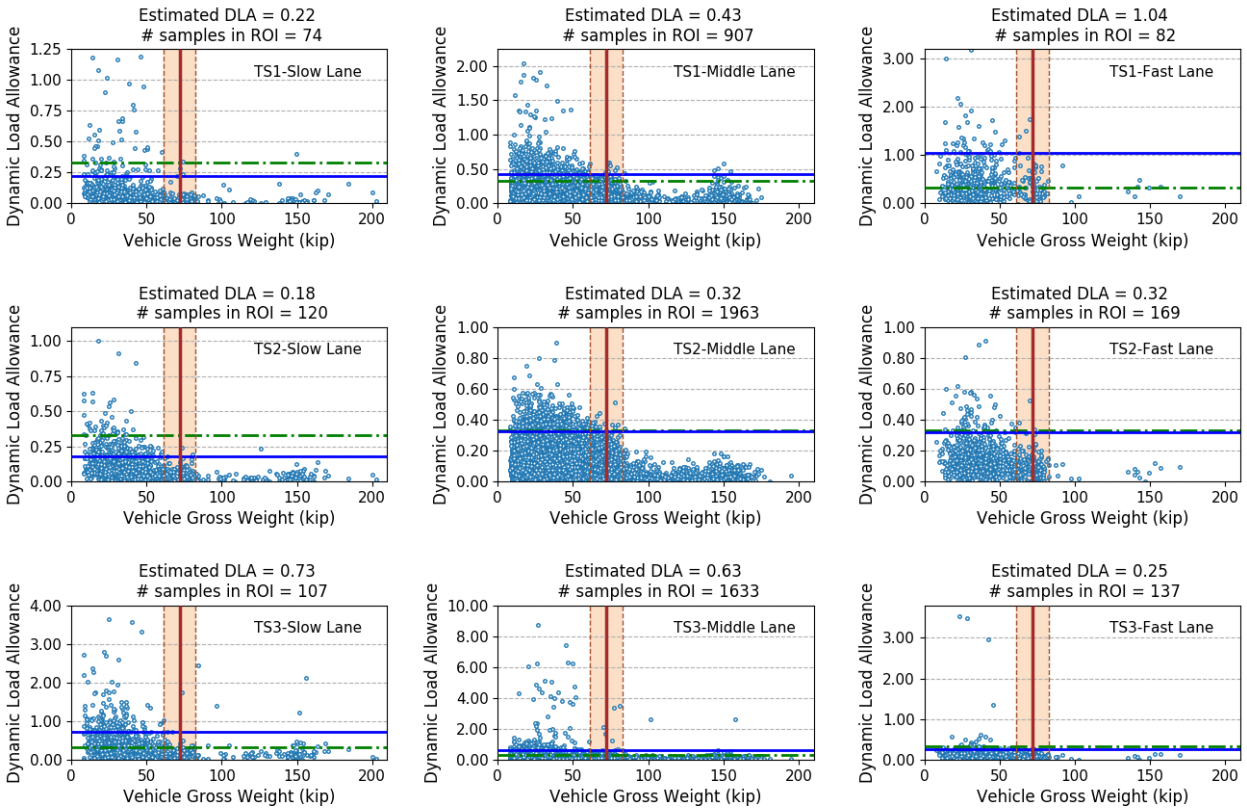

Figure 5-9: Dynamic load allowance (DLA) values extracted from the Telegraph Road Bridge girder strain data with truck in different lanes (slow, middle or fast lane) for the three sensing locations (TS1, TS2, TS3). (Note: solid vertical brown line corresponds to 72-kip HS-20 load, shaded brown region is the region of interest (ROI) for the HS-20 load considering measurement errors associated with weigh-in-motion station, green horizontal dash line corresponds to the AASHTO DLA (0.33) and the green solid line is the selected DLA value ($\mu + 3\sigma$) for samples in the ROI.)

5.4.2 Results and Discussion

Each extracted DLA value calculated as per Equation 5.4 has its corresponding truck gross weight measured by the WIM station. The scatter plots of extracted DLA values versus vehicle gross weight under different loading scenarios (i.e., truck lane and measured girder flexure) are shown in Figure 5-9 and Figure 5-10 for the TRB and NRB systems, respectively. Each subplot corresponds to a girder sensor location (i.e., TS1, TS2, TS3, NS1, NS2 or NS3) and assigned truck lane (i.e., slow, middle or fast lane). Only a few samples correspond to trucks using the fast lane on each bridge as previously observed in the data set collected. It can be observed in each subplot that the extracted DLA values vary widely with generally decreasing variation as vehicle weights get

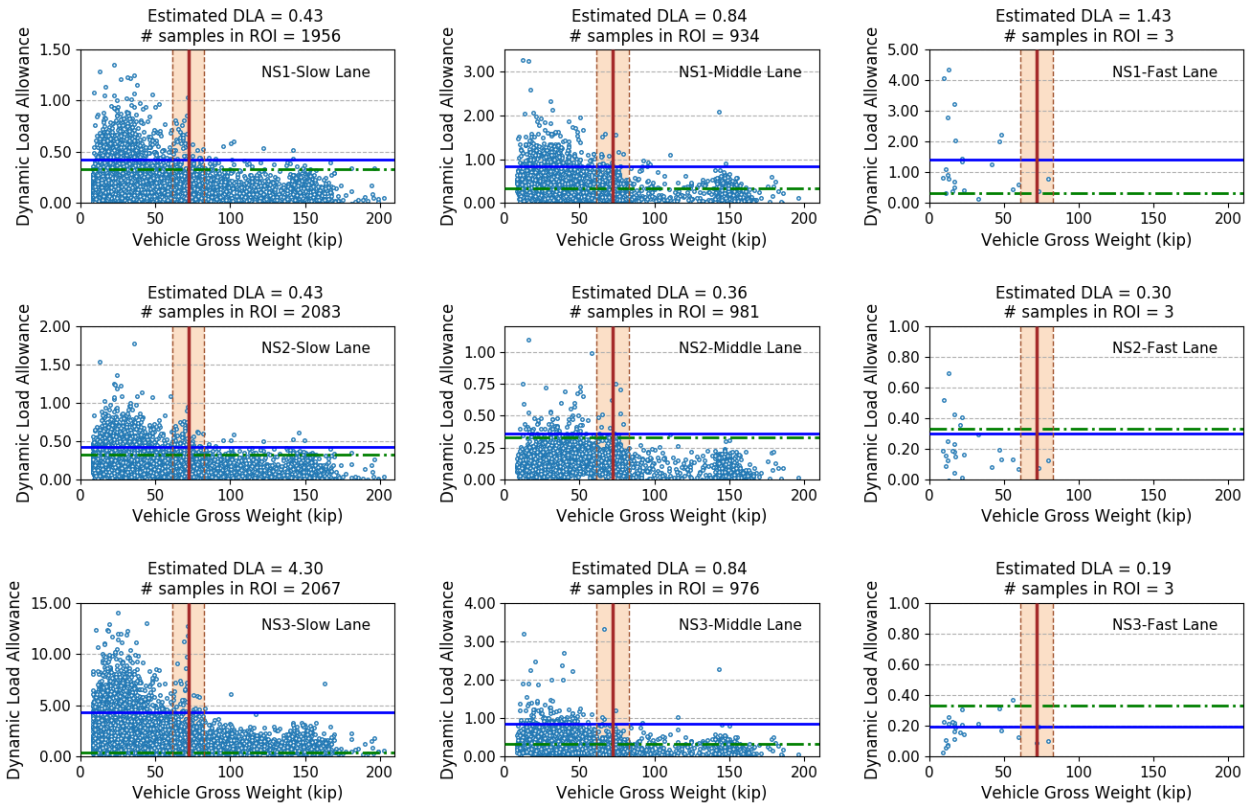

Figure 5-10: Dynamic load allowance (DLA) values extracted from the Newburg Road Bridge girder strain data with truck in different lanes (slow, middle or fast lane) for the three sensing locations (NS1, NS2, NS3). (Note: solid vertical brown line corresponds to 72-kip HS-20 load, shaded brown region is the region of interest (ROI) for the HS-20 load considering measurement errors associated with weigh-in-motion station, green horizontal dash line corresponds to the AASHTO DLA (0.33) and the green solid line is the selected DLA value ($\mu + 3\sigma$) for samples in the ROI.)

higher. This is expected as lower weight vehicles induce a smaller static strain response, leading to the DLA calculation being strongly influenced by external factors such as signal-to-noise ratios in the measurement and coexistence of passenger vehicles on the bridges. This outcome is consistent with observations reported by other researchers in that estimated DLA values decrease as vehicle gross weights increase [262, 263]. Considering the trend observed in the extracted DLA values, this study focuses on DLA values that correspond to truck loads consistent with LRFD and LRFR. For the TRB and the NRB, the HL-93 load pattern corresponds to an HS-20 truck with a uniform design lane load [35]. In each subplot of Figure 5-9 and Figure 5-10, the gross weight of the HS-20 design truck, namely 72 kips, is notated using a vertical solid brown line. A region of interest

	Slow lane	Middle lane	Fast lane
TS1 (girder 6)	0.22	0.43	1.04
TS2 (girder 4)	0.18	0.32	0.32
TS3 (girder 2)	0.73	0.63	0.25

Table 5-3: Extracted dynamic load allowance (DLA) value for the Telegraph Road Bridge.

	Slow lane	Middle lane	Fast lane
NS1 (girder 6)	0.43	0.84	1.43
NS2 (girder 4)	0.43	0.36	0.30
NS3 (girder 2)	4.30	0.84	0.19

Table 5-4: Extracted dynamic load allowance (DLA) value for the Newburg Road Bridge.

(ROI) is established around the HS-20 truck gross weight to account for the maximum 15% error in measured vehicle gross weight commonly associated with Type II WIM stations (such as that used in this study). All DLA samples within the ROI are considered for the extraction of a single DLA values for the HS-20 design truck load. The final DLA (shown as the solid blue horizontal line in Figure 5-9 and Figure 5-10) is taken as $\mu + 3\sigma$, where μ and σ are the mean and standard deviation of all the considered samples in the ROI, respectively. This value represents a 99.7% confidence interval as per a normal distribution and is selected to screen out unrealistically extreme values which might be caused by factors such as sensor noises or faulty WIM measurements. The DLA value recommended by the MBE, namely 0.33, is presented as the green dashed line in each subplot for reference. All extracted DLA values for the selected sensor locations under different loading scenarios at the two bridges are summarized in Table 5-3 and Table 5-4.

The results tabulated in Table 5-3 and Table 5-4 reveal that the lane assignment of the truck relative to the girder line has a big impact on the extracted DLA value. Specifically, the DLA value of a girder tends to be smaller (sometimes less than 0.33) when the vehicular load is in the lane closest to the girder with that girder taking the largest distribution of the load. This result is attributed to the larger strain responses for the girder lines closest to the vehicular load resulting in improved signal-to-noise ratios. The extracted DLA values also reveal the DLA recommended

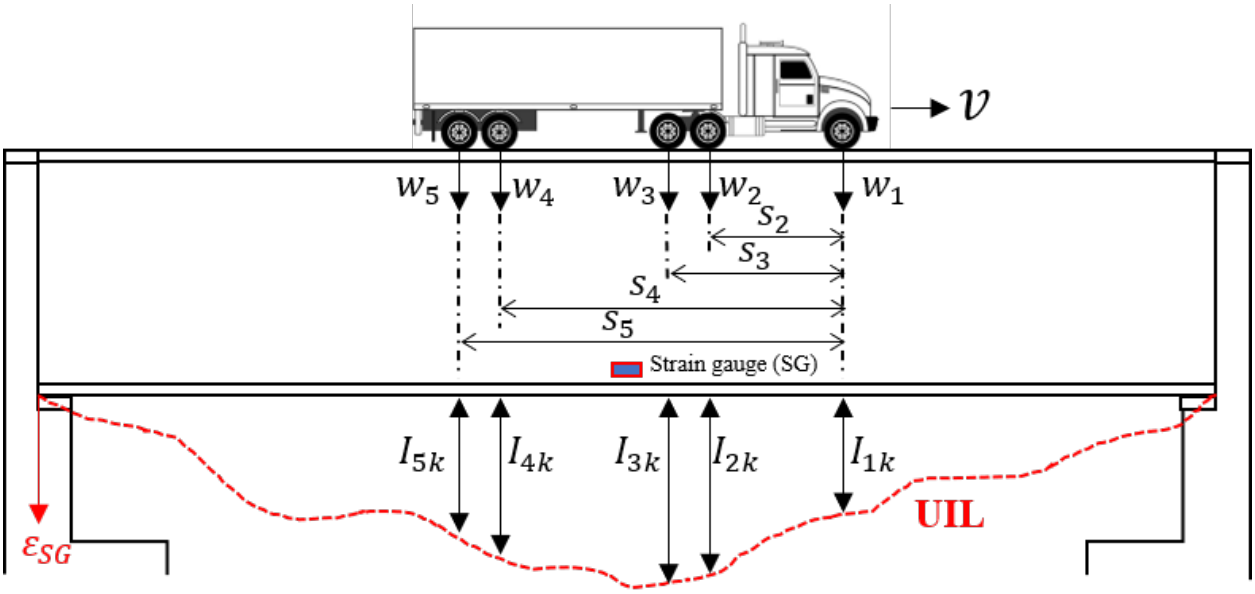

Figure 5-11: Illustration of the UIL extraction process under the assumption of the linear superposition principle.

by the MBE does not reflect realistic bridge conditions observed in the response data collected. . Taking TRB as an example, the MBE value of 0.33 overestimates the DLA when vehicular loads are in close proximity to the instrumented girder line (e.g., TS1-slow lane, TS2-middle lane, and TS3-fast lane) as shown in Figure 5-9 and Table 5-3. For cases where the truck load is not on the lane directly above the instrumented girder line, the estimated DLA can be larger than the MBE recommended value (e.g., TS3-slow lane); however, such a value usually corresponds to a small static bridge response as the load distributed to the girder far away is small and thus less significant [264]. On the other hand, the extracted DLA can be greater than the MBE recommended value such as that observed in a bridge like NRB as shown in Figure 5-10 and Table 5-4, even when the vehicular load is close to the instrumented girder line (e.g., NS1-slow lane).

5.5 Unit Influence Line

5.5.1 Unit Influence Line Extraction

A UIL of a bridge represents the load effect at a specific measurement location when a unit axle load of 1 kip traverses the bridge in a specific lane. In this study, the load effect mapped by the

UIL will be the girder strain (in $\mu\epsilon$) at the locations of the strain gauges While theoretically the UIL is a continuous function, here it is discretized along the bridge length and expressed as a finite vector for use in numerical computations. Following an assumption of the bridge being a linear system, the superposition principle can be applied to model truck loads as multiple unit axle loads. Assuming the truck has a constant velocity of v, the sampling frequency of the sensor is f, and the bridge length is L, the UIL is discretized into a total of $N_L = fL \,/\, v$ elements. The discretized length of the bridge is indexed by k. Hence, for any sensor measurement indexed at k, the following fundamental input-output relationship holds (as shown in Figure 5-11):

$$\epsilon_k = \sum_{i}^{N_A} \mathbb{1}_{ik} w_i I_{ik} \tag{5.5}$$

where ϵ_k is the strain response corresponding to index k, w_i is the i^{th} axle weight of the truck, I_{ik} is the UIL entry corresponding to the position of the i^{th} axle when the first axle is at index k and N_A is the total number of axles for the truck load. Also, $\mathbb{1}_{ik}$ is an indicator function that is equal to 1 when the i^{th} axle is on the bridge and 0 otherwise. The UIL entry I_{ik} can be expressed as [265, 266]:

$$I_{ik} = I_{k-c_i} \tag{5.6}$$

$$c_i = \frac{s_i f}{v} \tag{5.7}$$

where c_i the number of discretized indices in the UIL corresponding to s_i which is the distance from the first axle to the i^{th} axle (with $s_1 = 0$). Considering the entire process of a multi-axle truck load entering and exiting the bridge along a certain lane, an error function can be defined for UIL estimation [267] as follows:

$$e = \sum_{k=1}^{N_L} (\epsilon_k - \epsilon_k^m)^2 \tag{5.8}$$

where ϵ_k^m is the k^{th} indexed measured response and ϵ_k is the k^{th} indexed predicted response based on the UIL. Using the algorithm proposed by [265], the optimal UIL vector is found by minimizing the error in Equation 5.8 which is obtained by setting the partial derivative of the error with respect to the UIL ordinates to zero:

$$\frac{\partial e}{\partial I_k} = 0 \tag{5.9}$$

when $c_N \leq k \leq (N_L - c_N)$ (which corresponds to the times when all axles are on the bridge). The resultant set of $N_L - 2c_N$ equations can be posed as a matrix-vector multiplication [265]:

$$W \times I = R \tag{5.10}$$

where $I \in \mathbb{R}^{(N_L-2c_N)\times 1}$ is the UIL vector to be solved for, $W \in \mathbb{R}^{(N_L-2c_N)\times(N_L-2c_N)}$ is a sparse symmetric positive definite matrix with the following property:

$$W_{p,q} = \begin{cases} \sum_i^N w_i^2, if p = q \\ \sum_{i,j} w_i w_j, if |p-q| \in \{c_i - c_j\} \\ 0, otherwise \end{cases} \tag{5.11}$$

and $R \in \mathbb{R}^{(N_L-2c_N)\times 1}$ is a vector with

$$R_i = \sum_{j=1}^{N} w_j \epsilon_{i+c_j}^m \tag{5.12}$$

Using the set of measured bridge strain data, ϵ_k^m, and truck load configuration data (particularly axle weights, w_i, and spacings, s_i), a UIL can be extracted by inversely solving Equation 5.10 to yield I_k [265, 266].

In this study, the static (low-pass filtered) strain responses measured by the bridge SHM systems are used as the input strain for the UIL extraction as shown in Figure 5-7. For each observation of measured truck weight and bridge response in the database, the truck speed, v, is assumed constant throughout the loading process. While truck speed is measured at the WIM station, it is not

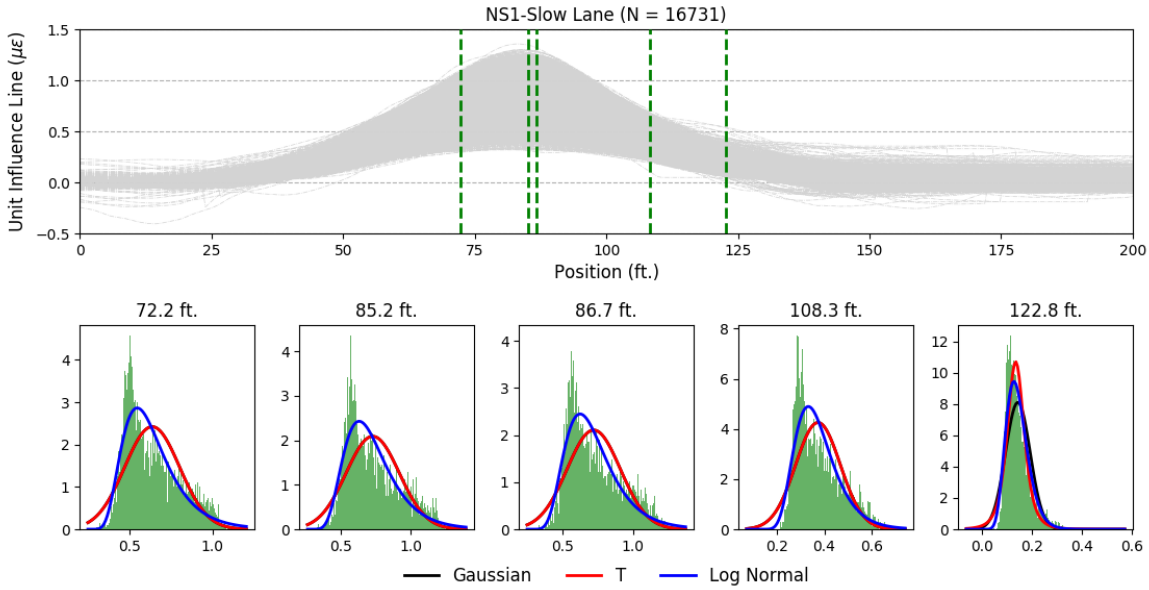

Figure 5-12: All unit influence lines extracted from strain gauge NS-1 when trucks travel along the middle lane of the Newburg Road Bridge and five examples of fitting unit influence line ordinates into three common distributions (e.g., Gaussian, T, and log normal distributions).

measured at each bridge. Hence, a range of truck speeds (±10%) centered at the speed measured at the WIM station is searched for to find the minimum error in Equation 5.8. Considering that the strain gauge sensor is programmed to sample data with a frequency of 100 Hz and the posted speed limit of trucks on I-275 is 65 mph, the UILs is discretized with a resolution of 11.4 inches (28.9 cm). While the UIL vector should be discretized to $N_L = 235$ and 111 for the TRB and NRB, respectively, the actual resultant vectors are longer. This is due to the fact that it is impossible to determine the exact instant in time when trucks enter and exit the bridges, so a larger time-history segment of the measured bridges strain responses are used in Equation 5.10. Consequently, small valued entries usually appear at the head and tail of the extracted UILs; these near-zero entries will not affect the maximum value of the final predicted response for bridge load rating [265].

5.5.2 Unit Influence Line for Load Rating

Given the large database of bridge-truck data sets available for this study (Table 5-1), an extensive set of UILs can be extracted for each sensing location and truck lane assignment. With UIL theo-

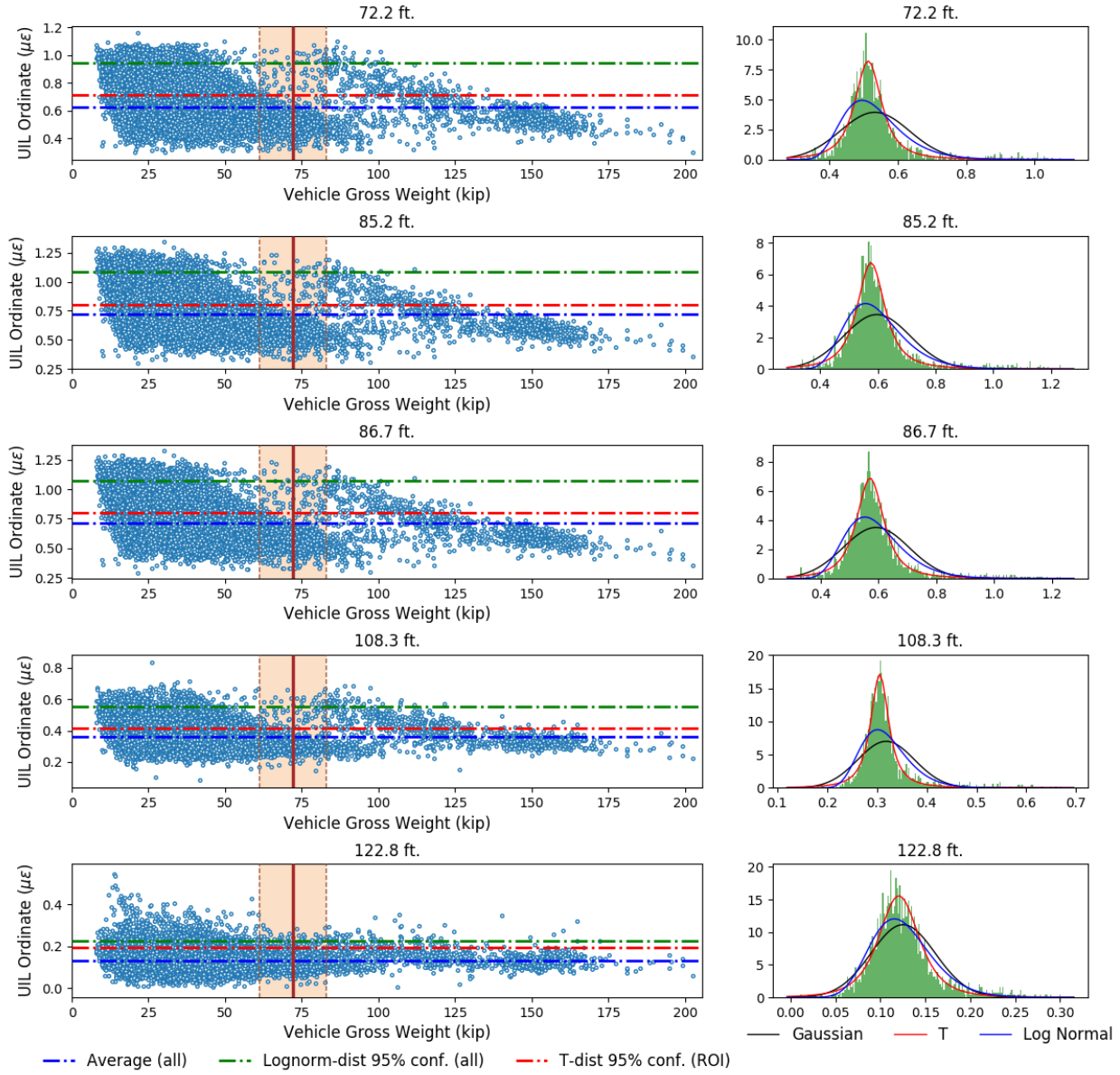

Figure 5-13: Correlation between UIL ordinates (5 random slices notated in Figure 5-12) and corresponding truck load weight (left side). (Note: the normalized histogram of ordinates within the ROIs are plotted on the right side with fitted distributions overlaid; the number of data samples within the ROIs is 1,479 for each of 5 cases.)

retically constant for a given strain sensor and lane assignment, the UILs extracted can be treated statistically to result in a final UIL. To illustrate, the data of strain gauge NS1 (NRB) with truck assigned to the slow lane will be utilized. Following the procedure previously presented, the UILs extracted from each sample of the bridge-truck data set are aligned as shown in Figure 5-12. It

can be observed that the extracted influence lines have similar shapes but vary in amplitude. This variation can be attributed to a number of likely factors such as variations in truck speed, variation in truck location within the lane, and measurement (WIM station and strain) noise. The UIL is also longer then the bridge itself, again attributed to the approach to UIL extraction; ultimately, the UIL will be reduced to the appropriate size based on the bridge length. Along the UIL length are histograms corresponding to the extracted UIL ordinates at five locations (notated as vertical dash lines in Figure 5-12). While different types of distributions have been attempted for fitting the UIL ordinates, three common distributions (e.g., Gaussian, log normal and T-distribution) are plotted. It can be visually noted that log normal distribution fits the ordinates best at each UIL location.

The UIL ordinates at the five locations can be further analyzed based on the vehicle gross weight of the truck event corresponding to each UIL as shown in Figure 5-13. The results of Figure 5-13 reveal that the amplitude of the extracted UILs are related to the gross weight of the trucks. Lighter truck loads are more likely to generate larger UILs when compared to heavier loads. It is suspected that this is due to two reasons: 1) extracting UILs is an inverse problem where solutions would be sensitive to small truck loads; 2) the co-presence of other small vehicles (e.g., passenger cars) during a truck would have a greater impact on the inversion problem for lighter truck loads leading to larger UILs. Similar to the approach of extracting final DLA values, a ROI is established around the HS-20 design truck load (i.e., the vertical shaded area in Figure 5-13 centered at 72 kips) for each slice of UIL ordinates. The T-distribution is deemed the best distribution model for describing the 1,497 data points within the ROIs, as shown in Figure 5-13. This is consistent with the observation made in [268] based on the UILs computed from field tests conducted when using several similar test trucks.

Taking the average of all extracted UILs is a common practice for the purpose of weigh-in-motion using bridge responses [266]. However, the average UIL might not be able to reflect the maximum vehicular live load for load ratings. As a result, three types of UIL are calculated from all of the extracted UILs can be used in the bridge load ratings herein. The three UILs are: 1) the average amplitude of all extracted ordinates (blue dash line in Figure 5-13), 2) the amplitude

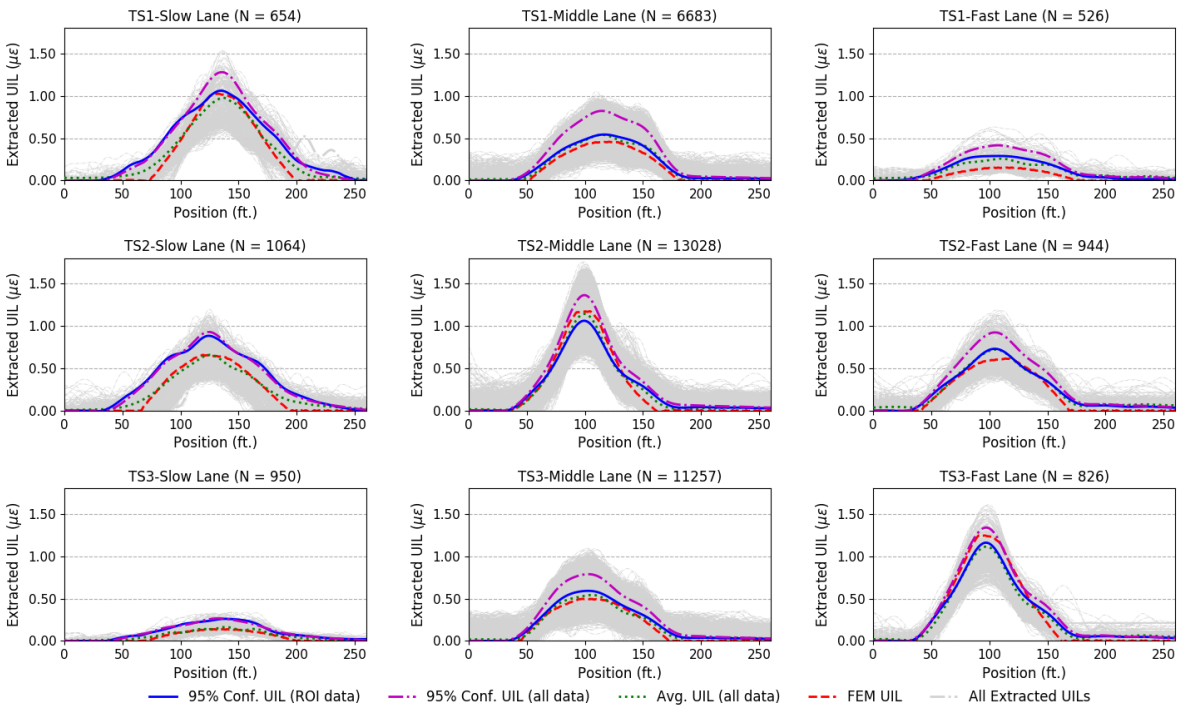

Figure 5-14: Unit influence lines (UILs) extracted for the Telegraph Road Bridge load rating including three sensing locations with three different loading lanes. (Note: in each subplot, the 95% confidence UIL of the UILs within the ROIs, the 95% confidence UIL of all extracted UILs, the average UIL of all extracted UILs, the UIL extracted from the finite element model is overlaid with all extracted UILs; the amount of data used for each case is notated inside parentheses.)

corresponding to the 95% confidence of the fitted lognormal distributions of all extracted ordinates (green dash line in Figure 5-13), or 3) the amplitude corresponding to the 95% confidence of the fitted T-distribution of ordinates within the HS-20 design truck load ROIs (red dash line in Figure 5-13). As expected, the amplitude of the 95% confidence using the log-normal distribution applied to all of the UIL ordinate data is the largest among all three.

5.5.3 Results and Discussion

The entire set of extracted UILs and three types of calculated UIL for load rating are plotted in Figure 5-14 and Figure 5-15 for the TRB and the NRB, respectively. Also plotted are the UILs obtained from the calibrated FE models with unit kip loads moving along the centerline of the lanes. It should be noted that the FE-based UILs should not be considered as ground truth since the FE models do not capture the true systemic bridge behaviors (and do not model vehicle-bridge

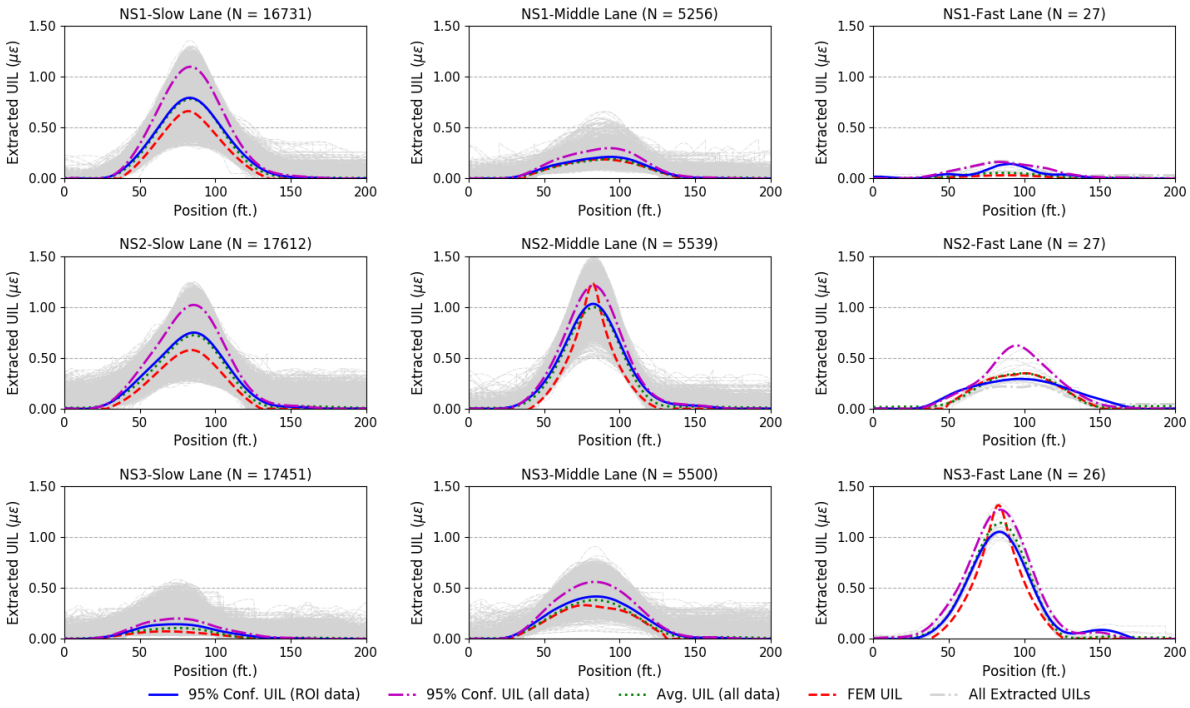

Figure 5-15: Unit influence lines (UILs) extracted for the Newburg Road Bridge load rating including three sensing locations with three different loading lanes. In each subplot, the 95% confidence UIL of the UILs within the ROIs, the 95% confidence UIL of all extracted UILs, the average UIL of all extracted UILs, the UIL extracted from the finite element model is overlaid with all extracted UILs. The amount of data used for each case is notated inside parentheses.

interactions) even when they are calibrated. Like the results of DLA extraction, there are fewer UILs for the case of trucks assigned to the fast lane. The number of UILs in each case is slightly less than the number of data sets reported in Table 5-1 if the sensor did not capture the entire process of the truck event (i.e., data acquisition ended before the truck exits the bridge).

5.6 Maximum Live Load Calculation

Given the DLA values and UILs extracted under different loading scenarios, the maximum live load effect (LL+IM) caused by the standard HL-93 design load can be calculated for all three girders following Equation 5.3. The LL component of the maximum live load effect are based on the three UILs for each sensor-lane combination with multi-presence factors utilized when placing the HL-93 design loads [35]. The DLA value is then used to assess the IM component. The

	TS1 (girder 6)	TS2 (girder 4)	TS3 (girder 2)
Data-driven method (average all)	228.58 $\mu\epsilon$	284.82 $\mu\epsilon$	232.67 $\mu\epsilon$
Data-driven method (95% conf. all)	333.17 $\mu\epsilon$	372.86 $\mu\epsilon$	306.63 $\mu\epsilon$
Data-driven method (95% conf. ROI)	256.79 $\mu\epsilon$	293.93 $\mu\epsilon$	253.54 $\mu\epsilon$
FEM-based method	202.88 $\mu\epsilon$	277.40 $\mu\epsilon$	243.11 $\mu\epsilon$
Conventional	271.56 $\mu\epsilon$	271.56 $\mu\epsilon$	271.56 $\mu\epsilon$

Table 5-5: Maximum live load effects computed using the proposed data-driven load rating method and the FEM-based method of the Telegraph Road Bridge girders.

	NS1 (girder 6)	NS2 (girder 4)	NS3 (girder 2)
Data-driven method (average all)	132.44 $\mu\epsilon$	216.16 $\mu\epsilon$	193.47 $\mu\epsilon$
Data-driven method (95% conf. all)	191.15 $\mu\epsilon$	296.26 $\mu\epsilon$	266.06 $\mu\epsilon$
Data-driven method (95% conf. ROI)	139.65 $\mu\epsilon$	211.88 $\mu\epsilon$	206.53 $\mu\epsilon$
FEM-based method	113.12 $\mu\epsilon$	194.11 $\mu\epsilon$	167.86 $\mu\epsilon$
Conventional	194.76 $\mu\epsilon$	194.76 $\mu\epsilon$	194.76 $\mu\epsilon$

Table 5-6: Maximum live load effects computed using the proposed data-driven load rating method and the FEM-based method of the Newburg Road Bridge girders.

results of the maximum live load effect are listed in Table 5-5 and Table 5-6 for the TRB and NRB, respectively. In addition, the maximum live load effect as predicted by the FE simulations in CSiBridge and conventional simplified analysis are included in the two tables. As is evident in both tables, the maximum live load effects for the data-driven method are mostly higher than those predicted from FE analyses. To perform load ratings in a manner consistent with the LRFR approach of the MBE, the maximum live load effect associated with the UIL corresponding to the 95% confidence level in the ROI will be used for the data-driven bridge load rating.

		NS1 (girder 6)	NS2 (girder 4)	NS3 (girder 2)
Inventory Level Rating Factor	Conventional	1.45	1.45	1.45
	FEM-based	3.25	1.84	2.21
	Data-driven	2.63	1.61	1.73
Operating Level Rating Factor	Conventional	1.88	1.88	1.88
	FEM-based	4.22	2.38	2.87
	Data-driven	3.31	2.08	2.24

Table 5-7: Rating factors of the Telegraph Road Bridge girders obtained using different methods.

		TS1 (girder 6)	TS2 (girder 4)	TS3 (girder 2)
Inventory Level Rating Factor	Conventional	1.17	1.17	1.17
	FEM-based	1.64	1.17	1.39
	Data-driven	1.29	1.10	1.33
Operating Level Rating Factor	Conventional	1.51	1.51	1.51
	FEM-based	2.12	1.55	1.80
	Data-driven	1.68	1.46	1.72

Table 5-8: Rating factors of the Newburg Road Bridge girders obtained using different methods.

5.7 Evaluation and Results

With the maximum live load effect and estimate of the dead load effects for each bridge, load ratings are conducted based on Equation 5.1. The selected γ or ϕ factors of Table 5-2 are also used. The resulting data-driven rating factors are compared with those obtained by the FE-based and the conventional approximate method in Table 5-7 and Table 5-8, respectively, for the TRB and the NRB. Both inventory and operating level ratings are performed for both bridges. The results show that the target girders of the two bridges pass the design load rating regardless of the rating methodology utilized as indicated by rating factors greater than 1. With the *RF* greater than 1 at the inventory level reliability, legal load ratings are not necessary for either bridge [35]. The rating factors obtained using the conventional method are identical for all three girders in each bridge as it is a common practice to distribute dead load evenly across all girders and the load distribution factors are the same for interior girders [35, 192, 269]. It can be observed that in most cases that rating factors calculated using the data-driven approach lie between the conventional and the

FE-based rating factors.

5.8 Summary and Conclusions

Load rating is a standard asset management approach used to assess the safety of highway bridges. The LRFR process specified by the MBE is the most popular load rating method in the United States offering load ratings consistent with the reliability levels associated with the LRFD design process. Approximate methods are commonly used for load rating of bridge girder lines but more recently refined analyses based on FE models have grown in popularity. While the FE-based approaches may offer a higher level of realism in modeling bridge behavior, it does not reflect the true systemic behavior of the bridge. In this work, a data-driven load rating approach that explicitly considers the true systematic behavior of a bridge is proposed. The approach is based on the availability of bridge response data due to a truck event along with measurement of the truck weight obtained from a WIM station along the corridor. The integration of bridge strain response data and truck weight data is only possible based on automated visual identification of trucks along a highway corridor using a CPS architecture. The data driven load rating method utilizes measured bridge strains to extract the dynamic load allowance (DLA) factor by subtracting the maximum measured bridge response from the maximum static response obtained by low-pass filtering the response signal. Similarly, the bridge response data and the measurement of the truck axle weights and spacing are used to extract UIL. With a large database of truck events on a bridge collected over a period of time, a statistical approach for estimating the DLA and UIL is proposed based on a region of interest surrounding the HS-20 design load with a 95% confidence level on the statistical distribution used in the ROI to model DLA and UIL. The DLA and UIL determined are used to estimate the maximum live load effect for the HL-93 load model used in the traditional LRFR load rating framework.

The data driven load rating method is applied to three girder lines on the Telegraph Road Bridge and Newburg Road Bridge (which are two bridges along the CPS-enable I-275 corridor in southeast Michigan) using flexural strain response data collected between July 2017 to April 2019.

Each data set contains paired structural responses measured at bridge girders and truck weight data (e.g., axle weight and axle spacing) measured at a WIM station. The proposed data driven load rating approach is shown to generally offer higher rating factors for both bridges than conservative approximate load rating methods prescribed by the MBE LRFR framework. They are also found to be lower than the refined load rating methods based on FE modeling which may fail to truly capture the true systemic behavior of the bridges. All results indicate that the load-carrying capacities of the selected girder components of both bridges pass the rating at the inventory level reliability with rating factors greater than 1.

CHAPTER 6.

Monitoring and Identification of Vehicle-bridge Interaction Using Mobile Truck-based Wireless Sensor

6.1 Introduction

In the United States there are almost 611,000 bridges in operation [270] but roughly one third of them are rated as structurally deficient or functionally obsolete [30]. To ensure the National Bridge Inventory (NBI) remains safe for use and to reduce the large number of deficient bridges, ongoing bridge maintenance and renovation is necessary. While the causes of deterioration in bridges can be tied to a diverse set of sources and factors, a dominant cause of long-term deterioration can be attributed to heavy vehicles (i.e., trucks). To better understand the impact trucks have on bridge health, vehicle-induced bridge behavior must be better understood. Furthermore, understanding of vehicle-bridge interaction (VBI) can potentially lead to the control of truck vibrations so that truck-induced bridge deterioration can be minimized. In VBI, the total response of a bridge can be divided into two parts. The first part consists of the truck-induced deflection of the bridge as the truck crosses. The second part is attributed to the dynamic behavior of the vehicle (i.e., sprung mass) which is based on a complex interaction that is induced by road roughness and the motion of the bridge itself. The second part of the bridge response is relatively complex to model yet can generally account for 20% to 30% of the total bridge response [271].

To date, there have been a large number of analytical studies that have explored the modeling of VBI including the dynamic coupling that develops between the vehicle and the bridge. Comparatively less research has been devoted to observing VBI experimentally. Kim and Lynch [124] installed a flexible wireless sensor network on the Yeondae Bridge (Icheon, Korea) to monitor its

Figure 6-1: Telegraph Road Bridge (Monroe, Michigan).

dynamic response to heavy truck traffic. In addition, they installed a wireless sensor network on a heavy truck to monitor the truck location and dynamics of its sprung mass. Their study considered the time-synchronized vertical accelerations of the truck (as measured at its center-of-gravity) and bridge deck accelerations within an input-output state-space model framework. Using a two-stage subspace system identification approach, their model accurately predicted bridge responses using truck vertical accelerations.

This chapter introduces a comprehensive wireless monitoring system that is capable of simultaneously recording the dynamic response of highway bridges and the trucks crossing over them. The study emphasizes a flexible wireless sensor network architecture that allows mobile wireless sensors installed on a heavy truck to register and transmit time-synchronized acceleration time histories to a permanent and static wireless sensor network installed on a bridge. The mobile sensors in the truck are intended to measure the truck location (using GPS), horizontal acceleration, and vertical acceleration of the truck axles and sprung masses. Similarly, the bridge wireless monitoring system includes accelerometers to measure vertical accelerations and strain gauges to measure bridge bending strain responses. For experimental validation, the wireless monitoring system is installed on the Telegraph Road Bridge (TRB) located in Monroe, Michigan (Figure 6-1). In addition, a four-axle tractor-trailer truck used to induce bridge responses is similarly instrumented with a set of wireless sensors. The study collects data from the mobile and stationary wireless sensor networks and uses the data to create state-space models of the coupled dynamical systems. The study highlights the application of the previously proposed subspace system identification

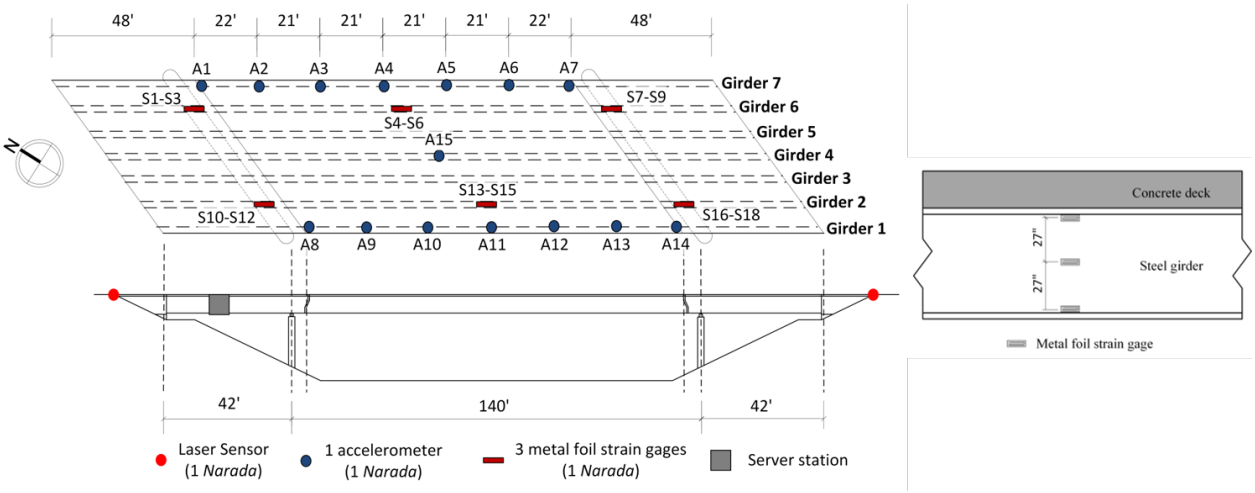

Figure 6-2: Instrumentation plan on the Telegraph Road Bridge for vehicle-bridge interaction experiments. (Note: the right figure corresponds to each array of the strain gauges notated using red rectangular on left.)

framework proposed by Kim and Lynch [4] using both bridge accelerations and strain responses.

6.2 Wireless Monitoring System Architecture

The TRB is a three-span highway bridge that carries northbound I-275 interstate highway traffic. The TRB is designed to support highway traffic using seven steel girders and a steel reinforced concrete deck. The total length of the bridge is approximately 224 feet (68.28 m) including a main span of 140 feet (42.67 m) and two end spans each 48 feet (14.63 m). A unique feature of the bridge is that it supports the main span using pin and hanger connections. Each end span cantilevers 6 feet (1.83 m) past the pier and uses hanger plates (also termed link plates) to catch the load from the main span girders.

A dense network of Narada wireless sensor nodes has been installed in the bridge (Figure 6-2) to measure bridge accelerations and strains. With girders being the primary load-carrying members, a total of 15 accelerometers and 18 strain gauges have been installed on the TRB girders to measure their responses during truck loading. Along the external girder lines, a total of 14 uniaxial accelerometers (Silicon Designs SD2012-002) have been installed to measure bridge vertical accelerations. In addition, a single tri-axial accelerometer (Crossbow CXL02TG3) is installed at

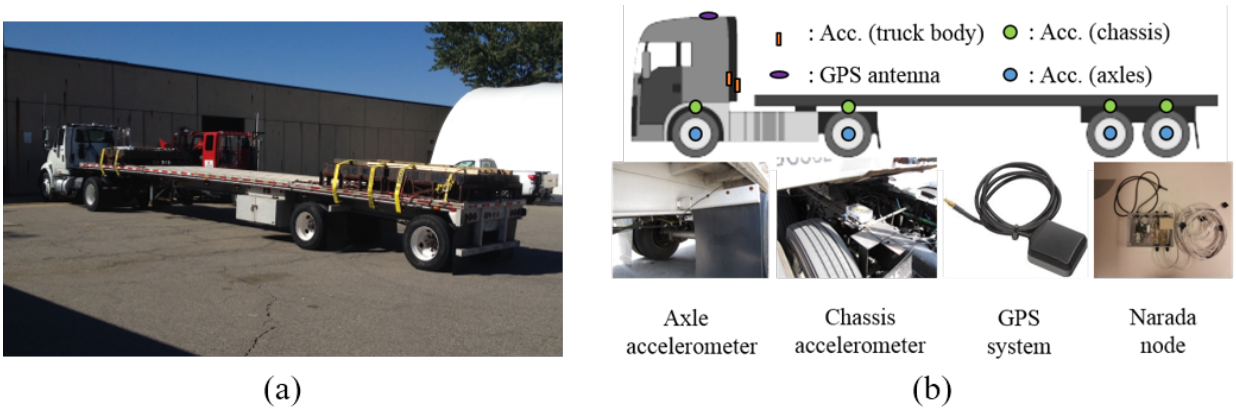

Figure 6-3: Truck instrumentation for vehicle-bridge interaction experiments: (a) a view of instrumented and loaded test truck; (b) instrumentation plan of mobile truck sensor network.

the center of the main span to measure vertical, longitudinal, and transverse accelerations. A strain gauge array is instrumented at six locations with three arrays along Girder 2 and another three along the span on Girder 6. At each location, three metal foil strain gauges (Tokyo-Sokki 120 Ω) are installed with one gauge on the web near the lower flange, another mid-height, and the last on the web near the upper flange. This strain gauge array is intended to measure bending strains and to identify the location of the cross-section neutral axis. External to the bridge, two laser sensors (Omron E3FA) are installed at both ends of the bridge to detect when vehicles enter and exit the bridge. In addition to the wireless sensors, a single base station has been installed to manage the on-site sensors and to communicate data from the bridge to a data server located at the University of Michigan [61].

The mobile wireless sensor network is installed in a four-axle tractor-trailer truck (Figure 6-3). The distance between the first axle and the last axle is 54.75 feet (16.7 m). The two front axles are associated with the truck while the last two axles are associated with the trailer. A total of 20 acceleration channels are installed on the truck. At each wheel location, one uni-axial accelerometer (Silicon Designs SD2012-010) is installed on the axle itself while another (Silicon Designs SD2012-005) is installed on the chassis above the axle. Two additional uni-axial accelerometers (Silicon Designs SD2012-002) are installed in a horizontal direction on the tractor body to measure truck motions at its center-of-gravity. The truck is also instrumented with a GPS module (U-blox)

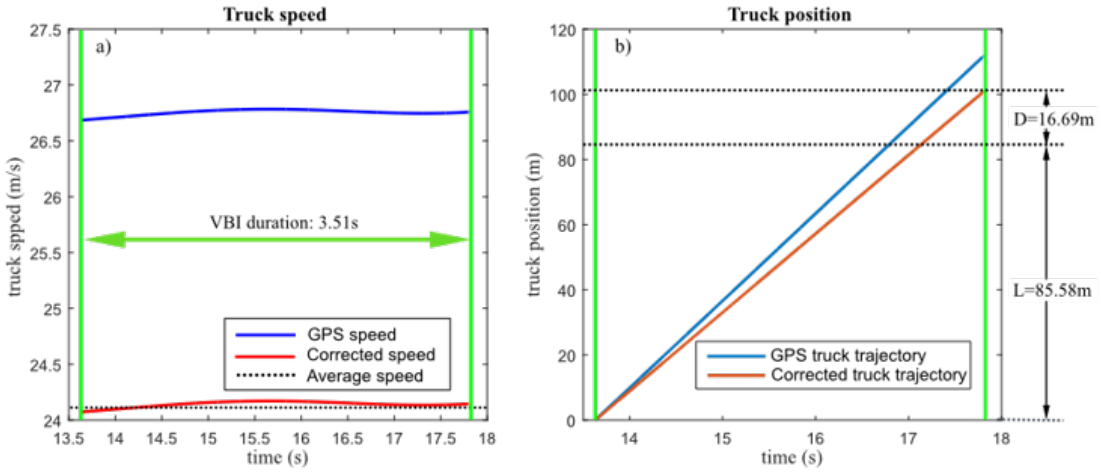

Figure 6-4: Truck speed and location estimation: (a) GPS and laser measured truck speed; (b) correction of truck position (L is the bridge length and D is the truck length).

to record its speed and location. Each sensor in the truck is connected to a Narada wireless sensor node allowing the mobile wireless sensors to communicate with the bridge wireless monitoring system.

6.3 Data Acquisition and Processing

Nine VBI field tests were conducted on the TRB using the instrumented truck. The stationary and mobile wireless sensor networks measure the response of the bridge and the truck, respectively; each network is time synchronized to the bridge base station. Prior to testing, the truck is placed 500 feet from the bridge so that the truck-based wireless sensors can register with the bridge wireless sensor network. Once registered, the truck is commanded to drive over the bridge at a fixed speed. The truck is driven over the bridge once at 53 mph (23.7 m/s), twice at 55 mph (24.59 m/s), and six times at 60 mph (26.82 m/s). As the truck is collecting accelerations and GPS location, the truck wireless sensor network communicates the data to the base station where it is synchronized with the bridge response data. The truck accelerations, truck GPS coordinates, bridge accelerations, and bridge strains are all sampled at 200 Hz for 30 seconds. In this chapter, the VBI test data in which the truck has the speed of 60 mph is taken as an example to showcase the method and results.

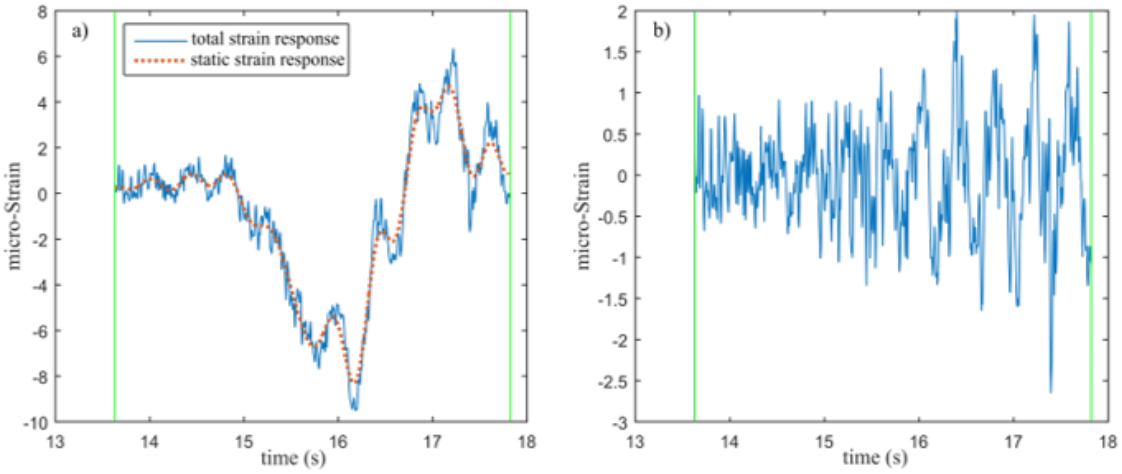

Figure 6-5: Extraction of the dynamic strain response of the Telegraph Road Bridge.

The duration of the VBI process can be obtained from the laser sensor data that captures the point in time when the truck enters and exits the bridge. Figure 6-4 plots the point in time when the truck arrives (13.5 sec) and when it exits (17.8 sec) using green vertical lines; these lines are repeated in the other figures that follow. The truck's average speed can be calculated by dividing the distance between the two laser sensors by the detected traversing time (24.1 m/s). The truck speed as recorded by the GPS receiver is also plotted and averages around 26.7 m/s. It is assumed that the 10% difference is attributed to error in the GPS reading. The GPS reading is corrected using a normalizing constant of 0.9. Using the corrected velocity time history, the location of the truck on the bridge can be estimated by standard numerical integration of the speed; the result is shown in Figure 3.1b for the uncorrected and corrected GPS velocities.

The vehicle-induced bridge response includes vertical accelerations and girder bending strains. The vertical accelerations directly reflect the bridge dynamic response. However, the girder strains represent a combination of the static deflection to the moving load and a dynamic response attributed to VBI. In order to crudely extract the dynamic component of the bending strain, a low-pass filter with a cutoff frequency at 5 Hz is applied to the measured strain response (Figure 6-5). The low-pass component is then subtracted from the original girder strain signal to reveal the dynamic component of the girder bending strain signal.

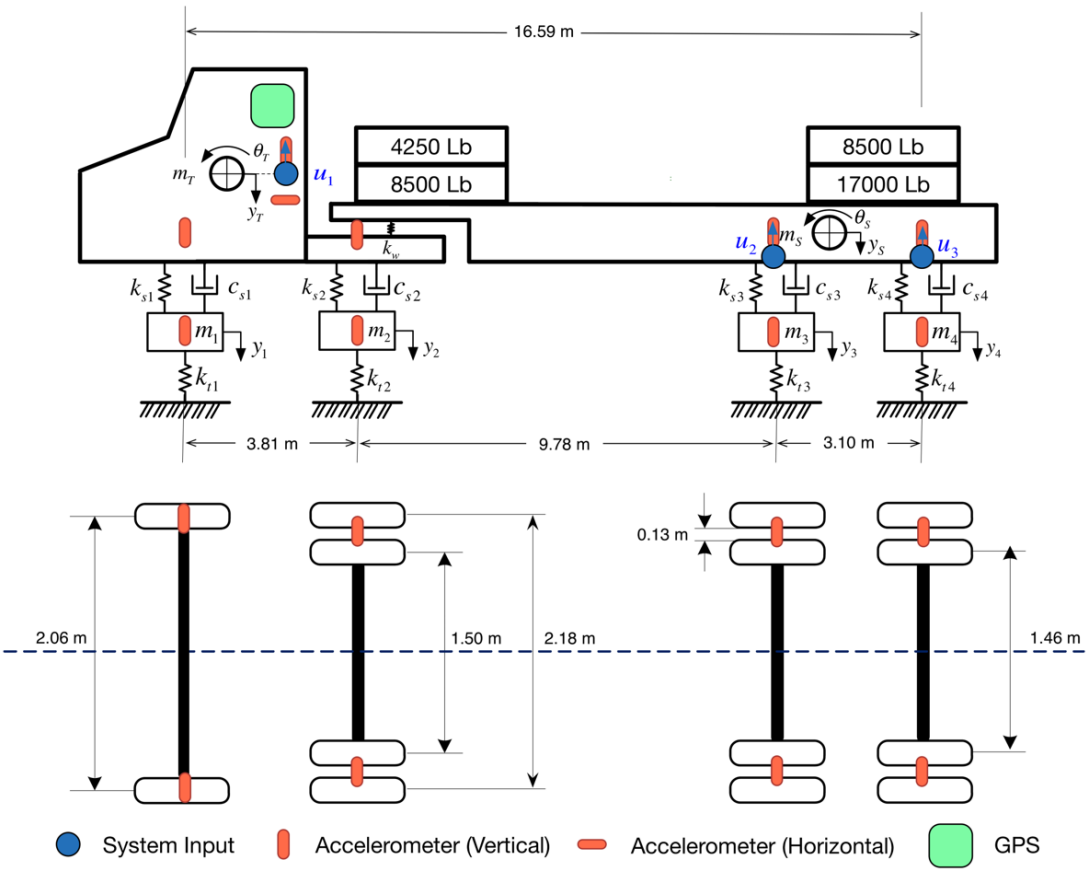

Figure 6-6: Truck model and system inputs with detailed dimensions notated.

6.4 System Identification for Vehicle-Bridge Interaction

The four-axle tractor-trailer truck is modeled as a pitch-plane whole-vehicle model as shown in Figure 6-6. In this model, the tractor and trailer are modeled as two sprung masses that are connected to each other by a spring. Four spring-dashpot suspensions assemblages support the tractor and trailer at each of the axles. The axle itself is treated as an un-sprung lumped mass connected to the truck or trailer through the spring-dashpot suspension. In total, this model consists of eight (8) degrees-of-freedom including the vertical displacements and rotation at the center-of-gravity of both the tractor and trailer and the vertical displacement at each axle.

As the truck drives over the bridge, the truck is dynamically excited by the road roughness and through interaction with the vibrating bridge. In turn, the vehicle dynamics are imposing dynamic loads on the bridge. The VBI modeling framework takes the vertical acceleration at the

center-of-gravity of the tractor and those above each rear axle (associated with the trailer chassis) as inputs u_1, u_2 and u_3; these inputs are shown in Figure 6-6 by three blue dots. In order to model the bridge vibrations, the VBI model considers the dynamic bridge responses (i.e., girder vertical accelerations and high-passed girder bending strains) as model outputs, y. A discrete-time linear multi-input multi-output (MIMO) state space is used to model the system

$$x(k+1) = Ax(k) + B(k)u(k) + w(k) \tag{6.1}$$

$$y(k) = Cx(k) + v(k) \tag{6.2}$$

where $u(k) \in \mathbb{R}^{p\times 1}$ is the system input at discrete time step k including the vertical accelerations at the tractor body and trailer chassis at the positions above the last two axles. Here, p is the number of inputs (which in this study is three). Furthermore, $y(k) \in \mathbb{R}^{l\times 1}$ is the system output vector consisting of strains or accelerations with l being the number of measurements considered as the measured bridge responses. Finally, $x(k) \in \mathbb{R}^n$ is an unknown n-dimensional state vector of the system, $w(k) \in \mathbb{R}^{n\times 1}$ is the process noise associated with the system dynamics, and $v(k) \in \mathbb{R}^{l\times 1}$ is the measurement noise associated with the sensor system measurement. The process and measurement noises are both assumed to be uncorrelated white noise signals with zero-mean. Based on the assumption that the truck will not influence the parameters of the bridge dynamics and the vibration amplitude of the bridge is small, the system matrix, $A \in \mathbb{R}^{n\times n}$, and output matrix, $C \in \mathbb{R}^{l\times n}$, are considered as time invariant. However, because the truck position is changing, the mapping of the system inputs to the state space is considered to be time variant; hence, the input matrix $B \in \mathbb{R}^{n\times p}$ is a function of time step k. The VBI system identification problem can be considered as the estimation of the matrices A, $B(k)$ and C given the measured system inputs (i.e., $u(k)$) and outputs (i.e., $y(k)$).

The two-stage system identification methodology (Figure 6-7) as originally proposed by Kim and Lynch [124] is adopted in this study to determine A, $B(k)$ and C. The modeling strategy consists of two parts: use of bridge free-vibrations to estimate A and C, and use of the forced vibration

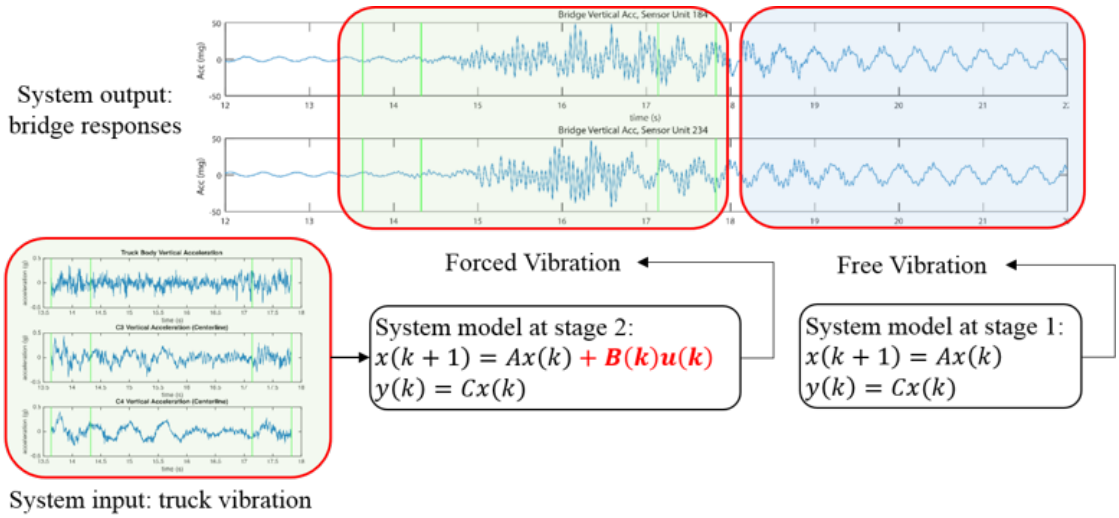

Figure 6-7: Two-stage system identification strategy.

of the bridge to estimate $B(k)$. The laser data is vital to precisely identifying when the truck is on and off the bridge allowing for the forced and free vibrations to be delineated. The system matrix A and output matrix C are estimated using the output-only stochastic subspace identification method [272]. During this period, there are no inputs from the truck and thus the input matrix B is effectively zero. After the matrices A and C are identified, the matrix B can be estimated at each discrete time step from $k = 1$ (the time step when the truck enters the bridge) to N (the time step when the truck exits the bridge) using the forced-vibration response of the bridge, the truck accelerations and the truck position by a least-squares method [124]. While the methodology of Kim and Lynch [124] is used, two major modifications are made in this implementation. First, the original study [124] only considered bridge accelerations as a system output. In contrast, bending strains of the girders will also be considered as a system output in this study. Second, the previous study [124] utilized a simpler truck that could be modeled as a single input (i.e., vertical acceleration of the truck sprung mass). Here, a more complex truck is utilized and multiple inputs are considered.

During free vibrations, the bridge has no imposed load because the truck is off the bridge. Hence, the original state space model (Eq. 6.1) can be modified as a stochastic discrete-time time-invariant model as:

$$x(k+1) = Ax(k) + w(k) \tag{6.3}$$

The output-only stochastic subspace identification (SSI) method proposed by van Overschee and De Moore [272] is used to determine the system matrix, A, in Eq. 6.3 and the output matric, C, in Eq. 6.2. A brief introduction of the SSI algorithm is introduced in this chapter but interested readers are still referred to the classical reference by van Overschee and De Moore [272]. The free-vibration response data is first assembled as the output Hankel block matrix which is partitioned as past and future outputs as shown:

$$Y_{o|2i-1} = \left[\begin{array}{cccc} y(0) & y(1) & \cdots & y(j-1)) \\ \vdots & \vdots & \ddots & \vdots \\ y(i-1) & y(i) & \cdots & y(i+j-2) \\ \hline y(i) & y(i+1) & \cdots & y(i+j-1)) \\ \vdots & \vdots & \ddots & \vdots \\ y(2i-1) & y(2i) & \cdots & y(2i+j-2) \end{array}\right] = \left[\begin{array}{c} Y_{0|i-1} \\ \hline Y_{i|2i-1} \end{array}\right] = \left[\begin{array}{c} Y_p \\ \hline Y_f \end{array}\right] \tag{6.4}$$

Orthogonal projections of the row space of the future output, Y_f, on the row space of the past output, Y_p, can be calculated using the partitioned Hankel matrix:

$$P_i = Y_f Y_p^T (Y_p Y_p^T)^\dagger Y_p \tag{6.5}$$

$$P_{i-1} = Y_f^- Y_p^{-T} (Y_p^- Y_p^{-T})^\dagger Y_p^- \tag{6.6}$$

Projection P_{i-1} differs from projection P_i based on shifting one block row in the delineation between past and future outputs in Eq. 6.4. Specifically, Y_f^- and Y_p^- are defined as $Y_{o|i}$ and $Y_{i+1|2i-1}$, respectively. Since the projection is equal to the product of the extended observability matrix, O_i, and the non-stationary Kalman filter state sequence, $\hat{X}_i$, the projection matrix P_i can be factorized by singular value decomposition (SVD):

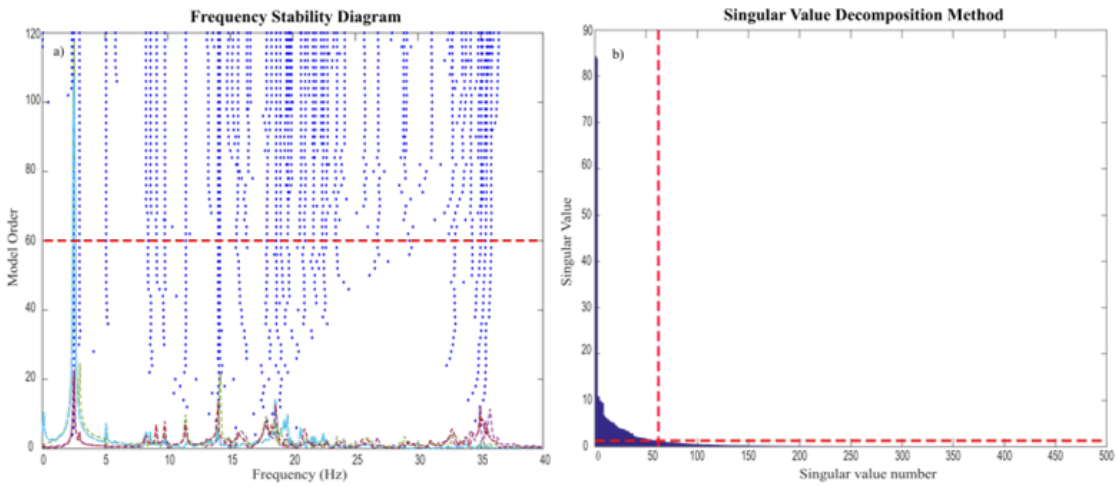

Figure 6-8: Determination of the system order: (a) stability diagram method; (b) Singular value decomposition (SVD) method.

$$P_i = USV^T \cong \begin{bmatrix} U_1 & U_2 \end{bmatrix} \begin{bmatrix} S_1 & 0 \\ 0 & 0 \end{bmatrix} \begin{bmatrix} V_1^T \\ V_2^T \end{bmatrix} = U_1 S_1 V_1^T = (U_1 S_1^{0.5})(S_1^{0.5} V_1^T) = O_i \hat{X}_i \tag{6.7}$$

The one-step shifted state sequence can be calculated

$$\hat{X}_{i+1} = O_{i-1}^{\dagger} P_{i-1} \tag{6.8}$$

where O_{i-1} is equivalent to O_i with the last block row eliminated. Finally, estimates of A and C can be calculated by a least-squares solution:

$$\begin{bmatrix} \hat{A} \\ \hat{C} \end{bmatrix} = \begin{bmatrix} \hat{X}_{i+1} \\ Y_{i|i} \end{bmatrix} \hat{X}_i^{\dagger} \tag{6.9}$$

A critical parameter associated with the SSI algorithm is the system order (i.e., the dimension (n) of the system matrix A). A stability diagram approach is applied [273] to the modal frequencies extracted from the estimated system matrix $\hat{A}$ by eigenvalue decomposition. As shown in Figure 6-8(a), the stability diagram is shown for modal frequency as the model order is varied from 1 to

120. The modal frequencies become relatively stable once the model order exceeds 60 with modal frequencies showing up as vertical columns. Hence, the system order is set to 60 based on visual inspection of the stability plot. The singular value decomposition method introduced in [272] is implemented to double check this model order, as shown in Figure 6-8(b).

In the second stage of the system identification methodology, the system model can now be formulated as

$$x(k+1) = \hat{A}x(k) + B(k)u(k) + w(k) \tag{6.10}$$

$$y(k) = \hat{C}x(k) + v(k) \tag{6.11}$$

where the matrices $(\hat{A}, \hat{C})$ are the estimated system matrices from the free vibration response. The objective in the second stage is to estimate the time-varying input matrix $B(k)$. To do so, the identification problem is formulated as an unconstrained optimization problem over a finite horizon where the difference between the measured bridge response, $y(k)$, and the predicted bridge response, $\hat{y}(k)$, is to be minimized

$$[\hat{B}(1), \hat{B}(2), \cdots, \hat{B}(N)] = \underset{[B(1),B(2),\cdots,B(N)]}{argmin} \frac{1}{N} \sum_{k=2}^{N+1} \|y(k) - \hat{y}(k|k-1)\|^2 \tag{6.12}$$

where $\hat{y}(k|k-1)$ is the one-step ahead prediction of the bridge response calculated at time step $k-1$ [124]. Before the truck arrives, the bridge is assumed to be at rest ($x(0) = 0$). Hence, the system state at $k = 1$, $x(1)$, is also equals zero and $\hat{y}(k|k-1)$ can be derived as:

$$\hat{y}(k|k-1) = \sum_{q-1}^{k} \hat{C}\hat{A}^{k-q}B(q)u(q) \tag{6.13}$$

The previous unconstrained optimization problem of Eq. 6.12 can be combined with Eq. 6.13 as:

$$[\hat{B}(1), \hat{B}(2), \cdots, \hat{B}(N)] = \underset{[B(1),B(2),\cdots,B(N)]}{argmin} \frac{1}{N} \sum_{k=2}^{N+1} \left\| y(k) - \sum_{q=1}^{k} \hat{C}\hat{A}^{k-q} B(q) u(q) \right\|^2 \tag{6.14}$$

A kernel approximation of $B(k)$ is made based on the estimated truck position at k. The construction of the binary kernel function is presented in [124] in detail and will not be covered here. In this study, the truck has more than one input variable; hence, several vehicle position-load effect kernel functions which allow the continuous moving load trajectory to be spatially mapped to a finite number of nodes in the bridge model are constructed as $\Phi_i(k) \in \mathbb{R}^n (i = 1, 2, \cdots, p)$. The input matrix $B(k)$ can be estimated through corresponding scalar time-varying functions, $\alpha_i(k) (i = 1, 2, \cdots, p)$

$$B(k) = [\alpha_1(k)\Phi_1(k), \alpha_2(k)\Phi_2(k), \cdots, \alpha_p(k)\Phi_p(k)] = \Phi(k)\alpha(k)^T \tag{6.15}$$

This representation of B is included in Eq. 6.13 to yield

$$\begin{aligned} \hat{y}(k|k-1) &= \sum_{q=1}^{k} \hat{C}\hat{A}^{k-q} \left[\sum_{i=1}^{p} \Phi_i(q)\alpha_i(q)u_i(q) \right] \\ &= \sum_{q=1}^{k} \hat{C}\hat{A}^{k-q} \Phi(q) \begin{bmatrix} u_1(q) & & & \\ & u_2(q) & & \\ & & \ddots & \\ & & & u_p(q) \end{bmatrix} \alpha(q)^T \end{aligned} \tag{6.16}$$

The previous optimization problem can then be re-formulated in terms of $\hat{\alpha}$:

$$[\hat{\alpha}(1), \hat{\alpha}(2), \cdots, \hat{\alpha}(N)] = \underset{[\alpha(1),\alpha(2),\cdots,\alpha(N)]}{argmin} \frac{1}{N} \sum_{k=2}^{N+1} \|y(k) - \hat{y}(k|k-1)\|^2 \tag{6.17}$$

The solution is obtained through application of the least-squares method and $B(k)$ is calculated

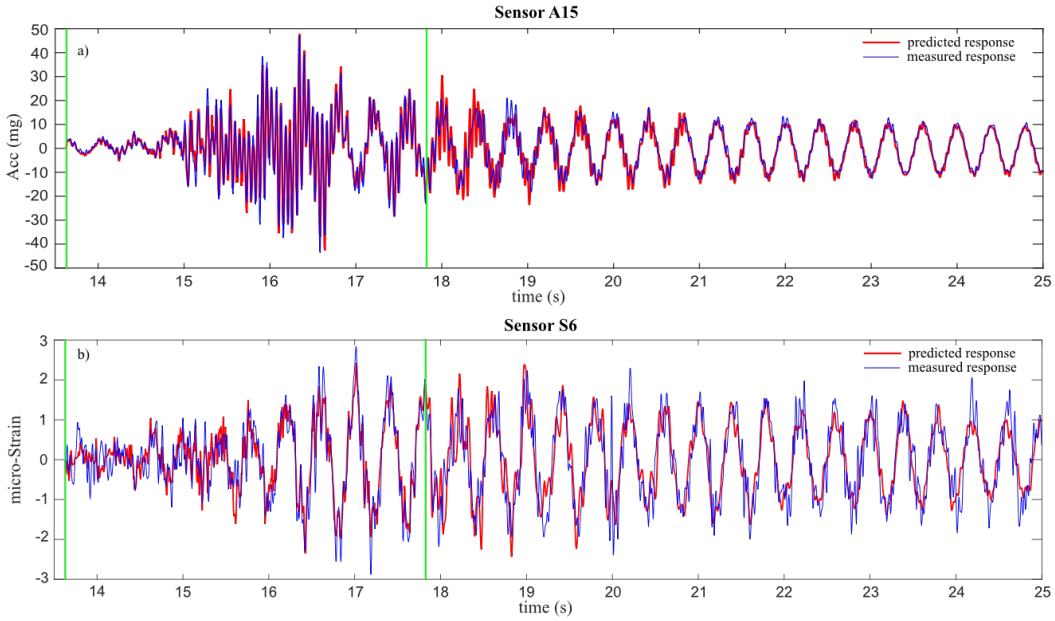

Figure 6-9: Predicted versus measured bridge response: (top) acceleration at A15; (bottom) strain at S6.

based on $\hat{\alpha}(k)$ from Eq. 6.15.

6.5 Results and Conclusions

The VBI model is applied to the TRB response data collected during forced truck loading. The system identification results are excellent with the predicted bridge response (strain and acceleration) matching the real measurements. Two system identification results are shown in Figure 6-9. The first, plotted in Figure 6-9 (top) shows the predicted bridge acceleration; in the second (Figure 6-9 (bottom)), the predicted girder strain is shown. There are some discrepancies between the predicted and measured bridge response that can be possibly due to the nonlinearities of the truck or bridge system. In addition, the result of the system taking dynamic strains as outputs are not as good as that of the system taking accelerations as outputs because the dynamic strains extracted from the measured strain may be not accurate enough (i.e., limitations of using low-pass filtering).

CHAPTER 7.

Time Series Forecasting For Joint Monitoring of Multiple Highway Bridges

7.1 Introduction

Recent advances in deep learning provide the civil engineering community with powerful and valuable tools to solve unique problems emerging within the field. Applications of such techniques range from the use of computer vision for infrastructure inspection [274] to damage detection for structural health monitoring (SHM) using measured structural responses [275]. Among all available deep learning-based methods, encoder-based algorithms have gained extensive attentions for damage detection. For example, modal properties (including modal frequencies and mode shapes) of a structure can be fed into a two-stage parallel auto-encoder to predict mass-stiffness parameters of the same structure [276, 277]. Such an auto-encoder model allows stiffness reduction which are linked with structural damages to be discovered from vibration data with a high sensitivity. In another study, by learning identical data reconstruction, an auto-encoder model is trained in a multi-task learning fashion to detect damages associated with a bridge using vibrations (i.e., acceleration data) of a passing vehicle measured during the vehicle-bridge interaction process [278]. Large amounts of bridge SHM data collected over time not only enable complicated deep learning models to be employed for structural monitoring purposes but also open new opportunities for data-driven SHM methods that purely rely on spatial and temporal relationships without considering mechanical models. For instance, correlation between sensor measurements of two adjacent bridges to the same traffic loads can be used for damage detection and localization in bridge structures [65].

This chapter builds upon the successful application of deep learning in civil engineering where

computer vision is used to track trucks in a corridor with bridges monitored (presented in Chapter 2) [254]. In the work, the traffic along a 20-mile northbound highway corridor is monitored via cameras. A deep learning technique is used to automatically identify trucks traveling on a bridge in the corridor and then re-identify the same truck as it traverses another bridge in the same corridor. Simultaneously, the structural response of the bridges to moving trucks are measured and synchronized to the same truck load (as confirmed by imagery). In this work, a data-driven model is built that enables forecasting the response of one bridge to a truck using that of another bridge whose response corresponds to the same truck. Such a model can be used for multiples purposes such as structural damage detection and anomaly detection within wireless sensor networks. For example, by building an accurate model that is capable of forecasting the response of one bridge using that of another, structural damages and faulty sensors can be identified from inaccurate predictions. Hence, this model enables joint health monitoring among multiple bridges located in close geographic proximity (e.g., on the same corridor), for which there is a high likelihood that the same truck loads are experienced. Another application of joint modeling of bridges would be enabled by connected vehicles technology. The response of an upstream bridge to a truck contains information on the characteristics of the truck (i.e., weight). The joint model between the two bridges can be employed to predict truck impacts on downstream bridges so that the speed of the truck approaching the second bridge can be set to minimize the response and consumed life of that bridge (and thus maximize the life span of the bridge). This requires the models to be exclusive to each bridge pair and take into account the unique complexities inherent to the bridges and the truck (e.g., suspension system). It is almost impossible to do this with physical models (e.g., finite element models) of the bridges which demands high computational powers and cannot be performed in a timely manner. Hence data-driven models are an attractively scalable solution.

In this work, the use of time series forecast models are explored for the aforementioned task of predicting bridge responses. A RNN-based sequence to sequence (Seq2Seq) models with two different types of unit cells are evaluated. Seq2Seq models are originated from the field of neural machine translation [279] but have been proven to be effective in many other applications such

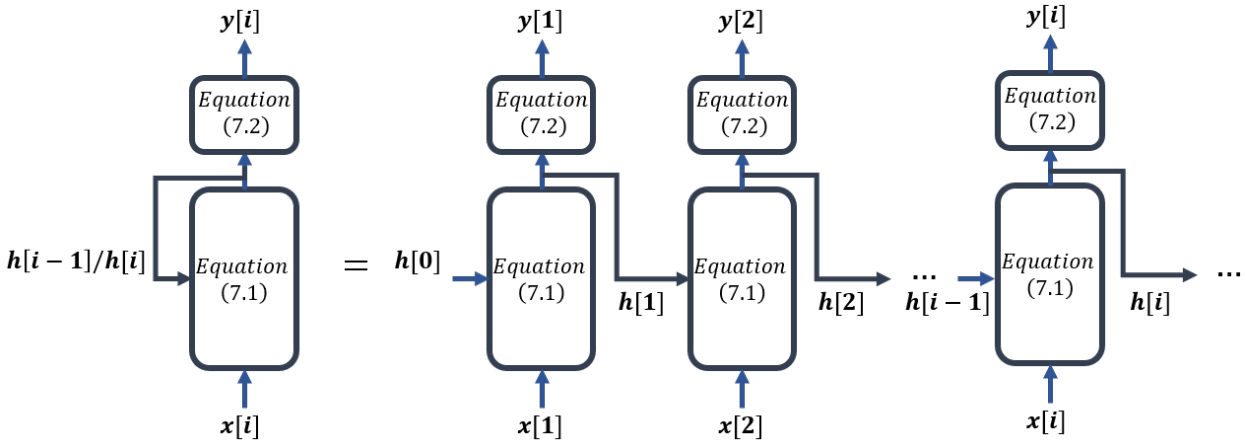

Figure 7-1: Illustration of a typical recurrent neural network.

as time series forecasting [280, 281] and anomaly detection [282]. Moreover, an auto-regressive with exogenous terms (ARX) model is also trained to perform comparison with the RNN-based Seq2Seq model. ARX models use a linear equation to predict the output of a system using previous outputs and the current inputs [283]. Such a time series structure is suitable for the purpose of this work and provides a linear twin for the non-linear Seq2Seq models.

The remainder of this chapter is organized as follows: the next section is devoted to the description of the encoder-decoder Seq2Seq methodologies. In Section 3, generation of training, evaluation and test data is first discussed, followed by training and test results using finite element modeling-based simulation data. The effectiveness of the trained model for bridge damage detection is also investigated using simulated damage data in Section 4. This chapter concludes with a summary of the results and a description of future work.

7.2 Recurrent Neural Networks

A recurrent neural network (RNN) can be viewed as a unit cell that is rolled over itself for a finite number of times. At each time step, the unit cell takes an external input $x[i]$ and the hidden state from the previous step $h[i-1]$ as inputs and returns the current hidden state $h[i]$ and the current output $y[i]$, which is illustrated in Figure 7-1. The network aims at capturing and memorizing sequential information within in the training data presented to it through the use of hidden states

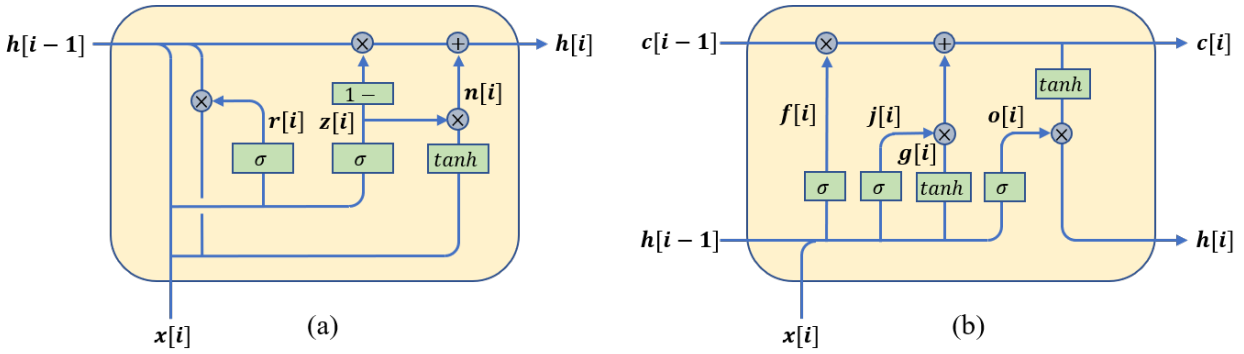

Figure 7-2: Illustration of two RNN unit types: (a) gated recurrent unit (GRU); (b) long short-term memory (LSTM) unit.

from the previous time steps. The main computation of an RNN is associated with the unit cell Φ. The RNN cells apply a combination of linear matrix multiplications and non-linear activation to generate the hidden state and output at each timestamp. A basic RNN cell can be formulated as follows:

$$h[i] = g_1(W_{hh}h[i-1] + W_{hx}x[i] + b_h) \tag{7.1}$$

$$y[i] = g_2(W_{yh}h[i] + b_y) \tag{7.2}$$

where W_{hh}, W_{hx}, W_{yh}, b_h, b_h are parameters (i.e., weights and bias) shared within the RNN temporally at each timestamp and g_1, g_2 are activation functions (e.g., ReLU or sigmoid) of choice. The RNN is able to process inputs of any length with weights shared across time. However, it has been shown that the RNN requires considerable computation time and suffers the difficulty of remembering information learned a long time ago [284]. Two different more advanced RNN cell types are used in this study, namely long short-term memory (LSTM) cells and gated recurrent unit (GRU). A brief description of the two cell types are presented in the following two sub-sections. For more detailed descriptions, interested readers are referred to [285, 286].

7.2.1 Gated Recurrent Unit

Figure 7-2(a) shows an illustration of the GRU block. The equations describing the GRU are given as [286]:

$$\begin{aligned} r[i] &= \sigma(W_{xr}x[i] + b_{xr} + W_{hr}h[i-1] + b_{hr}) \\ z[i] &= \sigma(W_{xz}x[i] + b_{xz} + W_{hz}h[i-1] + b_{hz}) \\ n[i] &= tanh(W_{xn}x[i] + b_{xn} + r[i] \odot W_{hn}h[i-1] + b_{hn}) \\ h[i] &= (1 - z[i]) \odot n[i] + z[i] \odot h[i-1] \end{aligned} \tag{7.3}$$

where $tanh$ is the hyperbolic tangent function, $\odot$ represents the entry-wise product, and σ represents the sigmoid function defined as:

$$\sigma(x) = \frac{1}{1 + exp(x)} \tag{7.4}$$

Additionally, the index i represents the time index to show how the current hidden state is related to both the current input and previous hidden state. $x[i]$ and $h[i]$ are the input and hidden state at time i, respectively. The terms $r[i]$, $z[i]$, and $n[i]$ are the reset, update and new gates, respectively. Finally, the W's and b's are the weights and biases of the linear transformations.

7.2.2 Long Short-term Memory Cell

Figure 7-2(b) shows an illustration of the LSTM block whose equations are expressed as [285]:

$$
\begin{aligned}
j[i] &= \sigma(W_{xj}x[i] + b_{xj} + W_{hj}h[i-1] + b_{hj}) \\
f[i] &= \sigma(W_{xf}x[i] + b_{xf} + W_{hf}h[i-1] + b_{hf}) \\
g[i] &= tanh(W_{xg}x[i] + b_{xg} + W_{hg}h[i-1] + b_{hg}) \\
o[i] &= \sigma(W_{xo}x[i] + b_{xo} + W_{ho}h[i-1] + b_{ho}) \\
c[i] &= f[i] \cdot c[i-1] + j[i] \cdot g[i] \\
h[i] &= o[i] \cdot tanh(c[i])
\end{aligned}
\tag{7.5}
$$

where h and c are called the hidden state and cell state. Moreover, j, f, g and o are referred to as the input, forget, cell and output gates, respectively. It is emphasized that for the LSTM cell, at each time step, two sets of vectors are received from the previous time step, namely the hidden and cell states (h and c). Compared to the standard RNN unit, LSTM can handle the information contained in a longer period of time.

7.2.3 Encoder-Decoder Sequence to Sequence Model

With its architecture shown in Figure 7-3, the encoder-decoder sequence to sequence model consists of two RNN sub-networks, namely encoder and decoder. In this study, the RNN cell for the encoder is denoted as Φ_E and that for the decoder is denoted as Φ_D. The same notation also ap-

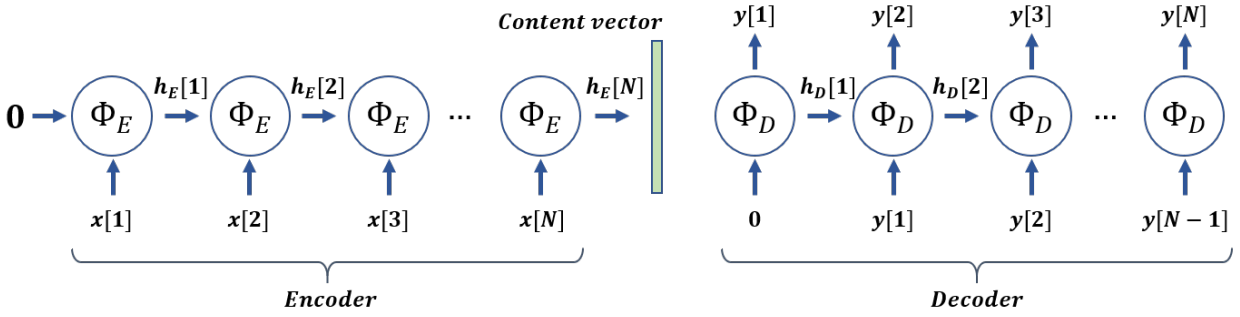

Figure 7-3: Sequence-to-sequence model schematics: from the encoder's side, the context vector is passed to the decoder with the decoder using it's own predictions at the previous time step as the input to the current time step.

plies for hidden states. The first sub-model, namely encoder, takes a sequence as its inputs and condenses the information of interest inside the input data into a fixed-length vectorized representation, which is referred to as the "content vector". Generally speaking, the functionality of a RNN cell (e.g., LSTM or GRU) in the encoder can be expressed as Equation 7.6 and the output is usually ignored. For the GRU cell, the hidden state is basically the h vector in Equations 7.3. While for the LSTM cell, this hidden state is a concatenated vector of the h and c vectors in Equations 7.5. The context vector is the last hidden state of the encoder but serves as the input on the decoder's side.

$$h_E[i] = \Phi_E(x[i], h_E[i-1]) \tag{7.6}$$

Given the context vector, the decoder model decodes and unrolls it into a sequential output. The functionality of a RNN cell in the decoder can be expressed as Equation 7.7 where both hidden state $h_D[i]$ and output $y_D[i]$ are generated at each time step i. For each time step, the decoder recurrent cell's output is used as the input to the cell at the next time step. This is in contrast to the encoder where the actual time series values are used at each time step.

$$y[i], h_D[i] = \Phi_D(y[i-1], h_D[i-1]) \tag{7.7}$$

In general, the sequence-to-sequence model learns a general transformation mapping one sequence into another. The RNN architecture is used to model an encoder whose weights is optimized through training to output the low-dimension context vector using input time series $x[i]$; the decoder then uses the context vector to feed another RNN that outputs another time series $y[i]$. In this study, x and y correspond to responses of two adjacent bridges to the same truck loads.

The dimensions of the hidden states of the encoder and the decoder have to be the same. Meanwhile, the dimensions of the hidden state of the decoder could be different than that of the output. Hence, a fully connected layer is used on the decoder side of the model. This layer acts as follows (Equation 7.8): let $h_D[i]$ be the decoder's hidden state at time step i; then, this hidden state is mul-

tiplied by a weight matrix W_{dh} such the product is a scalar; the scalar is then passed to a tanhshrink activation function.

$$\begin{aligned} y[i] &= d[i] - tanh(d[i]) \\ d[i] &= W_{dh} h_D[i] + b_{dh} \end{aligned} \tag{7.8}$$

There are a handful of non-linear transformations commonly used with neural networks, however, the non-linearity function should have a range of $(-\infty, \infty)$. The tanhshrink activation function is one of the few that has such characteristics. The weight matrix W_{dh}, bias vector b_{dh}, along with the internal weights and biases of the cells are optimized in the training stage so as to minimize the mean squared error (MSE) between the predicted response of the target bridge computed by the trained model and the actual ground-truth bridge response to the same truck load.

7.3 Bridge Response Forecasting

7.3.1 Dataset

The subjects of this study are the two instrumented bridge systems (Telegraph Road Bridge (TRB) and Newburg Road Bridge (NRB) which are illustrated again in Figure 7-4) along the I-275 corridor described in Chapter 2. As previously mentioned, bridge responses of the two bridges to the same truck loads are matched using computer vision-based truck re-identification algorithms. In this study, finite element method (FEM) models are created for both bridges in CSiBridge [221] according to the dimensions and properties of the bridges to evaluate the feasibility of the proposed Seq2Seq model. The detailed FEM bridge models are shown in Figure 7-5. Numerical simulations are carried out for the bridges using the same set of trucks to imitate the scenario of monitoring a given truck passing through the highway corridor loading the TRB and the NRB. For TRB, a total of 9,052 shell elements are used to model the reinforced concrete slab (1,750) and the steel girders (7,302). Lateral bracings and rebars are modeled using 454 brace elements. The pin-and-hanger mechanism and joints are modeled by link elements. The concrete has a Young's modulus of 3,600 ksi with a Poisson's ratio of 0.17, the steel used for girders and rebars has a Young's modulus of

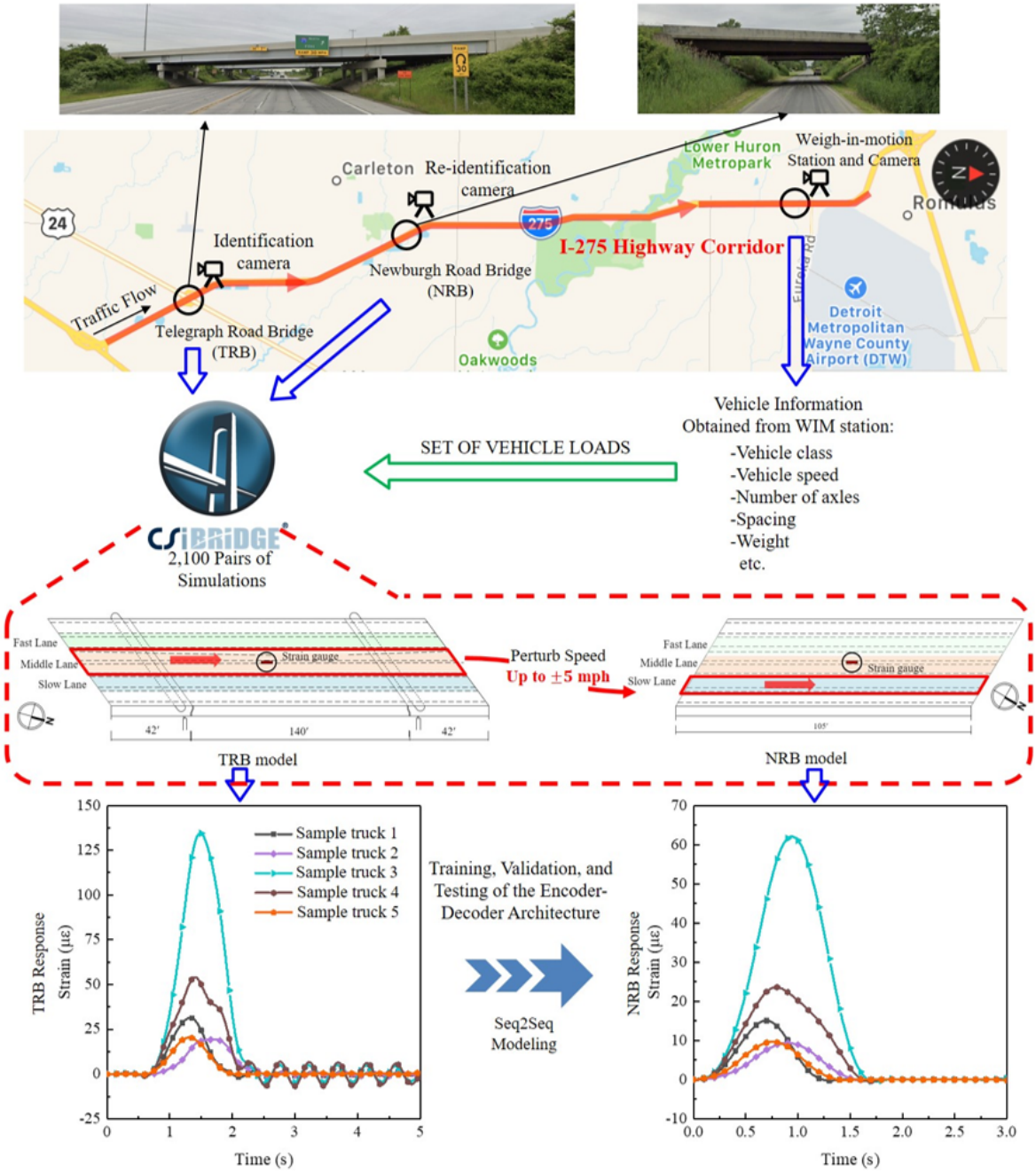

Figure 7-4: Illustration of bridge response forecasting framework.

29,000 ksi with a Poisson's ratio of 0.3 and the link plate steel had a Young's modulus of 30,000 ksi. The dominant modal frequency of TRB is 2.17 Hz. For NRB, a total of 12,139 shell elements are used to model the reinforced slab (3,840) and steel girders (8,299), and a total of 1,020 brace elements are used to model the lateral bracings. The concrete has a Young's modulus of 3,155 ksi with a Poisson's ratio of 0.2. The girder steel has a Young's modulus of 27,000 ksi and a Poisson's

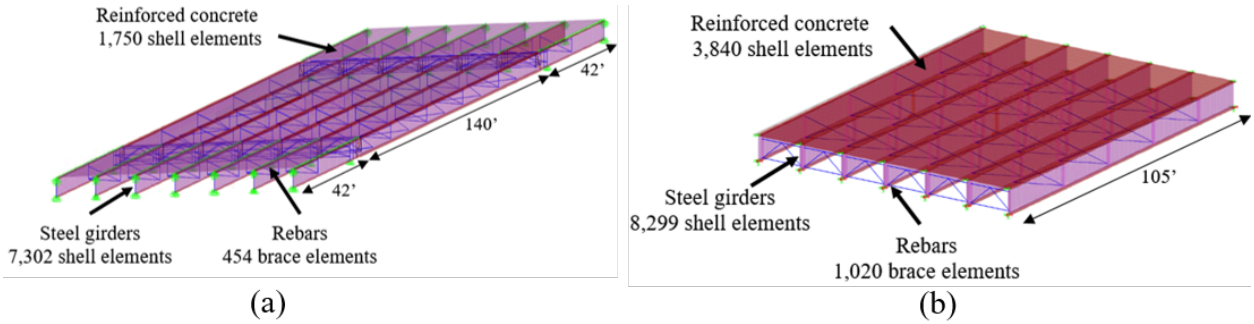

Figure 7-5: The CSiBridge models for: (a) Telegraph Road Bridge and (b) Newburg Road Bridge.

ratio of 0.28. The Young's modulus for the rebar steel is 29,000 ksi. Unlike the TRB, NRB has two dominant modal frequencies: 4.0Hz and 5.8Hz. The model properties for both bridges have been fine tuned by model updating, thus, their modal frequencies closely match those observed in the actual bridges. The simulated responses of both bridges are the strain values at the mid-span of the central girders as shown in Figure 7-4. Note that in this study, measurements (strains) are taken at only one point on both bridges.

For the truck load properties, the WIM station located on the same corridor measures nine truck attributes including: vehicle class based on the Federal Highway Administration (FHWA) protocol, vehicle speed, number of axles, axle weights and spacings, and the passing lane. The FHWA classification contains 13 vehicle categories where vehicle classes 1 to 3 represent light weight vehicles, whose loads on the bridges are not of major interest. Thus, the measured WIM data is pruned to only consider trucks with a vehicle class between 4 to 13. In addition, according to the local speed limit (60 mph for trucks) we range vehicle speeds in simulations from 40 to 85 mph. The sampled WIM data is used for generating TRB and NRB responses using CSiBridge. The speed of each truck is perturbed using a random variable between -5 and 5 mph so that simulations of the same truck on the two bridges can vary slightly making the response dataset more realistic. Trucks are passed over each bridge using a particular lane specific to each bridge. In the real-world, trucks aren't restricted to this one lane combination. There are 9 different lane combinations that the truck may travel over considering each bridge has three lanes. In this paper, only one scenario is used to validate the variability of the proposed Seq2Seq model. Based on field observations

(Table 2-2), the most common lane is: trucks pass through the middle lane on TRB and the slow lane on NRB.

The simulation has a time step of 0.01 seconds (sampling frequency is 100 Hz). Some sample strain response pairs for the two bridges are shown in Figure 7-4. As can be seen, the strain response contains not only the forced response triggered by truck but also the free vibration response after the truck is off the bridge. Thus, each bridge response can be divided into two parts: (1) forced response whose duration and amplitude depend on truck speed and weights, and (2) free vibration response after the truck departs the bridges. To capture enough structural information of the bridges, the simulation duration is set to 5 and 3 seconds for TRB and NRB, respectively. This ensures at least four cycles of free vibration are recorded for each bridge. A total of 2,100 truck events (pairs) are simulated on both bridges. 1,500 pairs of these simulations are used for training the models, 150 pairs for validation, and 450 pairs for testing.

7.3.2 Model Training

The Seq2Seq model is implemented in PyTorch [189]. This subsection contains technical details of the implementation and training of the model using PyTorch. A key parameter within the Seq2Seq model is the dimension of the context vector in the last hidden state of the encoder. A set of four different hidden dimensions, namely $\hat{H} = \{10, 30, 50, 70\}$ for both cell types are iterated on and the one that results in the highest performance is selected. To train the model, a stochastic gradient-based optimizer named Adam [188] is used. Similar to other stochastic gradient-based approaches, at each iteration, Adam takes a subset of the training dataset (called a mini-batch) and calculates the gradient of the MSE loss with respect to the weights. Consequently, the size of the mini-batches, referred to as the batch size, is another important training hyper-parameter. Four different batch sizes, namely $\hat{M} = \{10, 20, 50, 100\}$ are used and the one with the best performance is selected. The Adam optimizer then takes a step using the gradient at that iteration to update the weights using a pre-defined learning rate. Adjusting the learning rate throughout training is critically important in finding a set of network weights representing local minimum in the weight space. Initially, the

learning rate must be high to allow large enough steps towards the optimal weights but these steps must be gradually reduced to prevent overshooting a local minimum of the cost function. To adjust the learning rate, a built-in feature of PyTorch named "ReduceLROnPlateau" is used. This function keeps track of the MSE on the validation dataset used after each epoch to test the Seq2Seq model. If this value doesn't decrease for 10 epochs, it reduces the learning rate to a half of its previous value. It should be noted that it is up to the user to decide on the learning rate and the number of epochs to wait before reducing the rate. In this paper, the initial learning rate is selected as 0.02.

Epoch is another hyper-parameter to be set. It refers to the number of times the entire training dataset (consisting of multiple batches) is iterated to update the RNN weights. Here the dataset in training is 1500 observations divided into batches (with network weights updated after each batch). During an epoch the training will repeat the learning process on 15 batches when batch size is 100, 30 times when batch size is 50, and so on. The number of epochs used during training will be described shortly.

Overall, a maximum of 500 epochs are used for training the Seq2Seq model. However, it was realized that beyond a certain point, the model overfitted the training data where the error on the

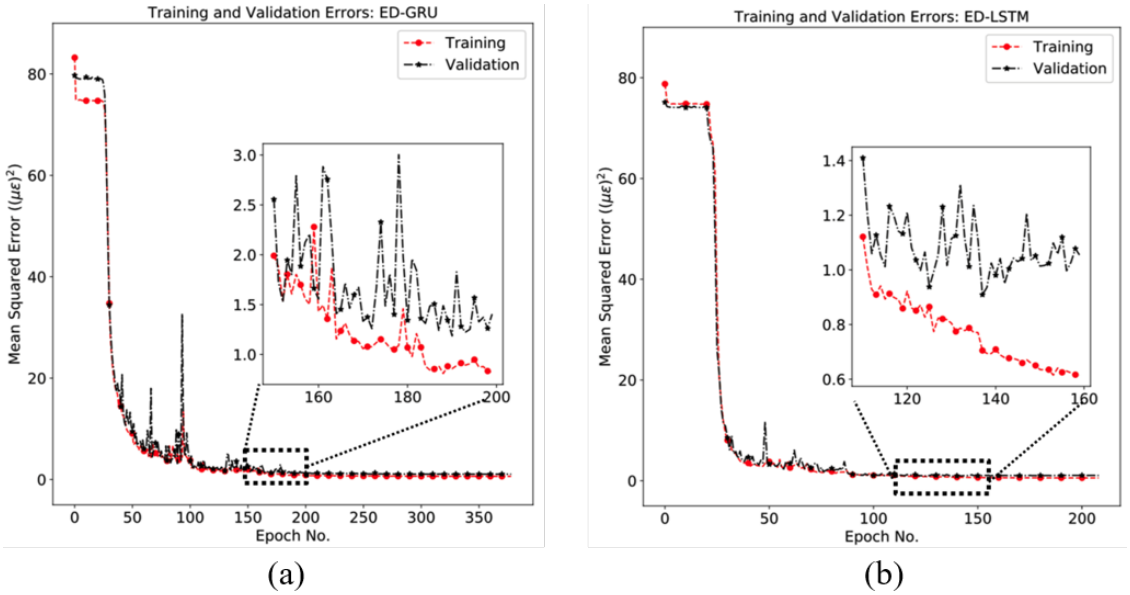

(a) (b)

Figure 7-6: Training error (MSE) for the proposed encoder-decoder methods: (a) GRU unit cell, and (b) LSTM unit cell.

validation dataset would not decrease (and may increase). Thus, to speed up the process of search for optimal hyperparameters, training was terminated if the validation error did not decrease for 70 epochs. For each value of hidden dimension and batch size, the set of weights that resulted in the minimum MSE on the validation dataset were stored. Training errors (MSE) for the encoder-decoder network model is shown in Figure 7-6. Additionally, a section of each plot has been magnified to depict the divergence of the training and validation errors.

7.3.3 Model Testing

Root mean squared error (RMSE) is a common metric for reporting the errors of time series models which will be used in this chapter. The units of the response time series data used is microstrain ($\mu\epsilon$) and hence the RMSEs have a unit of $\mu\epsilon$ as well. As shown in Table 7-1, for the encoder-decoder model with GRU cell units, it was found that using a batch size ($\hat{M}$) of 100 with a hidden dimension ($\hat{H}$) of 30 resulted in the lowest validation error. In that situation, the validation RMSE is 1.03 $\mu\epsilon$. Moreover, for the encoder-decoder model with LSTM cell units, it was found that using a batch size of 50 with a hidden dimension of 70 resulted in the lowest validation error of 0.95 $\mu\epsilon$. By selecting the model with the lowest error on the validation dataset, the issue of over-fitting can be avoided. Note that the total number of training epochs are different for the two cell types and this is due to terminating the training procedure when the validation error did not decrease for 70 epochs.

During the testing stage, the test dataset containing 450 observations was used. We emphasize

	RMSE of GRU ($\mu\epsilon$)				RMSE of LSTM ($\mu\epsilon$)			
$\hat{H} \setminus \hat{M}$	10	20	50	100	10	20	50	100
10	8.61	8.58	8.61	8.89	8.61	2.33	8.61	8.89
30	1.79	1.48	1.35	**1.03**	1.17	1.75	1.26	1.08
50	2.27	3.12	1.39	1.92	3.41	1.07	1.15	1.02
70	5.25	2.72	1.57	1.50	2.42	1.15	**0.95**	1.06

Table 7-1: Minimum RMSE of the GRU and LSTM cells during training with different batch sizes and hidden dimensions.

Method	RMSE ($\mu\epsilon$)	Average Inference Time (ms)
Encoder-decoder (GRU)	0.90	0.89
Encoder-decoder (LSTM)	1.03	1.90
ARX	1.26	5.14

Table 7-2: Test results of the Seq2Seq and ARX modes.

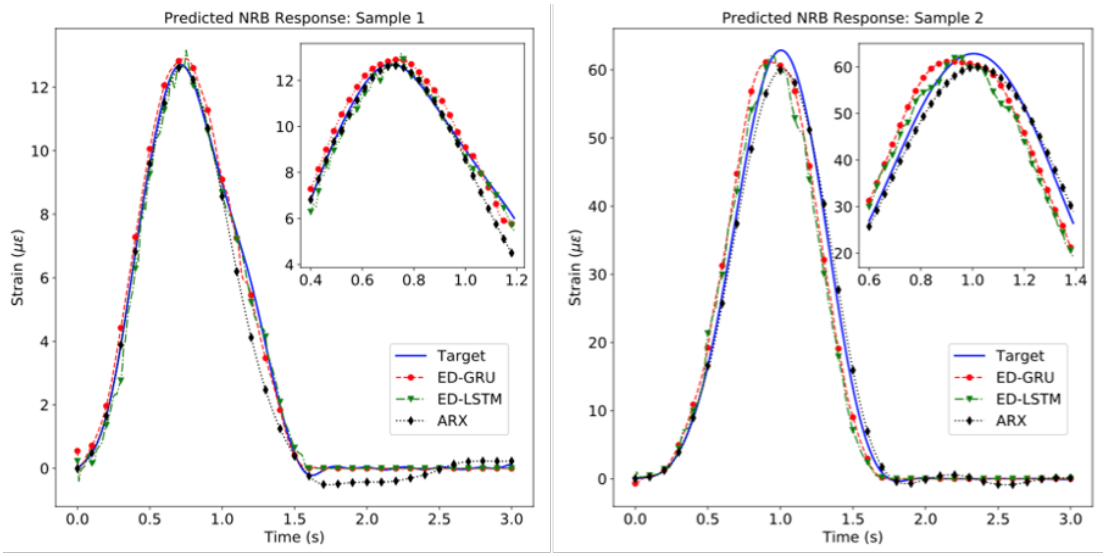

(a) (b)

Figure 7-7: Predicted responses for two observations: (a) Sample 1, the RMSE values are 0.28 $\mu\epsilon$, 0.27 $\mu\epsilon$ and 0.66 $\mu\epsilon$ for the GRU and LSTM of encoder-decode methods and ARX models respectively, and (b) Sample 2, the RMSE values are 2.90 $\mu\epsilon$, 3.26 $\mu\epsilon$ and 1.16 $\mu\epsilon$ for the GRU and LSTM of encoder-decode methods and ARX models respectively.

that the training process was fully independent of this testing dataset. The resulting RMSEs and the inference time for each model are listed in Table 7-2. The computations were carried out on a Nvidia GTX 1070 GPU. The RNN-based Seq2Seq is also compared with ARX-based sequence forecasting model whose performance is also listed in Table 7-2. The details regarding training of the ARX model can be found in [287].

Furthermore, for two sample observations in the test dataset, the model predictions along with the actual observations on NRB are shown in Figure 7-7. It can be seen that the GRU-based encoder-decoder model results in the best performance on the test dataset. The performance of the encoder-decoder model with LSTM units is close to that of the GRU case. Both encoder-decoder

models outperform the ARX model in terms of accuracy and inference speed. Despite the ARX model being simpler, the inference time for this model is much longer than that of the encoder-decoder models. This should be attributed to the fact that the Seq2Seq models takes batches of data (for GRU a batch of size 100 and for the LSTM a batch of size 50) whereas the ARX only takes one observation at a time. In addition, we emphasize the code used for implementing the Seq2Seq models takes advantage of the built-in features of PyTorch. The code used for implementing the ARX model is written by the authors without further optimization. It may affect the elapsed time but should not change the fact that ARX model requires more time than the other two models.

7.4 Conclusions and Future Work

In this study, encoder-decoder-based time series forecasting models are used for jointly modeling two bridges in a highway corridor. A synthetic dataset is generated using the CSiBridge finite element models to simulate the responses of two bridges to the same moving loads observed in the field. The load properties were sampled from the actual measurements captured by the WIMS station along the instrumented highway corridor. Slight perturbations were added to the speed of the load to make the dataset more realistic. For the encoder-decoder model, two types of recurrent cell units, namely GRU and LSTM, are tested to predict the responses of the NRB using those of the TRB as inputs. Both models showed equally competitive results. An ARX model is also tested as a linear variant of the Seq2Seq models for the task at hand. Both encoder-decoder models outperformed the ARX model in terms of accuracy and inference time required for the model.

In future studies, we will seek to implement these models on the experimental dataset captured from the actual bridges. In such data sets, a lower signal-to-noise ratio (SNR) is expected which may challenge the Seq2Seq models. Besides, actual datasets also reflect many more complicated factors that may influence the performance of the model, including the lateral position of a truck on its lane, larger speed variation for trucks passing two bridges, stochastic vehicle bounce and so forth. In fact, bridge response may not always resemble the same responses to the same vehicular loads due to possible causes like temporarily locked bearings [95]. Fortunately, as shown in Chap-

ter 2, a large set of data has already been collected on the two bridges and the size of the data is keep growing, allowing a more robust and complex model to be trained. Furthermore, we seek to investigate the capability of the models in damage detection using a synthetic dataset and compare it with those of the state-of-the-art methods.

CHAPTER 8.

Learning-based Bridge Weigh-in-motion

8.1 Introduction

Freight transportation is an indispensable part of everyday economic activities. Among all types of national freight transportation, truck-based freight transportation dominates as it accounts for 77.5% of the entire freight volume within the United States [270]. As trucks heavily rely on well-maintained highway infrastructures to travel, it has become a common practice across the world to implement laws limiting truck weight and size with the purpose of extending the lifespan of infrastructures (such as bridges) and protecting public safety from severe traffic accidents. Real-time truck weight measurements such as gross weight and axle weight play an important role in the enforcement of highway truck size and weight regulations. The long-term statistics also provide a rational basis for freight transportation planning and highway asset management. Conventional weigh stations and pavement-based weigh-in-motion (WIM) stations are two main types of highway infrastructures for obtaining truck weight measurements in the United States [288]. Conventional weigh station requires trucks to pull over from highways and measure weights of axle (or axle group) one by one. Doing so provides accurate measurements of truck load characteristics but adds additional travel time to freight transportation lowering the efficiency. On the contrary, the WIM station is capable of measuring truck weights without slowing them down at the expense of sacrificing accuracy. WIM stations usually have weighing sensors (e.g., piezoelectric sensors, bending plates scales or single load cell scales) buried underneath highway pavements and connected to data acquisition and power systems. As a result, it is naturally costly to install and maintain WIM stations.

Recently, the emergence of bridge WIM technology presents a more cost-effective alternative for weighing trucks. Extensive studies and field tests have been conducted over the past decade on bridge WIM technology [115, 289, 290]. With sensors (most commonly strain gauges) installed in bridges, bridge WIM methods rely on measured bridge responses (e.g., strain) to derive weights of passing trucks in real time. Existing bridge WIM methods are mainly based on Moses's algorithm developed in 1979 [267]. Based on the assumption of linear superposition, once an accurate unit influence line (UIL) is identified, the calculation can be formed as an inverse problem which is solvable through the least squares methods [267, 115]. This method can be combined with other optimization techniques such as Tikhonov regularization to further improve accuracy without adding new instrumentation [291]. The accuracy of such a method heavily depends on the quality of extracted UIL. Several methods have been proposed to improve the quality of UIL by using calibrated FEM models [292] or site-specific strain response measurements to test trucks [265, 293]. The UIL-based method also requires vehicle speed, the number of axles and axle spacing to be determined before the calculation of axle weight [294]. Conventional bridge WIM methods usually deploy axle detector (e.g., laser sensors) on bridge road surfaces to directly detect axles. Recently, researcher have proposed nothing-on-the-road (NOR) or Free-of-Axle Detector (FAD) approaches for bridge WIM [295]. Wavelet domain analysis [296, 297] and virtual simply supported beam methods [294] have been proven to be able to extract axle information from strain data. Optimization such Lasso regression with L1-norm is another approach to identify the number of axles for the target vehicle [298, 299, 300].

Apart from mechanics-based bridge WIM methods, studies have also been done to explore the use of machine learning in predicting truck weight information from bridge response measurements. The use of artificial neural networks (ANN) to compute axle weight can be traced back to as early as 1992 before the success of modern deep learning [301, 302]. Due to immature development of deep learning and limited computational power, the flexibility of the models is limited at that time. More recently, the ANN method was tested on real bridges with nearby WIM data and corresponding bridge response measurements as training data [303]. However, three separate

networks are required to derive axle weights and the models are only trained on truck with less than 6 axles. Besides, convolutional neural networks (CNN) can be used for identifying axle number, vehicle type and vehicle speed for UIL-based bridge WIM with a higher accuracy [304].

In this study, a novel learning-based bridge WIM method is proposed leveraging the recent advances in recurrent neural networks (RNN). Utilizing a large volume of paired bridge response and WIM data, a bidirectional RNN model is trained to predict truck weight characteristics including axle weight, axle spacing, gross weight and travel lane with length-variant bridge strain responses as inputs. The proposed method is evaluated using simulation data obtained from finite element models and proven to be more accurate than the influence line-based bridge WIM method. It is also shown that the proposed method is robust enough against sensing noises in training data, especially the noises contained in WIM data. A computer vision-enabled cyber-physical system is implemented as a test-bed along a 20-mile I-275 northbound highway corridor in Michigan to demonstrate the viability of such a learning-based bridge-WIM in real world.

8.2 RNN-based Bridge Weigh-in-motion

Considering the long-duration interaction between a bridge and vehicles, sequential bridge responses contain rich information regarding the characteristics of corresponding vehicles that induce the responses. In this study, an RNN-based machine learning model is proposed to map bridge responses to vehicular load parameters. The proposed model takes sequential bridge responses as inputs and outputs properties of interests of corresponding passing vehicles. Fed with sufficient training data (i.e., bridge responses and ground-truth traffic load properties), the model can learn the knowledge of the bridge system through proper training. Compared to pavement-based WIM stations, such an approach allows a handful of sensors to be easily deployed in a bridge with a relatively low cost for the same purposes.

8.2.1 Model Architecture

A bi-directional RNN model is utilized for predicting vehicular load parameters using induced bridge responses as inputs. The architecture of the model is shown in Figure 8-1. The input sequence (i.e., bridge responses) are represented by $S = \{s^1, s^2, s^3, ..., s^T\}$ where T is the length of the input sequence, $s^t \in \mathbb{R}^m$ contains bridge response measurements from multiple (m) installed sensors for any specific time step t and $s^t = \{s_1^t, s_2^t, ..., s_m^t\}$. The bi-directional RNN is made up of two sets of RNN, namely a forward RNN unit and a backward (or reverse) RNN unit. The

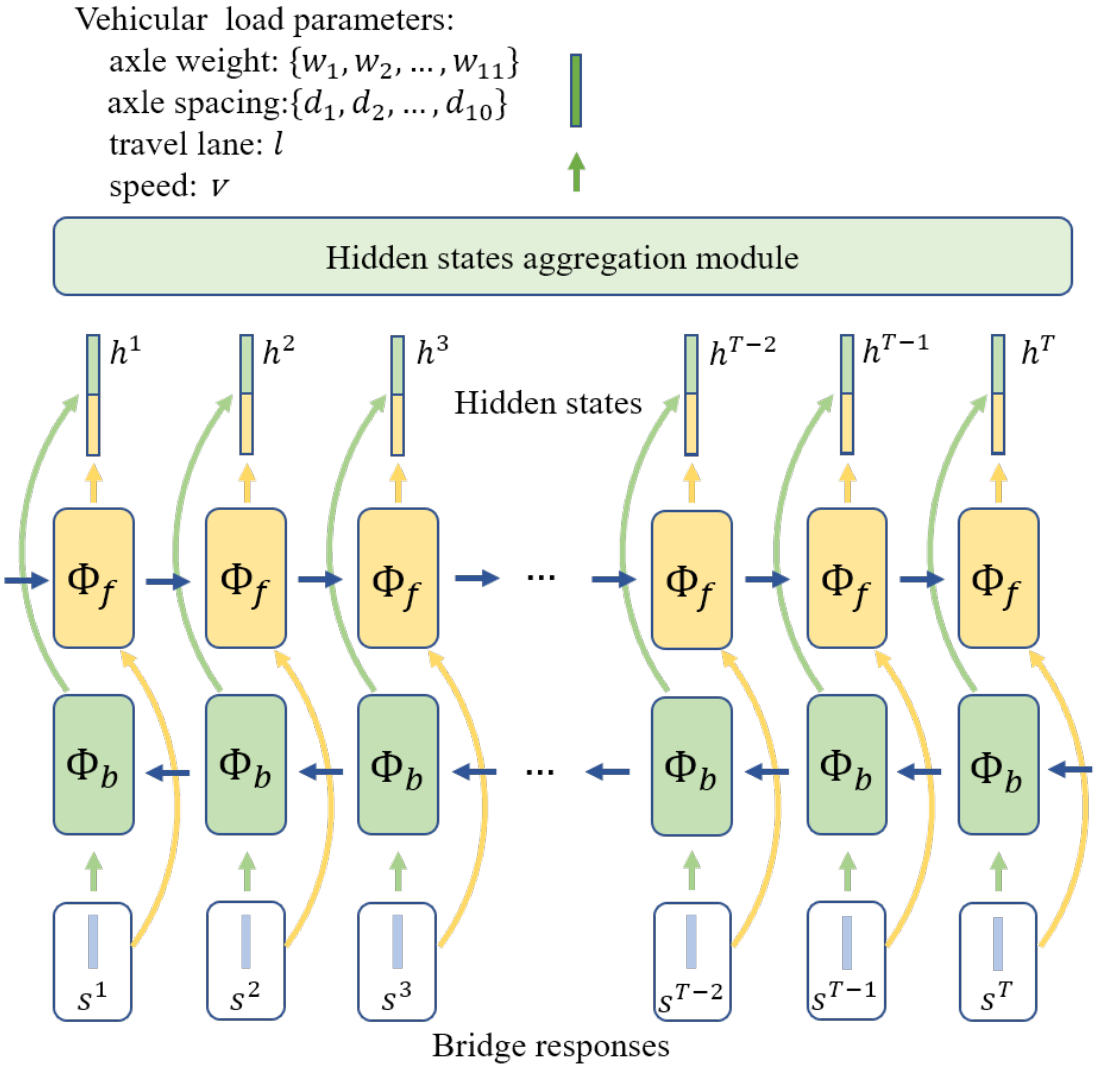

Figure 8-1: Bi-directional RNN architecture for estimating traffic load characteristics using corresponding sequential bridge responses.

forward RNN, represented by Φ_f, goes through the sequential inputs from the beginning to the end and the backward RNN, represented by Φ_b does the opposite. The RNN used in this section is the long short-term memory (LSTM) unit described in subsection 7.2.2 and it is a common practice to define the two RNNs in the opposite directions with weights of the same dimensions. The entire input sequence is available before inference instead of being seen by the model in an online (one-by-one) manner. At each time step t, a bridge measurement vector s^t is fed into both the forward RNN and the backward RNN along with the hidden states (h in Figure 7-2(b)) and cell states (c in Figure 7-2(b)) from the previous step. In the meanwhile, a concatenation of the hidden states from two directions will be returned at each time step as $h^t \in \mathbb{R}^{2\hat{H}}$, resulting in a sequence of hidden states containing extracted information eventually. The $\hat{H}$ is the pre-defined dimension of the hidden state in each direction. The returned hidden state sequence can be treated as a matrix, H, of shape $\mathbb{R}^{T\times 2\hat{H}}$. Given the hidden states, different types of manipulations, which will be described in the following subsections, can be used to convert them to the form of desired outputs. The model outputs are vehicular load characteristics such as axle weight, axle spacing, travel lane on the bridge and vehicle speed, etc. Depending on the design and training data available, the model can predict one or multiple types of load characteristics in a multi-task learning fashion. The axle weight is expressed as a 11-dimension vector as the maximum number of axles allowed in Michigan is 11. If a truck has less than 11 axles, the extra entries at the tail of this vector will just be set as 0. The same logic is also used to handle axle spacing such that the output has a fixed length.

8.2.2 Hidden States Aggregation Module

This subsection describes several types of hidden states aggregation modules evaluated in this study. Such a module aims to encoding a variable length of hidden state sequence to a fixed length embedding and ultimately truck load characteristics. The most straightforward approach is to concatenate the last-step hidden state of the forward RNN ($t = T$) and that of the backward RNN ($t = 1$) and then feed the concatenated hidden state into a multi-layer full connected neural

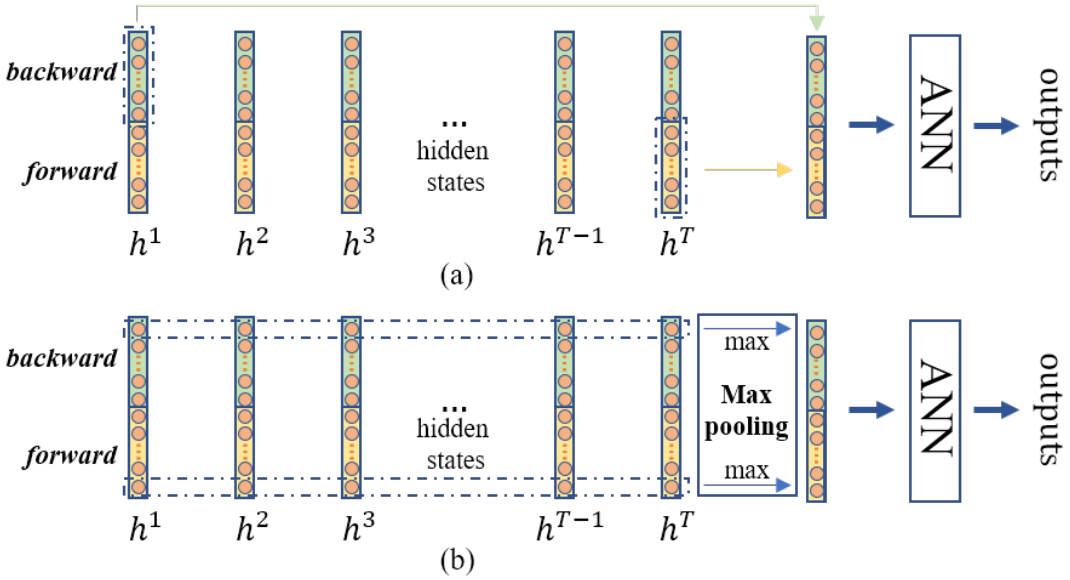

Figure 8-2: Architectures of hidden states aggregation module: (a) concatenation of last-step hidden states of RNNs in forward and backward directions; (b) max-pooling of all hidden states generated by the bi-directional RNN model along the direction of input sequence.

network (same as ANN). The function of the ANN is to perform another layer of linear and non-linear transformation for dimension reduction such that the final desired output can be generated. This process is illustrated in Figure 8-2(a).

Another way of aggregation is to take hidden states at all time steps into account and use a max pooling layer to extract the max value in each dimension of the hidden states along the sequence direction as shown in Figure 8-2(b). The extracted hidden state vector will also be passed through a ANN to produce the final predictions. Even though the bi-directional RNN goes through the entire sequence of strain response input, it is known that RNN may perform poorly on memorizing the information extracted from early steps till the last step [305]. As a result, max-pooling the entire set of hidden states has the benefit of aggregating all potentially useful information extracted by the RNN along the sequence. In addition, compared with the module taking the last-step hidden states in two directions, this max-pooling approach only adds a negligible computation overhead.

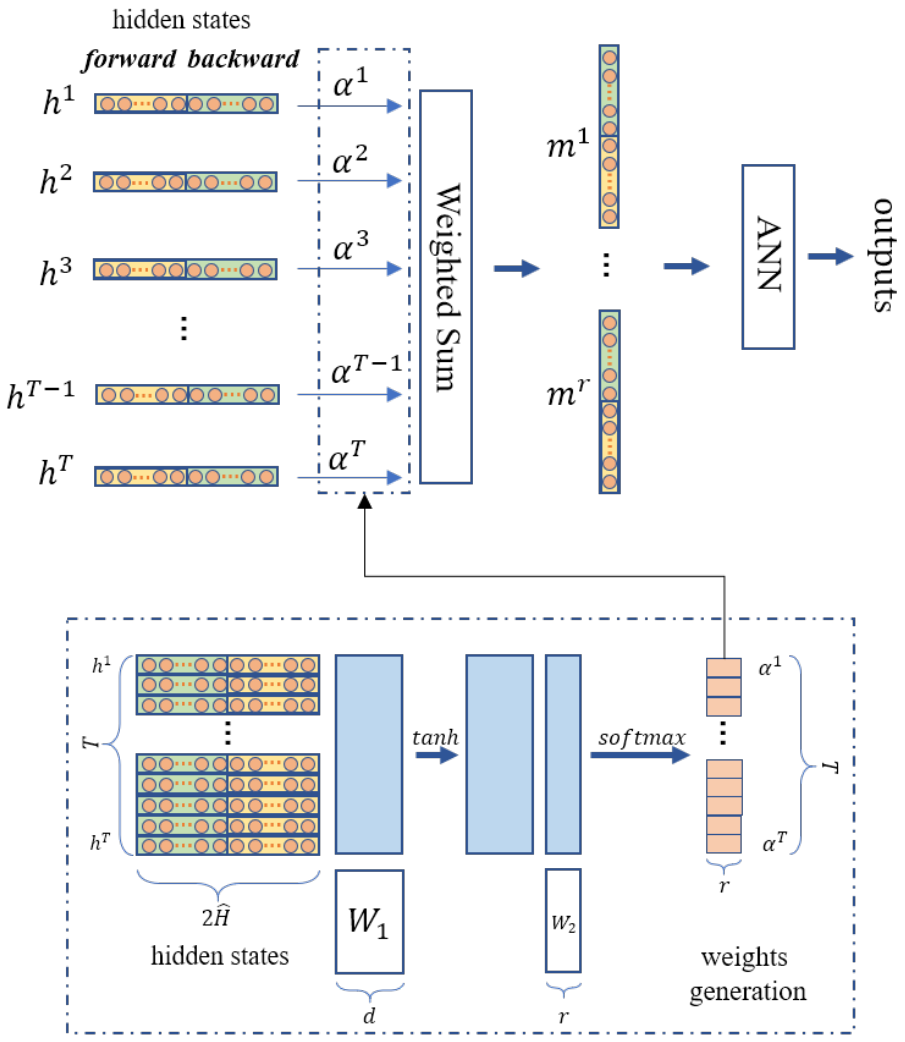

Figure 8-3: Architecture of the self-attention mechanism .

8.2.3 Attention Mechanism

A more complicated approach to aggregate the generated hidden states is to use the self-attention mechanism, whose process is illustrated in Figure 8-3 [306]. In general, the attention mechanism can be considered as a way to take one or multiple weighted sum of the hidden states generated at all time steps [306]. It is called self-attention in that the weights used for weighted summation of hidden states are computed directly from the hidden states themselves. The process takes the entire set of hidden states, $H \in \mathbb{R}^{T \times 2\hat{H}}$, as inputs and outputs a matrix $A \in \mathbb{R}^{r \times T}$ for aggregating the hidden states in a weighted summation approach where $A = \{\alpha^1, \alpha^2, ..., \alpha^T\}$ and $\alpha^t \in \mathbb{R}^r$.

This process can be formulated as

$$A = \textit{softmax}(W_{s2} tanh(W_{s1} H^T)) \tag{8.1}$$

where $W_{s1} \in \mathbb{R}^{d \times 2\hat{H}}$ and $W_{s2} \in \mathbb{R}^{r \times d}$ are two trainable weight matrices responsible for linear transformation. In addition, $tanh(x)$ is the hyperbolic tangent activation function:

$$tanh(x) = \frac{e^x - e^{-x}}{e^x + e^{-x}} \tag{8.2}$$

and the general *softmax* function takes a vector x as its input and outputs a normalized vector whose summation is 1, which can be expressed as Equation 8.3. It is used to convert a vector of a finite number of entries to a virtual probability distribution, which is used here as the weights for weighted summation. In this sense, the purpose of self-attention mechanism is actually to redistribute the importance of hidden states at different time steps for aggregation. It should be noted that the A contains r groups of weights which can be used to generate r distinct aggregated vectors. These r vectors can be concatenated as an integrated embedding and fed into ANN for final predictions. In addition to r, the dimension d of the two intermediate weight matrices is also a parameter that needs to be defined manually. Compared with the two approaches described in the previous section, the self-attention mechanism shown here provides a more flexible and dynamic way for encoding the bridge response sequence into a fixed-length embedding. In this study, we simply set $r = 1$.

$$softmax(\mathbf{x}) = e^{\mathbf{x}} / \sum e^{\mathbf{x}} \tag{8.3}$$

8.3 Experiments on FEM Simulation Generated Data

The proposed method is first evaluated using simulation data generated from a finite element model before being applied to the real-world dataset. For supervised learning like the proposed learning-based bridge WIM, the training data always includes model inputs (i.e., bridge responses) and

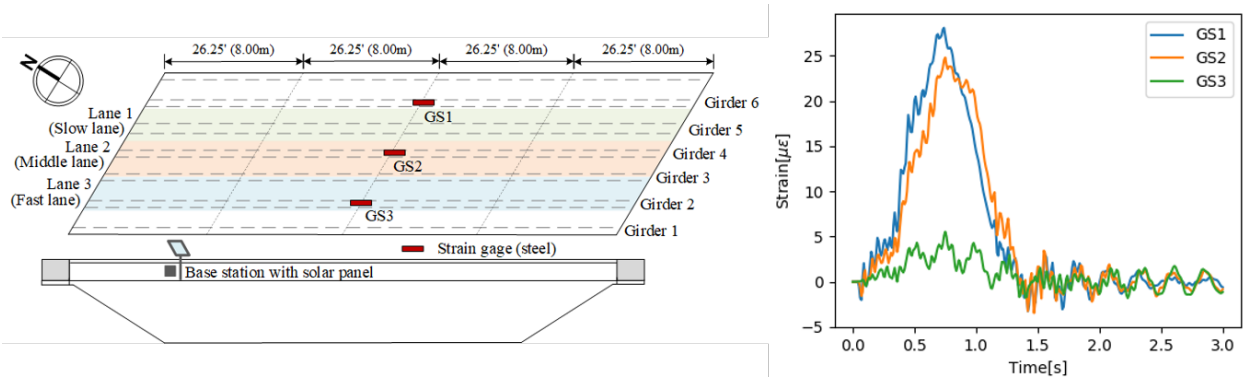

Figure 8-4: Sample of simulation data (from left to right): a) layout of Newburg Road Bridge wireless sensor network; b) time-histories of strain gauge measurements generated from finite element modeling simulation.

ground-truth labels (truck load characteristics such as truck axle weights). In this study, the labels are the WIM measurements that have been matched with corresponding bridge responses. However, errors are associated with load measurements captured by real-world WIM sensors due to intrinsic system errors in equipment and dynamic interaction between vehicle axle and pavements. The WIM station along the I-275 is a type II WIM station which may subject to up to 30% relative error with respect to axle weight and 15% relative error with respect to vehicle gross weight in terms of the 95^{th} percentile error [255]. As a result, the labels of training data available in real-world dataset is noisy. Evaluating the model with simulation data allows us to start with training data without noises to test the effectiveness of models with different types of hidden state aggregation modules and its robustness against noises in labels, which cannot be achieved with real-world data.

8.3.1 Dataset

A picture of the selected finite element model is shown in Figure 7-5(b). The bridge model is built based on the engineering drawings of the Newburg Road Bridge and calibrated using bridge response measurements. In this experiment, only a single loading scenario where trucks traverse the bridge using the slow lane is considered. The slow lane is the most common lane that trucks use in reality. Additionally, the model output is set to be only the 11-dimension truck axle weight

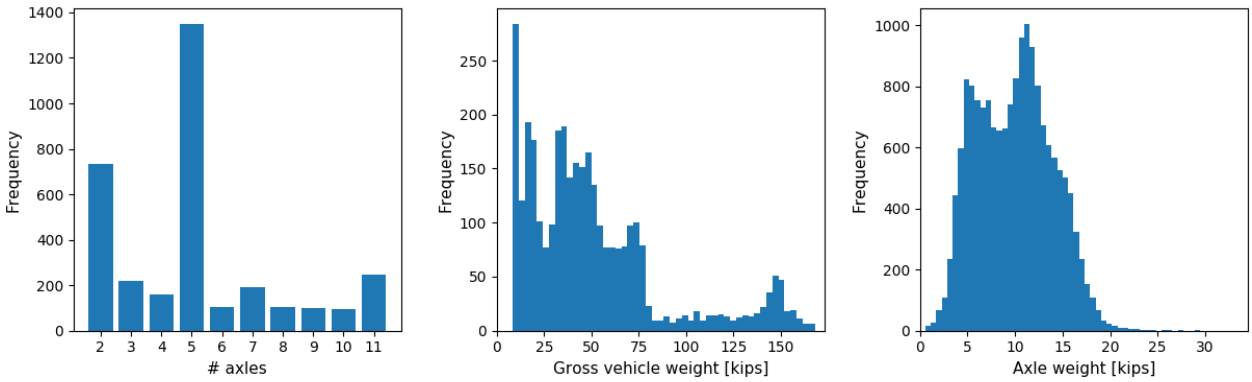

Figure 8-5: Statistics of simulation data for model training (from left to right): 1) distribution of axle numbers; 2) distribution of gross vehicle weight; 3) distribution of axle weight.

at this stage and the vehicle gross weight can be calculated easily by summing all axle weights. More complicated combination of model outputs is left for future work using a multi-task learning method. To generate bridge responses, we randomly take samples of real truck load measurements captured by the WIM station along the I-275 northbound corridor as truck loads to stimulate the bridge model. Bridge response time-histories from 3 virtual sensors (GS1, GS2 and GS3 shown in Figure 8-4(a)) are extracted through simulation and a sample dataset is plotted in Figure 8-4(b). The three sensors are installed to the girder web at mid span 3 inches (7.62 cm) above the bottom flange on the corresponding girders. Accordingly, the m described in the subsection 8.2.1 is 3. A simulation dataset containing totally 3800 bridge response sequences to truck events are generated eventually. Among these 3800 sequences, 3300 of them are used for model training, 200 are used for model evaluation and the rest 300 are used for model testing. Statistics regarding training data including the distribution of the number of axles, axle weight and vehicle gross weight are shown in Figure 8-5. The distributions for the evaluation and test datasets are similar. It can be observed that the data is imbalanced in terms of the number of axles as it is most common to see 5-, 2- and 11-axle trucks and less common for the other types. The gross vehicle weight in the sample dataset ranges from 8.42 kips to 168.93 kips and the axle weight ranges from 0.54 kips to 29.46 kips. Since the bridge response sequences are generated from the finite element model, it is possible to make all of them have the same length which is 301 here.

8.3.2 Model Training

To train the proposed model to learn to predict truck load axle weights from bridge responses, we feed the training data with a mini-batch of 20 sequences. The Adam optimizer [188] with an initial learning rate of 0.01 is used for updating network weight through the training. The learning rate (lr) is decreased following an exponential function of epoch number as follows:

$$lr_{epoch} = lr_0 \times 0.96^{epoch} \tag{8.4}$$

In addition, a norm-based gradient clip with the maximum set to be 2 is employed for a more stable convergence. The dimension of hidden state in each direction is set to be 512 and all initial hidden states are set to vectors containing all zeros. The maximum training epoch is set to 250 and an early stop strategy is used depending on the evolution of evaluation loss through training. For the experiments described in this section, we only predict a 11-dimension axle weight w for each set of bridge strain response sequences. The loss function is formulated as follows to impose supervision on each axle weight value:

$$\mathbb{L} = L1_{smooth}(w_{pred}, w_{label}) \tag{8.5}$$

where the w_{pred} is the predicted axle weight vector, w_{label} is the ground-truth axle weight vector, and the L1 smooth function is defined as follows:

$$\begin{aligned} L1_{smooth}(x, y) &= \frac{1}{n}\sum_i z_i \\ z_i &= \begin{cases} 0.5(x_i - y_i)^2, if\ |x_i - y_i| < 1 \\ |x_i - y_i| - 0.5, otherwise \end{cases} \end{aligned} \tag{8.6}$$

	Avg. axle weight error	95^{th} axle weight error	Avg. gross weight error	95^{th} gross weight error	# axle accuracy	Inference time
Last-step	13.86%	46.33%	3.35%	9.56%	65.67%	**0.0121 sec**
Max-pooling	**7.56%**	**25.97%**	**1.66%**	**5.88%**	**89.00%**	0.0123 sec
Self-attention	13.04%	44.89%	2.71%	8.83%	83.67%	0.0125 sec

Table 8-1: Test results for the proposed model with three types of hidden state aggregation modules.

8.3.3 Evaluation

The evaluation in this section includes two parts. Firstly, the accuracy of the three types of hidden state aggregation modules is investigated to select the best for real-world use. Secondly, the robustness of the proposed model against noises in training labels is tested for the selected model after the first stage.

The accuracy of the model is evaluated with five metrics, namely average axle weight error, average vehicle gross weight error, 95^{th} percentile of axle weight error, 95^{th} percentile of vehicle gross weight error and axle number accuracy. For a specific kind of weight xw (i.e., axle weight or gross weight), the error, e, is defined as Equation 8.7 [255]:

$$e = \frac{|xw_{pred} - xw_{label}|}{xw_{label}} \tag{8.7}$$

The error is only calculated based on ground-truth labels and zero-value axle weight is not counted. For example, if the model predicts out 6 non-zero axle weights for a 5-axle truck the last axle weight is not calculated since the error will be infinite. The amplitude of the 95^{th} percentile error is determined such that 95% of the calculated errors are smaller than this value. Regarding the accuracy of axle number, for a specific truck, if the model predict the correct number of axles it counts one towards true positives and the final accuracy is calculated as the ratio of true positives over the total number of trucks. Apart from accuracy, we also compare the inference time to proceed a single sequence with the same length among three different variations. The training and test are both performed using a Nvidia XP GPU.

Noisiness Level (95^{th} percentile)	0%	2.5%	5%	10%	20%	30%
Avg. axle weight error	7.56%	8.27%	9.02 %	9.48%	9.43%	10.09%
95^{th} axle weight error	25.97%	27.93%	30.41%	31.27%	29.76%	31.94%
Avg. gross weight error	1.66%	1.63%	2.56%	2.57%	2.79%	2.95%
95^{th} gross weight error	5.88%	5.11%	8.62%	8.16%	9.68%	8.69%
# axle accuracy	89.00%	87.67%	86.67%	86.67%	88.67%	88.67%

Table 8-2: Test results for the proposed model with training labels corrupted with Gaussian noise errors.

Three variations of the proposed model with different hidden state modules are trained and tested using the test dataset with the metrics described above. The results are shown in Table 8-1. It can be observed from the table that the max-pooling approach obtained the best performance in terms of accuracy. Both the 95^{th} axle weight error (25.97%) and the 95^{th} gross weight error (5.88%) meet the accuracy requirement of a Type II WIM station. All three approaches exhibit very close inference speed. Compared to the ground-truth labels, most of the negative samples with wrongly predicted axle numbers have a difference of 1. Based on the above outcome, the bi-directional LSTM model with the max-pooling aggregation module is selected for further analysis.

Real-world WIM station measurements suffer a certain level of noises following a normal distribution [307]. To test the robustness of the model against noisy training labels, Gaussian noises are randomly sampled to corrupt the training labels (i.e., axle weights). The mean of the Gaussian noise is always 0 and the noises are added in terms of relative error according to Equation 8.7. Five stages of noisiness levels are tested where the standard deviation of the Gaussian error distribution, σ, is increased following the set $\{0, 0.0125, 0.025, 0.05, 0.01, 0.015\}$ resulting in the 95^{th} percentile error in axle weights being 0, 2.5%, 5%, 10%, 20% and 30%, respectively. It should be noted that even though the model is trained using noisy labels it is still tested using uncorrected test labels. The results of the experiment is shown in Table 8-2 and Figure 8-6. It can be observed that with an increased level of noisiness, the accuracy of the model doesn't degrade much. With a 30% noisiness level, the accuracy of the model can still nearly satisfy the requirements of a Type II WIM station. As a result, it can be concluded that it is possible to train a model based on corrupted

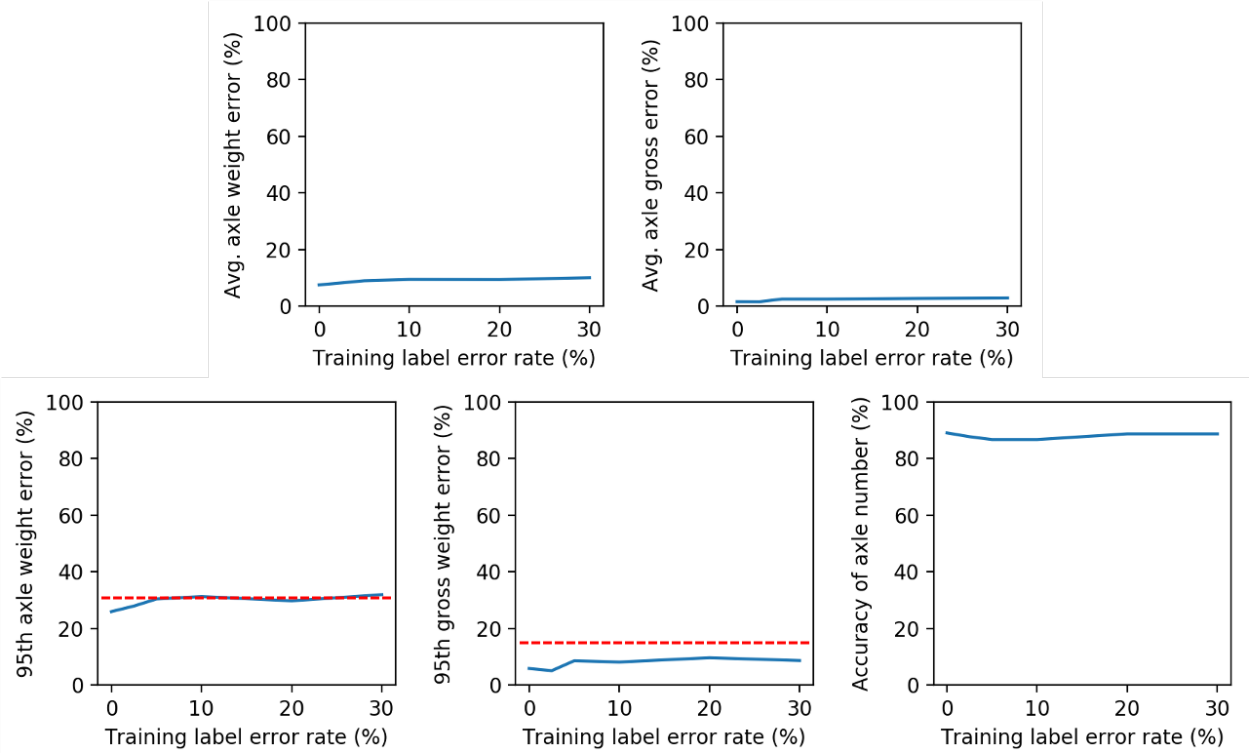

Figure 8-6: Model performance degradation trends with increased levels of noisiness. (Note: red dash lines represent precision requirements for a type II WIM station.)

training data generated from a Type II WIM station to meet the same criterion for the same type of WIM station. Besides, it is very likely that better tuned parameters and more training data can help further improve model performance.

8.4 Experiments on Collected Data

In this section, the proposed bi-directional LSTM method, especially the variant with the max-pooling hidden state aggregation module, will be tested using real-world data for learning-based bridge WIM.

8.4.1 Dataset and Model Training

Bridge strain responses measured by three strain gauges installed in the same locations as the virtual sensors, namely GS1, GS2 and GS3 are used as model inputs to test the effectiveness of the proposed method. Unlike the experiments conducted on simulation data, the loading scenarios of

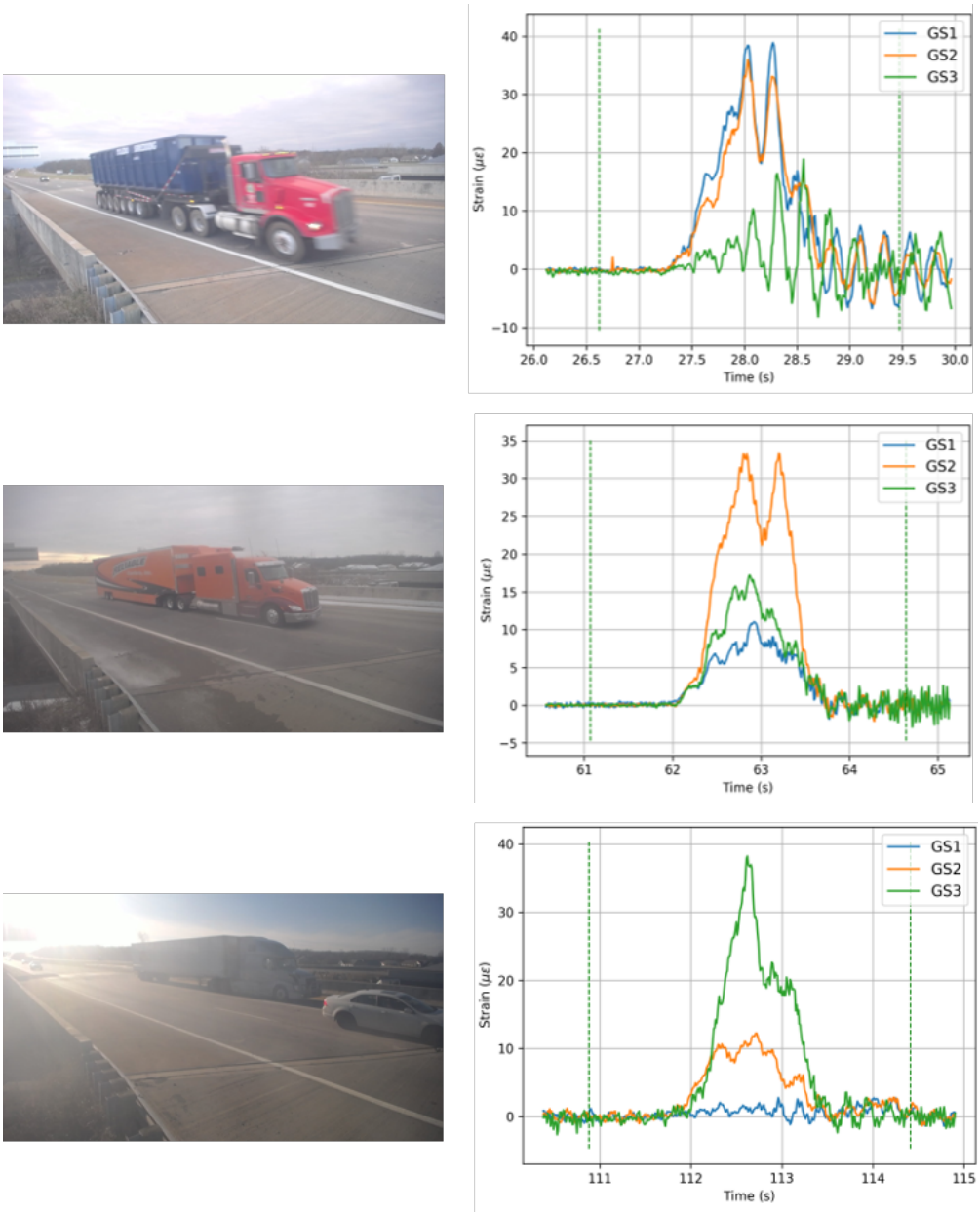

Figure 8-7: Bridge response samples using different lanes of the Newburg Road Bridge along with corresponding traffic images. (Note: two vertical dash lines represent the left and right boundaries based on which bridge responses to truck events are segmented accordingly.)

all three lanes are considered in real data-based experiments. However, the dataset is still limited to the cases where only one truck is on the bridge. Three sample sets of strain response sequences with trucks using different lanes are shown in Figure 8-7 along with corresponding traffic images. The responses to specific truck events are segmented from the entire collected data sequences. The left and right boundaries are notated using vertical dash lines in Figure 8-7.

In total, a dataset containing 7410 truck events, with each event includes bridge strain responses measured at 3 the strain gauges and corresponding truck load measurements, is used to demonstrate the propose method using real-world data. Among the 7410 truck events, 3751, 3635 and 24 trucks passed the bridge using the slow lane, middle lane and fast lane, respectively. The distribution of the number of truck axles, axle weights and vehicle gross weights are similar to the ones shown in Figure 8-5. The dataset is split into three sub-dataset, namely training, evaluation and test, consisting of 6670, 370 and 370 events, respectively. For this dataset, the maximum sequence length is 1160 which is much longer than the simulation data. Such a fact makes learning on real-world data more challenging. To achieve batch training, sequences with length less than 1160 are padded with zeros at tail such that all input sequences share the same length.

The model with the max-pooling method is trained with the dataset with the aim of predicting 11-dimension axle weights. The training strategy (including batch size, optimizer, etc.) and loss function are kept identical to the experiments performed on simulation data. The only difference is that the initial learning rate is adjusted to 0.025 for a more rapid learning.

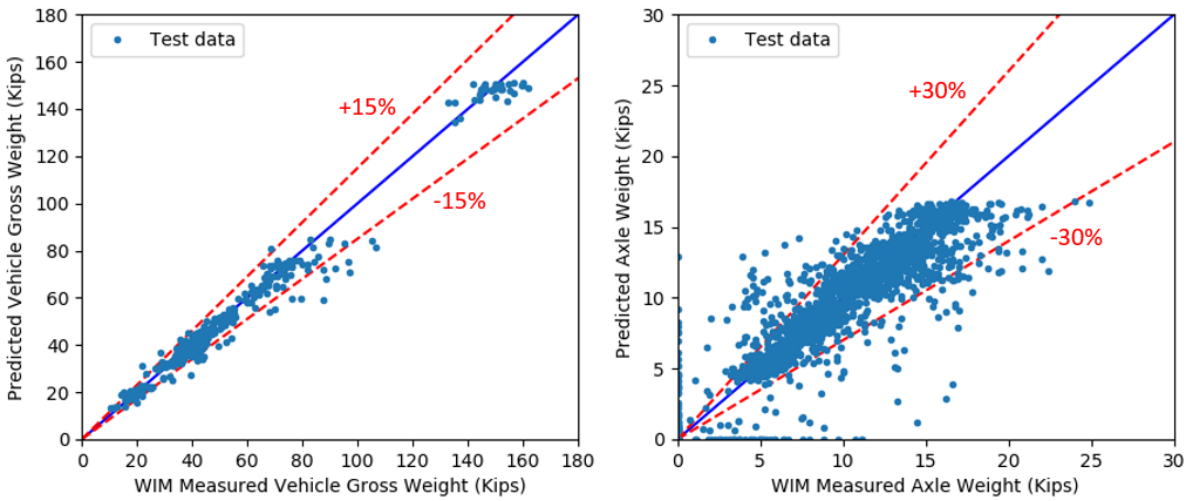

Figure 8-8: Scatter plots on the predicted values of vehicle gross weights and axle weights and corresponding WIM measurements in the test dataset.

8.4.2 Evaluation

Due to the lack of ground-truth labels (i.e., static axle weights), it is impossible to evaluate the accuracy of the trained model like what has been conducted in the previous section. Instead, for the test dataset, predicted truck weights (both gross weights and axle weights) and WIM-measured truck weights are plotted in Figure 8-8 in the form of scatter plots to show their correlation. Plotted at the same are the precision limits represented by red dash lines. The limits for gross weights and axle weights are $\pm 15\%$ and $\pm 30\%$, respectively.

8.5 Summary and Conclusions

Real-time truck weight measurements such as gross weight and axle weight play an important role in the enforcement of highway truck size and weight regulations. The long-term statistics also provide a rational basis for freight transportation planning and highway asset management. Recently, the emergence of bridge WIM technology presents a more cost-effective alternative for weighing trucks. With sensors installed in bridges, bridge WIM relies on measured bridge responses to derive weights of passing trucks in real time. In this study, a learning-based bridge WIM method is proposed. Utilizing a large volume of paired bridge response and WIM data, a bidirectional LSTM network is trained to predict truck weight characteristics including axle weights and gross weight with bridge strain responses as inputs. The proposed method is evaluated using simulation data obtained from finite element models and proven to be sufficiently accurate for a type II WIM station. The robustness of the proposed method against sensing noises in training data is also investigated. A computer vision-enabled cyber-physical system is implemented as a test-bed along a 20-mile I-275 northbound highway corridor in Michigan. Evaluation using real-world dataset also demonstrates the feasibility of the proposed bridge WIM approach.

With proper cyber-physical system-enabled enhancements, existing bridge structural health monitoring systems can be transformed into a bridge WIM station using the proposed method. According to the traffic statistics made available by the MDOT, the commercial annual average

daily traffic (AADT) along the selected I-275 corridor is 8,836, which means a few days' CPS data might be sufficient for the training of the proposed learning-based bridge WIM method. For future work,the effects of more factors, such as ambient temperature, size of training dataset, sensor locations, sensing sampling rate, etc. on the accuracy of the bridge WIM system will be investigated.

CHAPTER 9.

Conclusions

9.1 Summary of Results and Contributions

Bridge structural health monitoring (SHM) has been intensively studied by researchers and industrial companies over the last decade and increasingly more real-world bridges have been instrumented with long-term SHM systems for structural condition monitoring [38]. While rapid improvements in bridge SHM have been achieved, there remain technical challenges associated with existing methodologies. A major limitation is the lack of information and data of traffic loads (such as vehicle weight) which is one of the major consumers of the service life of bridge infrastructures, especially for medium- and short-span bridges [129]. As a result, existing bridge SHM approaches heavily rely on bridge response data and output-only methods hindering their accuracy. To resolve this issue, this dissertation focuses on the development and applications of cyber-physical systems (CPS) to enhance existing highway bridge SHM systems including tracking truck loads in highway corridors and in doing so, offering insight to loads (inputs) inducing the bridge responses (outputs) measured. With a powerful CPS deployed, novel SHM applications can be built upon it that improve asset management decisions.

In this study, a CPS-enabled bridge SHM framework is proposed where bridge SHM systems and intelligent transportation system sensing technologies (e.g., traffic cameras and WIM stations) are linked together to form an integrated information network. The work focused on linking two bridges (Telegraph Road Bridge and Newburg Road Bridge) with measurement of truck weights along a 20-mile long corridor of northbound I-275 between Newport and Romulus, Michigan. Leveraging the implemented CPS, this thesis managed to collect abundant bridge input and output

data which has not been available for SHM analysis in the past. The acquired data not only allows novel bridge SHM methods to be developed and but also opens up the possibility of using SHM systems for traffic load monitoring. In addition, the value of SHM methods to inform infrastructure management is clearly showed in this thesis using the practical real-world implementation of two operational bridges. Specific infrastructure management applications included the assessment of long-term bridge deck deterioration and bridge load rating. To the author's best knowledge, this is the first time such a system has been developed to scalably collect truck weight data for improved assessment of bridge performance and health by the SHM community. With that said, the major contribution of this study can be summarized as: 1) proposed and implemented a CPS-enabled bridge SHM network and demonstrated the viability and effectiveness of an automated data collection network in real world bridge applications; 2) proposed and evaluated several novel data-driven bridge SHM and highway traffic load monitoring methods based on the wealth of collected CPS data collected over multiple years, showing the great value that bridge SHM systems can bring to highway asset management. The summary and contribution of each chapter are summarized as follows.

In Chapter 2 and Chapter 3, a cyber-physical system (CPS) framework was proposed, designed and deployed to track truck loads in a highway corridor, to trigger SHM systems to record bridge responses, and to automate the linking of bridge response data with truck weights collected by weigh-in-motion (WIM) stations installed along the corridor but not collocated (i.e., separated miles apart) with the bridges. To link truck weights to bridge responses, computer vision methods based on convolutional neural network (CNN) architectures were used to automate the detection and re-identification of trucks using traffic cameras. The single-stage CNN object detector YOLO was trained using a customized dataset to identify trucks from camera images at each instrumentation site; a high precision in vehicle detection was obtained with the YOLO detector exceeding 95% average precision (AP) for an intersection over union (IOU) threshold of 0.75. To re-identify the same truck at different locations in the corridor, a CNN-based encoder trained via a triplet network and a mutual nearest neighbor strategy using feature vectors extracted from images at each

measurement location were adopted. The proposed re-identification method was implemented in the CPS cloud environment and obtained an F1-score of 0.97. The study also explored the triggering of bridge monitoring systems based on visual detection of trucks by a traffic camera installed upstream to the bridges. The triggering strategy proved to be highly efficient with 99% of the triggered data collection cycles capturing truck events at each bridge. To validate, the CPS architecture was implemented on the aforementioned 20-mile highway corridor along I-275 that has a WIM station already installed; four traffic cameras and two bridge SHM systems were installed along the corridor and integrated with a CPS architecture hosted on the cloud. In total, over 20,000 trucks were observed at all measurement locations over a one year period alone, allowing peak bridge responses to be correlated to both measured truck weights and to one another.

In Chapter 4, long-term bridge monitoring data collected by the deployed CPS architecture was used to quantitatively assess the composite action exhibited in slab-on-girder highway bridges and to investigate the potential relationship between composite action and deck deterioration over negative bending regions. Telegraph Road Bridge, a three-span highway bridge in Michigan, was instrumented with a wireless structural monitoring system to observe the flexural response of the three spans to vehicular loads. The monitoring system was designed to offer data for quantitative assessment of the degree of composite action in composite and non-composite sections of the bridge spans using the position of neutral axis and the magnitude of slip strain at the concrete-steel interface as key response parameters correlated to composite action. It was shown that unintended (i.e., not accounted for in the slab design) nonlinear partial composite action exists in negative bending regions of the bridge. A calibrated analytical model and a finite-element model were developed based on empirical observation allowing tensile strains in the deck to be estimated under load. Estimated surface strains were compared with those with the design assumption of no composite action at the slab–girder interface in the negative bending regions. It was concluded that the observed partial composite action is resulting in higher tensile strains in the deck top surface which is a likely culprit to accelerated deck deterioration.

Chapter 5 presented a data-driven approach for site-specific bridge load rating empowered by

measurements of truck loads. Current bridge rating practices rely on simplified (i.e. approximate) analytical models and empirical parameters which do not reflect site-specific behavioral properties of the target bridge, rendering resultant rating factors overly conservative [234, 235]. To reduce the conservatism associated with conventional bridge rating methods, this study proposed a data-driven approach to incorporate bridge-specific behavioral responses to offer more accurate model parameters into the rating process detailed by the Load and Resistance Factor Rating framework of AASHTO. Among all relevant parameters, those used for calculating live load effects, especially dynamic load allowance and unit influence lines, were extracted in a probabilistic manner from integrated bridge structural responses and weigh-in-motion truck weight data collected by the CPS framework leveraging computer vision techniques. To demonstrate the proposed data-driven rating method, the Telegraph Road Bridge and Newburg Road Bridge instrumented with long-term wireless bridge SHM systems were selected as test targets. Totally, six girder components of the two instrumented highway bridges were rated using the proposed method and the rating factors were compared with those obtained using conventional approximate and refined (i.e., finite element model-based) methods.

Chapter 6 introduced a comprehensive wireless monitoring system that seamlessly integrated a mobile wireless sensor network installed in a tractor-trailer truck to measure dynamic truck behavior with a stationary wireless monitoring system installed in a bridge to measure vibrations and strains. Doing so showed the potential to add vehicle dynamic loads, especially sprung-mass trucks, as an integral part of the proposed CPS system. This approach to including vehicles in the CPS has great promise as vehicles get more instrumented with connected vehicle technology. For example, in-situ measurement of truck behavior can be used to change trucks for consumed service life in tool-based transportation systems. Time-synchronized truck-bridge response data was used as the basis for modeling the interactions between the truck and the bridge. A two-stage subspace system identification modeling framework was introduced to create accurate input-output models of bridge behavior. The Telegraph Road Bridge (TRB) was used again as a validation platform.

In Chapter 7, time series forecast models were explored as a tool for jointly modeling the

response of bridges on the same corridor exposed to identical load conditions. Forecasting models could be a basis for observing a truck at one bridge to predict how another bridge would behave to the same truck. This prediction could be used by the CPS to control the truck to lowers its response on a bridge. Two types of forecast models were built for the task at hand. An encoder-decoder architecture with two different cell types, namely gated recurrent unit (GRU) and long short-term memory (LSTM), were explored. To evaluate the performance of the forecast models in taking the output of one bridge to predict the response of another under the same truck load, finite element models were built for the Telegraph Road Bridge and Newburg Road Bridge; the finite element models were then used to simulate a dataset containing 2,100 pairs of bridge responses to the same truck load. The two encoder-decoder models provided more accurate prediction capabilities of bridge responses compared to the ARX baseline approach.

Finally, in Chapter 8, a learning-based method was proposed to further explore the use of deep learning to advance bridge WIM (BWIM) technology. Utilizing a large volume of paired bridge response and WIM data, a bidirectional recurrent neural network (RNN) was trained to predict truck weight characteristics including axle weight, axle spacing and gross weight with measured bridge strain responses used as inputs. The proposed method was evaluated using simulation data obtained from finite element models and proven to have sufficient precision equivalent to a Type II WIM station for axle weight and vehicle gross weight prediction. The proposed method was also proven to be robust against sensing noise in the training labels, which makes it possible to be implemented in the real world using the proposed CPS-enabled SHM network. The learning-based BWIM method was also evaluated using the paired bridge response and WIM data collected from the Newburg Road Bridge showing its effectiveness in real operational bridges.

9.2 Future Research Work

Many aspects of this Ph.D. research can be further improved and explored. For the CPS system, the computer vision-based truck identification approach can be extended to hardware-based methods such as radio-frequency identification (RFID), dedicated short-range communications (DSRC) or

5G. Doing so can enable the CPS architecture to perform well even during night time when truck detection suffers using computer vision. The accuracy of the computer vision-based truck detection and re-identification modules can also be further improved by using more advanced computer vision algorithms that are just emerging. The analysis done in Chapter 3 to model bridge composite action behavior can be extended for a longer period of time such that changes in bridge measured composite properties over time can be observed and linked to bridge structural condition (especially deck deterioration) in a more conclusive manner. The encoder-decoder method proposed in Chapter 7 for joint bridge response forecasting should be evaluated using real-world data and tested for bridge damage detection. For example, damage may detrimentally impact the forecast model allowing it to be used to flag when damage in the two bridges begin to emerge. In Chapter 8, the effects of factors such as training data size and temperature on the accuracy of the proposed learning-based BWIM system should be further investigated. More sophisticated models and loss functions can also be developed to predict more types of truck load characteristics including speed and axle spacing. Addressing the scenario where multiple trucks load a bridge simultaneously is another important needed to make the proposed method more practical for real operational settings.

Additionally, more work should be done to expand the role of the proposed CPS framework for load control of the trucks. Future research can be conducted to control the trucks (e.g., speed, lane and distance between adjacent trucks) based on observations made by the CPS architecture to mitigate in real-time bridge deterioration due to dynamic trucks and to improve traffic efficiency (throughput). For example, observed trucks in a corridor can inform how they can be driven in the corridor when crossing bridges downstream to minimize their dynamic amplification factors. This could extend the life of bridge with fatigue-like (i.e., repeated cyclic response) deterioration mechanisms such as deck breakdown and metallic fatigue cracking.

The proposed CPS framework can also be applied to other civil infrastructure domains. For example, human-beings can be placed in the loop of CPS to form a cyber-physical-social-system (CPSS) for urban sensing. With people as analog loads, public resources (e.g., public space, furniture) can be better managed and maintained through monitoring resource usage. For example, the

presented CPS architecture could be used to detect people using computer vision detectors (like YOLO). People interactions in time and space could be tracked much like truck loads were tracked in this thesis to understand how they use infrastructure in public spaces (e.g., in transit systems, parck, etc.)

REFERENCES

[1] E. A. Lee and S. A. Seshia, *Introduction to embedded systems: A cyber-physical systems approach*. Mit Press, 2016.

[2] L. Monostori, B. Kádár, T. Bauernhansl, S. Kondoh, S. Kumara, G. Reinhart, O. Sauer, G. Schuh, W. Sihn, and K. Ueda, "Cyber-physical systems in manufacturing," *Cirp Annals*, vol. 65, no. 2, pp. 621–641, 2016.

[3] V. Gunes, S. Peter, T. Givargis, and F. Vahid, "A survey on concepts, applications, and challenges in cyber-physical systems.," *KSII Transactions on Internet & Information Systems*, vol. 8, no. 12, 2014.

[4] E. A. Lee, "Cyber-physical systems-are computing foundations adequate," in *Position paper for NSF workshop on cyber-physical systems: research motivation, techniques and roadmap*, vol. 2, pp. 1–9, Citeseer, 2006.

[5] R. Rajkumar, I. Lee, L. Sha, and J. Stankovic, "Cyber-physical systems: the next computing revolution," in *Design Automation Conference*, pp. 731–736, IEEE, 2010.

[6] K. Sampigethaya and R. Poovendran, "Aviation cyber–physical systems: Foundations for future aircraft and air transport," *Proceedings of the IEEE*, vol. 101, no. 8, pp. 1834–1855, 2013.

[7] I. Lee and O. Sokolsky, "Medical cyber physical systems," in *Design automation conference*, pp. 743–748, IEEE, 2010.

[8] S. F. Ochoa, G. Fortino, and G. Di Fatta, "Cyber-physical systems, internet of things and big data," 2017.

[9] K. Dolui and S. K. Datta, "Comparison of edge computing implementations: Fog computing, cloudlet and mobile edge computing," in *2017 Global Internet of Things Summit (GIoTS)*, pp. 1–6, IEEE, 2017.

[10] D. A. Linares, C. Anumba, and N. Roofigari-Esfahan, "Overview of supporting technologies for cyber-physical systems implementation in the aec industry," *Computing in Civil Engineering*, 2019.

[11] S. K. Khaitan and J. D. McCalley, "Design techniques and applications of cyberphysical systems: A survey," *IEEE Systems Journal*, vol. 9, no. 2, pp. 350–365, 2014.

[12] G. Xiong, F. Zhu, X. Liu, X. Dong, W. Huang, S. Chen, and K. Zhao, "Cyber-physical-social system in intelligent transportation," *IEEE/CAA Journal of Automatica Sinica*, vol. 2, no. 3, pp. 320–333, 2015.

[13] Y. Lin, P. Wang, and M. Ma, "Intelligent transportation system (its): Concept, challenge and opportunity," in *2017 ieee 3rd international conference on big data security on cloud (bigdatasecurity), ieee international conference on high performance and smart computing (hpsc), and ieee international conference on intelligent data and security (ids)*, pp. 167–172, IEEE, 2017.

[14] D. P. Möller and H. Vakilzadian, "Cyber-physical systems in smart transportation," in *2016 IEEE International Conference on Electro Information Technology (EIT)*, pp. 0776–0781, IEEE, 2016.

[15] J. Guerrero-Ibáñez, S. Zeadally, and J. Contreras-Castillo, "Sensor technologies for intelligent transportation systems," *Sensors*, vol. 18, no. 4, p. 1212, 2018.

[16] R. Khatoun and S. Zeadally, "Smart cities: concepts, architectures, research opportunities," *Communications of the ACM*, vol. 59, no. 8, pp. 46–57, 2016.

[17] S. K. Khaitan, J. D. McCalley, and C. C. Liu, *Cyber physical systems approach to smart electric power grid*. Springer, 2015.

[18] B. H. Krogh, E. Lee, I. Lee, A. Mok, R. Rajkumar, L. Sha, A. Vincentelli, K. Shin, J. Stankovic, J. Sztipanovits, *et al.*, "Cyber-physical systems: Executive summary," *CPS Steer Group, Wash. DC*, 2008.

[19] M. Schmidt and C. Åhlund, "Smart buildings as cyber-physical systems: Data-driven predictive control strategies for energy efficiency," *Renewable and Sustainable Energy Reviews*, vol. 90, pp. 742–756, 2018.

[20] B. Kerkez, C. Gruden, M. Lewis, L. Montestruque, M. Quigley, B. Wong, A. Bedig, R. Kertesz, T. Braun, O. Cadwalader, *et al.*, "Smarter stormwater systems," 2016.

[21] S. Eggimann, L. Mutzner, O. Wani, M. Y. Schneider, D. Spuhler, M. Moy de Vitry, P. Beutler, and M. Maurer, "The potential of knowing more: A review of data-driven urban water management," *Environmental science & technology*, vol. 51, no. 5, pp. 2538–2553, 2017.

[22] C. G. Cassandras, "Smart cities as cyber-physical social systems," *Engineering*, vol. 2, no. 2, pp. 156–158, 2016.

[23] D. Legatiuk, K. Dragos, and K. Smarsly, "Modeling and evaluation of cyber-physical systems in civil engineering," *PAMM*, vol. 17, no. 1, pp. 807–808, 2017.

[24] X. Yuan, C. J. Anumba, and M. K. Parfitt, "Cyber-physical systems for temporary structure monitoring," *Automation in Construction*, vol. 66, pp. 1–14, 2016.

[25] G. Hackmann, W. Guo, G. Yan, Z. Sun, C. Lu, and S. Dyke, "Cyber-physical codesign of distributed structural health monitoring with wireless sensor networks," *IEEE Transactions on Parallel and Distributed Systems*, vol. 25, no. 1, pp. 63–72, 2013.

[26] M. Z. A. Bhuiyan, J. Wu, G. Wang, and J. Cao, "Sensing and decision making in cyber-physical systems: The case of structural event monitoring," *IEEE Transactions on Industrial Informatics*, vol. 12, no. 6, pp. 2103–2114, 2016.

[27] J. M. Brownjohn, "Structural health monitoring of civil infrastructure," *Philosophical Transactions of the Royal Society A: Mathematical, Physical and Engineering Sciences*, vol. 365, no. 1851, pp. 589–622, 2007.

[28] S. Jeong, R. Hou, J. P. Lynch, H. Sohn, and K. H. Law, "Cloud-based cyber infrastructure for bridge monitoring," in *The 14th International Symposium on Structural Engineering*, 2016.

[29] B. Li, Z. Sun, K. Mechitov, G. Hackmann, C. Lu, S. J. Dyke, G. Agha, and B. F. Spencer Jr, "Realistic case studies of wireless structural control," in *Proceedings of the ACM/IEEE 4th International Conference on Cyber-Physical Systems*, pp. 179–188, 2013.

[30] A. S. of Civil Engineers (ASCE), "2017 report card for america's infrastructure," tech. rep., American Society of Civil Engineers (ASCE), 2017.

[31] F. H. A. (US) and F. T. A. (US), "Status of the nation's highways, bridges, and transit conditions & performance, 23rd edition," tech. rep., Federal Highway Administration (US) and Federal Transit Administration (US), 2019.

[32] D. Agdas, J. A. Rice, J. R. Martinez, and I. R. Lasa, "Comparison of visual inspection and structural-health monitoring as bridge condition assessment methods," *Journal of Performance of Constructed Facilities*, vol. 30, no. 3, p. 04015049, 2016.

[33] G. Webb, P. J. Vardanega, and C. R. Middleton, "Categories of shm deployments: technologies and capabilities," *Journal of Bridge Engineering*, vol. 20, no. 11, p. 04014118, 2015.

[34] F. H. A. (FHWA), "National bridge inspection standards (nbis) 23 cfr part 650.," 2004.

[35] A. A. of State Highway and T. O. (AASHTO), *Manual for Bridge Evaluation (3rd Edition)*. Washington, DC: American Association of State Highway and Transportation Officials (AASHTO), 2018.

[36] C. Maierhofer, H.-W. Reinhardt, and G. Dobmann, *Non-Destructive Evaluation of Reinforced Concrete Structures: Non-Destructive Testing Methods*. Elsevier, 2010.

[37] G. A. Washer, "Developing nde technologies for infrastructure assessment," *Public Roads*, vol. 63, no. 4, 2000.

[38] J. Seo, J. W. Hu, and J. Lee, "Summary review of structural health monitoring applications for highway bridges," *Journal of Performance of Constructed Facilities*, vol. 30, no. 4, p. 04015072, 2016.

[39] J. P. Lynch and K. J. Loh, "A summary review of wireless sensors and sensor networks for structural health monitoring," *Shock and Vibration Digest*, vol. 38, no. 2, pp. 91–130, 2006.

[40] J. J. Moughty and J. R. Casas, "A state of the art review of modal-based damage detection in bridges: development, challenges, and solutions," *Applied Sciences*, vol. 7, no. 5, p. 510, 2017.

[41] K. H. Hsieh, M. W. Halling, and P. J. Barr, "Overview of vibrational structural health monitoring with representative case studies," *Journal of Bridge Engineering*, vol. 11, no. 6, pp. 707–715, 2006.

[42] F. Wang and T. Chan, "Review of vibration-based damage detection and condition assessment of bridge structures using structural health monitoring," in *Proceedings of The Second Infrastructure Theme Postgraduate Conference: Rethinking Sustainable Development - Planning, Infrastructure Engineering, Design and Managing Urban Infrastructure* (L. Wang and S. Jaiswal, eds.), (Australia), pp. 35–47, Queensland University of Technology, 2009.

[43] A. Cardini and J. T. DeWolf, "Long-term structural health monitoring of a multi-girder steel composite bridge using strain data," *Structural Health Monitoring*, vol. 8, no. 1, pp. 47–58, 2009.

[44] W. Hong, Y. Cao, and Z. Wu, "Strain-based damage-assessment method for bridges under moving vehicular loads using long-gauge strain sensing," *Journal of Bridge Engineering*, vol. 21, no. 10, p. 04016059, 2016.

[45] B. Phares, P. Lu, T. Wipf, L. Greimann, and J. Seo, "Field validation of a statistical-based bridge damage-detection algorithm," *Journal of Bridge Engineering*, vol. 18, no. 11, pp. 1227–1238, 2013.

[46] S.-Z. Chen, G. Wu, and D.-C. Feng, "Damage detection of highway bridges based on long-gauge strain response under stochastic traffic flow," *Mechanical Systems and Signal Processing*, vol. 127, pp. 551–572, 2019.

[47] S. M. O'Connor, *Wireless Monitoring Systems for Long-Term Reliability Assessment of Bridge Structures based on Compressed Sensing and Data-Driven Interrogation Methods.* PhD thesis, University of Michigan, Ann Arbor, 2015.

[48] T. Harms, S. Sedigh, and F. Bastianini, "Structural health monitoring of bridges using wireless sensor networks," *IEEE Instrumentation & Measurement Magazine*, vol. 13, no. 6, pp. 14–18, 2010.

[49] C. R. Farrar and K. Worden, "An introduction to structural health monitoring," *Philosophical Transactions of the Royal Society A: Mathematical, Physical and Engineering Sciences*, vol. 365, no. 1851, pp. 303–315, 2007.

[50] S. Kim, S. Pakzad, D. Culler, J. Demmel, G. Fenves, S. Glaser, and M. Turon, "Health monitoring of civil infrastructures using wireless sensor networks," in *Proceedings of the 6th international conference on Information processing in sensor networks*, pp. 254–263, 2007.

[51] A. B. Noel, A. Abdaoui, T. Elfouly, M. H. Ahmed, A. Badawy, and M. S. Shehata, "Structural health monitoring using wireless sensor networks: A comprehensive survey," *IEEE Communications Surveys & Tutorials*, vol. 19, no. 3, pp. 1403–1423, 2017.

[52] F. N. Catbas and M. Malekzadeh, "A machine learning-based algorithm for processing massive data collected from the mechanical components of movable bridges," *Automation in Construction*, vol. 72, pp. 269–278, 2016.

[53] G. Feltrin, J. Meyer, R. Bischoff, and M. Motavalli, "Long-term monitoring of cable stays with a wireless sensor network," *Structure and Infrastructure Engineering*, vol. 6, no. 5, pp. 535–548, 2010.

[54] K.-Y. Koo, J. Brownjohn, D. List, and R. Cole, "Structural health monitoring of the tamar suspension bridge," *Structural Control and Health Monitoring*, vol. 20, no. 4, pp. 609–625, 2013.

[55] S. Jang, H. Jo, S. Cho, K. Mechitov, J. A. Rice, S.-H. Sim, H.-J. Jung, C.-B. Yun, B. F. Spencer Jr, and G. Agha, "Structural health monitoring of a cable-stayed bridge using smart sensor technology: deployment and evaluation," *Smart Structures and Systems*, vol. 6, no. 5-6, pp. 439–459, 2010.

[56] Y. Gebremichael, W. Li, B. Meggitt, W. Boyle, K. Grattan, B. McKinley, L. Boswell, K. Aarnes, S. Aasen, B. Tynes, *et al.*, "A field deployable, multiplexed bragg grating sensor system used in an extensive highway bridge monitoring evaluation tests," *IEEE Sensors Journal*, vol. 5, no. 3, pp. 510–519, 2005.

[57] R. Kromanis, P. Kripakaran, and B. Harvey, "Long-term structural health monitoring of the cleddau bridge: evaluation of quasi-static temperature effects on bearing movements," *Structure and Infrastructure Engineering*, vol. 12, no. 10, pp. 1342–1355, 2016.

[58] M. Kurata, J. Kim, J. Lynch, G. Van Der Linden, H. Sedarat, E. Thometz, P. Hipley, and L.-H. Sheng, "Internet-enabled wireless structural monitoring systems: development and permanent deployment at the new carquinez suspension bridge," *Journal of structural engineering*, vol. 139, no. 10, pp. 1688–1702, 2013.

[59] S. Yu and J. Ou, "Structural health monitoring and model updating of aizhai suspension bridge," *Journal of Aerospace Engineering*, vol. 30, no. 2, p. B4016009, 2017.

[60] K.-Y. Wong, "Instrumentation and health monitoring of cable-supported bridges," *Structural Control and Health Monitoring*, vol. 11, no. 2, pp. 91–124, 2004.

[61] S. M. O'Connor, Y. Zhang, J. P. Lynch, M. M. Ettouney, and P. O. Jansson, "Long-term performance assessment of the telegraph road bridge using a permanent wireless monitoring system and automated statistical process control analytics," *Structure and infrastructure engineering*, vol. 13, no. 5, pp. 604–624, 2017.

[62] O. Huth, G. Feltrin, J. Maeck, N. Kilic, and M. Motavalli, "Damage identification using modal data: Experiences on a prestressed concrete bridge," *Journal of Structural Engineering*, vol. 131, no. 12, pp. 1898–1910, 2005.

[63] B. Peeters and G. De Roeck, "One-year monitoring of the z24-bridge: environmental effects versus damage events," *Earthquake engineering & structural dynamics*, vol. 30, no. 2, pp. 149–171, 2001.

[64] H. Sohn, "Effects of environmental and operational variability on structural health monitoring," *Philosophical Transactions of the Royal Society A: Mathematical, Physical and Engineering Sciences*, vol. 365, no. 1851, pp. 539–560, 2007.

[65] C. Liu, Y. Gong, S. Laflamme, B. Phares, and S. Sarkar, "Bridge damage detection using spatiotemporal patterns extracted from dense sensor network," *Measurement Science and Technology*, vol. 28, no. 1, p. 014011, 2016.

[66] S. Jeong, M. Ferguson, R. Hou, J. P. Lynch, H. Sohn, and K. H. Law, "Sensor data reconstruction using bidirectional recurrent neural network with application to bridge monitoring," *Advanced Engineering Informatics*, vol. 42, p. 100991, 2019.

[67] R. V. Farahani and D. Penumadu, "Damage identification of a full-scale five-girder bridge using time-series analysis of vibration data," *Engineering Structures*, vol. 115, pp. 129–139, 2016.

[68] S. W. Doebling and C. R. Farrar, "Statistical damage identification techniques applied to the i-40 bridge over the rio grande river," tech. rep., Los Alamos National Lab., NM (United States), 1998.

[69] G. D. Roeck, "The state-of-the-art of damage detection by vibration monitoring: the simces experience," *Journal of Structural Control*, vol. 10, no. 2, pp. 127–134, 2003.

[70] K.-C. Chang and C.-W. Kim, "Modal-parameter identification and vibration-based damage detection of a damaged steel truss bridge," *Engineering Structures*, vol. 122, pp. 156–173, 2016.

[71] J. Ko and Y. Q. Ni, "Technology developments in structural health monitoring of large-scale bridges," *Engineering structures*, vol. 27, no. 12, pp. 1715–1725, 2005.

[72] Z. Sun, Z. Zou, and Y. Zhang, "Utilization of structural health monitoring in long-span bridges: case studies," *Structural Control and Health Monitoring*, vol. 24, no. 10, p. e1979, 2017.

[73] C. A. Tokognon, B. Gao, G. Y. Tian, and Y. Yan, "Structural health monitoring framework based on internet of things: A survey," *IEEE Internet of Things Journal*, vol. 4, no. 3, pp. 619–635, 2017.

[74] M. Z. A. Bhuiyan, J. Wu, G. Wang, J. Cao, W. Jiang, and M. Atiquzzaman, "Towards cyber-physical systems design for structural health monitoring: Hurdles and opportunities," *ACM Transactions on Cyber-Physical Systems*, vol. 1, no. 4, pp. 1–26, 2017.

[75] Y. Zhang, S. M. O'Connor, G. W. van der Linden, A. Prakash, and J. P. Lynch, "Senstore: A scalable cyberinfrastructure platform for implementation of data-to-decision frameworks for infrastructure health management," *Journal of Computing in Civil Engineering*, vol. 30, no. 5, p. 04016012, 2016.

[76] D. Inaudi, B. Glisic, and S. Vurpillot, "Standardization of database structures for monitoring data," in *First International conference on Bridge Maintenance, Safety and Managment, IABMAS*, vol. 2, p. 2002, 2002.

[77] K. Y. Koo, N. D. Battista, and J. M. Brownjohn, "Shm data management system using mysql database with matlab and web interfaces," in *5th International Conference on Structural Health Monitoring of Intelligent Infrastructure (SHMII-5), Cancún, México*, pp. 589–596, 2011.

[78] S. Jeong, Y. Zhang, S. O'Connor, J. P. Lynch, H. Sohn, and K. H. Law, "A nosql data management infrastructure for bridge monitoring," *Smart Structures and Systems*, vol. 17, no. 4, pp. 669–690, 2016.

[79] S. Jeong, R. Hou, J. P. Lynch, H. Sohn, and K. H. Law, "A scalable cloud-based cyberinfrastructure platform for bridge monitoring," *Structure and Infrastructure Engineering*, vol. 15, no. 1, pp. 82–102, 2019.

[80] Y. Qin, R. Xiao, Y. Wang, and K. H. Law, "A bridge information modeling framework for model interoperability," in *Computing in Civil Engineering 2019: Visualization, Information Modeling, and Simulation*, pp. 447–454, American Society of Civil Engineers Reston, VA, 2019.

[81] B. Glisic, M. T. Yarnold, F. L. Moon, and A. E. Aktan, "Advanced visualization and accessibility to heterogeneous monitoring data," *Computer-Aided Civil and Infrastructure Engineering*, vol. 29, no. 5, pp. 382–398, 2014.

[82] F.-J. Wu, Y.-F. Kao, and Y.-C. Tseng, "From wireless sensor networks towards cyber physical systems," *Pervasive and Mobile computing*, vol. 7, no. 4, pp. 397–413, 2011.

[83] S. M. Khan, S. Atamturktur, M. Chowdhury, and M. Rahman, "Integration of structural health monitoring and intelligent transportation systems for bridge condition assessment: current status and future direction," *IEEE Transactions on Intelligent Transportation Systems*, vol. 17, no. 8, pp. 2107–2122, 2016.

[84] B. Glisic, M. Yarnold, F. Moon, and A. Aktan, "Advanced visualization and accessibility to shm results involving real-time and historic multi-parameter data and camera images," in *Structures Congress 2012*, pp. 735–746, 2012.

[85] T. Guo, D. M. Frangopol, and Y. Chen, "Fatigue reliability assessment of steel bridge details integrating weigh-in-motion data and probabilistic finite element analysis," *Computers & Structures*, vol. 112, pp. 245–257, 2012.

[86] D. Cantero and A. González, "Bridge damage detection using weigh-in-motion technology," *Journal of Bridge Engineering*, vol. 20, no. 5, p. 04014078, 2015.

[87] T. J. Matarazzo, P. Santi, S. N. Pakzad, K. Carter, C. Ratti, B. Moaveni, C. Osgood, and N. Jacob, "Crowdsensing framework for monitoring bridge vibrations using moving smartphones," *Proceedings of the IEEE*, vol. 106, no. 4, pp. 577–593, 2018.

[88] A. Malekjafarian, P. J. McGetrick, and E. J. OBrien, "A review of indirect bridge monitoring using passing vehicles," *Shock and vibration*, vol. 2015, 2015.

[89] S. A. Putra, B. R. Trilaksono, M. Riyansyah, D. S. Laila, A. Harsoyo, and A. I. Kistijantoro, "Intelligent sensing in multiagent-based wireless sensor network for bridge condition monitoring system," *IEEE Internet of Things Journal*, vol. 6, no. 3, pp. 5397–5410, 2019.

[90] M. Abdulkarem, K. Samsudin, F. Z. Rokhani, and M. F. A Rasid, "Wireless sensor network for structural health monitoring: A contemporary review of technologies, challenges, and future direction," *Structural Health Monitoring*, p. 1475921719854528, 2019.

[91] G. Loubet, A. Takacs, and D. Dragomirescu, "Implementation of a battery-free wireless sensor for cyber-physical systems dedicated to structural health monitoring applications," *IEEE access*, vol. 7, pp. 24679–24690, 2019.

[92] M. Z. A. Bhuiyan, G. Wang, J. Wu, J. Cao, X. Liu, and T. Wang, "Dependable structural health monitoring using wireless sensor networks," *IEEE Transactions on Dependable and Secure Computing*, vol. 14, no. 4, pp. 363–376, 2015.

[93] L. Alonso, J. Barbarán, J. Chen, M. Díaz, L. Llopis, and B. Rubio, "Middleware and communication technologies for structural health monitoring of critical infrastructures: A survey," *Computer Standards & Interfaces*, vol. 56, pp. 83–100, 2018.

[94] D. A. T. Burgos, R. C. G. Vargas, C. Pedraza, D. Agis, and F. Pozo, "Damage identification in structural health monitoring: a brief review from its implementation to the use of data-driven applications," *Sensors*, vol. 20, no. 3, p. 733, 2020.

[95] R. Kromanis and P. Kripakaran, "Data-driven approaches for measurement interpretation: analysing integrated thermal and vehicular response in bridge structural health monitoring," *Advanced Engineering Informatics*, vol. 34, pp. 46–59, 2017.

[96] R. Yao and S. N. Pakzad, "Autoregressive statistical pattern recognition algorithms for damage detection in civil structures," *Mechanical Systems and Signal Processing*, vol. 31, pp. 355–368, 2012.

[97] C. R. Farrar and K. Worden, *Structural health monitoring: a machine learning perspective*. John Wiley & Sons, 2012.

[98] E. Cross, K. Koo, J. Brownjohn, and K. Worden, "Long-term monitoring and data analysis of the tamar bridge," *Mechanical Systems and Signal Processing*, vol. 35, no. 1-2, pp. 16–34, 2013.

[99] Y. Zhang, M. Kurata, and J. P. Lynch, "Long-term modal analysis of wireless structural monitoring data from a suspension bridge under varying environmental and operational conditions: System design and automated modal analysis," *Journal of Engineering Mechanics*, vol. 143, no. 4, p. 04016124, 2017.

[100] P. Asadollahi and J. Li, "Statistical analysis of modal properties of a cable-stayed bridge through long-term wireless structural health monitoring," *Journal of Bridge Engineering*, vol. 22, no. 9, p. 04017051, 2017.

[101] H. Sohn, J. A. Czarnecki, and C. R. Farrar, "Structural health monitoring using statistical process control," *Journal of structural engineering*, vol. 126, no. 11, pp. 1356–1363, 2000.

[102] F. Cavadas, I. F. Smith, and J. Figueiras, "Damage detection using data-driven methods applied to moving-load responses," *Mechanical Systems and Signal Processing*, vol. 39, no. 1-2, pp. 409–425, 2013.

[103] D. Xu, H. Chong, I. Main, M. Mineter, R. De Bold, M. Forde, C. Gair, P. Madden, E. Angus, and C. Ho, "Using statistical models and machine learning techniques to process big data from the forth road bridge," in *International Conference on Smart Infrastructure and Construction 2019 (ICSIC) Driving data-informed decision-making*, pp. 411–419, ICE Publishing, 2019.

[104] J. P. Santos, C. Cremona, A. D. Orcesi, and P. Silveira, "Early damage detection based on pattern recognition and data fusion," *Journal of Structural Engineering*, vol. 143, no. 2, p. 04016162, 2017.

[105] V. Alves, A. Cury, N. Roitman, C. Magluta, and C. Cremona, "Structural modification assessment using supervised learning methods applied to vibration data," *Engineering Structures*, vol. 99, pp. 439–448, 2015.

[106] R. de Almeida Cardoso, A. Cury, and F. Barbosa, "Automated real-time damage detection strategy using raw dynamic measurements," *Engineering Structures*, vol. 196, p. 109364, 2019.

[107] H. Pan, M. Azimi, F. Yan, and Z. Lin, "Time-frequency-based data-driven structural diagnosis and damage detection for cable-stayed bridges," *Journal of Bridge Engineering*, vol. 23, no. 6, p. 04018033, 2018.

[108] O. Bahrami, S. Tsiapoki, M. W. Häckell, M. B. Kane, J. P. Lynch, and R. Rolfes, "Extraction of environmental and operational conditions of wind turbine from tower response data for improved structural health monitoring," *Proceedings of Structural Health Monitoring*, 2017.

[109] Y. Ni, H. Xia, K. Wong, and J. Ko, "In-service condition assessment of bridge deck using long-term monitoring data of strain response," *Journal of Bridge Engineering*, vol. 17, no. 6, pp. 876–885, 2012.

[110] E. P. Carden and J. M. Brownjohn, "Fuzzy clustering of stability diagrams for vibration-based structural health monitoring," *Computer-Aided Civil and Infrastructure Engineering*, vol. 23, no. 5, pp. 360–372, 2008.

[111] M. Yarnold and F. Moon, "Temperature-based structural health monitoring baseline for long-span bridges," *Engineering Structures*, vol. 86, pp. 157–167, 2015.

[112] Z. Lin, H. Pan, X. Wang, and M. Li, "Data-driven structural diagnosis and conditional assessment: From shallow to deep learning," in *Sensors and Smart Structures Technologies for Civil, Mechanical, and Aerospace Systems 2018*, vol. 10598, p. 1059814, International Society for Optics and Photonics, 2018.

[113] A. Lenjani, S. J. Dyke, I. Bilionis, C. M. Yeum, K. Kamiya, J. Choi, X. Liu, and A. G. Chowdhury, "Towards fully automated post-event data collection and analysis: pre-event and post-event information fusion," *Engineering Structures*, p. 109884, 2020.

[114] Y. Bao, Z. Tang, H. Li, and Y. Zhang, "Computer vision and deep learning–based data anomaly detection method for structural health monitoring," *Structural Health Monitoring*, vol. 18, no. 2, pp. 401–421, 2019.

[115] M. Lydon, S. E. Taylor, D. Robinson, A. Mufti, and E. Brien, "Recent developments in bridge weigh in motion (b-wim)," *Journal of Civil Structural Health Monitoring*, vol. 6, no. 1, pp. 69–81, 2016.

[116] F. F. H. Administration), "National bridge inventory," tech. rep., Washington, DC: FHWA, 2018.

[117] X. Hu, C. Daganzo, and S. Madanat, "A reliability-based optimization scheme for maintenance management in large-scale bridge networks," *Transportation Research Part C: Emerging Technologies*, vol. 55, pp. 166–178, 2015.

[118] M. L. Wang, J. P. Lynch, and H. Sohn, *Sensor technologies for civil infrastructures, volume 2: Applications in structural health monitoring*. Elsevier, 2014.

[119] B. Peeters, *System identification and damage detection in civil engineering*. Phd thesis, Katholieke Universiteit Leuven, 2000.

[120] F. N. Catbas, R. Zaurin, M. Gul, and H. B. Gokce, "Sensor networks, computer imaging, and unit influence lines for structural health monitoring: Case study for bridge load rating," *Journal of Bridge Engineering*, vol. 17, no. 4, pp. 662–670, 2012.

[121] D. M. Frangopol, A. Strauss, and S. Kim, "Bridge reliability assessment based on monitoring," *Journal of Bridge Engineering*, vol. 13, no. 3, pp. 258–270, 2008.

[122] O. Ditlevsen, "Traffic loads on large bridges modeled as white-noise fields," *Journal of engineering mechanics*, vol. 120, no. 4, pp. 681–694, 1994.

[123] X. Zhu and S. Law, "Structural health monitoring based on vehicle-bridge interaction: accomplishments and challenges," *Advances in Structural Engineering*, vol. 18, no. 12, pp. 1999–2016, 2015.

[124] J. Kim and J. P. Lynch, "Experimental analysis of vehicle–bridge interaction using a wireless monitoring system and a two-stage system identification technique," *Mechanical Systems and Signal Processing*, vol. 28, pp. 3–19, 2012.

[125] I. Darwish and S. J. Cook, "Infrastructure monitoring data management final report," tech. rep., Alfred Benesch & Company, East Lansing, MI, 2015.

[126] A. Micu, R. McKinstray, E. Angus, E. J. OBrien, A. Malekjafarian, and M. Lydon, "Estimation of traffic load effects on Forth Road Bridge using camera measurements," *Civil Engineering Research in Ireland 2018*, 2018.

[127] U. Vespier, A. Knobbe, J. Vanschoren, S. Miao, A. Koopman, B. Obladen, and C. Bosma, "Traffic events modeling for structural health monitoring," in *Advances in Intelligent Data Analysis X.*, vol. 7014 LNCS, pp. 376–387, Springer, Berlin, Heidelberg, 2011.

[128] T. Gandhi, R. Chang, and M. M. Trivedi, "Video and seismic sensor-based structural health monitoring: Framework, algorithms, and implementation," *IEEE Transactions on Intelligent Transportation Systems*, vol. 8, no. 2, pp. 169–180, 2007.

[129] M. Fraser, A. Elgamal, X. F. He, and J. P. Conte, "Sensor network for structural health monitoring of a highway bridge," *Journal of Computing in Civil Engineering*, vol. 24, no. 1, pp. 11–24, 2010.

[130] Y. Chen, C.-A. Tan, M. Q. Feng, and Y. Fukuda, "A video assisted approach for structural health monitoring of highway bridges under normal traffic," in *Smart Structures and Materials 2006: Sensors and Smart Structures Technologies for Civil, Mechanical, and Aerospace Systems*, vol. 6174, p. 61741V, International Society for Optics and Photonics, 2006.

[131] R. Zaurin and F. N. Catbas, "Integration of computer imaging and sensor data for structural health monitoring of bridges," *Smart Materials and Structures*, vol. 19, no. 1, 2010.

[132] R. Zaurin and F. Necati Catbas, "Structural health monitoring using video stream, influence lines, and statistical analysis," *Structural Health Monitoring: An International Journal*, vol. 10, no. 3, pp. 309–332, 2011.

[133] W. Han, J. Wu, C. S. Cai, and S. Chen, "Characteristics and dynamic impact of overloaded extra heavy trucks on typical highway bridges," *Journal of Bridge Engineering*, vol. 20, no. 2, p. 05014011, 2014.

[134] T.-L. Wang, C. Liu, D. Huang, and M. Shahawy, "Truck loading and fatigue damage analysis for girder bridges based on weigh-in-motion data," *Journal of Bridge Engineering*, vol. 10, no. 1, pp. 12–20, 2004.

[135] P. Lou, H. Nassif, D. Su, and P. Truban, "Effect of overweight trucks on bridge deck deterioration based on weigh-in-motion data," *Transportation Research Record: Journal of the Transportation Research Board*, vol. 2592, no. 1, pp. 86–97, 2016.

[136] D. Cantero and A. González, "Bridge damage detection using weigh-in-motion technology," *Journal of Bridge Engineering*, vol. 20, no. 5, p. 04014078, 2015.

[137] A. Adibfar and A. Costin, "Next generation of transportation infrastructure management: Fusion of intelligent transportation systems (its) and bridge information modeling (brim)," in *Advances in Informatics and Computing in Civil and Construction Engineering*, pp. 43–50, Springer, 2019.

[138] K. K. Hyun, A. Tok, and S. G. Ritchie, "Long distance truck tracking from advanced point detectors using a selective weighted bayesian model," *Transportation Research Part C: Emerging Technologies*, vol. 82, pp. 24–42, 2017.

[139] Y. Yin, S. Lawphongpanich, and Y. Lou, "Estimating investment requirement for maintaining and improving highway systems," *Transportation Research Part C: Emerging Technologies*, vol. 16, no. 2, pp. 199–211, 2008.

[140] A. J. Jara, D. Genoud, and Y. Bocchi, "Big data for cyber physical systems an analysis of challenges, solutions and opportunities," in *Proceedings - 2014 8th International Conference on Innovative Mobile and Internet Services in Ubiquitous Computing, IMIS 2014*, pp. 376–380, IEEE, 2014.

[141] H. Abid, L. T. T. Phuong, J. Wang, S. Lee, and S. Qaisar, "V-Cloud: vehicular cyber-physical systems and cloud computing," in *Proceedings of the 4th International Symposium on Applied Sciences in Biomedical and Communication Technologies*, p. 165, ACM, 2011.

[142] J. W. Liu, C. S. Shih, and E. T. Chu, "Cyberphysical elements of disaster-prepared smart environments," *Computer*, vol. 46, no. 2, pp. 69–75, 2013.

[143] Y. Simmhan, S. Aman, A. Kumbhare, R. Liu, S. Stevens, Q. Zhou, and V. Prasanna, "Cloud-based software platform for big data analytics in smart grids," *Computing in Science and Engineering*, vol. 15, no. 4, pp. 38–47, 2013.

[144] R. A. Swartz, D. Jung, J. P. Lynch, Y. Wang, D. Shi, and M. P. Flynn, "Design of a wireless sensor for scalable distributed in-network computation in a structural health monitoring system," in *Proceedings of the 5th International Workshop on Structural Health Monitoring*, pp. 12–14, 2005.

[145] R. Hou, Y. Zhang, S. O'Connor, Y. Hong, and J. P. Lynch, "Monitoring and identification of vehicle-bridge interaction using mobile truck-based wireless sensors," in *Proceedings of 11th International Workshop on Advanced Smart Materials and Smart Structures Technology*, pp. 1–2, 2015.

[146] S. Jeong, R. Hou, J. P. Lynch, H. Sohn, and K. H. Law, "An information modeling framework for bridge monitoring," *Advances in Engineering Software*, vol. 114, pp. 11–31, 2017.

[147] R. Hou, J. P. Lynch, M. M. Ettouney, and P. O. Jansson, "Partial composite-action and durability assessment of slab-on-girder highway bridge decks in negative bending using long-term structural monitoring data," *Journal of Engineering Mechanics*, vol. 146, no. 4, p. 04020010, 2020.

[148] B. McCall and W. C. Vodrazka Jr, "States' successful practices weigh-in-motion handbook," tech. rep., U.S. Department of Transportation, Washington, DC, 1997.

[149] Y. J. Kim and D. K. Yoon, "Identifying critical sources of bridge deterioration in cold regions through the constructed bridges in north dakota," *Journal of Bridge Engineering*, vol. 15, no. 5, pp. 542–552, 2009.

[150] S. Newman, *Building microservices: designing fine-grained systems*. Sebastopol, California: O'Reilly Media, Inc., 1 ed., 2015.

[151] J. Canny, "A computational approach to edge detection," *IEEE Transactions on pattern analysis and machine intelligence*, no. 6, pp. 679–698, 1986.

[152] J. P. Lewis, "Fast normalized cross-correlation," in *Proceedings of Vision Interface*, 1995.

[153] R. Hou, Y. A. Dedhia, S. Jeong, K. H. Law, M. M. Ettouney, and J. P. Lynch, "Fusion of weigh-in-motion system and bridge monitoring data for bridge load rating," in *Proceedings of the 9th International Conference on Structural Health Monitoring of Intelligent Infrastructure*, (St. Louism Missouri, USA), 2019.

[154] X. Liu, W. Liu, H. Ma, and H. Fu, "Large-scale vehicle re-identification in urban surveillance videos," in *2016 IEEE International Conference on Multimedia and Expo (ICME)*, pp. 1–6, IEEE, 2016.

[155] M.-C. Chang, Y. Wei, N. Song, and S. Lyu, "Video analytics in smart transportation for the aic'18 challenge," in *Proceedings of the IEEE Conference on Computer Vision and Pattern Recognition Workshops*, pp. 61–68, 2018.

[156] S. R. E. Datondji, Y. Dupuis, P. Subirats, and P. Vasseur, "A survey of vision-based traffic monitoring of road intersections," *IEEE transactions on intelligent transportation systems*, vol. 17, no. 10, pp. 2681–2698, 2016.

[157] A. Al-Fuqaha, M. Guizani, M. Mohammadi, M. Aledhari, and M. Ayyash, "Internet of things: A survey on enabling technologies, protocols, and applications," *IEEE communications surveys & tutorials*, vol. 17, no. 4, pp. 2347–2376, 2015.

[158] J. Redmon, S. Divvala, R. Girshick, and A. Farhadi, "You only look once: Unified, real-time object detection," in *Proceedings of the IEEE conference on computer vision and pattern recognition*, pp. 779–788, 2016.

[159] Y. Wang, D. Zhang, Y. Liu, B. Dai, and L. H. Lee, "Enhancing transportation systems via deep learning: A survey," *Transportation research part C: emerging technologies*, vol. 99, pp. 144–163, 2019.

[160] R. Girshick, J. Donahue, T. Darrell, and J. Malik, "Rich feature hierarchies for accurate object detection and semantic segmentation," *Proceedings of the IEEE Computer Society Conference on Computer Vision and Pattern Recognition*, pp. 580–587, 2014.

[161] S. Ren, K. He, R. Girshick, and J. Sun, "Faster R-CNN: towards real-time object detection with region proposal networks," *IEEE Transactions on Pattern Analysis and Machine Intelligence*, vol. 39, no. 6, pp. 1137–1149, 2017.

[162] J. Redmon and A. Farhadi, "Yolo9000: better, faster, stronger," in *Proceedings of the IEEE conference on computer vision and pattern recognition*, pp. 7263–7271, 2017.

[163] J. Redmon and A. Farhadi, "YOLOv3: an incremental improvement," *arXiv preprint arXiv:1804.02767*, 2018.

[164] W. Liu, D. Anguelov, D. Erhan, C. Szegedy, S. Reed, C. Y. Fu, and A. C. Berg, "SSD: Single shot multibox detector," in *European conference on computer vision*, pp. 21–37, Springer, Cham, 2016.

[165] T.-Y. Lin, P. Goyal, R. Girshick, K. He, and P. Dollár, "Focal loss for dense object detection," in *Proceedings of the IEEE international conference on computer vision*, pp. 2980–2988, 2017.

[166] T.-Y. Lin, P. Dollár, R. Girshick, K. He, B. Hariharan, and S. Belongie, "Feature pyramid networks for object detection," in *Proceedings of the IEEE conference on computer vision and pattern recognition*, pp. 2117–2125, 2017.

[167] H. Law and J. Deng, "Cornernet: Detecting objects as paired keypoints," in *Proceedings of the European Conference on Computer Vision (ECCV)*, pp. 734–750, 2018.

[168] Z. Tian, C. Shen, H. Chen, and T. He, "Fcos: Fully convolutional one-stage object detection," in *Proceedings of the IEEE International Conference on Computer Vision*, pp. 9627–9636, 2019.

[169] S. Ioffe and C. Szegedy, "Batch normalization: Accelerating deep network training by reducing internal covariate Shift," *arXiv preprint arXiv:1502.03167*, 2015.

[170] A. L. Maas, A. Y. Hannun, and A. Y. Ng, "Rectifier nonlinearities improve neural network acoustic models," in *Proc. icml*, vol. 30, p. 3, 2013.

[171] K. He, X. Zhang, S. Ren, and J. Sun, "Deep residual learning for image recognition," in *Proceedings of the IEEE conference on computer vision and pattern recognition*, pp. 770–778, 2016.

[172] K. Simonyan and A. Zisserman, "Very deep convolutional networks for large-scale image recognition," *arXiv preprint arXiv:1409.1556*, 2014.

[173] O. Russakovsky, J. Deng, H. Su, J. Krause, S. Satheesh, S. Ma, Z. Huang, A. Karpathy, A. Khosla, M. Bernstein, *et al.*, "Imagenet large scale visual recognition challenge," *International journal of computer vision*, vol. 115, no. 3, pp. 211–252, 2015.

[174] J. Redmon, "Darknet: Open source neural networks in C." \url{http://pjreddie.com/darknet/}, 2016.

[175] R. Girshick, I. Radosavovic, G. Gkioxari, P. Dollár, and K. He, "Detectron." https://github.com/facebookresearch/detectron, 2018.

[176] M. Everingham, L. Van Gool, C. K. Williams, J. Winn, and A. Zisserman, "The pascal visual object classes (voc) challenge," *International journal of computer vision*, vol. 88, no. 2, pp. 303–338, 2010.

[177] P. Pritchett and A. Zisserman, "Wide baseline stereo matching," in *Sixth International Conference on Computer Vision (IEEE Cat. No. 98CH36271)*, pp. 754–760, IEEE, 1998.

[178] M. A. Fischler and R. C. Bolles, "Random sample consensus: a paradigm for model fitting with applications to image analysis and automated cartography," *Communications of the ACM*, vol. 24, no. 6, pp. 381–395, 1981.

[179] D. Mishkin, J. Matas, and M. Perdoch, "Mods: Fast and robust method for two-view matching," *Computer Vision and Image Understanding*, vol. 141, pp. 81–93, 2015.

[180] D. G. Lowe, "Object recognition from local scale-invariant features," in *Proceedings of the seventh IEEE international conference on computer vision*, vol. 2, pp. 1150–1157, Ieee, 1999.

[181] H. Bay, T. Tuytelaars, and L. Van Gool, "Surf: Speeded up robust features," in *European conference on computer vision*, pp. 404–417, Springer, 2006.

[182] J.-M. Morel and G. Yu, "Asift: A new framework for fully affine invariant image comparison," *SIAM journal on imaging sciences*, vol. 2, no. 2, pp. 438–469, 2009.

[183] M. D. Zeiler and R. Fergus, "Visualizing and understanding convolutional networks," in *European conference on computer vision*, pp. 818–833, Springer, 2014.

[184] M. Lin, Q. Chen, and S. Yan, "Network In network," *arXiv preprint arXiv:1312.4400*, 2013.

[185] R. Hadsell, S. Chopra, and Y. LeCun, "Dimensionality reduction by learning an invariant mapping," in *2006 IEEE Computer Society Conference on Computer Vision and Pattern Recognition (CVPR'06)*, vol. 2, pp. 1735–1742, IEEE, 2006.

[186] F. Schroff, D. Kalenichenko, and J. Philbin, "Facenet: A unified embedding for face recognition and clustering," in *Proceedings of the IEEE conference on computer vision and pattern recognition*, pp. 815–823, 2015.

[187] X. Glorot and Y. Bengio, "Understanding the difficulty of training deep feedforward neural networks," in *Proceedings of the thirteenth international conference on artificial intelligence and statistics*, pp. 249–256, 2010.

[188] D. P. Kingma and J. Ba, "Adam: A method for stochastic optimization," *arXiv preprint arXiv:1412.6980*, 2014.

[189] A. Paszke, S. Gross, S. Chintala, G. Chanan, E. Yang, Z. DeVito, Z. Lin, A. Desmaison, L. Antiga, and A. Lerer, "Automatic differentiation in pytorch," 2017.

[190] D. M. Powers, "Evaluation: from precision, recall and f-measure to roc, informedness, markedness and correlation," *Journal of Machine Learning Technologies*, 2011.

[191] F. F. H. Administration), "National bridge inventory," tech. rep., Washington, DC: FHWA, 2016.

[192] AASHTO, *AASHTO LRFD bridge design specifications (8th edition)*. Washington, DC: American Association of State Highway and Transportation Officials (AASHTO), 2017.

[193] L. Galuppi and G. Royer-Carfagni, "Effective width of the slab in composite beams with nonlinear shear connection," *Journal of Engineering Mechanics*, vol. 142, no. 4, p. 04016001, 2016.

[194] C. Higgins and H. Mitchell, "Behavior of composite bridge decks with alternative shear connectors," *Journal of Bridge Engineering*, vol. 6, no. 1, pp. 17–22, 2001.

[195] MDOT, "State long-range transportation plan 2005-2030: highway/bridge technical report," tech. rep., Michigan Department of Transportation, 2006.

[196] G. Manfredi, G. Fabbrocino, and E. Cosenza, "Modeling of steel-concrete composite beams under negative bending," *Journal of engineering mechanics*, vol. 125, no. 6, pp. 654–662, 1999.

[197] H.-K. Ryu, S.-P. Chang, Y.-J. Kim, and B.-S. Kim, "Crack control of a steel and concrete composite plate girder with prefabricated slabs under hogging moments," *Engineering Structures*, vol. 27, no. 11, pp. 1613–1624, 2005.

[198] E. Spacone and S. El-Tawil, "Nonlinear analysis of steel-concrete composite structures: State of the art," *Journal of Structural Engineering*, vol. 130, no. 2, pp. 159–168, 2004.

[199] N. Newmark, C. Siess, and I. Viest, "Tests and analysis of composite beams with incomplete interaction," 1951.

[200] P. Foraboschi, "Analytical solution of two-layer beam taking into account nonlinear interlayer slip," *Journal of engineering mechanics*, vol. 135, no. 10, pp. 1129–1146, 2009.

[201] Y. Wu, D. Oehlers, and M. Griffith, "Partial-interaction analysis of composite beam/column members," *Mechanics of Structures and Machines*, vol. 30, no. 3, pp. 309–332, 2002.

[202] A. Zona and G. Ranzi, "Finite element models for nonlinear analysis of steel–concrete composite beams with partial interaction in combined bending and shear," *Finite Elements in Analysis and Design*, vol. 47, no. 2, pp. 98–118, 2011.

[203] F. Focacci, P. Foraboschi, and M. De Stefano, "Composite beam generally connected: Analytical model," *Composite Structures*, vol. 133, pp. 1237–1248, 2015.

[204] P. Foraboschi, "Three-layered plate: Elasticity solution," *Composites Part B: Engineering*, vol. 60, pp. 764–776, 2014.

[205] F. Queiroz, P. Vellasco, and D. Nethercot, "Finite element modelling of composite beams with full and partial shear connection," *Journal of Constructional Steel Research*, vol. 63, no. 4, pp. 505–521, 2007.

[206] J. Turmo, J. A. Lozano-Galant, E. Mirambell, and D. Xu, "Modeling composite beams with partial interaction," *Journal of Constructional Steel Research*, vol. 114, pp. 380–393, 2015.

[207] A. Chen and M. Yossef, "Analytical model for deck-on-girder composite beam system with partial composite action," *Journal of Engineering Mechanics*, vol. 142, no. 2, p. 04015087, 2016.

[208] C. Faella, E. Martinelli, and E. Nigro, "Shear connection nonlinearity and deflections of steel–concrete composite beams: a simplified method," *Journal of Structural Engineering*, vol. 129, no. 1, pp. 12–20, 2003.

[209] H.-G. Kwak and Y.-J. Seo, "Long-term behavior of composite girder bridges," *Computers & Structures*, vol. 74, no. 5, pp. 583–599, 2000.

[210] K. A. Flanigan, N. R. Johnson, R. Hou, M. Ettouney, and J. P. Lynch, "Utilization of wireless structural health monitoring as decision making tools for a condition and reliability-based assessment of railroad bridges," in *Sensors and Smart Structures Technologies for Civil, Mechanical, and Aerospace Systems 2017*, vol. 10168, p. 101681X, International Society for Optics and Photonics, 2017.

[211] D. Sigurdardottir and B. Glisic, "Neutral axis as damage sensitive feature," *Smart Materials and Structures*, vol. 22, no. 7, p. 075030, 2013.

[212] J. Li, H. Hao, K. Fan, and J. Brownjohn, "Development and application of a relative displacement sensor for structural health monitoring of composite bridges," *Structural Control and Health Monitoring*, vol. 22, no. 4, pp. 726–742, 2015.

[213] R. Hou, S. Jeong, Y. Wang, K. H. Law, and J. P. Lynch, "Camera-based triggering of bridge structure health monitoring systems using a cyber-physical system framework," in *International Workshop on Structural Health Monitoring 2017 (IWSHM 2017)*, 2017.

[214] S. S. Chen, A. J. Aref, M. Chiewanichakorn, and I.-S. Ahn, "Proposed effective width criteria for composite bridge girders," *Journal of bridge engineering*, vol. 12, no. 3, pp. 325–338, 2007.

[215] S. Chakraborty and J. T. DeWolf, "Development and implementation of a continuous strain monitoring system on a multi-girder composite steel bridge," *Journal of Bridge Engineering*, vol. 11, no. 6, pp. 753–762, 2006.

[216] L. An and K. Cederwall, "Push-out tests on studs in high strength and normal strength concrete," *Journal of Constructional Steel Research*, vol. 36, no. 1, pp. 15 – 29, 1996.

[217] R. F. Lorenz and F. W. Stockwell, "Concrete slab stresses in partial composite beams and girders," *Engineering Journal, American Institute of Steel Construction*, vol. 21, no. 3, pp. 185–188, 1984.

[218] D. J. Oehlers and M. A. Bradford, *Composite steel and concrete structures: fundamental behaviour: fundamental behaviour*. Elsevier, 1995.

[219] C. K. Williams, "Prediction with gaussian processes: From linear regression to linear prediction and beyond," in *Learning in graphical models*, pp. 599–621, Springer, 1998.

[220] F. Leonhardt, "Cracks and crack control in concrete structures," *PCI Journal*, vol. 33, pp. 124–145, 1988.

[221] I. Computer and Structure, "CsiBridge 2016: introduction to CSiBridge," 2016.

[222] J. G. Ollgaard, "Shear strength of stud connectors in lightweight and normal-weight concrete," *AISC Engineering Journal*, pp. 55–64, 1971.

[223] R. P. Johnson and I. N. Molenstra, "Partial shear connection in composite beams for buildings," *Proceedings of the Institution of Civil Engineers Part 2*, vol. 91, no. 4, pp. 679–704, 1991.

[224] A. A. Mosavi, H. Sedarat, S. M. O'Connor, A. Emami-Naeini, V. Jacob, A. Krimotat, and J. Lynch, "Finite element model updating of a skewed highway bridge using a multi-variable sensitivity-based optimization approach," in *Nondestructive Characterization for Composite Materials, Aerospace Engineering, Civil Infrastructure, and Homeland Security 2012*, vol. 8347, p. 834727, International Society for Optics and Photonics, 2012.

[225] G. E. Ramey, A. R. Wolff, and R. L. Wright, "Structural design actions to mitigate bridge deck cracking," *Practice Periodical on Structural Design and Construction*, vol. 2, no. 3, pp. 118–124, 1997.

[226] P. D. Cady, "Corrosion of reinforcing steel in concrete— a general overview of the problem," in *Chloride Corrosion of Steel in Concrete*, pp. 3–11, ASTM International, West Conshohocken, PA, 1977.

[227] M. Šahinagić-Isović, M. Šahinagić-Isović, G. Markovski, and M. Ćećez, "Shrinkage strain of concrete-causes and types," *Graevinar*, vol. 64, no. 09, pp. 727–734, 2012.

[228] P. D. Krauss and E. A. Rogalla, *Transverse cracking in newly constructed bridge decks*. Washington, DC: Transportation Research Board, 1996.

[229] R. M. Barker and J. A. Puckett, *Design of highway bridges: an LRFD approach, second edition*. John Wiley & Sons, Hoboken, NJ., 2013.

[230] R. J. Frosch, "Another look at cracking and crack control in reinforced concrete," *ACI Structural Journal*, vol. 96, no. 3, pp. 437–442, 1999.

[231] M. G. M. Stewart and D. D. V. Rosowsky, "Structural Safety and Serviceability of Concrete Bridges Subject to Corrosion," *Journal of Infrastructure Systems*, vol. 4, no. 4, pp. 146–155, 1998.

[232] K. A. T. Vu and M. G. Stewart, "Structural reliability of concrete bridges including improved chloride-induced corrosion models," *Structural Safety*, vol. 22, no. 4, pp. 313–333, 2000.

[233] M. D. Bowman and R. N. Chou, "Review of load rating and posting procedures and requirements," tech. rep., Purdue University, West Lafayette, IN, 2014.

[234] M. Sanayei, A. J. Reiff, B. R. Brenner, and G. R. Imbaro, "Load rating of a fully instrumented bridge: Comparison of lrfr approaches," *Journal of Performance of Constructed Facilities*, vol. 30, no. 2, p. 04015019, 2015.

[235] J. Yost, J. Schulz, and B. Commander, "Using ndt data for finite element model calibration and load rating of bridges," in *Structures Congress 2005: Metropolis and Beyond*, pp. 1–9, 2005.

[236] M. J. Chajes, D. R. Mertz, and B. Commander, "Experimental load rating of a posted bridge," *Journal of Bridge Engineering*, vol. 2, no. 1, pp. 1–10, 1997.

[237] B. Bakht and L. G. Jaeger, "Bridge testing—a surprise every time," *Journal of Structural Engineering*, vol. 116, no. 5, pp. 1370–1383, 1990.

[238] M. V. Gangone and M. J. Whelan, "Impact of measurement uncertainty from experimental load distribution factors on bridge load rating," in *Nondestructive Characterization and Monitoring of Advanced Materials, Aerospace, Civil Infrastructure, and Transportation XII*, vol. 10599, p. 1059921, International Society for Optics and Photonics, 2018.

[239] E. S. Bell, P. J. Lefebvre, M. Sanayei, B. Brenner, J. D. Sipple, and J. Peddle, "Objective load rating of a steel-girder bridge using structural modeling and health monitoring," *Journal of Structural Engineering*, vol. 139, no. 10, pp. 1771–1779, 2013.

[240] J. R. Casas and J. D. Gómez, "Load rating of highway bridges by proof-loading," *KSCE Journal of Civil Engineering*, vol. 17, pp. 556–567, Apr 2013.

[241] D. Huang, "Structure identification and load capacity rating of veteran's memorial curved steel box girder bridge," *Transportation Research Record*, vol. 2200, no. 1, pp. 98–107, 2010.

[242] E. O. Lantsoght, C. van der Veen, A. de Boer, and D. A. Hordijk, "State-of-the-art on load testing of concrete bridges," *Engineering Structures*, vol. 150, pp. 231 – 241, 2017.

[243] N. Wang, B. R. Ellingwood, and A.-H. Zureick, "Bridge rating using system reliability assessment. ii: Improvements to bridge rating practices," *Journal of Bridge Engineering*, vol. 16, no. 6, pp. 863–871, 2011.

[244] M. Alipour, D. K. Harris, and O. E. Ozbulut, "Vibration testing for bridge load rating," in *Dynamics of Civil Structures, Volume 2* (S. Pakzad and C. Juan, eds.), (Cham), pp. 175–184, Springer International Publishing, 2016.

[245] A. K. Ndong, M. S. Dizaji, M. Alipour, O. E. Ozbulut, and D. K. Harris, "Load rating of a reinforced concrete t-beam bridge through ambient vibration testing and finite element model updating," in *Dynamics of Civil Structures, Volume 2* (S. Pakzad, ed.), (Cham), pp. 337–343, Springer International Publishing, 2019.

[246] A. Bagheri, O. E. Ozbulut, D. K. Harris, M. Alipour, and A. Zare Hosseinzadeh, "A hybrid experimental-numerical approach for load rating of reinforced concrete bridges with insufficient structural properties," *Structure and Infrastructure Engineering*, vol. 15, no. 6, pp. 754–770, 2019.

[247] Y. Deng and B. M. Phares, "Automated bridge load rating determination utilizing strain response due to ambient traffic trucks," *Engineering Structures*, vol. 117, pp. 101 – 117, 2016.

[248] J. Seo, B. M. Phares, P. Lu, T. J. Wipf, and J. Dahlberg, "Bridge rating protocol using ambient trucks through structural health monitoring system," *Engineering Structures*, vol. 46, pp. 569 – 580, 2013.

[249] J. Seo, B. M. Phares, P. Lu, T. J. Wipf, and J. Dahlberg, "Use of a structural health monitoring system for the assessment of bridge load rating," in *6th Congress on Forensic Engineering: Gateway to a Safer Tomorrow*, pp. 18–27, 2013.

[250] M. J. Chajes, I. Harry W. Shenton, and D. O'Shea, "Bridge-condition assessment and load rating using nondestructive evaluation methods," *Transportation Research Record*, vol. 1696, no. 1, pp. 83–91, 2000.

[251] H. T. Al-Khateeb, H. W. Shenton, and M. J. Chajes, "Computing continuous load rating factors for bridges using structural health monitoring data," *Journal of Civil Structural Health Monitoring*, vol. 8, pp. 721–735, Nov 2018.

[252] B. Bhattacharya, D. Li, M. Chajes, and J. Hastings, "Reliability-based load and resistance factor rating using in-service data," *Journal of Bridge Engineering*, vol. 10, no. 5, pp. 530–543, 2005.

[253] B. Bhattacharya, D. Li, and M. Chajes, "Bridge rating using in-service data in the presence of strength deterioration and correlation in load processes," *Structure and Infrastructure Engineering*, vol. 4, no. 3, pp. 237–249, 2008.

[254] R. Hou, S. Jeong, J. P. Lynch, and K. H. Law, "Cyber-physical system architecture for automating the mapping of truck loads to bridge behavior using computer vision in connected highway corridors," *Transportation Research Part C: Emerging Technologies*, vol. 111, pp. 547–571, 2020.

[255] E. ASTM, "E1318-09. standard specification for highway weigh-in-motion (wim) systems with user requirements and test methods," *ASTM International*, 2017.

[256] N. Wang, C. O'Malley, B. R. Ellingwood, and A.-H. Zureick, "Bridge rating using system reliability assessment. i: Assessment and verification by load testing," *Journal of Bridge Engineering*, vol. 16, no. 6, pp. 854–862, 2011.

[257] L. Deng, Y. Yu, Q. Zou, and C. Cai, "State-of-the-art review of dynamic impact factors of highway bridges," *Journal of Bridge Engineering*, vol. 20, no. 5, p. 04014080, 2015.

[258] P. Paultre, O. Chaallal, and J. Proulx, "Bridge dynamics and dynamic amplification factors—a review of analytical and experimental findings," *Canadian Journal of Civil Engineering*, vol. 19, no. 2, pp. 260–278, 1992.

[259] L. Deng, W. He, and Y. Shao, "Dynamic impact factors for shear and bending moment of simply supported and continuous concrete girder bridges," *Journal of Bridge Engineering*, vol. 20, no. 11, p. 04015005, 2015.

[260] S. P. Brady, E. J. O'Brien, and A. Žnidarič, "Effect of vehicle velocity on the dynamic amplification of a vehicle crossing a simply supported bridge," *Journal of Bridge Engineering*, vol. 11, no. 2, pp. 241–249, 2006.

[261] C. Carey, E. J. OBrien, A. Malekjafarian, M. Lydon, and S. Taylor, "Direct field measurement of the dynamic amplification in a bridge," *Mechanical Systems and Signal Processing*, vol. 85, pp. 601–609, 2017.

[262] D. B. Ashebo, T. H. Chan, and L. Yu, "Evaluation of dynamic loads on a skew box girder continuous bridge part ii: Parametric study and dynamic load factor," *Engineering Structures*, vol. 29, no. 6, pp. 1064–1073, 2007.

[263] E.-S. Hwang and A. S. Nowak, "Simulation of dynamic load for bridges," *Journal of structural engineering*, vol. 117, no. 5, pp. 1413–1434, 1991.

[264] L. Kwasniewski, J. Wekezer, G. Roufa, H. Li, J. Ducher, and J. Malachowski, "Experimental evaluation of dynamic effects for a selected highway bridge," *Journal of performance of constructed facilities*, vol. 20, no. 3, pp. 253–260, 2006.

[265] E. J. OBrien, M. Quilligan, and R. Karoumi, "Calculating an influence line from direct measurements," in *Proceedings of the Institution of Civil Engineers-Bridge Engineering*, vol. 159, pp. 31–34, Thomas Telford Ltd, 2006.

[266] H. Zhao, N. Uddin, X. Shao, P. Zhu, and C. Tan, "Field-calibrated influence lines for improved axle weight identification with a bridge weigh-in-motion system," *Structure and Infrastructure Engineering*, vol. 11, no. 6, pp. 721–743, 2015.

[267] F. Moses, "Weigh-in-motion system using instrumented bridges," *Journal of Transportation Engineering*, vol. 105, no. 3, 1979.

[268] E. J. OBrien, L. Zhang, H. Zhao, and D. Hajializadeh, "Probabilistic bridge weigh-in-motion," *Canadian Journal of Civil Engineering*, vol. 45, no. 8, pp. 667–675, 2018.

[269] E. Bell, P. Lefebvre, M. Sanayei, J. Sipple, M. Iplikcioglu, and B. Brenner, "Experimental load rating of a steel girder bridge using structural health monitoring and modeling," in *Bridge Maintenance, Safety, Management, Resilience and Sustainability: Proceedings of the Sixth International IABMAS Conference, Stresa, Lake Maggiore, Italy, 8-12 July 2012*, p. 322, CRC Press, 2012.

[270] B. o. T. S. U.S. Department of Transportation (USDOT), "National transportation statistics," tech. rep., U.S. Department of Transportation (USDOT), Washington, DC, 2018.

[271] P. Rattigan, E. OBrien, and A. Gonzalez, "The dynamic amplification on highway bridges due to traffic flow," *University College Dublin*, 2005.

[272] P. Van Overschee and B. De Moor, *Subspace identification for linear systems: Theory—Implementation—Applications*. Springer Science & Business Media, 2012.

[273] J. Kim, K. Kim, and H. Sohn, "Subspace model identification of guided wave propagation in metallic plates," *Smart materials and structures*, vol. 23, no. 3, p. 035006, 2014.

[274] B. F. Spencer Jr, V. Hoskere, and Y. Narazaki, "Advances in computer vision-based civil infrastructure inspection and monitoring," *Engineering*, 2019.

[275] H. Salehi and R. Burgueno, "Emerging artificial intelligence methods in structural engineering," *Engineering structures*, vol. 171, pp. 170–189, 2018.

[276] R. Wang, L. Li, and J. Li, "A novel parallel auto-encoder framework for multi-scale data in civil structural health monitoring," *Algorithms*, vol. 11, no. 8, p. 112, 2018.

[277] C. S. N. Pathirage, J. Li, L. Li, H. Hao, W. Liu, and P. Ni, "Structural damage identification based on autoencoder neural networks and deep learning," *Engineering Structures*, vol. 172, pp. 13–28, 2018.

[278] J. Liu, S. Chen, M. Bergés, J. Bielak, J. H. Garrett, J. Kovačević, and H. Y. Noh, "Diagnosis algorithms for indirect structural health monitoring of a bridge model via dimensionality reduction," *Mechanical Systems and Signal Processing*, vol. 136, p. 106454, 2020.

[279] I. Sutskever, O. Vinyals, and Q. V. Le, "Sequence to sequence learning with neural networks," in *Advances in neural information processing systems*, pp. 3104–3112, 2014.

[280] H. Wilms, M. Cupelli, and A. Monti, "Combining auto-regression with exogenous variables in sequence-to-sequence recurrent neural networks for short-term load forecasting," in *2018 IEEE 16th International Conference on Industrial Informatics (INDIN)*, pp. 673–679, IEEE, 2018.

[281] D. Salinas, V. Flunkert, J. Gasthaus, and T. Januschowski, "Deepar: Probabilistic forecasting with autoregressive recurrent networks," *International Journal of Forecasting*, 2019.

[282] P. Malhotra, A. Ramakrishnan, G. Anand, L. Vig, P. Agarwal, and G. Shroff, "Lstm-based encoder-decoder for multi-sensor anomaly detection," *arXiv preprint arXiv:1607.00148*, 2016.

[283] L. Lennart, "System identification: theory for the user," *PTR Prentice Hall, Upper Saddle River, NJ*, pp. 1–14, 1999.

[284] T. Mikolov, M. Karafiát, L. Burget, J. Černockỳ, and S. Khudanpur, "Recurrent neural network based language model," in *Eleventh annual conference of the international speech communication association*, 2010.

[285] S. Hochreiter and J. Schmidhuber, "Long short-term memory," *Neural computation*, vol. 9, no. 8, pp. 1735–1780, 1997.

[286] J. Chung, C. Gulcehre, K. Cho, and Y. Bengio, "Empirical evaluation of gated recurrent neural networks on sequence modeling," *arXiv preprint arXiv:1412.3555*, 2014.

[287] O. Bahrami, R. Hou, W. Wang, and J. P. Lynch, "Time series forecasting to jointly model bridge responses," in *Tenth International Conference on Bridge Maintenance, Safety and Management (IABMAS)*, IABMAS JAPAN, 2020.

[288] F. H. A. U.S. Department of Transportation (USDOT), "Traffic monitoring guide," tech. rep., U.S. Department of Transportation (USDOT), Washington, DC, 2016.

[289] Y. Yu, C. Cai, and L. Deng, "State-of-the-art review on bridge weigh-in-motion technology," *Advances in Structural Engineering*, vol. 19, no. 9, pp. 1514–1530, 2016.

[290] N. Zolghadri, M. W. Halling, N. Johnson, and P. J. Barr, "Field verification of simplified bridge weigh-in-motion techniques," *Journal of Bridge Engineering*, vol. 21, no. 10, p. 04016063, 2016.

[291] E. J. O'Brien, C. Rowley, A. González, *et al.*, "A regularised solution to the bridge weigh in motion equations," *International Journal of Heavy Vehicle Systems*, vol. 16, no. 3, pp. 310–327, 2009.

[292] Z. Zhao, N. Uddin, and E. J. O'Brien, "Bridge weigh-in-motion algorithms based on the field calibrated simulation model," *Journal of Infrastructure Systems*, vol. 23, no. 1, p. 04016021, 2017.

[293] A. Žnidarič, J. Kalin, and M. Kreslin, "Improved accuracy and robustness of bridge weigh-in-motion systems," *Structure and Infrastructure Engineering*, vol. 14, no. 4, pp. 412–424, 2018.

[294] W. He, L. Deng, H. Shi, C. Cai, and Y. Yu, "Novel virtual simply supported beam method for detecting the speed and axles of moving vehicles on bridges," *Journal of Bridge Engineering*, vol. 22, no. 4, p. 04016141, 2017.

[295] C. J. Wall, R. E. Christenson, A. McDonnell, and A. Jamalipour, "A non-intrusive bridge weigh-in-motion system for a single span steel girder bridge using only strain measurements," *Rep. SPR-2251*, vol. 7, 2009.

[296] P. Chatterjee, E. OBrien, Y. Li, and A. González, "Wavelet domain analysis for identification of vehicle axles from bridge measurements," *Computers & structures*, vol. 84, no. 28, pp. 1792–1801, 2006.

[297] Y. Yu, C. Cai, and L. Deng, "Vehicle axle identification using wavelet analysis of bridge global responses," *Journal of Vibration and Control*, vol. 23, no. 17, pp. 2830–2840, 2017.

[298] Y. Zhang, *Scalable Data Management and Data-Driven Analytics for Structural Condition Assessment using Structural Monitoring Data.* PhD thesis, University of Michigan, Ann Arbor, 2016.

[299] C.-D. Pan, L. Yu, H.-L. Liu, Z.-P. Chen, and W.-F. Luo, "Moving force identification based on redundant concatenated dictionary and weighted l1-norm regularization," *Mechanical Systems and Signal Processing*, vol. 98, pp. 32–49, 2018.

[300] W. He, T. Ling, E. J. OBrien, and L. Deng, "Virtual axle method for bridge weigh-in-motion systems requiring no axle detector," *Journal of Bridge Engineering*, vol. 24, no. 9, p. 04019086, 2019.

[301] N. Gagarine, I. Flood, and P. Albrecht, "Weighing trucks in motion using gaussian-based neural networks," in *[Proceedings 1992] IJCNN International Joint Conference on Neural Networks*, vol. 2, pp. 484–489, IEEE, 1992.

[302] N. Gagarin, I. Flood, and P. Albrecht, "Computing truck attributes with artificial neural networks," *Journal of Computing in Civil Engineering*, vol. 8, no. 2, pp. 179–200, 1994.

[303] S. Kim, J. Lee, M.-S. Park, and B.-W. Jo, "Vehicle signal analysis using artificial neural networks for a bridge weigh-in-motion system," *Sensors*, vol. 9, no. 10, pp. 7943–7956, 2009.

[304] T. Kawakatsu, K. Aihara, A. Takasu, and J. Adachi, "Deep sensing approach to single-sensor vehicle weighing system on bridges," *IEEE Sensors Journal*, vol. 19, no. 1, pp. 243–256, 2018.

[305] J. Cheng, L. Dong, and M. Lapata, "Long short-term memory-networks for machine reading," *arXiv preprint arXiv:1601.06733*, 2016.

[306] Z. Lin, M. Feng, C. N. d. Santos, M. Yu, B. Xiang, B. Zhou, and Y. Bengio, "A structured self-attentive sentence embedding," *arXiv preprint arXiv:1703.03130*, 2017.

[307] J. A. Prozzi and F. Hong, "Effect of weigh-in-motion system measurement errors on load-pavement impact estimation," *Journal of Transportation Engineering*, vol. 133, no. 1, pp. 1–10, 2007.